EJA

European Journal of Anatomy

Volume 28 - Number 1 January 2024

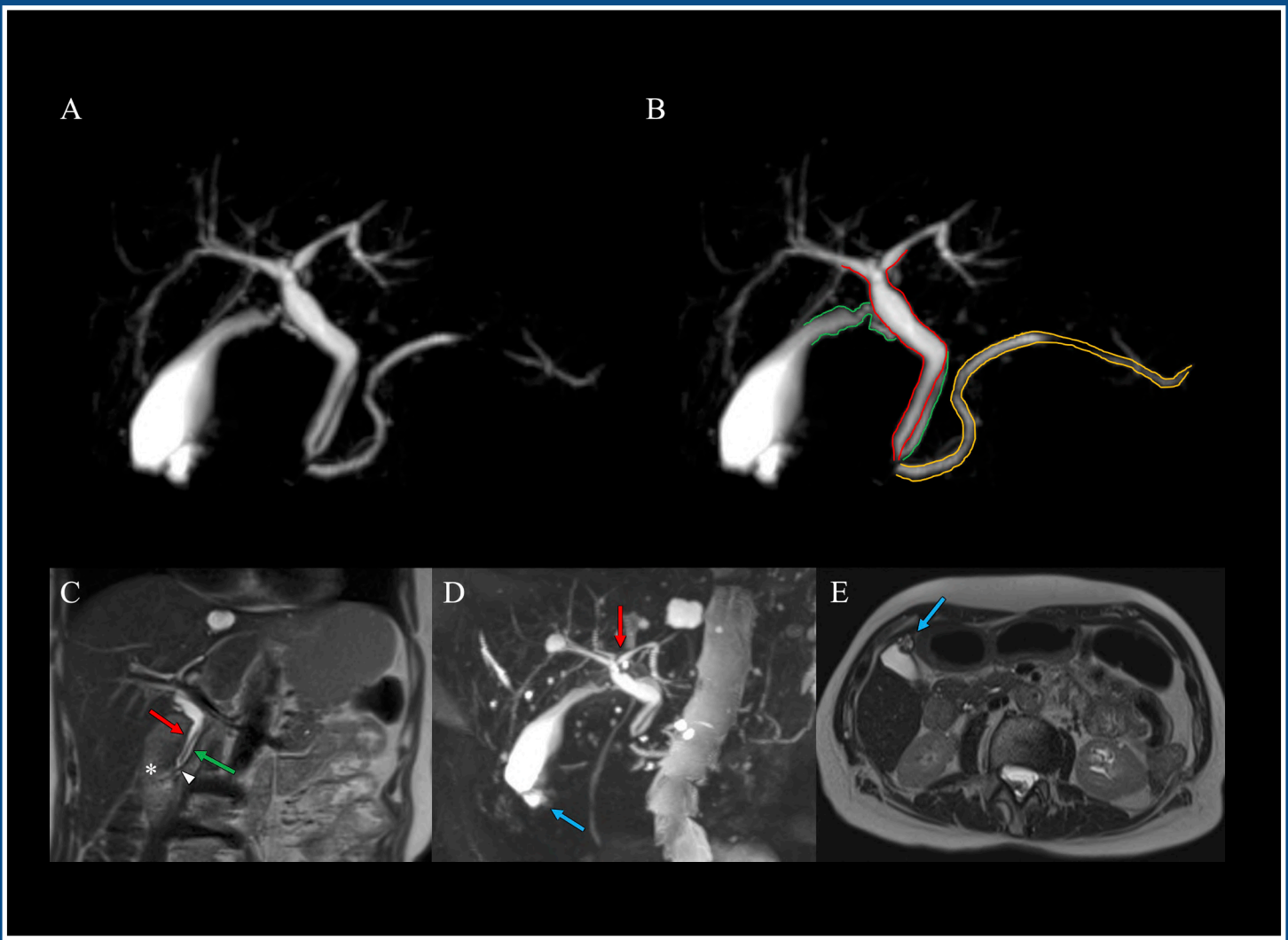

Indexed in:

CLARIVATE
- JCR:2020
- Q4 (21/23)
- I.F. J.C.I.: 0.19

DIALNET

EMBASE / Excerpta Medica

SCOPUS
- SJCR: 2020
- Q4 (31/39)
- I.F.: 0.162

Emerging Sources Citation Index

LATINDEX. Catálogo v1.0 (2002-2017)

Official Journal of the Spanish Society of Anatomy

Published by: **LOKI & DIMAS**

www.eurjanat.com

EJA
European Journal of Anatomy

Volume 28 - Number 1 January 2024

ORIGINAL ARTICLES

CASE REPORT

REVIEW

The relationship between body mass index and lower extremity biomechanics in children aged 10-12 years: a comprehensive analysis

Carlos Lahoz[1], Jorge Pérez-Rey[2], David González[3], José Gallart[3], Mercedes Ruidíaz[4], Mª José Luesma[2]

[1] Department of Education of the Government of Navarra, Santos Justo y Pastor Public School, Fustiñana, Navarra, Spain

[2] Department of Human Anatomy and Histology, University of Zaragoza, 50009 Zaragoza, Spain

[3] Private Practice, Gallart & González Podiatric Clinic, 50004, Zaragoza, Spain

[4]Department of Physiatry and Nursing, University of Zaragoza, 50009 Zaragoza, Spain

SUMMARY

Childhood obesity has emerged as a global health concern leading to complications, such as bones and muscles misalignment of knees, flat feet and changes in walking patterns. Although some studies have individually linked these conditions to body mass index (BMI), the relationship between these variables needs to be explored. This study aimed to investigate the associations between BMI and knee position, foot position and plantar footprint in children aged 10 to 12 years. Data were collected from 59 children by measuring their BMI, knee alignment, foot position and plantar footprint. Spearman's correlation coefficient was used to examine the relationship between BMI and inter-malleolar distance (DIM), foot position and plantar footprint. The Mann-Whitney U test was used to compare these variables between boys and girls (p-value < 0.05).

Higher BMI values were associated with higher DIM in both boys and girls. Furthermore, we observed that genu valgum was positively correlated with foot pronation and a flattened plantar footprint. No significant differences were found in relation to BMI, variations in foot position or footprint types. Our research provides evidence that there is a connection, between BMI and genu valgum in children between the ages of 10 and 12. We have also found a correlation between genu valgum and foot pronation among children in this age group. These findings highlight the significance of addressing childhood obesity to prevent any health issues.

Keywords: Body mass index – Paediatric obesity – Genu valgum – Flatfoot – Biomechanics

Corresponding author:
M.J. Luesma, PhD. Department of Human Anatomy and Histology, University of Zaragoza, Calle Domingo Miral s/n, 50009 Zaragoza, Spain. Phone: +34 656230642. E-mail: mjluesma@unizar.es

Submitted: September 14, 2023. **Accepted:** October 7, 2023

https://doi.org/10.52083/XRNO9569

INTRODUCTION

The human body is a system with interconnected parts that influence each other, providing functionality and overall well-being. One area of interest in biomechanics is the study of the impact of body mass index (BMI) on knee alignment, foot position and plantar footprint type (Domjanic et al., 2015). Investigating the interaction between these variables is crucial for understanding the underlying mechanisms influencing gait and foot function, as well as identifying risk factors associated with foot-related dysfunctions and injuries (Hoang et al., 2023).

Childhood obesity has become a major global health problem (Liebert, 2010). In recent years, its prevalence has raised concern worldwide. According to a report by the World Health Organization, the number of obese or overweight children and adolescents aged 5-19 years exceeded 340 million in 2021 (Jankowicz-Szymanska and Mikolajczyk, 2016).

Children who are overweight or obese have an increased risk of developing type 2 diabetes and cardiovascular disease in adulthood. In addition, excess weight in children is associated with musculoskeletal problems, as well as valgus misalignment of the knees or flat feet (Ratu Alicia, 2023; Ryzhov et al., 2020). It can also affect balance, posture, and the ability to move efficiently, and may even increase the risk of osteoarthritis at an early age (Calcaterra et al., 2022).

Genu valgum is a pathological condition characterised by a misalignment in the frontal plane of the knee joint, which can affect stability, biomechanics and energy efficiency during gait (Shapouri et al., 2019). The occurrence of this phenomenon can be attributed to genetic factors, trauma or specific medical conditions, with its prevalence in obese children aged 10-12 years being 53.3% (Putri et al., 2020).

Moreover, current evidence suggests that there is a correlation between foot position and BMI, revealing a higher prevalence of pronated feet among individuals with higher BMI values (Carvalho et al., 2017) and in turn, pronated feet are often associated with flat feet (Sadeghi-Demneh et al., 2015). Flat feet are a condition in which the medial longitudinal arch of the foot is decreased or absent. This condition is seen in up to 10% of the childhood population (Boryczka-Trefler et al., 2021) and can lead to a different gait patterns, which can make walking or running biomechanically less efficient leading to premature fatigue, or to foot, ankle and leg pain (Kayll et al., 2022).

Although there is strong evidence suggesting individual associations between each of these conditions with BMI, there is a lack of research that comprehensively addresses the intricate relationships between each of the lower limb joints with each other and with BMI (Jankowicz-Szymanska and Mikolajczyk, 2016).

Gaining a comprehensive understanding of the complex relationship between these variables is of utmost importance in implementing a holistic preventive strategy to address childhood obesity and its associated musculoskeletal complications. To achieve this goal and complement the current scientific literature, the present study aims to analyse the relationship between BMI and knee position in the transverse plane, foot position and plantar footprint together in children aged 10-12 years.

MATERIALS AND METHODS

Participants

The sample was taken from the Primary Education classes of the San Bartolomé Public School in Ribaforada (Navarra), with the prior acceptance of the school. The study included students in 5th and 6th grade of primary school enrolled in the 2021-22 academic year, who provided consent to participate in the research signed by their parents and/or guardians. Pupils who were not between 10 and 12 years of age were excluded. Finally, 59 pupils were included in the study. The principles of the Declaration of Helsinki were followed. The protocol was verified and approved by the Research Ethics Committee of the

Community of Aragon (CEICA) (Registration nº: PI20/263), and the legal guardians of the children signed the informed consent.

Protocol

To calculate body mass index, participants were weighed barefoot using a portable electronic scale. The child stood in the centre of the scale platform distributing his/her weight between both feet, facing forward, with arms alongside the body, and without any movement. Light clothing was allowed, excluding long trousers, shoes and sweatshirt.

Height was measured with a standard tape measure at the highest point of the head, the hair being compressed. Body mass index (BMI, weight in kg divided by height in metres squared) was calculated, determining the weight status of the participants (normal weight, overweight and obese) using BMI cut-off points according to the tables established by the World Health Organisation according to age and sex.

Knee alignment was assessed with the limbs in extension, in neutral rotation and trying to bring the two legs together, so that either the femoral condyles or the tibial malleoli touched (Gupta et al., 2021). It was measured with a tape measure expressed in centimetres (cm). If the participant, when bringing the legs together, joined the knees before the malleoli, the inter-malleolar distance (IMD) was measured and its value was expressed in positive values.

If, on the other hand, the malleolus was touched first, the inter-condylar distance (ICD) was measured, representing this measurement in negative values. The result of this measurement gives a variable called inter-malleolar-intercondylar distance (IMD-IC) which allows us to work as a quantitative variable. Given that the result of this variable is affected by the height of the child (length of the lower limbs), the relative intermaleolar-intercondylar distance (relative IMD-IC) is taken into account using the following equation: Relative DIM-IC= DIM-IC (cm)/ Height (cm) x 100.

Foot position was assessed statically using the Foot Posture Index (FPI-6) through 6 visual criteria about the rearfoot, midfoot and forefoot (Redmond et al., 2006). This clinical instrument is used to score values from -2 to +2 for each of the 6 criteria that the FPI-6 gives according to the degree of pronation or supination. The result of this method gives an FPI value ranging from -12 to +12. This result allows the foot to be classified into different positions, as shown in Table 1. Negative FPI values represent a supination position (the lower the value, the greater the supination), and the higher the FPI value the greater the degree of pronation, which allows us to work quantitatively with the numerical value of the FPI

Table 1. Typification of foot position with FPI values according to Redmond et al. (2006).

FPI values	Position of the foot	Position of the foot (simplified)
-5 a -12	Foot in extreme supination	Foot in supination position
-1 a -4	Foot in supination	
0 a +5	Foot in normal position	Foot in normal position
+6 a +9	Pronating foot	
+10 a+12	Foot in extreme pronation	Foot in a pronated position

and as a nominal qualitative variable according to the classification of the authors by the score obtained (Table 1).

The acquisition of the plantar footprint was performed with an ink pedigraph with which each subject in an orthostatic position left their footprints printed on a piece of paper as described by Gonzalez-Martin et al. (2021) in their study. Measurements to determine the type of footprint were performed according to the method described by Hernández Corvo (1989) and Lara Diéguez et al. (2011). This is a quantitative method by which a numerical value is obtained, the Hernández Corvo Index (IHC), which represents the percentage of the width of the midfoot area concerning the forefoot. Its value ranges from 0 to 100 and allows the classification of the plantar footprint into different types according to this value, ranging from flat feet (IHC values close to 0) to extreme cavus (IHC values close to 100) (Table 2). This method allows working quantitatively with the value of the Hernández Corvo Index and presents good precision, with high inter-observer reproducibility, obtaining a high Lin's concordance correlation coefficient (>0.98) (Buendía- Lozada, 2011).

Data analysis

Data were collected in an Excel spreadsheet (Microsoft Office Professional Plus 2016, Microsoft Inc., USA). IBM SPSS software version 24 (SPSS®IBM® Corporation, New York, USA) was used for data analysis. A descriptive analysis of the variables disaggregated by gender was performed. It was checked whether the analysed variables followed normality criteria for the choice of statistical tests. Spearman's correlation coefficient was used to analyse the correlation between BMI and relative DIM-IC, FPI and IHC, given the absence of normality, and the Mann-Whitney U-test was used to compare the variables between boys and girls.

Statistical significance was assumed for a p-value < 0.05.

RESULTS

Of the 59 students, 33 (55.9%) were girls and 26 (44.1%) were boys with a mean age of 11.49 (±0.66). The mean BMI was 20.44 (±4.27) with no significant differences in BMI between boys and girls in the study (p-value =0.29). According to this parameter, 30 students (50.8%) had a nor-

Table 2. Typification of plantar footprint according to Hernandez Corvo Index value.

IHC (%)	Type of foot	Type of foot (simplified)
0-34	Flat feet	Flat feet
35-39	Flat/normal feet	
40-54	Normal foot	Normal foot
55-59	Normal/cavity foot	
60 74	Pes cavus	Pes cavus
75-84	Strong pes cavus	
85 100	Extreme pes cavus	

Table 3. BMI and body status.

Descriptive characteristics of BMI and body status according to WHO tables.							
	n	**Age (years)**	**BMI**	**Body status n (% within gender)**			
				Underweight	**Normoweight**	**Overweight**	**Obesity**
Children	26	11.50(±0.66)	20.84(±3.78)	0 (0%)	12 (46.2%)	6 (23.1%)	8 (30.8%)
Girls	33	11.48(±0.66)	20.13(± .65)	2 (6.1%)	18 (54.5%)	8 (24.2%)	5 (15.2%)
Total	59	11.49(±0.66)	20.44(± .27)	2 (3.4%)	30 (50.8%)	14 (23.7%)	13 (22%)

Mean (standard deviation)
n= number of cases; BMI (body mass index)

mal body weight status, 14 (23.7%) were overweight, 13 (22%) obese and 2 cases (3.4%) were underweight. The body status of the students according to gender is described in Table 3.

The mean relative DIM-IC obtained in the total sample was 1, 67 (±1.76). In the boys' group, it was 1.59 (±2.08) and 1.74 (±1.5) in the girls, with no significant differences between the two groups (p-value =0.89).

The mean FPI value for the feet of the total sample (n= 118) was 3 (±4.29); for boys' feet (n=52) the mean value was 2.56 (±4.41) and for girls' feet (n=66) it was 3.35 (±4.29). The Mann-Whitney U test, with a p-value of 0.61 showed no difference between genders. The classification of foot position according to the value of this parameter is described in Table 4.

The mean value of the IHC of the 118 footprints analysed was 54.06 ± 12.81; the difference between the mean value of the IHC according to gender was significant with a p-value = 0.014 in the Mann-Whitney U-test. The mean value of the footprints for boys was 50.76 ± 14.51 vs. 54.06 ± 12.81 for girls. The distribution by gender of the footprint typology obtained after the IHC analysis is shown in Table 4.

Correlation analysis between BMI and the variables analysed found a direct and moderate association between BMI and relative DIM-DIC both in the total sample (rho=0.47; p-value = 0.00) and separated by gender (Boys: rho=0.63; p-value = 0.00 / Girls: rho= 0.4; p-value = 0.02).

In contrast, there was no evidence of an association between BMI and total and gender- disaggregated values of FPI and IHC (p-value < 0.05) (Table 5).

A direct and weak association (rho < 0.3) was found between the values of relative DIM-DIC and FPI when analysing the data of the sample as a whole (rho= 0.27; p-value =0.00) and in the group of girls (rho=0.29; p-value =0.01), so that the higher the DIM, the greater the pronation of the foot, but no such correlation was found in the group of boys (Table 5).

A weak and indirect association was found between the relative DIM-DIC and IHC values for the total sample (rho= -0.185; p-value =0.04), so that the greater the inter-malleolar distance the greater the flattening of the plantar footprint. This relationship was not found when analysing these variables disaggregated by gender (Table 5).

Correlation analysis between FPI and IHC values determined that there is an indirect and moderate association between these two variables, both in the total sample (rho=- 0.39; p-val-

ue = 0.00), and separated by gender (Boys: rho=-0.49; p-value = 0.00 / Girls: rho= -0.34; p-value = 0.00), that is, the greater the degree of pronation the greater the degree of flattening.

DISCUSSION

The present study aimed to investigate the effect of body weight on frontal plane knee posi-

Table 4. Description of the variables foot position and footprint type; comparison between boys and girls and statistical significance.

		Total n (%)		Children n (%)		Girls n (%)		Sig*
Foot position (FPI-6)	**Neutral foot**	59	50%	28	53.8%	31	47%	0.67[a]
	Pronated foot	39	33.1%	15	28.8%	24	36.4%	
	Supinated foot	20	16.9%	9	17.3%	11	16.7%	
Plantar footprint type (IHC)	**Flat feet**	8	6.8%	5	9.6%	3	4.5%	0.051[b]
	Flat/normal feet	3	2.5%	0	0%	3	4.5%	
	Normal foot	42	35.6%	24	46.2%	18	27.3%	
	Pes cavus	24	20.3%	9	17.3%	15	22.7%	
	Strong pes cavus	41	34.7%	14	26.9%	27	40.9%	

Table 5. Correlation between BMI and relative DIM-DIC. FPI and IHC values by gender and statistical significance for Spearman correlation coefficient test.

	Children		Girls		Total	
	Correlation Coefficient	**Sig**	**Correlation Coefficient**	**Sig**	**Correlation Coefficient**	**Sig**
BMI and relative DIM-DIC	0.630	**0.001**	0.403	**0.02**	0.474 0.**00**	
BMI and IPF	-0.004	0.97	0.109	0.38	0.043 0.64	
BMI and IHC	-0.039	0.78	-0.21	0.08	-0.171 0.06	
Relative DIM-DIC and FPI	0.239	0.08	0.296	**0.01**	0.277 0.**00**	
Relative DIM-DIC and IHC	-0.257	0.06	-0.094	0.45	-0.185 0.**04**	
IPF and HCI	-0.491	**0.00**	-0.342	**0.00**	-0.394 0.**00**	

tion, foot position and plantar footprint type, and whether there is an interrelationship between all these variables. It is important to note that the present study focused specifically on the relationship between BMI and variables measuring lower limb joint alignment without considering other potential factors that may influence these variables.

Genu valgum is a dysfunction of the knee joint characterised by inward angulation of the knees, causing a misalignment of the lower limbs, so that when the knees are together the inner malleoli of the ankle do not touch. This condition is often seen in people with excess body weight, as this causes an increased load on the lower limb joints and can lead to misalignment of the knee joint (Khandha et al., 2016), indeed our results show that children with a higher BMI were more likely to have a valgus deviation of the knee.

On the other hand, our results showed no statistically significant relationship between BMI and foot position or plantar footprint type, suggesting that pronated foot or plantar footprint flattening is not dependent on the weight of the subject and that there are therefore other factors that cause these mismatches. These findings contrast with the results of previous studies that have found associations between BMI and foot position (Molina-García et al., 2023; Escalona-Marfil et al., 2022; Bann et al., 2022). Other study showed that subjects with higher BMI were at higher risk of ossification of the posterior longitudinal ligament and the yellow ligament of the spine, which may affect foot position (Zhao et al., 2022). In our study, we did not record variables relating to these spinal ligaments.

When we studied the relationship between knee alignment with foot position and plantar footprint type, we found that an increase in the relative inter-malleolar distance (genu valgum) was associated with an increase in foot pronation, both in the overall analysis of the population and in the group of girls, and that this alteration of the knee was also related to a flattening of the plantar footprint.

With the above mentioned, it seems plausible to hypothesise that in these interrelationships, valgus knee position is more of a risk factor for pronated foot position and flat footprint than BMI, and although genu valgus does have a direct relationship with weight, the fact that overweight or obesity has no impact on foot position or footprint raises the question of what other factors influence foot position and footprint type. Bourgleh et al. (2019) state in their study that genu valgum can lead to altered biomechanics of the lower limb and is also related to increased pronation of the foot, which in turn can contribute to the development of flat feet which supports the results found in our research.

When we independently analysed the relationship between foot position and footprint type, we found that the greater the degree of foot pronation, the greater the flattening of the footprint. This finding reinforces current evidence showing a relationship between the two variables (Latey et al., 2018).

Although clinical measurement by goniometer and radiographic measurement of the femorotibial angle provides a more accurate way of quantifying genu valgum (Liou et al., 2022; Colazo et al., 2020), at the clinical level it has been shown that the measurement of the intermalleolar distance is a valid system for the diagnosis of genu valgum (Ciaccia et al., 2017; Witvrouw et al., 2009).

However, to estimate the degree of genu valgum realistically we opted to utilize the DIM method as explained in our methodology. While this decision does not impact our obtained results, it does pose a limitation when comparing our findings to studies that directly measure the angle, between the thigh and leg for quantifying knee deviation. It is worth noting that our research specifically focuses on a population and caution should be exercised when attempting to draw associations within adult populations.

To address this limitation and enhance the body of evidence on this subject future research should explore these relationships across age

groups. Moreover, future studies need to consider factors that may influence limb alignment to establish a direct relationship between weight and such alterations.

In conclusion, our study provides insights into the connection between BMI, genu valgum, foot position and footprint type. The findings support research indicating a correlation between BMI and genu valgum as well as between genu valgum and foot pronation. However, no significant differences were observed in terms of BMI, foot position or footprint type.

These findings show that the relationship, between these variables is intricate and indicate that there could be factors influencing foot position and type of footprint. It is important to research to better understand how these mechanisms interact and explore interventions, for addressing these lower limb conditions.

REFERENCES

BANN D, WRIGHT L, HARDY R, WILLIAMS DM, DAVIES NM (2022) Polygenic and socioeconomic risk for high body mass index: 69 years of follow-up across life. *PLoS Genet,* 18(7): e1010233.

BORYCZKA-TREFLER A, KALINOWSKA M, SZCZERBIK E, STĘPOWSKA J, ŁUKASZEWSKA A, SYCZEWSKA M (2021) Effect of plano-valgus foot on lower-extremity kinematics and spatiotemporal gait parameters in children of age 5-9. *Diagnostics,* 12(1): 2.

BOURGLEH SM, NEMEȘ RN, HETAIMISH BM, CHIUȚU LC (2019) Prevalence of musculoskeletal normal variations of the lower limbs in the paediatric orthopaedic clinic. *Saudi Med J*, 40(9): 930-935.

BUENDÍA-LOZADA E (2011) Reproductibilidad del instrumento HC. *Rev Int Med Cienc Act Fís Deporte,* 10(41): 1-13.

CALCATERRA V, MARIN L, VANDONI M, ROSSI V, PIRAZZI A, GRAZI R, PATANÉ P, SILVESTRO GS, CARNEVALE-PELLINO V, ALBANESE I, FABIANO V, FEBBI M, SILVESTRI D, ZUCCOTTI G (2022) Childhood obesity and incorrect body posture: impact on physical activity and the therapeutic role of exercise. *Int J Environ Res Public Health,* 19(24): 16728.

CARVALHO BKGD, PENHA PJ, PENHA NLJ, ANDRADE RM, RIBEIRO AP, JOÃO SMA (2017) The influence of gender and body mass index on the FPI-6 evaluated foot posture of 10- to 14-year-old school children in São Paulo, Brazil: a cross-sectional study. *J Foot Ankle Res,* 10: 1.

CIACCIA MCC, PINTO CN, GOLFIERI FDC, MACHADO TF, LOZANO LL, SILVA JMS, RULLO, VEVV (2017) Prevalência de genu valgo em escolas públicas do ensino fundamental na cidade de Santos (SP), Brasil. *Rev Paul Pediatr*, 35(4): 443-447.

COLAZO JM, REASONER SA, HOLT G, FAUGERE MCM, DAHIR KM (2020) Hereditary hypophosphatemic rickets with hypercalciuria (HHRH) presenting with genu valgum deformity: treatment with phosphate supplementation and surgical correction. *Case Rep Endocrinol,* 2020: 1047327.

DOMJANIC J, SEIDLER H, MITTEROECKER P (2015) A combined morphometric analysis of foot form and its association with sex, stature, and body mass. *Am J Phys Anthropol*, 157(4): 582-591.

ESCALONA-MARFIL C, PRATS-PUIG A, ORTAS-DEUNOSAJUT X, FONT-LLADÓ R, RUIZ-TARRAZO X, EVANS AM (2022) Children's foot parameters and basic anthropometry - do arch height and midfoot width change? *Eur J Pediatr,* 182(2): 777-784.

GONZÁLEZ-MARTIN C, FERNÁNDEZ-LÓPEZ U, MOSQUERA-FERNÁNDEZ A, BALBOA-BARREIRO V, GARCÍA-RODRÍGUEZ MT, SEIJO-BESTILLEIRO R, VEIGA-SEIJO R (2021) Concordance between pressure platform and pedigraph. *Diagnostics¸* 11(12): 2322.

GUPTA R, NAYYAR AK, GHATAK S (2021) Clinical measurement of intermalleolar distance in Western Indian population. *Int J Res Med Sci,* 9(2): 494-497.

HERNÁNDEZ CORVO R (1989) *Functional sports morphology: The locomotor system*. Paidotribo.

HOANG DV, AKTER S, INOUE Y, KUWAHARA K, FUKUNAGA A, ISLAM Z, NAKAGAWA T, HONDA T, YAMAMOTO S, OKAZAKI H, MIYAMOTO T, OGASAWARA T, SASAKI N, UEHARA A, YAMAMOTO M, KOCHI T, EGUCHI M, SHIRASAKA T, SHIMIZU M, NAGAHAMA S, HORI A, IMAI T, NISHIHARA A, TOMITA K, NISHIURA C, KONISHI M, KABE I, YAMAMOTO K, MIZOUE T, DOHI S (2021) Metabolic syndrome and the increased risk of medically certified long-term sickness absence: a prospective analysis among Japanese workers. *J Epidemiol,* 33(6): 311-320.

JANKOWICZ-SZYMANSKA A, MIKOLAJCZYK E (2016) Genu valgum and flat feet in children with healthy and excessive body weight. *Pediatr Phys Ther,* 28(2): 200-206.

KAYLL SA, HINMAN RS, BENNELL KL, BRYANT AL, ROWE PL, PATERSON KL (2022) The effect of biomechanical foot-based interventions on patellofemoral joint loads during gait in adults with and without patellofemoral pain or osteoarthritis: a systematic review protocol. *J Foot Ankle Res*, 15(1): 91.

KHANDHA A, MANAL K, WELLSANDT E, CAPIN J, SNYDER-MACKLER L, BUCHANAN TS (2016) Gait mechanics in those with/without medial compartment knee osteoarthritis 5 years after anterior cruciate ligament reconstruction. *J Orthop Res*, 35(3): 625-633.

LARA-DIÉGUEZ S, LARA-SÁNCHEZ AJ, ZAGALAZ-SÁNCHEZ ML, MARTÍNEZ-LÓPEZ EJ (2011) Analysis of different methods to evaluate the footprint. *Retos*, 19: 49-53.

LATEY PJ, BURNS J, NIGHTINGALE EJ, CLARKE JL, HILLER CE (2018) Reliability and correlates of the cross-sectional area of abductor hallucis and the medial belly of the flexor hallucis brevis measured by ultrasound. *J Foot Ankle Res,* 11: 28.

LIEBERT MA (2010) Reversing the epidemic of childhood obesity: the time is now! *Childhood Obesity,* 6(4): 161.

LIM JU, LEE JH, KIM JS, HWANG YI, KIM TH, LIM SY, YOO KH, JUNG KS, KIM YK, RHEE CK (2017) Comparison of World Health Organization and Asia-Pacific body mass index body mass index classifications in COPD patients. *Int J Chron Obstruct Pulmon Dis*, 12: 2465-2475.

LIOU YL, LEE WC, KAO HK, YANG WE, CHANG CH (2022) Genu valgum after distal femur extension osteotomy in children with cerebral palsy. *J Pediatr Orthop,* 42(4): e384-e389.

MOLINA-GARCÍA C, JIMÉNEZ-GARCÍA JD, VELÁZQUEZ-DÍAZ D, RAMOS-PETERSEN L, LÓPEZ-DEL-AMO-LORENTE A, MARTÍNEZ-SEBASTIÁN C, ÁLVAREZ-SALVAGO F (2023) Overweight and obesity: its impact on foot type, flexibility, foot strength, plantar pressure and stability in children from 5 to 10 years of age: descriptive observational study. *Children,* 10(4): 696.

PUTRI VRS, TIANING NW, INDRAYANI AW, WIBAWA A, THANAYA SAP (2020) Prevalence of genu valgum in children aged 10-12 years with excessive body weight (overweight/obesity) in Sanur Kaja Village, Denpasar. *J E K K*, 5(2): 77-81.

RATU-ALICIA DN (2023) Childhood obesity as a predictor of type 2 diabetes mellitus in adults: A systematic review. *J Adv Res Med Health Sci,* 9(5): 63-68.

REDMOND AC, CROSBIE J, OUVRIER RA (2006) Development and validation of a novel rating system for scoring standing foot posture: The Foot Posture Index. *Clin Biomech,* 21(1): 89-98.

RYZHOV PV, PIROGOVA NV, BAGDULINA OD, SHMELKOV AV (2020) Flat and valgus deformation of feet in children: ways of treatment (literature review). *Asp Vest Pov,* 20(5): 114-118.

SADEGHI-DEMNEH E, AZADINIA F, JAFARIAN F, SHAMSI F, MELVIN JMA, JAFARPISHE M, REZAEIAN Z (2015) Flatfoot and obesity in school-age children: a cross-sectional study. *Clin Obes*, 6(1): 42-50.

SHAPOURI J, AGHAALI M, AGHAEI M, IRANIKHAH A, AHMADI R, HOVSEPIAN S (2019) Prevalence of lower extremities' postural deformities in overweight and normal weight school children. *Iran J Pediatr*, 29(5): e89138.

WITVROUW E, DANNEELS L, THIJS Y, CAMBIER D, BELLEMANS J (2009) Does soccer participation lead to genu varum? *Knee Surg Sports Traumatol Arthrosc,* 17(4): 422-427.

ZHAO Y, XIANG Q, LIN J, JIANG S, LI W (2022) High body mass index is associated with an increased risk of the onset and severity of ossification of spinal ligaments. *Front Surg,* 9: 941672.

Decellularized fetal collagen exhibits chondroinductive potential for bone marrow-derived mesenchymal stem cells by enhancing glycosaminoglycan production

Soosai M. Amirtham[1*], Ganesh Parasuraman[2*], Jeya Lisha J[1], Deepak V. Francis[3], Abel Livingston[4], Grace Rebekah[5], Solomon Sathishkumar[1], Elizabeth Vinod[1,2]

[1] Department of Physiology, Christian Medical College, Vellore, India

[2] Centre for Stem Cell Research, (A unit of InStem, Bengaluru), Christian Medical College, Vellore, India

[3] Department of Anatomy, Christian Medical College, Vellore, India

[4] Department of Orthopaedics, Christian Medical College, Vellore, India

[5] Department of Biostatistics, Christian Medical College, Vellore, India

** Equal contribution*

SUMMARY

Articular cartilage repair is challenging due to limited access to reparative cells and a lack of self-healing mechanisms. Bone marrow-derived mesenchymal stem cells (BM-MSCs) are a promising therapeutic option, but their tendency to form fibrocartilage during repair necessitates the optimization of culture conditions. To overcome this limitation, optimizing in-vitro culture conditions with biological coating using extracellular matrix-derived proteins has been efficient in mimicking in-vivo cellular behavior. Fetal cartilage, with abundant collagen, proteoglycans and glycosaminoglycans has emerged as a potential source for cartilage repair. No studies have so far evaluated the effect of fetal cartilage-derived collagen on BM-MSCs. This study aimed to evaluate the chondro-inductive potential of decellularized collagen derived from fetal cartilage, which was used as a coating material for expansion of BM-MSCs.

The extraction of fetal collagen was performed from the tibiofemoral joint of a 36+4-week gestational age fetus. The freeze-dried collagen type II was reconstituted at a concentration of 10µg/ml and used to coat the culture flasks. Passage 3 BM-MSCs were divided into two groups: a) standard expansion medium (BM-MSCs) and b) collagen-coated plasticware (collagen-coated BM-MSCs). Growth kinetics, surface markers, gene expression, and differentiation potential were assessed. The decellularized collagen coating did not influence the growth kinetics, surface marker and gene expression of BM-MSCs. However, it positively influenced GAG accumulation and collagen type II deposition. Further studies utilizing

Corresponding author:
Dr. Elizabeth Vinod. Associate Professor/Adjunct Scientist. Department of Physiology/ Centre for Stem Cell Research (A unit of inStem, Bangalore), Christian Medical College, Vellore, India. Phone: +91 9677651977. E-mail: elsyclarence@cmcvellore.ac.in - ORCID: 0000-0001-7340-8320

Submitted: June 5, 2023. **Accepted:** July 8, 2023

https://doi.org/10.52083/KJJC3228

in-vivo models are warranted to evaluate the potential of collagen-coated BM-MSCs and exploit their adjuvant effect on chondrogenesis.

Key words: Fetal cartilage – Extracellular matrix collagen – Collagen type II – Chondrogenesis – BM-MSCs – Glycosaminoglycans

INTRODUCTION

Hyaline cartilage plays an integral role in the mobility and weight-bearing functions of the articular joint. Cartilage loss due to inflammation or trauma, compounded by its restricted intrinsic regenerative capacity, can lead to the progression of osteochondral defects and conditions such as osteoarthritis (Sophia Fox et al., 2009). The most common treatment strategies currently used include debridement, microfracture, and intraarticular injections of biological scaffolds such as hyaluronic acid or platelet rich plasma. Despite symptomatic relief and the proposed minimization of disease progression, these techniques do not provide sustained clinical benefits (Armiento et al., 2019). Therefore, cell-based therapies and tissue engineering have recently received considerable attention to facilitate cartilage regeneration with hyaline-like properties (Negoro et al., 2018).

Cell-based therapies using mesenchymal stem cells (MSCs) and chondrocytes have demonstrated promising results in clinical trials (Filardo et al., 2013; Zhang et al., 2019). Bone-marrow-derived mesenchymal stem cells (BM-MSCs), due to their ease of harvest and availability, proliferative potential, immunomodulatory and multilineage capabilities, have been the most commonly used MSCs. Despite functional improvements, MSCs display a predilection for a hypertrophic phenotype, resulting in fibrocartilage formation, thus a repair tissue with inferior biomechanical properties (Charlier et al., 2019; Mueller and Tuan, 2009). To circumvent this limitation, a crucial strategy involves the optimization of in-vitro cell culture conditions. One effective approach is the implementation of extracellular matrix-derived proteins as a biological coating, which has demonstrated efficacy in enhancing the cellular phenotype to closely mimic in-vivo behavior (Kleinman et al., 1987).

Fetal cartilage is another significant source that has been studied for its potential use in cartilage repair, specifically in conditions such as osteoarthritis (OA) and other degenerative joint disorders (Krivoruchko et al., 2014). Collagen is the main protein component of fetal cartilage, making up approximately 60-80% of the cartilage's dry weight (Quintin et al., 2010). Its unique characteristics include a higher concentration of chondroprogenitor cells, which further differentiate into chondrocytes that play a vital role in producing and maintaining the extracellular matrix of the cartilage (Choi et al., 2016). Second, fetal cartilage has a high concentration of extracellular matrix molecules, such as proteoglycans and glycosaminoglycans, that are essential for maintaining the structural integrity and mechanical properties of cartilage tissue (Fuchs et al., 2002). These molecules are critical for repairing and rebuilding damaged cartilage tissue.

Extracellular matrix (ECM) materials can be obtained from either cell-derived matrices secreted during in vitro culture or native tissues, with tissue-specific ECM reported to promote cell proliferation and lineage-specific differentiation by retaining biophysical and biochemical cues within native tissues (Benders et al., 2013). Decellularized ECM (Quintin et al., 2010) derived from cartilage tissues have been extensively researched as biological scaffolds for cartilage engineering due to their inherent components, unique structure, and micromechanical properties, which create a niche-like nanostructured microenvironment that supports chondrogenesis - cell adhesion, proliferation, migration, and differentiation (Schwarz et al., 2012; Yang et al., 2010).

Armed with their inherent properties, decellularized scaffolds seeded with stem cells are gaining attention in both basic research and clinical studies and have the potential for translating into functional tissues. No studies have so far evaluated the effect of fetal cartilage-derived collagen on BM-MSCs. The current study aimed to evaluate the chondro-inductive potential of decellularized collagen derived from fetal cartilage when

applied as a coating material for the expansion of BM-MSCs, using growth kinetics, surface marker expression, gene expression, biochemical GAG content, and differentiation study analysis. Additionally, the influence of fetal collagen on the hypertrophic markers was evaluated.

MATERIALS AND METHODS

Approval and study design

The study was performed after approval of the Institution Review Board and Ethics Committee. Following written informed consent, bone marrow aspirates were obtained from the surgical site of patients requiring total knee replacement surgery for severe OA (grade 4 Kellgren-Lawrence score). BM-MSCs were isolated from bone marrow aspirate, expanded to passage 3, and characterized using flow cytometry. After obtaining written informed consent from the parent the fetal cartilage sample was extracted from the tibiofemoral joint of a fetus at 36+4 weeks gestational age, following termination of pregnancy due to medical reasons associated with intrauterine death.

The fetal cartilage shavings were decellularized and lyophilized to obtain collagen, which was subsequently utilized to coat the culture flasks. The BM-MSCs at passage 3 were seeded onto flasks coated with collagen and uncoated flasks (control) at a loading density of 5000 cells/cm^2. The cells were cultured until they reached sub-confluence. The harvested cells were then subjected

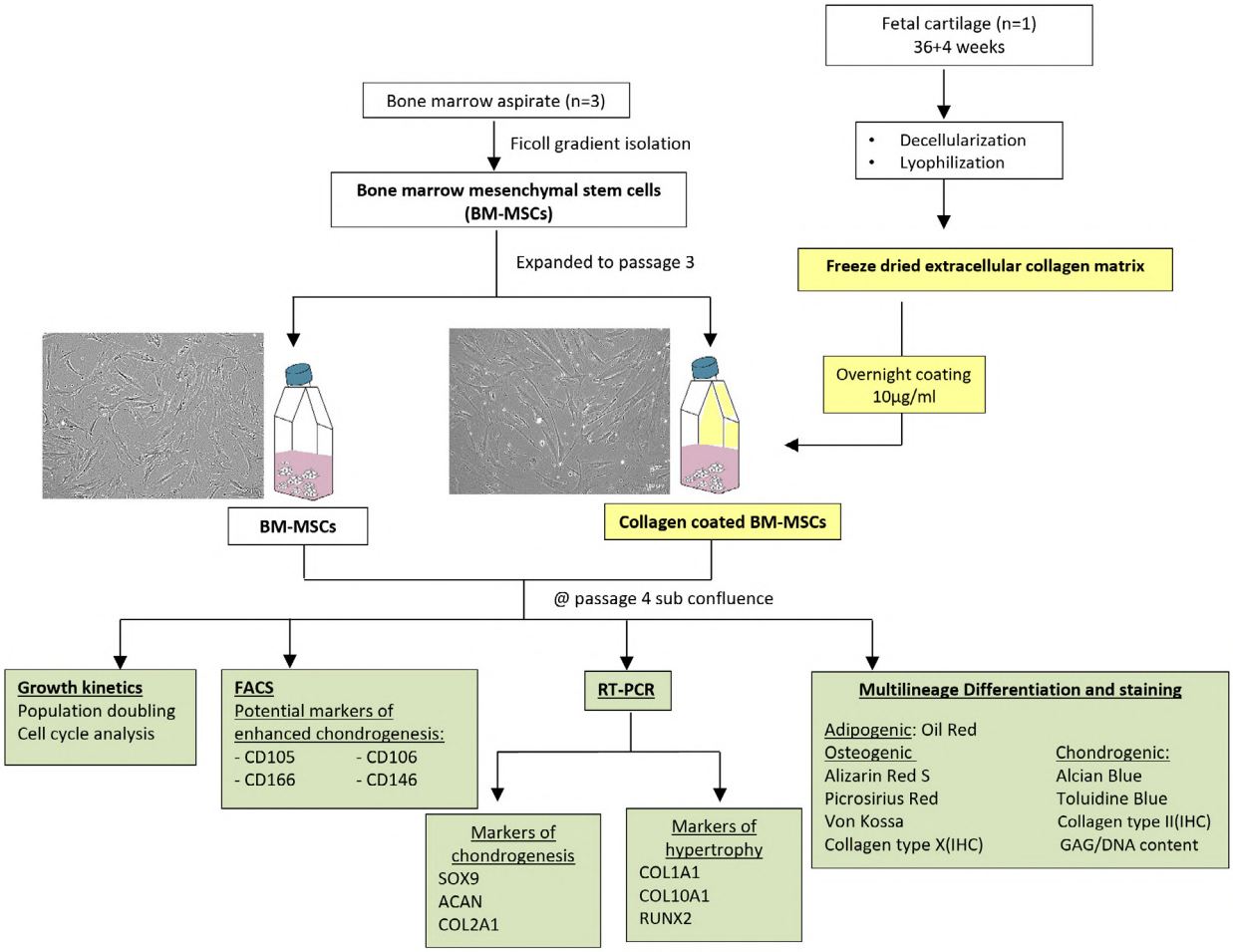

Fig. 1.- Study algorithm describing the evaluation parameters of bone marrow derived mesenchymal stem cells (BM-MSCs) grown under two culture conditions, namely the standard culture conditions (BM-MSC) and expansion on collagen coated plates (collagen coated BM-MSCs), which were derived from fetal cartilage. FACS: fluorescence activated cell sorting, CD: cluster of differentiation, SOX-9:(sex-determining region Y)-box 9, ACAN: aggrecan, COL: collagen, RUNX2: Runt-related transcription factor-2, IHC: immunohistochemistry and GAG: glycosaminoglycan.

to analysis based on the following parameters: a) growth kinetics, including population doubling and cell cycle analysis; b) FACS analysis for potential markers of chondrogenesis; c) quantitative real-time polymerase chain reaction (qRT-PCR) analysis to examine markers of chondrogenesis and hypertrophy; and d) trilineage differentiation, along with confirmatory staining (Fig. 1).

Extraction and characterization of fetal collagen

The extraction of fetal collagen was performed using a modified protocol originally described by Feng et al. (2020). In brief, the tibio-femoral joint from the fetus was dissected and immediately placed in sterile phosphate-buffered saline solution (PBS). The joint was then transferred to a biosafety cabinet, washed in PBS and cleared of its external tissues. The cartilage was harvested and minced to 6-8 mm size using a 22-scalpel blade (Fig. 2A). A small portion of the section was formalin-fixed and subjected to DAPI (4',6-diamidino-2-phenylindole) staining to confirm the presence of nuclei before decellularization (Fig. 2D). The remaining cryo-sectioned cartilage was washed with PBS to remove the optimal cutting temperature (OCT) compound residue and immersed at 25°C in 1% sodium dodecyl sulfate (SDS) for a period of 48 hours; this was followed by a wash with deionized water (Fig. 2B-E). This step was repeated three more times. DAPI staining was performed on the decellularized sheets for immunofluorescence analysis to confirm the absence of nuclei (Fig. 2F). The decellularized cartilage sections were transferred to a 100µM cell strainer and thoroughly washed to remove the SDS. The sections and the cell strainer were placed in a 6-well plate and pre-frozen overnight at -80˚C. The following day, the tissue was transferred to a freeze-dryer and processed for lyophilization for 6 h (Fig. 2G). 10 mg freeze-dried extracellular matrix was further digested with pepsin (1mg/ml; Sigma) containing 0.01N HCl, using a shaking water bath maintained at 37°C for 72 h. The digest was neutralized with 0.01N NaOH to a pH of 7.4 and lyophilized again for 6 h. The freeze-dried vacuum end product was gamma irradiated at 10 gy, reconstituted with PBS, and used to coat the culture flasks at a final concentration of 10 µg/ml (overnight incubation at 4°C) (Fig. 2H). Western blot analysis using SDS-PAGE was performed to confirm the isolation of collagen type II (Fig. 2I).

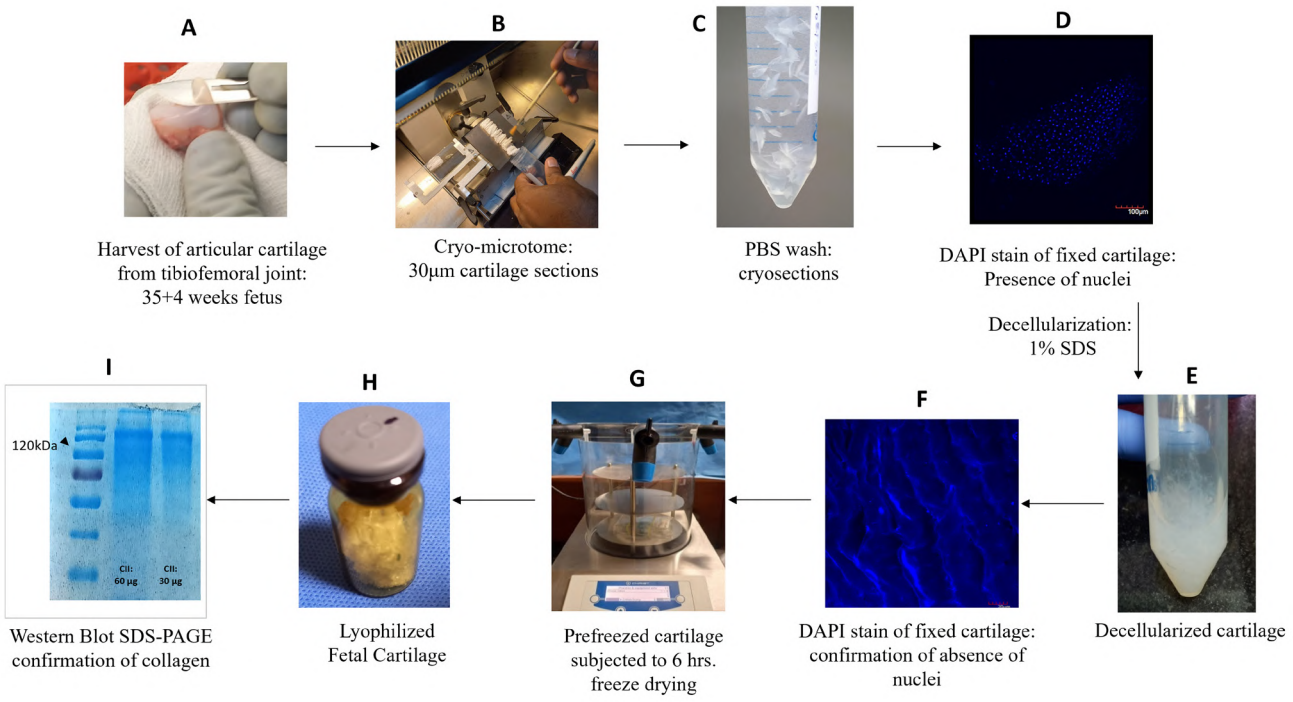

Fig. 2.- Flow algorithm illustrating the sequential steps involved in the isolation of freeze-dried extracellular collagen matrix from fetal cartilage.

Isolation and culture of BM-MSCs

The bone marrow-derived aspirate was collected and transferred to vacutainers containing a pre-heparinized solution. Paque PREMIUM was added to the anticoagulated sample in the same proportion and gently mixed. Subsequently, the mixture was centrifuged at a force of 400 g for a duration of 45 minutes. The mononuclear cell layer obtained after two washes was loaded into T-75 flasks. After 24 hours, the non-adherent cells were washed with PBS and then replenished with a standard expansion medium. The expansion medium consisted of Alpha Eagle minimum essential medium containing 10% fetal bovine serum (FBS) and basic fibroblast growth factor 2 at a concentration of 1ng/mL The adherent cells were cultured under standard conditions, maintaining 5% CO_2 at 37°C, until passage 3 for further experimentation. At passage 3 the BM-MSCs were loaded either on plain culture or collagen-coated culture flasks at a seeding density of 5000 cells/cm^2. At sub-confluence, the cells were harvested and subjected for further analysis.

Growth Kinetics: Cell cycle analysis, cell diameter and population doubling time

To determine the distribution of cells in different phases of the cell cycle, an analysis using DAPI (4',6-diamidino-2-phenylindole) was performed. The cells were trypsinized when they reached 60-70% confluence, and the analysis was conducted a day after changing the medium. The size of the cells was assessed using the CellDrop BF, DeNovix automated counter. Passage 4 BM-MSCs were washed with PBS and fixed for 1 hr with 70% cold ethanol. Following a wash, the cells were incubated with DAPI (1 µg/ml for 30 minutes using 0.1% TritonX-100) and subjected to flow cytometry analysis. The Flo-Jo software utilized the Watson algorithm to assess the proportion of cells in different phases during the analysis. To estimate the population doubling time (PDT) at passage 4 the following formulae were used:

PDT = log 2*days in culture/log (N1) – log (No),

N1: number of cells at confluence

No: initial number of cells seeded

Fluorescence Activated Cell Sorting (FACS) for cell surface markers

The two cell groups were subjected to phenotypic analysis using the BD FACS CytoFLEX Flow Cytometer CytExpert. This analysis involved the inclusion of controls that were not stained with the antibody. The resulting data were then analyzed using BD FACS Diva v 8.0.1.1. Antibodies against the conjugated human surface antigens (BD-Bioscience) included: CD105-FITC, CD106-APC, CD166 BB515 and CD146-PE.

qRT-PCR for gene expression

RNA was isolated from BM-MSCs and collagen-coated BM-MSCs using the Qiagen RNeasy Mini Kit. After determining the A260/A280 ratio and concentration using a Nanodrop Spectrophotometer, 280 ng of RNA was reverse-transcribed into cDNA using the Takara Bio First-Strand synthesis system. Quantitative real-time PCR (qRT-PCR) was performed using TakyonTM Low Rox SYBR Master Mix dTTP Blue (Eurogentec) with a final concentration of 7 ng of cDNA per reaction. The qRT-PCR was conducted using the Quantstudio 12K Flex thermocycler (Applied Biosystems). The gene profile analysis included SOX-9, ACAN, and COL2A1 for assessing chondrogenesis, as well as COL1A1, COL10A1, and RUNX2 to evaluate the hypertrophic expression profile. The relative mRNA expression for each gene was normalized to the reference housekeeping gene GAPDH (ΔCt). The individual ΔCt values were compared to the collagen-coated BM-MSC group (ΔΔCt), and the relative expression was calculated using the 2^-ΔΔCt method. Table S1 provides a comprehensive list of detailed primer sequences, gene identifiers, accession codes, and base pair lengths.

Trilineage differentiation and confirmatory staining

To induce differentiation into adipogenic, osteogenic, and chondrogenic lineages, Stem Pro differentiating kits from GIBCO were employed. For adipogenic differentiation, the cells were initially seeded at a density of 1000 cells/cm^2 and allowed to expand until reaching 80% confluence. Subsequently, the culture medium was replaced with adipogenic differentiation medium with me-

Table S1. Sequence of the primers used for RT-PCR. SOX9: sex determining region Y-box 9, ACAN: Aggrecan, COL2A1: Collagen type 2 alpha 1 chain, COL1A1: Collagen type 1 alpha 1 chain, COL10A1: Collagen type 10 alpha 1 chain, RUNX2: Runt related transcription factor-2 and MMP13: Matrix metalloproteinase type 13. GAPDH: glyceraldehyde 3-phosphate dehydrogenase.

Gene of Interest	Primers (5'-3')		Accession number (reference link)	Product size (bp)
	Forward primer	Reverse primer		
SOX-9	GACTTCCGCGACGTGGAC	GTTGGGCGGCAGGTACTG	NM_000346.4 https://www.ncbi.nlm.nih.gov/nucleotide/1519242934	99
ACAN, transcript variant 1	TCGAGGACAGCGAGGCC	TCGAGGGTGTAGCGTGTAGAGA	NM_001135.4 https://www.ncbi.nlm.nih.gov/nucleotide/1890265422	85
COL2A1, transcript variant 2	CCTGAGTGGAAGAGTGGAGAC	TTGCTGCTCCACCAGTTCTT	NM_033150.3 https://www.ncbi.nlm.nih.gov/nucleotide/1674985896	149
COL1A1	TCTGCGACAACGGCAAGGTG	GACGCCGGTGGTTTCTTGGT	NM_000088.4 https://www.ncbi.nlm.nih.gov/nucleotide/1777425449	146
COL10A1	CAAGGCACCATCTCCAGGAA	AAAGGGTATTTGTGGCAGCATATT	NM_000493.4 https://www.ncbi.nlm.nih.gov/nucleotide/1519245829	70
RUNX2, transcript variant 2	CCTAAATCACTGAGGCGGTC	CAGTAGATGGACCTCGGGAA	NM_001015051.4 https://www.ncbi.nlm.nih.gov/nucleotide/1890358904	91
GAPDH transcript variant 7	TCAGCAATGCCTCCTGCAC	TCTGGGTGGCAGTGATGGC	NM_001357943.2 https://www.ncbi.nlm.nih.gov/nucleotide/1676440496	117

dium change once in every three days for a period of three weeks. Oil Red O staining (0.5%) was performed following differentiation on the formalin fixed cells to confirm the accumulation of lipid vacuoles.

Osteogenic and chondrogenic differentiation was performed using a pellet culture system for a period of 28 days. In brief, one million cells were centrifuged at 400g for 12 min and left undisturbed for 48 hours to form a pellet. Following differentiation with respective differentiation medium, the pellets were washed and fixed with 4% paraformaldehyde, embedded in paraffin and sectioned. The 4 µm sections obtained were hydrated with descending grades of ethanol and subjected to their confirmatory staining.

To confirm the osteogenic staining, the pellets underwent staining with Alizarin Red S and Von Kossa. This was done to verify the presence of mineralized matrix accumulation. Additionally, Picrosirius red staining was used to determine the total collagen content, while immunohistochemical analysis was conducted to assess the presence of collagen type X. For the Von Kossa staining, the slides were immersed in a 1% silver nitrate solution (Qualigens, Cat no: Q27462) and exposed to UV light in a chamber for 20 minutes. Subsequently, the excess silver nitrate was eliminated by treating it with a 5% sodium thiosulphate solution (Sigma, Cat no: 7772-98-7) for 5 minutes. Then, the samples were counterstained with nuclear fast red (ThermoFischer Scientific, Cat no: 211980050) for 5 minutes. Regarding the Alizarin Red staining (Sigma, Cat no: A5533), the slides were stained using a 2% Alizarin red solution (pH: 4.2, adjusted with ammonium hydroxide) for a duration of 5 minutes. PicroSirius Red (C.I.35782) staining was carried out utilizing a 0.1% concentration of the stain, followed by counterstaining with Hematoxylin. For immunohistochemistry, the paraffin sections were subjected to antigen retrieval using chondroitinase ABC (0.1 units/ml: 1 hour, C3667, Sigma Aldrich) and pepsin (pH 2.2, 1 mg/ml: 15 minutes, R2283, Sigma Aldrich). Following this, the sections were inhibited for endogenous peroxidase activity and subjected to protein block (6% FCS and 1% bovine serum albumin). Incubation with primary antibodies specific to collagen type X (1:200 dilution, 37°C) for 4 hours (ab49945, Abcam, Cambridge, UK) followed

by treatment with a secondary antibody, goat anti-mouse HRP-labeled immunoglobulin (31430, Pierce, Wisconsin, USA; 1:100 dilution) was performed. The final step involved staining with a chromogen solution containing 3,3-diaminobenzidine (DAB, Sigma, Cat no: D5637), followed by counterstaining with hematoxylin.

To confirm chondrogenic differentiation, the following protocol was employed for each stain: to assess the accumulation of glycosaminoglycans, the sections were treated with Alcian blue (pH: 2.5, Cat no: J60122, Alfa Aesar, US) for a duration of 5 minutes. Following this, the sections were counterstained with neutral red. In addition, Toluidine blue staining was conducted by incubating the sections in a 0.1% dye solution for 5 minutes (C.I. 52040 Qualigens).

To assess the Collagen type II content the paraffin sections were treated with pronase and hyaluronidase to retrieve them. The sections were then incubated with primary mouse monoclonal Anti-Collagen type II antibody (5 g/mL) (DSHB Hybridoma Product II-II6B3) at a temperature of 4°C overnight. This was followed by a 30-minute incubation with a secondary antibody at a dilution of 1:100, specifically HRP labelled goat anti-mouse immunoglobulin (31430, Pierce, Wisconsin, USA). Subsequently, the sections were stained with a 3,3-DAB for a duration of 5 minutes and counterstained with hematoxylin. After staining, all slides underwent dehydration and were cleared using xylene before being mounted with DPX for imaging.

Total GAG/DNA ratio

The pellets following chondrogenic differentiation were subjected to digestion with papain solution containing cysteine, maintained at a temperature of 65°C for a duration of 16 hrs. Subsequently, quantitative analysis was performed to determine the content of glycosaminoglycans (GAG) and DNA. The concentration of DNA was measured using the Quant-iT Picogreen dsDNA reagent, with the standard curve generated using Lambda DNA. The fluorescence intensity (Ex λ: 480 nm, Em λ: 520 nm) was measured using a SpectraMax i3x Reader (Norwalk, CT, USA). The total GAG content was analyzed using the dimethyl methylene blue (DMMB) dye method, with Chondrex, Inc Cat No: 6022 being utilized. Chondroitin 6-sulfate served as the standard for comparison. The optical density was measured using an Elisa plate reader at an absorbance of 525 nm. The resulting GAG values were then normalized to the DNA values, enabling the calculation of the total GAG/DNA ratio.

Statistical Analysis

For data analysis, Microsoft Excel was used, while IGOR Pro Wave metrics Inc. (Version 5.0.4.8) was utilized for visual data presentation. The statistical analyses were performed using the Mann-Whitney U test for independent sample. In this study, the mean values along with the standard deviation or standard error of the mean were used to represent the data. P value less than 0.05 was considered significant.

RESULTS

Growth Kinetics

BM-MSCs displayed spindle shaped morphology in monolayer culture and expanded with similar morphological features up to passage 3. At passage 4, BM-MSCs cultured on collagen-coated plates displayed maintained fibroblastic appearance when compared to the control arm. Population Doubling Time (PDT) was assessed from cells at passage 4 subjected to the two different culture conditions. It was noted that both the groups showed similar PDT without any statistical difference between them (BM-MSC: 5.25±01.11 and collagen coated BM-MSC: 4.61±0.21). The examination of cell cycle distribution revealed that collagen coating did not significantly influence the growth kinetics of BM-MSCs during its expansion (Fig. 3A).

FACS for cell surface markers

In comparing potential markers of enhanced chondrogenesis, both groups exhibited high expression levels of CD105 and CD166, as well as low expression of CD106, with no significant difference between them. However, when considering CD146, the collagen-coated BM-MSCs demonstrated a slightly higher average expression, although the difference was not statistically significant (Fig. 3B).

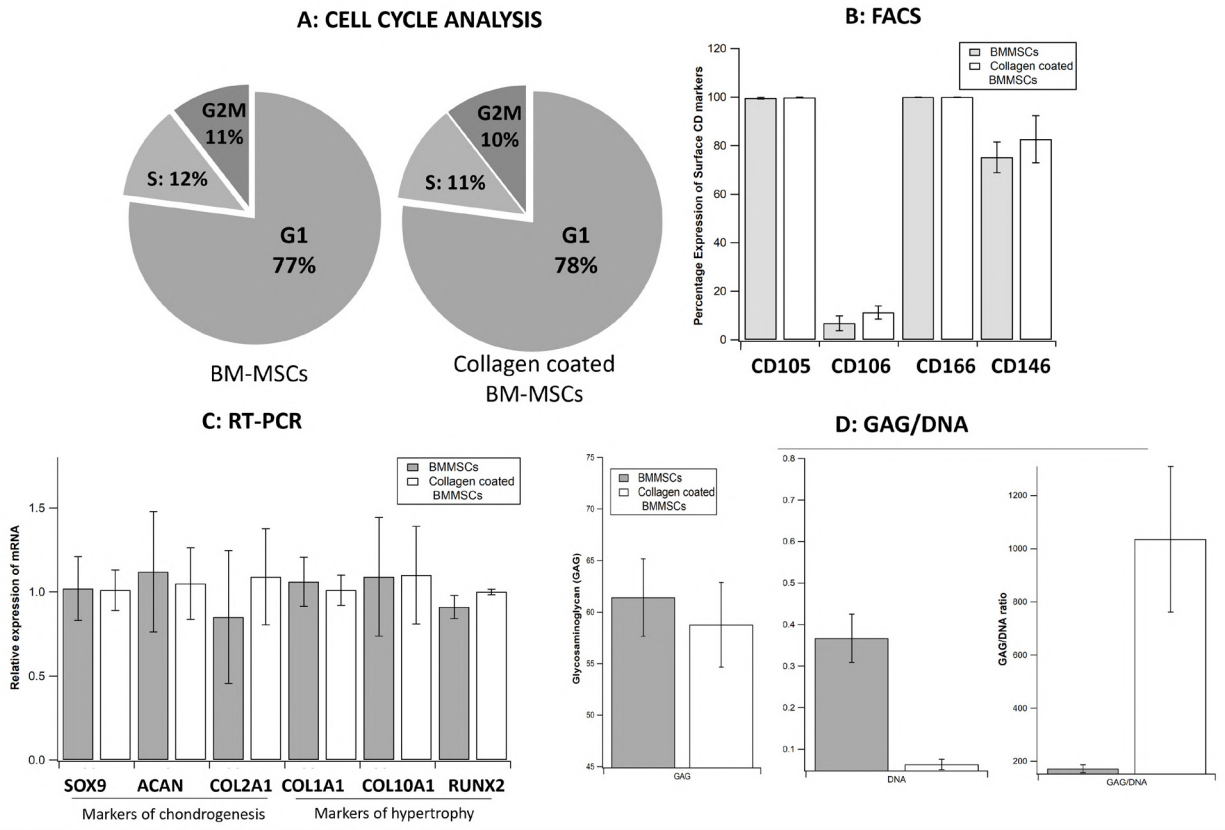

Fig. 3.- Comparative analysis between two groups of passage-4 BM-MSCs: the control group (BM-MSCs) and the collagen-coated BM-MSCs group. **A)** Percentage of cells in different phases of the cell cycle. **B)** Comparison of the percentage expression of cell surface markers associated with enhanced chondrogenesis. **C)** Comparison of the relative expression of SOX-9, ACAN, COL2A1, COL1A1, COL10A1, and RUNX2 among the two study groups. ΔCt indicates values that were normalized to GAPDH. To obtain the ΔΔCt, the individual ΔCt values were compared to the collagen-coated BM-MSC group, and the relative expression was calculated using the 2^-ΔΔCt method. Data are presented as Mean ± SD, n=3, with each sample performed in duplicates. SOX-9: (sex-determining region Y)-box 9, ACAN: aggrecan, COL2A1: collagen type 2A1, COL1A1: collagen type 1A1, COL10A1: collagen type 10A1, and RUNX2: Runt-related transcription factor-2. **D)** Quantitative estimation of GAG/DNA content in the chondrogenic differentiated pellet from the two groups. Values are expressed as Mean ± SEM, n=3. GAG: glycosaminoglycans.

qRT-PCR, trilineage differentiation and GAG/DNA

Comparable gene expression levels were observed in both groups, with high expression of SOX-9, ACAN, and COL1A1, and moderate expression of COL2A1, RUNX2, and COL10A1 (Fig. 3C). Both study groups demonstrated the ability for multilineage differentiation. Qualitative analysis of adipogenic differentiation showed similar uptake of Oil Red O by lipid droplets, while comparable uptake of Alizarin Red, Picrosirius Red, and Von Kossa stain indicated the deposition of calcified matrix (Fig. 4). Evaluation of pellets subjected to chondrogenic differentiation revealed improved staining with Alcian blue and Toluidine blue, as well as collagen type II deposition in the BMMSC collagen-coated pellets (Fig. 5). After digesting the chondrogenic-induced pellets and measuring the DNA and GAG contents, it was observed that the BM-MSC collagen-coated group demonstrated markedly higher levels of GAG/DNA compared to the BM-MSC group. Specifically, the collagen-coated cells exhibited a substantial 4-11-fold increase in the total GAG/DNA ratio (Fig. 3D).

DISCUSSION

Articular cartilage presents a compelling focus for tissue engineering due to the lack of direct access to a substantial supply of reparative cells and the absence of natural self-healing mechanisms following cartilage injuries (Sophia Fox et al., 2009). The utilization of BM-MSCs as a prominent cell-based therapeutic modality has garnered considerable attention due to their accessibility, abundant availability, notable proliferative potential, and immunomodulatory capacities (Zhang et

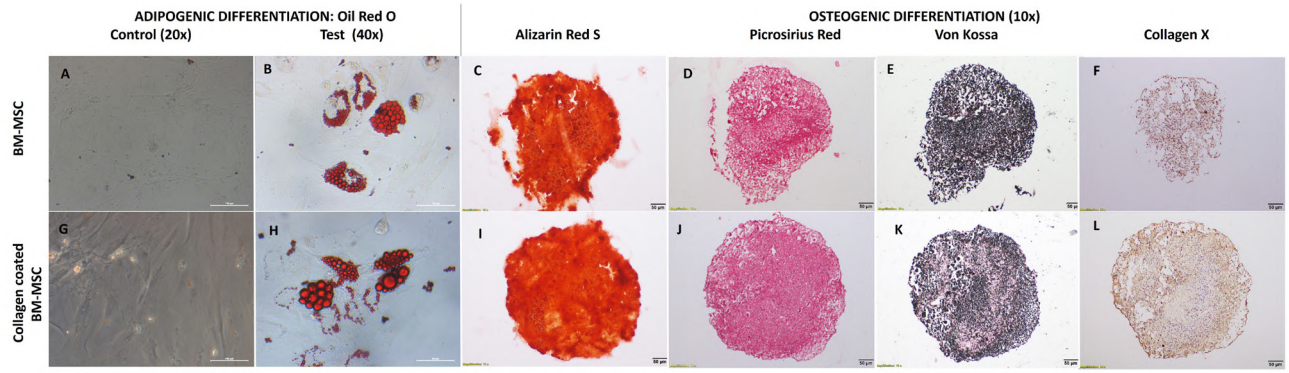

Fig. 4.- Adipogenic and osteogenic differentiation and staining of the two groups. Representative microscopic images of Oil Red O (**A-B**, **G-H**), Alizarin Red S (**C, I**), Picrosirius red (**D, J**), Von Kossa (**E, K**) and Collagen type X (**F, L**).

al., 2019). Nevertheless, researchers are increasingly directing their efforts towards optimizing in-vitro culture conditions to counteract the development of a hypertrophic phenotype and to enhance the quality of repair tissue generated by these cells. Fetal cartilage has been proposed as a promising source for cartilage repair because the extracellular matrix (ECM) contains high amounts of collagen II and glycosaminoglycan (GAG), similar to articular cartilage (Choi et al., 2016; Fuchs et al., 2002; Vinod et al., 2023). Fetal cartilage-derived cells have been successfully used in the treatment of arthritis (Krivoruchko et al., 2014). However, no studies have so far evaluated if collagen derived from fetal cartilage can be utilized for coating materials for refining the cellular behavior and phenotype of cells during culture. This study aimed to develop a collagen-based coating for BM-MSC expansion and assess whether the microenvironment would enhance the chondrogenic ability of BM-MSCs.

In this study, collagen was successfully isolated from fetal cartilage, and its presence was confirmed by western blot analysis, revealing the presence of collagen type II. Culturing BM-MSCs on the collagen-coated surface did not impact their proliferative potential or morphological characteristics. CD106, a well-established marker for mesenchymal stem cells, has been recognized as a potential predictive marker for osteogenesis (Liu et al., 2008). Additionally, CD105, apart from its role as an MSC marker, has been documented as a predictive marker for chondrogenesis (Fan et al., 2016; Wang et al., 2013). Conversely, CD166 and CD146 are regarded as putative markers associated with improved chondrogenesis (Dicks et al., 2019; Vinod et al., 2021; Wu et al., 2016). It was noted that the expansion of BM-MSCs on collagen

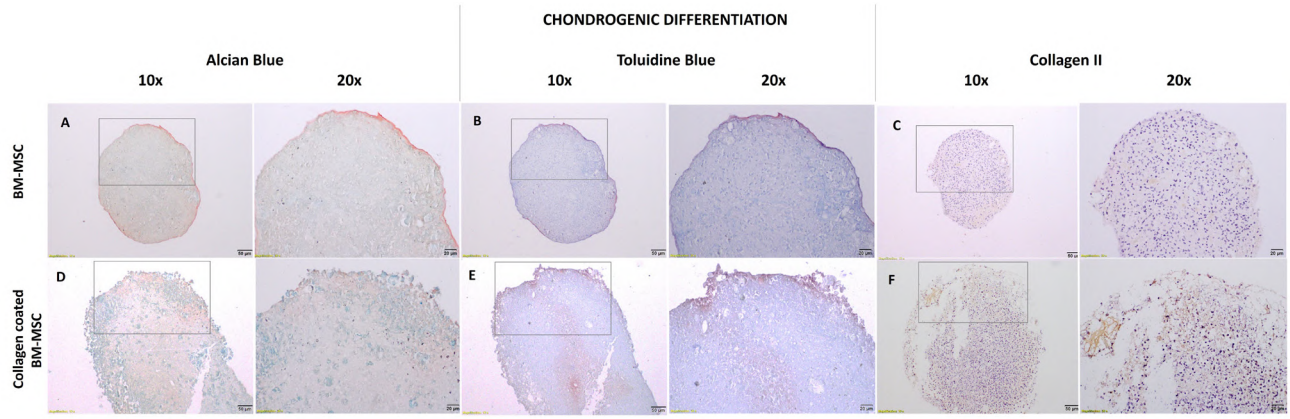

Fig. 5.- Chondrogenic differentiation and staining of the two groups. Representative microscopic images of Alcian blue (**A, D**), Toluidine blue (**B, E**) to assess uptake of glycosaminoglycans and Collagen type II (**C, F**).

coating did not influence their surface marker profile, as no significant difference was observed when comparing the putative markers of chondrogenesis with the group grown under standard conditions. A comparison between BM-MSCs and collagen-coated BM-MSCs revealed that the latter exhibited higher levels of collagen type II, which aligned with the staining observed in the immunohistochemical analysis. In terms of GAG/DNA analysis, collagen coating positively influenced BM-MSCs, resulting in a seven-fold increase in GAG accumulation with the differentiated pellets demonstrating improved uptake of Alcian blue and toluidine blue.

This study represents the first in-vitro investigation to utilize collagen derived from fetal cartilage and examine its influence on BM-MSCs. Although not statistically significant, it is noteworthy that fetal collagen coated BM-MSCs demonstrated an increase in GAG accumulation. Another significant finding was that, despite the presence of mineralization following osteogenic differentiation with collagen-coated BM-MSCs, there were no changes observed in their hypertrophy gene expression. Further studies utilizing in-vivo models are warranted to evaluate the potential of collagen-coated BM-MSCs and exploit their adjuvant effect on chondrogenesis.

ACKNOWLEDGEMENTS

SMA and EV were involved in the study's conception and design. SMA, GP, JLJ, DVF, AL and EV performed the experiments and collected data. All authors were involved in data analysis and interpretation. EV and SMA provided financial support. All authors were involved in preparing the final version of the manuscript. We acknowledge Ms. Sevanthy Suresh, Mr. Abdul Muthallib, Ms. Esther Rani and Mr. Ashok Kumar for technical support, and the Centre for Stem Cell Research (A unit of inStem Bengaluru), Christian Medical College, Vellore for infrastructural support. This project was supported by the Fluid Research Grant (IRB Min No: 14498 dated 23.02.2022), Christian Medical College, Vellore.

REFERENCES

ARMIENTO AR, ALINI M, STODDART MJ (2019) Articular fibrocartilage—Why does hyaline cartilage fail to repair? *Adv Drug Delivery Rev*, 146: 289-305.

BENDERS KEM, VAN WEEREN PR, BADYLAK SF, SARIS DBF, DHERT WJA, MALDA J (2013) Extracellular matrix scaffolds for cartilage and bone regeneration. *Trends Biotechnol*, 31(3): 169-176.

CHARLIER E, DEROYER C, CIREGIA F, MALAISE O, NEUVILLE S, PLENER Z, MALAISE M, DE SENY D (2019) Chondrocyte dedifferentiation and osteoarthritis (OA). *Biochem Pharmacol*, 165: 49-65.

CHOI WH, KIM HR, LEE SJ, JEONG N, PARK SR, CHOI BH, MIN B-H (2016) Fetal cartilage-derived cells have stem cell properties and are a highly potent cell source for cartilage regeneration. *Cell Transplant*, 25(3): 449-461.

DICKS A, WU C-L, STEWARD N, ADKAR SS, GERSBACH CA, GUILAK F (2019) Prospective Isolation of chondroprogenitors from human iPSCs based on cell surface markers identified using a CRISPR-Cas9-generated reporter. *BioRxiv*, 675983.

FAN W, LI J, WANG Y, PAN J, LI S, ZHU L, GUO C, YAN Z (2016) CD105 promotes chondrogenesis of synovium-derived mesenchymal stem cells through Smad2 signaling. *Biochem Biophys Res Commun*, 474(2): 338-344.

FENG B, JI T, WANG X, FU W, YE L, ZHANG H, LI F (2020) Engineering cartilage tissue based on cartilage-derived extracellular matrix cECM/PCL hybrid nanofibrous scaffold. *Materials Design*, 193: 108773.

FILARDO G, MADRY H, JELIC M, ROFFI A, CUCCHIARINI M, KON E (2013) Mesenchymal stem cells for the treatment of cartilage lesions: From preclinical findings to clinical application in orthopaedics. *Knee Surg Sports Traumatol Arthrosc*, 21(8): 1717-1729.

FUCHS JR, TERADA S, HANNOUCHE D, OCHOA ER, VACANTI JP, FAUZA DO (2002) Engineered fetal cartilage: Structural and functional analysis in vitro. *J Pediat Surg*, 37(12): 1720-1725.

KLEINMAN HK, LUCKENBILL-EDDS L, CANNON FW, SEPHEL GC (1987) Use of extracellular matrix components for cell culture. *Analytical Biochem*, 166(1): 1-13.

KRIVORUCHKO N, TUGANBEKOVA S, RAKHIMBEKOVA G, KUZEMBAEVA K, ZARIPOVA L (2014) The results of fetal chondrocytes transplantation in patients with rheumatoid arthritis. *Central Asian J Global Health*, 3(Suppl), 164.

LIU F, AKIYAMA Y, TAI S, MARUYAMA K, KAWAGUCHI Y, MURAMATSU K, YAMAGUCHI K (2008) Changes in the expression of CD106, osteogenic genes, and transcription factors involved in the osteogenic differentiation of human bone marrow mesenchymal stem cells. *J Bone Mineral Metab*, 26(4): 312-320.

MUELLER MB, TUAN RS (2008) Functional characterization of hypertrophy in chondrogenesis of human mesenchymal stem cells. *Arthritis Rheum*, 58(5): 1377-1388.

NEGORO T, TAKAGAKI Y, OKURA H, MATSUYAMA A (2018) Trends in clinical trials for articular cartilage repair by cell therapy. *NPJ Regen Med*, 3: 17.

QUINTIN A, SCHIZAS C, SCALETTA C, JACCOUD S, APPLEGATE LA, PIOLETTI DP (2010) Plasticity of fetal cartilaginous cells. *Cell Transplant*, 19(10): 1349-1357.

SCHULZE-TANZIL G (2009) Activation and dedifferentiation of chondrocytes: Implications in cartilage injury and repair. *Ann Anat*, 191(4): 325-338.

SCHWARZ S, KOERBER L, ELSAESSER AF, GOLDBERG-BOCKHORN E, SEITZ AM, DÜRSELEN L, IGNATIUS A, WALTHER P, BREITER R, ROTTER N (2012) Decellularized cartilage matrix as a novel biomatrix for cartilage tissue-engineering applications. *Tissue Eng. Part A*, 18(21-22): 2195-2209.

SOPHIA FOX AJ, BEDI A, RODEO SA (2009) The basic science of articular cartilage. *Sports Health*, 1(6): 461-468.

VINOD E, PADMAJA K, LIVINGSTON A, JAMES JV, AMIRTHAM SM, SATHISHKUMAR S, RAMASAMY B, REBEKAH G, DANIEL AJ, KACHROO U (2021) Prospective isolation and characterization of chondroprogenitors from human chondrocytes based on CD166/CD34/CD146 surface markers. *Cartilage*, 13(2 suppl): 808S-817S.

VINOD E, PARASURAMAN G, LISHA JJ, AMIRTHAM SM, LIVINGSTON A, VARGHESE JJ, RANI S, VINOD FRANCIS D, REBEKAH G, DANIEL AJ, RAMASAMY B, SATHISHKUMAR S (2023) Human fetal cartilage-derived chondrocytes and chondroprogenitors display a greater commitment to chondrogenesis than adult cartilage resident cells. *PloS One*, 18(4): e0285106.

WANG M, CHEN P, LIU C, HAO Y, ZHANG Y, ZHANG X (2013) Experimental study on CD105+/CD166+ cells and its chondrogenic potential in early osteoarthritis cartilage. *Zhongguo Xiu Fu Chong Jian Wai Ke Za Zhi = Chinese J Rep Reconst Surg*, 27(7): 793-799.

WU C-C, LIU F-L, SYTWU H-K, TSAI C-Y, CHANG D-M (2016) CD146+ mesenchymal stem cells display greater therapeutic potential than CD146– cells for treating collagen-induced arthritis in mice. *Stem Cell Res Therapy,* 7: 23.

YANG Z, SHI Y, WEI X, HE J, YANG S, DICKSON G, TANG J, XIANG J, SONG C, LI G (2010) Fabrication and repair of cartilage defects with a novel acellular cartilage matrix scaffold. *Tissue Eng Part C Methods*, 16(5): 865-876.

ZHANG R, MA J, HAN J, ZHANG W, MA J (2019) Mesenchymal stem cell related therapies for cartilage lesions and osteoarthritis. *Am J Translat Res,* 11(10): 6275-6289.

Testicular morphometry and epididymal sperm qualities of donkeys in Bolgatanga, Ghana

A.J. Ayang[1], J. Atawalna[1], Banjamin O. Emikpe[1], D. Abiliba[1], E.P. Dongbataazie[1], E. Adom[3], A.D. Asare[4], M.P. Amponsah[2]

[1] *School of Veterinary Medicine, KNUST, Kumasi, Ghana*
[2] *Veterinary Disease Investigative Laboratory, Amakom, Ghana*
[3] *Department of Pharmacognosy and Herbal Medicine, UDS, Ghana*
[4] *School of Veterinary Medicine, Legon, Accra, Ghana*

SUMMARY

The application of artificial insemination in donkeys must be based on a knowledge of breeding soundness, while other reproductive physiology of the donkey including testicular morphometric parameters and sperm production is scanty in literature. This study sought to assess the testicular morphometry and epididymal sperm qualities of donkeys in Bolgatanga and to determine the effect of season on spermatogenesis and epididymal sperm parameters. Twelve sexually mature donkeys, aging 10 to 15 years old, had their testes and epididymis surgically harvested immediately after slaughter, semen parameters were assessed thereafter and testicular volume calculated. Epididymal sperm was harvested by retrograde flushing technique and sperm parameters were obtained. This study showed no significant difference (p-value >0.05) between the length, width and volume of the left and right testes, and that the rainy season showed greater values in seminiferous tubule diameter, epithelial height, and luminal diameter. The study revealed that donkeys showed a greater level of spermatogenesis in the rainy season compared to the dry season, indicating that donkeys are seasonal breeders.

Key words: Testis – Morphometry – Donkeys – Epididymal – Spermatogenesis

INTRODUCTION

Donkeys are members of the family *Equidae*, along with horses and zebras (Nasr et al., 2021). More than 40 million donkeys live in Asia, Africa, and Latin America, mostly in dry and semi-arid areas (Starkey and Starkey, 1996). Donkeys are adaptable to the temperature changes of the desert regions of Africa and Asia (Nasr et al., 2021). Globally they are essential to farmers and traders, because they can provide draught power and rural transportation at minimal cost (Starkey and Starkey, 1996). The donkey population in Ghana is estimated to be 14,500 (FAOSTAT, 2015), and they are often used for work like transportation, pack transport, or pulling carts in Northern Ghana (Chiarini-Garcia et al., 2009).

Corresponding author:
Benjamin Emikpe. School of Veterinary Medicine, KNUST, Kumasi, Ghana. E-mail: banabis2001@yahoo.com

Submitted: May 18, 2023. **Accepted:** July 18, 2023

https://doi.org/10.52083/KVOV3346

Donkey hides are a crucial component of the traditional Chinese Medicine treatment e'jiao, and manufacturers of e'jiao need four to ten million donkey skins annually (Matlhola et al., 2020). The demand for donkey hides in China has triggered a global increase in the illegal slaughter of donkeys leading to a drastic decline in the population of working donkeys in low-and middle-income countries (Zhu et al., 2017; McLean et al., 2018). Donkeys are therefore at risk of extinction; hence the need to take drastic steps towards their conservation.

The population of Donkeys can be increased using assisted reproductive techniques such as artificial insemination, which has been successfully implemented in livestock and poultry production (Hagstrom et al., 2004). The application of artificial insemination in donkeys must be based on a knowledge of breeding soundness (Atawalna et al., 2015), while other reproductive physiology of the donkey including testicular morphometry parameters and sperm production is scanty in literature. Unfortunately, the influence of season (rainy and dry) on testicular morphometry has never been reported in Donkeys in Ghana. In view of this gap, this study sought to investigate the testicular morphometry and epididymal sperm qualities of donkeys in Bolgatanga and to determine the effect of season on spermatogenesis and their overall epididymal sperm parameters.

MATERIALS AND METHODS

Study Area

The study samples were taken in the Bolgatanga Central Municipality, which is the regional capital of the Upper East region. It is located on the north-eastern corridor of Ghana between longitude 1°W and 0°E and 10°N and 11°N and covers an area of 1,509 km² (Ghana Statistical Services, 2015/2022). The municipality is bordered to the North by the Bongo District, South and East by Talensi-Nabdam District and Kassena-Nankana District to the West. Bolgatanga is about 775.4km from Accra, the capital of Ghana. It has a tropical climate with two distinct seasons – a wet season that runs from May to October and a long dry season that stretches from October to April; with hardly any rains (Ghana Meteorological Services Report, 2021).

Study Population

The study population included adult donkeys aged 10-15 years. The ages of the donkeys were estimated by comparing the appearance of their unique dentition as described by Muylle et al. (1999). A sum total of 12 donkey testicle pairs of the age ranging from 10 to 15 years old were used for this study. Six (6) donkey testicle pairs were used in the rainy season and six (6) donkey pairs were used in the dry season making a sum total of 12 donkey pairs for the study.

Study Duration

The study lasted from January to July 2022. Samples were taken in January to represent the dry season, and in July to represent the rainy season.

Sample Collection

The testes samples were obtained with the scrotum intact from apparently healthy animals immediately after slaughter. The collected samples were wrapped in plastic bags and placed on ice packs and transported to the laboratory using Coleman boxes. In the laboratory, the testes and epididymis were then dissected and separated.

For each sample, the length and width of right and left testis were measured using a measuring tape. Three measurements were taken per sample and the mean value was calculated and recorded. The volume of the testes was estimated as described by Mohammed et al. (2018) using the formula $V=0.5236LW^2$ where; V= volume of testes, L= Length of testes, W = width of testes. This procedure was repeated for the rainy season.

Histological Processing

The parenchyma of the left testis was fixed in 10% neutral buffered formalin solution for histological examination. The samples were first immersed in the fixative 10% formalin for 24-48 hours. The testicular tissue was then thoroughly washed using running tap water to remove fixative and then treated in ascending grades of ethanol concentrations

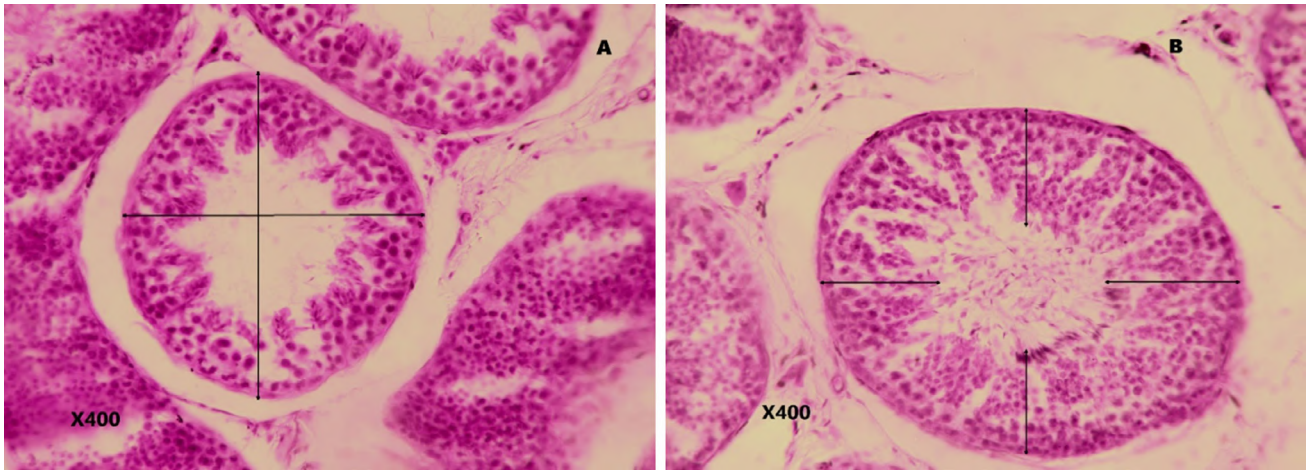

Fig. 1.- Measurement of diameter (A) and epithelial height of seminiferous tubules (B).

(70, 80, 90 and 100%), cleared in xylene to remove alcohol and to permit the fixed tissues to be miscible with paraffin wax. The tissue was then embedded in paraffin and the testicular tissue was cut 5µm thickness and stained with Haematoxylin and Eosin (H&E), as described by Burry et al., (2010).

Measurement of seminiferous tubules parameters

The diameter, height of epithelium and luminal diameter of seminiferous tubules were the histological measurements that were taken from the prepared slides. These measurements were made from randomly selected 50 round and nearly round seminiferous tubules per sample using Imaging light microscopy Amscope Software (Yalçin et al., 2020).

As is seen in Fig. 1A, for each tubule, the diameter is calculated by taking the averages of the five diameters perpendicular to each other measured in µm (Kazemi et al., 2016).

The height of the epithelium was measured by measuring the thickness of the epitheliums of at least 30 tubules from the randomly selected different areas of each sample at x40 magnification, measuring from the four sides and from the four angles as seen in Fig. 1B, and the calculation was completed by taking their averages (Kazemi et al., 2016).

The luminal diameter of the seminiferous tubules was then calculated by subtracting the epithelial heights from the diameters obtained.

Testicular Biopsy Score

Testicular Biopsy Score was performed using the Johnsens Score. This is a semi-quantitative method that was used to determine the degree of spermatogenesis. For the method, fifty (50) round and nearly round seminiferous tubules per testicular sample at x40 magnification were randomly selected and graded on a score of 1 to 10, based on the criteria in Table 1 below. The level of spermatogenesis in both the dry and rainy season was then extrapolated using the scores from the Johnsens Mean Testicular Biopsy Score (MTBS).

Table 1. Johnsens testicular biopsy score.

Score	Description
10	There is full spermatogenesis
9	Incomplete spermatogenesis with many late spermatids
8	There are less than 5 spermatozoa per tubules and a few late spermatids
7	There are many early spermatids but no spermatozoa or late spermatids.
6	There are few early spermatids but no spermatozoa or late spermatids
5	There are many spermatocytes but no spermatozoa or spermatids
4	There are few spermatocytes but no spermatozoa or spermatids
3	There are only spermatogonia
2	There are only spermatogonia
1	There is no seminiferous epithelium

Source: (Gune et al., 2019).

Table 2. Gross testicular measurements of the left and right testicles of donkeys.

Parameters	Left testis	Right testis	t- value	p-value
Length (cm)	13.65 ± 1.084	14.29 ± 1.220	1.1000	0.2897
Width (cm)	9.620 ± 0.9737	9.938 ± 0.8307	0.7016	0.4944
Volume (cm^3)	659.7 ± 159.2	748.9 ± 174.8	0.068	0.3037

Evaluation of Epididymal Sperm

The Epididymis from samples collected in July were separated from the testis in the left scrotal sac, packed in plastic bags and stored in Coleman vacuum boxes on ice packs. In the Laboratory, the epididymides were allowed to thaw and sperm retrieved from them by the aspiration flotation procedure (Cary et al., 2004; Gloria et al., 2011).

After separation of the epididymis, the vas deferens was clamped to avoid loss of semen; then some semen was aspirated from the epididymis for estimation of concentration and motility, followed by several parallel incisions made on the dissected epididymis, and suspended Phosphate Buffer Solution (PBS). This was allowed for about 15 minutes for the sperm cells to swim into the medium. The retrieved epididymal spermatozoa were evaluated for concentration, motility and morphology. Sperm concentration was determined using a hemocytometer by performing a 1:20 dilution of semen with distilled water (Cary et al., 2004). The 20-ml sample of the immobilized sperm preparation was then transferred to the counting chamber and counted using a light microscope (Sokol et al., 2000). The motility was obtained by viewing each sample under a light microscope with a stage warmer set to 37°C, then placing a drop of semen sample on a glass slide and gently covered with a cover slip. At least 2 x 100 sperm/sample were counted and rated as motile or non-motile (Merkies et al., 2000).

Sperm Morphology was determined by placing a drop of semen on a slide preheated to 40°C and mixed with one part of 5% bluish eosin solution, and four parts of 10% negrosin aqueous solution. The spermatozoa were classified as those with a cell membrane structure unstained (living) and those with a damaged membrane structure stained pink (dead) (Łacka et al., 2016).

RESULTS

Gross testicular parameters

Table 2 shows the gross testicular morphometric parameters. The results showed no significant difference (P> 0.05) between the length, width and volume of the left and right testes. However, the values for the right testes were numerically higher than those of the left testis.

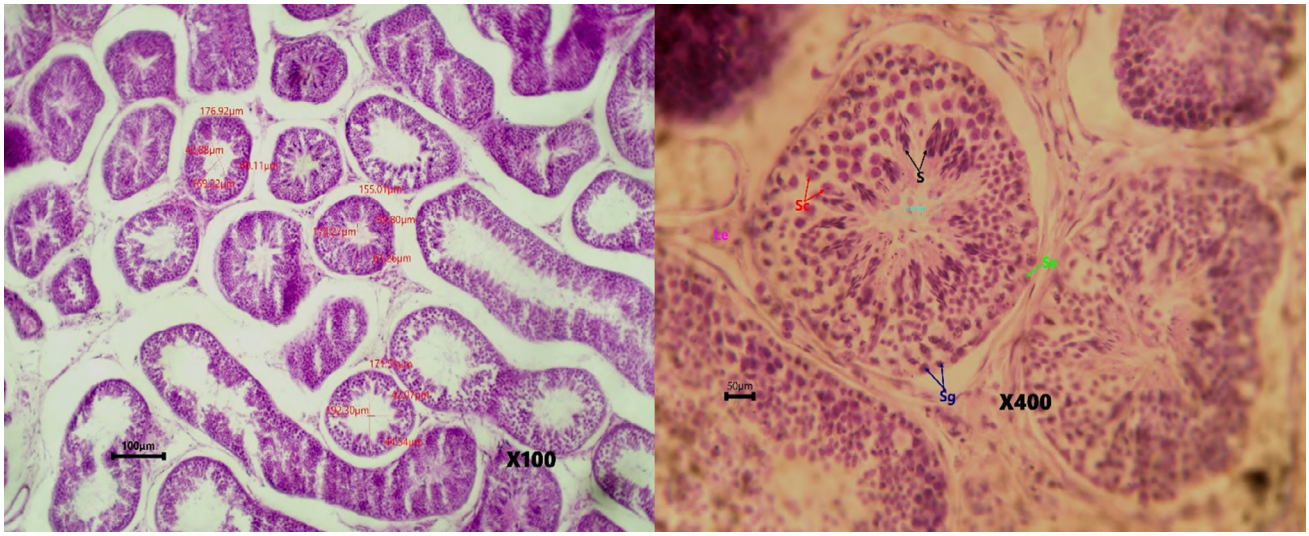

Fig. 2.- Seminiferous tubule showing spermatogenesis in the Rainy Season. Le: Leydig cells, Se: Sertoli cells, Sg: Spermatogonia, Sc: Spermatocytes, S: Spermatozoa.

Table 3. Histo-morphometric parameters of donkeys.

Parameters	Rainy season	Dry season	t-value	p-value
ST Diameter (µm)	199.5 ± 23.03	125.3 ± 3.316	6.422	0.0002*
Epithelial Height (µm)	56.57± 3.987	37 ± 2.970	5.913	0.0004*
Luminal Diameter (µm)	86.81 ± 20.65	48.98 ± 6.053	4.397	0.0023*
Johnsen's score (µm)	8.688 ± 0.3953	8.100 ± 0.5237	6.422	0.0239*

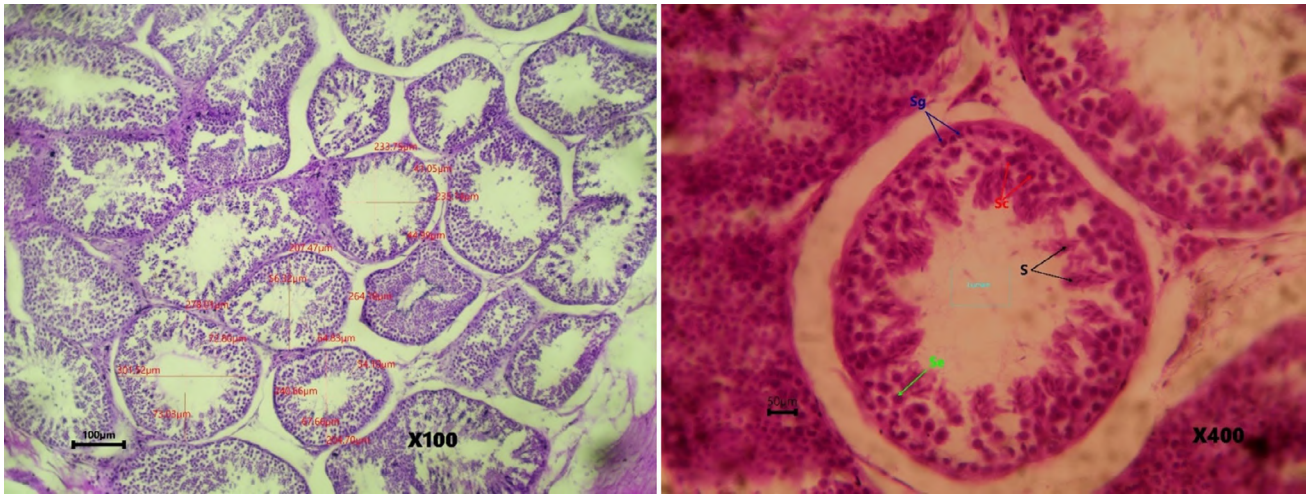

Fig. 3.- Seminiferous tubule showing spermatogenesis in the Dry Season. Le: Leydig cells, Se: Sertoli cells, Sg: Spermatogonia, Sc: Spermatocytes, S: Spermatozoa.

Histo-morphometric parameters

The results of the seminiferous tubular diameters, epithelial height and luminar diameter are shown in Table 3. The histo-morphometric parameters (the Seminiferous tubule diameter, epithelial height, luminal diameter and Johnsen's score) of the testes were significantly ($P< 0.05$) higher in the rainy season than in the dry season.

Testicular biopsy score

The degree of spermatogenesis in the dry and rainy seasons was assessed using the modified Johnsen's score. The results indicated the Johnsen score was significantly higher in the rainy season than in the dry season. The rainy season (Fig. 2) shows a greater level of spermatogenesis with several layers of spermatocytes than the dry season (Fig. 3) with a scanty layer of spermatocytes.

Epididymal sperm parameters

Table 4 below shows the results of the epididymal sperm parameters obtained during the study. The spermatozoa concentration ((10^6/ml), percentage (%) of motile, live normal cells, abnormal cells, and dead cells for the wet season were 272.12 ± 4.81, 88.46 ± 0.35, 63.84 ± 0.32, 20.75 ± 0.26, 15.41 ± 0.22 respectively, whilst that of

Table 4. Epididymal sperm quality parameters with respect to season.

Sperm Parameter	Rainy Season	Dry Season	p-value
Concentration (106/ml)	272.12 ± 4.81	167.68 ± 1.56	0.003*
Motility (%)	88.46 ± 0.35	54.51 ± 1.86	0.09
Live Normal Cells (%)	63.84 ± 0.32	39.34 ± 0.65	0.186
Live Abnormal (%)	20.75 ± 0.26	12.79 ± 2.34	0.845
Dead Cells (%)	15.41 ± 0.22	9.50 ± 0.71	0.078

the dry season were 167.68 ± 1.56, 54.51 ± 1.86, 39.34 ± 0.65, 12.79 ± 2.34, 9.50 ± 0.71 for spermatozoa concentration ((10^6/ml), percentage (%) of motile, live normal cells, abnormal cells, and dead cells. The epididymal sperm quality parameters were relatively higher in the wet season as compared to the dry season. Nevertheless, the differences in all the sperm quality parameters were not statistically significant ($p>0.05$) except for the sperm concentration ($p=0.003$). Sperm concentration was significantly high in the rainy season as compared to the dry season.

DISCUSSION

This current study assessed the testicular morphometry and epididymal sperm qualities of donkeys in Bolgatanga and also determined the effect of season on spermatogenesis and epididymal sperm parameters. The findings of the study revealed that the donkeys' right testes were slightly longer in length and width as compared to the left testes; however, the differences recorded were statistically insignificant (p-value > 0.05). This finding is in agreement with the findings of Contri et al. (2012), who, upon examination of the testes in light horse breeds, reported that their right testes were longer than their left testes, but the difference was not statistically significant. Carluccio et al. (2013) also found no significant differences in length and width of the testes in their study on the northeast breed of Brazilian donkeys, even though they recorded lower testicular volume compared to this study. The findings from this study, however, differs from previous research work done in Tori breed stallions by Kavak et al. (2003), where they found the left testis to be significantly larger than the right testes.

From this study, some differences existed in the histo-morphometric parameters. The measured seminiferous diameter recorded in the rainy season (199.5 ± 23.03) and dry season (125.3 ± 3.316) were lower values compared to the 222 ± 6 recorded by Contri et al. (2012). Also, the epithelial heights measured were relatively lower as compared to work done by Contri et al. (2012); however, the luminal diameters were higher in this study as compared to work done by Nipken et al. (1997). The findings indicate that there exists some sort of seasonal variation in the seminiferous tubules' diameters. This could be attributed to seasonal variations in the reproductive activity of the donkeys in the year. In addition, seminal tubule activity and sperm production increases during winter and autumn, which is equivalent to the rainy season as reported by Carluccio et al. (2013).

In this study, the mean sperm concentration recorded (272.12×10^6/mL) is in agreement with values reported in donkeys by Miragaya et al. (2018). However, the recorded motility of 88.46% in this study is lower than 90.8% observed by Gloria et al. (2011) in sexually mature Martina Franca jackasses between 5 and 6 years of age, but greater than the 82.5% recorded by Contri et al. (2012) for sexually mature Martina Franca jackasses also between 5 and 6 years of age in the winter. This could be attributed to the differences in geographical areas, as well as possible differences in the breeds and ages of donkeys used in the different studies. This study used donkeys between the ages of 10-15 years. Therefore, it could be possible that sperm production concentration and quality could have been affected by the increasing age of the donkeys. Sperm concentration was significantly ($p<0.05$) affected by the season, as the sperm concentration reduced during the dry season when compared to the rainy season. This contradicts the findings of Carluccio et al. (2013), who found out that the mean sperm concentration was significantly lower in Martina Franca jackasses in the winter period compared with the spring and the summer. This finding ascertains that donkeys are seasonal breeders.

This assertion on age affecting sperm quality has been indicated by Kidd et al. (2001), who suggested that increased male age is associated with a decline in semen volume, sperm motility, and sperm normal morphology, but not with sperm concentration. Several mechanisms have been proposed to explain how aging in males may cause changes in semen parameters. These changes can be related to seminal vesicle inadequacy, which reduces semen volume or prostate atrophy such as reduction in water and protein content, which might affect sperm motility and ejaculate volume (Kidd et al., 2001). Major chang-

es associated with age must be related to testicular degeneration (Nipken and Wrobel, 1997), which impacts spermatogenesis and may justify deterioration of seminal quality, as supported by decreased motility (Miró et al., 2005).

CONCLUSION

The season of year influenced the histo-morphometric parameters of donkeys and that the donkey is a seasonal breeder with peak spermatogenesis occurring in the rainy season. Also, the epididymal sperm parameters of donkeys are of a good quality that can be utilized in artificial insemination programs. Future research should be carried out on the use of locally available materials as semen extenders for the improvement of donkey populations.

REFERENCES

ATAWALNA J, EMIKPE BO, SALLAH EK, SHAIBU W, FOLITSE RD (2015) The health problems, gastrointestinal and blood parasites commonly associated with donkeys in the upper East Region of Ghana. *Afr J Biomed Res,* 18(1): 37-41.

CARLUCCIO A, PANZANI S, CONTRI A, BRONZO V, ROBBE D, VERONESI MC (2013) Influence of season on testicular morphometry and semen characteristics in Martina Franca jackasses. *Theriogenology*, 79(3): 502-507.

CARY JA, MADILL S, FARNSWORTH K, HAYNA JT, DUOOS L, FAHNING ML (2004) A comparison of electroejaculation and epididymal sperm collection techniques in stallions. *Can Vet J*, 45(1): 35-41.

CHIARINI-GARCIA H, ALVES-FREITAS D, BARBOSA IS, ALMEIDA FRLC (2009) Evaluation of the seminiferous epithelial cycle, spermatogonial kinetics and niche in donkeys (*Equus asinus*). *Animal Reprod Sci*, 116(1-2): 139-154.

CONTRI A, GLORIA A, ROBBE D, DE AMICIS I, CARLUCCIO A (2012) Characteristics of donkey spermatozoa along the length of the epididymis. *Theriogenology*, 77(1): 166-173.

GLORIA A, CONTRI A, DE AMICIS I, ROBBE D, CARLUCCIO A (2011) Differences between epididymal and ejaculated sperm characteristics in donkey. *Anim Reprod Sci,* 128(1-4): 117-122.

GUNE AR, PATIL AD, GUNE RP, PATIL RS (2019) Histopathological patterns of testicular biopsies in azoospermic infertile males. *Int J Health Sci Res,* 9(5): 22-27.

HAGSTROM DJ (2004) Donkeys are different: an overview of reproductive variations from horses. *University of Illinois, USA, Department of Agriculture, Local Extension Councils Cooperating*, 1-5.

KAZEMI S, FEIZI F, AGHAPOUR F, JOORSARAEE GA, MOGHADAMNIA AA (2016) Histopathology and histomorphometric investigation of bisphenol A and nonylphenol on the male rat reproductive system. *North Am J Med Sci*, 8(5): 215-221.

ŁACKA K, KONDRACKI S, IWANINA M, WYSOKIŃSKA A (2016) Assessment of stallion semen morphology using two different staining methods, microscopic techniques, and sample sizes. *J Vet Res (Poland),* 60(1): 99-104.

MATLHOLA DM, CHEN R (2020) Telecoupling of the trade of donkey-hides between Botswana and China: challenges and opportunities. *Sustainability (Switzerland)*, 12(5): 1-10.

MCLEAN AK, NAVAS GONZALEZ FJ (2018) Can scientists influence donkey welfare? Historical perspective and a contemporary view. *J Equine Vet Sci*, 65: 25-32.

MIRAGAYA MH, NEILD DM, ALONSO AE (2018) A review of reproductive biology and biotechnologies in donkeys. *J Equine Vet Sci*, 65: 55-61.

MUYLLE S, SIMOENS P, LAUWERS H, VAN LOON G (1999) Age determination in mini-Shetland ponies and donkeys. *Zentralbl Veterinarmed A,* 46(7): 421-429.

NASR M, RASHED R, SHOGY K, HASSANIN A (2021) Morphometric and morphological characterization of the donkey testis in relation to age. *J Curr Vet Res,* 3(2): 41-54.

NIPKEN C, WROBEL KH (1997) A quantitative morphological study of age-related changes in the donkey testis in the period between puberty and senium. *Andrologia,* 29(3): 149-161.

SOKOL RZ, SHULMAN P, PAULSON RJ (2000) Comparison of two methods for the measurement of sperm concentration. *Fertil Steril*, 73(3): 591-594.

STARKEY P, STARKEY M (1996) Regional and world trends in donkey populations. *Donkeys, People and Development, July*, 10-21. http://www.atnesa.org

TÖPFER-PETERSEN E, EKHLASI-HUNDRIESER M, KIRCHHOFF C, LEEB T, SIEME H (2005) The role of stallion seminal proteins in fertilisation. *Anim Reprod Sci*, 89(1-4): 159-170.

YALÇIN T, KAYA S., KAYA TEKTEMUR N, OZAN İE (2020) The Methods Used in Histopathological Evaluation of Testis Tissues. *Batman University Journal of Life Sciences* Batman Üniversitesi Yaşam Bilimleri Dergisi, 10(1): 148.

Morphometric analysis of distal femur through MRI in Turkish population and review of the literature

Mehmet Selcuk[1], Nadire U. Dogan[2], Mehmet Ozturk[3], Ahmet K. Karabulut[2], Zeliha Fazliogullari[2]

[1] Karamanoglu Mehmetbey University, Health Care Services Department, Vocational School of Health Services, Karaman, Turkey

[2] Selcuk University, Department of Anatomy, Faculty of Medicine, Konya, Turkey

[3] Selcuk University, Department of Radiology, Faculty of Medicine, Konya, Turkey

SUMMARY

Measurements of the distal femur are highly variable among different subjects. To obtain the best stability and longevity of the knee implants, anthropometric data of the distal femur is required. The aim of this study was to investigate the anatomical structure of the distal femur according to age and gender and to determine the changes in the groups, of the patients with meniscopathy and controls. A total of 488 patients were included in the study according to age groups (0-15, 16-30, 31-45, 46-60, 61 and above). Intercondylar width, intercondylar anteroposterior distance, medial condylar width, lateral condylar width, bicondylar width, medial condyle anteroposterior distance, and lateral condyle anteroposterior distance were measured on axial Magnetic Resonance Imaging (MRI).

Intercondylar width, medial condylar width, lateral condylar width and bicondylar width were significantly higher in men in all age groups compared to women ($p < 0.05$). Intercondylar anteroposterior distance, medial condyle anteroposterior distance and lateral condyle anteroposterior distance were statistically significantly higher in males than in females except 0-15 age group ($p < 0.05$). There was no significant difference in medial and lateral anteroposterior distance values in men ($p > 0.05$), and found to be statistically significant ($p < 0.05$) on the right and left side in women. Although personalized implant production is expensive compared to today's conditions, we think that age and gender changes should be considered in the selection of prosthesis, since the dimensions of the distal femur will affect the stability and duration of use of knee implants.

Key words: Anatomy – Femur – Magnetic resonance imaging – Morphometry – Total knee arthroplasty

INTRODUCTION

Total knee arthroplasty is an effective surgical intervention that can relieve the pain of patients who suffered from end-stage arthritis and restore their joint functions (Singh and Sloan, 2008; Dusad et al., 2015). The distal part of the femur has two condyles, lateral and medial, separated by an

Corresponding author:
Mehmet Selcuk, PhD, Lecturer. Karamanoglu Mehmetbey University, Vocational School of Health Services, 70100, Karaman, Turkey. Phone: 0090-338-226-2762. E-mail: fizyomehmetselcuk@gmail.com - Orcid: 0000-0003-0798-1772.

Submitted: June 4, 2023. **Accepted:** July 21, 2023

https://doi.org/10.52083/BWQV4453

intercondylar notch (Adhikari et al., 2017; Eboh and Igbinedion, 2020). Measurements of the distal part of the femur are very valuable for total knee arthroplasty (Berger et al., 1993; Arima et al., 1995). Anthropometric data must be accurate and reliable to obtain the best stability and longevity for the implant (Westrich et al., 1995).

Menisci are fibrocartilaginous discs located between the femur and the medial and lateral articular surfaces of the tibia in the knee. The most important tasks of these are weight transfer, dynamic shock absorption during movement, and protection of joint cartilage (Walker and Erkman, 1975). Meniscal injuries occur as a result of rotation of the tibia on the os femoris or the rotation of the os femoris on the tibia, especially when the knee joint is partially flexed, while the knee joint carries body weight (Hai-Nan et al., 2014). Meniscal tears have been classified because the location, size, and type of meniscopathy are very important in terms of treatment planning (Jee et al., 2003).

In this study, it was aimed to examine the morphometric and morphological structure of the anatomical formations of the distal femur according to age and gender in individuals with meniscopathy and in the control group, and to determine the changes in the groups. This study also aimed to determine a guideline for the femoral component of total knee prostheses for theTurkish population.

MATERIALS AND METHODS

What have been studied are 488 knee Magnetic Resonance Imaging (MRI) belonging to 488 patients. In the Picture Archiving and Communication Systems (PACS) archive of the Selcuk University Faculty of Medicine Radiology Department were included in the study. The data of the cases were obtained by retrospectively scanning the (MR) images between January 15, 2013, and January 15, 2018.

The study was carried out on a 1.5 T Toshiba brand device serving in the Department of Radiology. Measurements were made on the axial images of the fat-suppressed proton density sequence. Imaging parameters TR: 2125, TE: 45. Section thickness was 3.7 mm, the gap was 0.4-1 mm, the field of view was 14-18 cm, and the display matrix was 640 x 640.

The cases diagnosed with meniscopathy by the radiologists in the Radiology Department and the cases without any pathological findings (such as meniscopathy, chondromalacia, trauma, or tumor) in knee MRIs were evaluated as healthy and included in the study. There were 244 females (117 right knee, 127 left knee) and 244 males (119 right knee, 125 left knee) in our study. They were grouped according to 5 different age ranges (0-15, 16-30, 31-45, 46-60, 61 and over), between 7-92 years of age (Table 1). The grades of meniscopathy were determined by a radiologist with 15 years of experience according to MR images of these cases.

Table 1. Distribution of cases according to age groups and gender.

Age groups	Genders		Total
	Female	Male	
0-15	48	48	96
16-30	49	49	98
31-45	48	51	99
46-60	52	48	100
61+	47	48	95
Total	**244**	**244**	**488**

Measurements

In the study, distal femur parameters; intercondylar width (ICW), intercondylar anteroposterior distance (ICD), medial condylar width (MCW), lateral condylar width (LCW), bicondylar width (BW), medial condyle anteroposterior distance (MAP), and lateral condyle anteroposterior distance (LAP) were measured on axial MRI. In all cases, measurements were made on axial plane MRI images passing through both epicondyles in the axial plane.

ICW: longest transverse width of the intercondylar notch; it is the length between the medial point of the lateral condyle and the medial point of the medial condyle. ICD: vertical line drawn from the upper part of the intercondylar notch to the lowest level of the imaged condyles (Murshed et al., 2005; Terzidis et al., 2012; Yazar et al., 2012) (Fig. 1). MCW: the shortest mediolateral width of the medial condyle. LCW: the shortest mediolateral

Fig. 1.- Measured parameters. **A:** The intercondylar notch width of the femur (ICW). **B:** The intercondylar notch anteroposterior distance of the femur (ICD). **C:** The medial condylar width of the femur (MCW). **D:** The lateral condylar width of the femur (LCW). **E:** Medial condyle anteroposterior distance of the femur (MAP). **F:** Lateral condyle anteroposterior distance of the femur (LAP). **G:** The bicondylar width of the femur (BW) (M: Medial L: Lateral).

width of the lateral condyle (Murshed et al., 2005; Yazar et al., 2012; Kim et al., 2013; Pinskerova et al., 2014) (Fig. 1). BW: longest mediolateral dimension. The longest horizontal line connecting the lateral and medial condyles (Murshed et al., 2005; Terzidis et al., 2012; Pinskerova et al., 2014) (Fig. 1). MAP: the longest distance between the anterior and posterior point of the medial condyle. LAP: the longest distance between the anterior and posterior point of the lateral condyle (Mensch and Amstutz, 1975; Terzidis et al., 2012; Kim et al., 2013; Fan et al., 2017) (Fig. 1).

In the evaluation of the degree of meniscopathy, Kaya (2008) reported the classification based on MRI as follows. Grade 0: Homogeneous intensity. Grade 1: Point-like intensity. Grade 2: Internal intensity that does not extend to the surface. Grade 3: Intrameniscal intensity extending to the joint surface (Fig. 2).

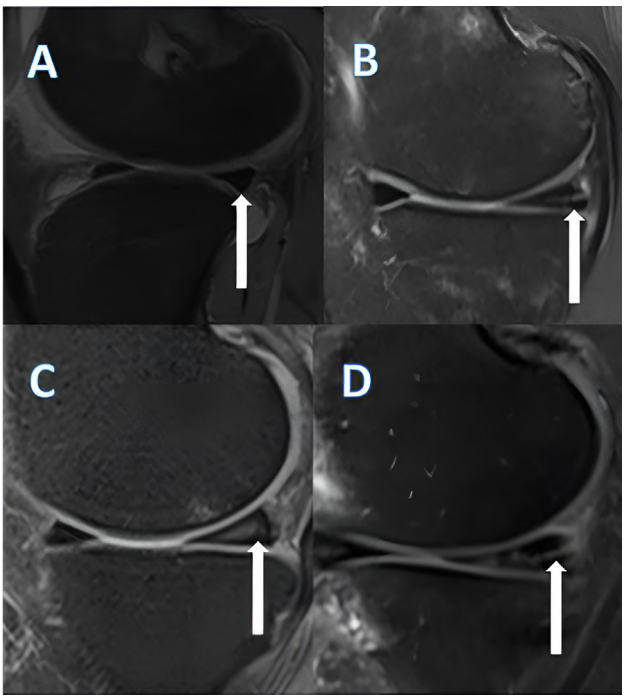

Fig. 2.- Evaluation of the degree of meniscopathy. **A:** Homogeneous intensity grade 0 (normal meniscus) in the posterior horn of the lateral meniscus on MRI of the left knee. **B:** Grade 1 degeneration of the medial meniscus posterior horn on MRI of the right knee. **C:** Grade 2 degeneration of medial meniscus and lateralis on MRI of the left knee. **D:** Grade 3 horizontal tear of posterior horn of a degenerated lateral meniscus on MRI of the right knee.

Statistical analysis

All measurements were evaluated according to age groups, gender, right-left knee difference, and degree of meniscopathy.

Shapiro Wilks Test was used to test the conformity of the distribution of the data of all variables related to the normality assumption, one of the parametric test assumptions, to the normal distribution. T-test for independent samples (Independent Samples T-Test) from parametric tests to test whether the variables that fit the normal distribution differ according to the groups in the comparisons of two groups, and the Mann-Whitney U test to test whether the variables that do not fit the normal distribution differ according to the groups used. In more than two group comparisons ANOVA, one of the parametric tests, was used to test whether it was different according to the groups, and the Kruskal-Wallis test, one of the non-parametric tests, was used to test whether the variables not suitable for normal distribution were different according to the groups. Chi-square test

Table 2. Differences (mean±standard deviation) (mm) values of the parameters in each age group as per gender.

Age		ICW		ICD		MCW		LCW		BW		MAP		LAP	
		mean+SD	p	mean+SD	p	mean+SD	p	mean+SD	p	mean+SD	p	mean+SD	p	mean+SD	p
0-15	Female (48)	18.35±2.25	0.002*	26.66±5.04	0.487*	21.53±3.28	0.001*	46.57±8.16	0.000*	62.34±8.28	0.000*	22.99±3.50	0.281	46.68±8.35	0.07
	Male (48)	20.05±2.87		27.38±5.04		23.97±3.53		48.98±8.22		69.38±8.75		25.79±3.89		50.17±8.09	
16-30	Female (49)	0.02±2.50	0.000*	28.47±3.15	0.000*	23.33±2.14	0.000*	53.48±3.41	0.000*	67.86±4.14	0.000*	24.40±2.19	0.000*	54.48±4.04	0.000*
	Male (49)	22.28±2.35		32.52±3.57		27.26±2.12		60.76±4.37		78.70±4.29		28.68±2.78		61.83±4.30	
31-45	Female (48)	20.54±2.33	0.000*	28.50±3.20	0.000*	24.82±2.45	0.000*	55.25±3.85	0.000*	70.44±4.44	0.000*	25.52±2.53	0.000*	55.99±4.05	0.000*
	Male (51)	22.35±2.61		30.97±3.14		27.32±2.66		59.92±4.83		77.05±5.37		28.14±3.15		59.88±5.08	
46-60	Female (52)	19.86±2.38	0.000*	28.30±2.52	0.000*	24.90±1.87	0.000*	55.34±3.47	0.000*	69.17±3.63	0.000*	25.11±2.30	0.000*	55.58±4.37	0.000*
	Male (48)	22.55±2.58		31.58±3.65		27.53±1.94		59.97±4.85		77.40±4.17		28.12±2.73		59.82±5.36	
61+	Female (47)	20.26±2.16	0.000*	27.88±2.43	0.000*	24.63±1.36	0.000*	54.38±3.99	0.000*	68.72±3.68	0.000*	25.27±1.67	0.000*	55.18±3.73	0.000*
	Male (48)	22.57±2.77		30.89±3.27		26.91±2.28		59.06±4.21		75.94±5.04		27.61±2.99		59.23±4.51	

*p<0.05 (ICW; intercondylar width. ICD; intercondylar anteroposterior distance. MCW; medial condylar width. LCW; lateral condylar width. BW; bicondylar width. MAP; medial condyle anteroposterior distance. LAP; lateral condyle anteroposterior distance)

Table 3. The relationship of the parameters (mean±standart deviation) (mm) values in male and female. according to the right and left side.

Parameter	Female		Male		p	
	Right (117)	Left (127)	Right (119)	Left (125)	Female	Male
ICW	20.01±2.43	19.62±2.43	22.11±2.95	21.82±2.63	0.168	0.345
ICD	28.02±3.54	27.93±3.34	30.26±4.31	31.08±3.95	0.535	0.077
MCW	23.85±2.92	23.86±2.34	26.76±2.87	26.47±2.87	0.945	0.325
LCW	24.44±2.57	24.87±2.71	28.00±3.02	27.37±3.46	0.254	0.129
BW	67.33±6.36	68.09±5.22	76.59±6.42	74.90±6.66	0.375	0.065
MAP	53.73±6.20	52.41±5.48	58.32±7.01	57.26±6.97	0.002	0.202
LAP	54.21±6.56	53.06±5.85	58.56±6.60	57.90±7.21	0.014	0.599

*$p < 0.05$ (ICW; intercondylar width. ICD; intercondylar anteroposterior distance. MCW; medial condylar width. LCW; lateral condylar width. BW; bicondylar width. MAP; medial condyle anteroposterior distance. LAP; lateral condyle anteroposterior distance).

was used in the analysis of categorical data. All analyses were evaluated at the 5% significance level (95% confidence level).

RESULTS

In our study on axial MRI; the mean values of ICW, BW, MCW, and LCW were statistically significantly higher in males than females in each age group ($p < 0.05$). Mean values of ICD, MAP, and LAP were statistically significantly higher in males than females in all age groups except the 0-15 age group ($p < 0.05$) (Table 2).

Considering the mean values of ICW, ICD, MCW, LCW, and BW in our study, it was not found statistically significant between the right and left knees in men and women. However, while there was no significant difference between the right and left in the mean values of MAP and LAP in men ($p > 0.05$), it was found that it was statistically significantly higher ($p < 0.05$) on the right than on the left in women (Table 3).

DISCUSSION

Most anatomical morphometric studies have been performed with different methods such as radiography, computed tomography, magnetic resonance imaging, cadavers, and 3D modeling (Mensch and Amstutz, 1975; Murshed et al., 2005; Cheng et al., 2009; Yue et al., 2011; Yazar et al., 2012; Terzidis et al., 2012). In the literature, there are significant differences between bone parameters with different radiological measurements (Herzog et al., 1994; Uslu et al., 2005). Herzog et al., (1994) compared direct cadaveric intercondylar notch measurements with radiographic and MRI measurements, and found no difference in caliper measurement of cadaver bones (20.3 mm) and MRI (20.8 mm) measurements, but with caliper measurement of cadaver bones and radiographic measurements. 22 mm were found to be significant differences. With this study, Herzog et al. (1994) confirmed the accuracy of magnetic resonance measurements and their superiority over flat film measurements.

Many studies emphasize the differences between genders and ethnic groups (Urabe et al., 2008; Cheng et al., 2009; Chin et al., 2011; Yue et al., 2011; Yazar et al., 2012). The distal part of the femur, especially the two condyles, is morphologically different in males from females (Murshed et al., 2005; Guy et al., 2012; Terzidis et al., 2012; Kim et al., 2013; Fan et al., 2017). However, some studies have shown that there is no significant difference in the morphology of the distal femoral condyle between men and women (Poilvache et al., 1996; Griffin et al., 2000). Many studies have found that the same type of prosthesis is not suitable for different populations (Ho et al., 2006; Kwak et al., 2007). While studies are reporting that the knee morphometry of Asian people is smaller than that of Western people (Kwak et al., 2007), there are also researchers reporting that they could not find any difference between European and Afri-

Table 4. Comparison of parameters (mean±standard deviation) (mm) values.

Researchers	Research plane	Method	Group	ICW		ICD		MCW		LCW	
				Female	Male	Female	Male	Female	Male	Female	Male
Mensch and Amstutz (1975)	North America	X-Ray	Male (44) Female (39)	18.9±1.5	22.6±6.0			24.5±1.2	29.9±2.2	26.5±1.8	31.4±2.3
Mensch and Amstutz (1975)	North America	Dry bone	Male (44) Female (39)	18.7±2.5	20.8±3.6			24.5±1.5	29.9±2.6	26.6±1.5	31.4±2.6
Charlton et al.. (2002)	Pennsylvania	MRI	Male (28) Female (20)	17.4	17.7						
Murshed et al.. (2005)	Turkey	MRI	Male (100) Female (100)	19.1±2.0	21.3±2.4	29.0±2.6	33.2±2.8	23.7±2.2	27.0±2.1	23.2±2.3	26.6±2.8
Yue et al.. (2011)	China	CT	Male (20) Female (20)	18.6±1.4	21.8±0.8			22.0±1.3	24.9±1.4	24.2±1.7	27.5±2.5
Terzidis et al.. (2012)	Caucasia	Dry bone	Male (192) Female (168)	18.7±0.1	22.0±0.18	23.07±0.12	27.8±0.16				
Yazar et al.. (2012)	Turkey	CT	66	20.85±2.76		27±2.9		24.61±2.58		23.61±2.18	
Kim et al.. (2013)	Korea	CT	Male (88) Female (114)	18.97±2.75	21.66±2.66	27.16±1.85		23.46±2.39	25.78±1.85	24.05±2.00	27.96±1.91
Pinskerova et al.. (2014)	Czech Republic	MRI	Male (100) Female (100)					26.95±3.37	23.28±1.75	26.8±3.26	23.78±1.60
Our study (2018)	Konya	MRI	Male (196) Female (196)	20.16±2.35	22.43±2.56	28.29±2.83		24.42±2.08	27.26±2.26	25.07±2.22	28.14±2.92

(CT: Computerized Tomography. MRI: Magnetic Resonances Imaging.) (ICW; intercondylar width. ICD: intercondylar anteroposterior distance. MCW; medial condylar width. LCW; lateral condylar width)

can population parameters (Tillman et al., 2002). Artificial knee joint prosthesis systems, which are widely used in China, are designed according to the anatomical characteristics of European and American populations. When these joint replacement systems designed for Western patients are used in Asian patients, prosthesis mismatch often occurs due to ethnic differences (Yip et al., 2004; Cheng et al., 2009). In some studies, the Chinese population has been found to have lower and flatter anterior condyles and wider posterior condyles than westerners (Yip et al., 2004; Sun et al., 2007). In a study comparing the morphology of the distal femur between Caucasian and Japanese women, morphological measurements of the distal femur reported that Caucasian women had significantly longer anteroposterior width of the condyles (Urabe et al., 2008). In a study investigating the anthropometric differences between Koreans and Westerners, it was reported that Koreans were shorter, less overweight, had a smaller skeletal structure, and had a higher incidence of constitutional varus alignment of the lower extremity. This study also reported that Koreans have lifestyles that require high flexion positions of the knee such as squatting, kneeling and sitting cross-legged, and that the incidence of postoperative deep vein thrombosis and pulmonary thromboembolism is lower in Koreans than in Westerners (Kim et al., 2015). In a study investigating the causes of failure after total knee arthroplasty in Korea in the last 5 years, it was reported that the most common cumulative cause was infection, followed by loosening, wear, instability and stiffness (Koh et al., 2014). Considering the anatomical differences between races in the development of implants to be used in the Turkish population, we think that the data of our study, in which we examined the distal femur measurements in 488 cases in different age groups, should be made according to each race.

In the existing literature, studies examining intercondylar notch dimensions (ICW, ICD), condyle widths (MCW, LCW), condyle anteroposterior distance (MAP, LAP) and bicondylar width measurements were conducted in different races, in men and women, and only in adults, and differences according to age groups were not evaluated. In our study, the statistically significant differences we obtained in 5 different age groups determined that the measurements showed serious differences between different age groups in men and in women.

Studies examining the dimensions of the intercondylar notch (ICW and ICD) in different races and with different methods are available in the literature (Table 4). The differences between the dimensions of the intercondylar notch in these studies may be related to the method used, the number of samples and racial differences. In the studies of Murshed et al. (2005), Kim et al. (2013), Terzidis et al. (2012) and Yue et al. (2011) in the ICW, there was a significant difference in males (over 16 years) compared to females, in line with our data on the adult group (over 16 years of age) was found to be statistically larger ($p < 0.05$). In the ICH, Murshed et al. (2005), Kim et al. (2013), and Terzidis et al. (2012) were found to be statistically significant in males compared to females, consistent with our data on the adult group (over 16 years of age) was found to be larger ($p < 0.05$). Kim et al. (2013), in their study on Koreans, stated that they aimed to develop a Korean-specific equation with intercondylar notch dimensions and to show the usefulness of the equations for specific population groups.

The studies of Murshed et al. (2005), Kim et al. (2013), Yue et al. (2011) and Pinskerova et al. (2014) in MCW and LCW were consistent with the data of our adult group (over 16 years old) in our study. It was found to be larger in men than in women ($p < 0.05$), and the difference was statistically significant.

BW is the most frequently measured anatomical parameter of the distal femur. In the literature, there is great variability in the definition of measurement points of bicondylar width, measurement techniques, and races. In BW, the studies of Murshed et al. (2005), Cheng et al. (2009), Terzidis et al. (2012) and Pinskerova et al. (2014) showed statistically significant differences in males compared to females, in line with our data on the adult group (over 16 years of age). It was found to be significantly larger ($p < 0.05$) (Table 5).

In the literature, MAP and LAP has been defined as the maximum anteroposterior diameter of

Table 5. Comparison of parameters (mean±standard deviation) (mm) values.

Researchers	Research plane	Method	Group	BW		MAP		LAP	
				Female	Male	Female	Male	Female	Male
Mensch and Amstutz (1975)	North America	X-Ray	Male (44) Female (39)			61.1±2.2	68.2±4.1	62.6±2.3	70.3±4.3
Mensch and Amstutz (1975)	North America	Dry bone	Male (44) Female (39)			61.1±2.7	68.1±3.6	67.9±3.3	69.9±2.6
Murshed et al.. (2005)	Turkey	MRI	Male (100) Female (100)	74.4±4.3	83.1±7.7				
Kim et al.. (2013)	Korea	CT	Male (88) female (114)			55.25±3.02	61.22±3.06	58.39±2.76	64.63±3.65
Yue et al.. (2011)	China	CT	Male (20) Female (20)			55.3±2.7	62.2±3.9	58.8±2.5	65.0±2.8
Cheng et al.. (2009)	China	CT	Male (94) Female (78)	66.8±3.1	74.4±2.9	49.8±3.2	52.6±2.4	49.3±4.1	51.8±3.7
Terzidis et al.. (2012)	Caucasia	Dry bone	Male (192) Female (168)	78.5±0.3	88.6±0.42	55.9±0.29	61.1±0.34	55.4±0.21	61.1±0.33
Yazar et al.. (2012)	Turkey	CT	66	78.43±5.76		57±4.71		60.94±4.5	
Pinskerova et al.. (2014)	Czech Republic	MRI	Male (100) Female (100)	78.19±3.54	88.81±3.33	63.43±2.15	69.84±3.29	65.64±3.42	71.79±3.12
Fan et al.. (2017)	Southeast china	MRI	Male (114) Female (130)			59.6±3.6	64.9±3.5	58.3±3.9	64.0±3.8
Our study (2018)	Konya	MRI	Male (196) Female (196)	69.05±4.06	77.27±4.82	54.62±3.73	59.93±4.58	55.31±4.07	60.19±4.89

(CT: Computerized Tomography. MRI: Magnetic Resonances Imaging.). (BW; bicondylar width. MAP; medial condyle anteroposterior distance. LAP; lateral condyle anteroposterior distance)

each femoral condyle (Cheng et al., 2009, Yue et al., 2011; Terzidis et al., 2012, Yazar et al., 2012, Kim et al., 2013, Pinskerova et al., 2014, Fan et al., 2017). But there are serious differences between measurement techniques and methods in studies. In our study, as in other studies, the adult group (over 16 years of age) was found to be statistically larger in males than females ($p < 0.05$), which is consistent with our data.

Distal femur measurements were made in adults in all studies in the literature. For this reason, we could not find the opportunity to evaluate our data on the 0-15 age group in our study.

In studies on distal femur measurements in the literature, the differences between the left and right sides in women and men were examined, and it was found that there were no statistically significant differences between the right and left in these studies, consistent with our study (Souryal and Freeman, 1993; Anderson et al., 2001; Charlton et al., 2002; Murshed et al., 2005; Cheng et al., 2009; Terzidis et al., 2012; Yazar et al., 2012; Kim et al., 2013). However, in our study, distal femur measurements (MAP of on the right side (53.73±6.20 mm) in women on the left (52.41±5.48 mm) and LAP of on the right side in women (54, 21±6.56) were found to be statistically significantly ($p < 0.05$) higher than the left (53.06±5.85).

The most important limitation of our study is the inability to examine the height and weight, living conditions, occupation, and sports habits of the subjects, since it is a retrospective study. These criteria are very important criteria affecting the distal femur, and there is a need for prospective studies in which these criteria can be taken into account.

CONCLUSION

By this article, ICW, MCW, LCW and BW were statistically significantly greater in men than in women in all age groups ($p < 0.05$). ICD, MAP and LAP were statistically significantly greater in males than females in all age groups except the 0-15 age group ($p < 0.05$).

Our study will support other literature studies in terms of providing the morphological definition of the distal femur and contributing to the anatomical evaluation of the distal femur region before orthopedic operations such as knee implants. Although personalized implant production is expensive compared to today's conditions, we think that age and gender changes should be considered in the selection of prosthesis, since the dimensions of the distal femur will affect the stability and duration of use of knee implants.

Additionally, the data obtained from this study can be used as a guideline in designing femoral component of the total knee prosthesis in Turkish population.

ETHICS STATEMENT

All procedures performed in this study involving human participants were in accordance with the ethical standards of the institutional and/or national research committee and with the 1964 Helsinki declaration and its later amendments or comparable ethical standards. Ethical approval (approval number 2018/347) was given by the Local Ethics Committee of the Medical Faculty. This single-center retrospective study was approved by the local institutional review board with a waiver of the requirement for written, informed consent. This study was conducted at Selcuk University Faculty of Medicine.

REFERENCES

ADHİKARİ RK, YADAV B, YADAV SK, SİNGH AC (2017) Comparative study of angle of inclination and neck length of dry femur. *J Nobel Med Coll,* 6(1): 44-47.

ANDERSON AF, DOME DC, GAUTAM S, AWH MH, RENNIRT GW (2001) Correlation of anthropometric measurements, strength, anterior cruciate ligament size, and intercondylar notch characteristics to sex differences in anterior cruciate ligament tear rates. *Am J Sports Med,* 29(1): 58-66.

ARIMA J, WHITESIDE LA, MCCARTHY DS, WHITE SE (1995) Femoral rotational alignment, based on the anteroposterior axis, in total knee arthroplasty in a valgus knee. A technical note. *JBJS,* 77(9):1331-1334.

BERGER RA, RUBASH HE, SEEL MJ, THOMPSON WH, CROSSETT LS (1993) Determining the rotational alignment of the femoral component in total knee arthroplasty using the epicondylar axis. *Clin Orthop Relat Res,* 286: 40-47.

CHARLTON WP, JOHN TAS, CICCOTTI MG, HARRISON N, SCHWEITZER M (2002) Differences in femoral notch anatomy between men and women: a magnetic resonance imaging study. *Am J Sports Med,* 30(3): 329-333.

CHENG FB, JI XF, LAI Y, FENG JC, ZHENG WX, SUN YF, FU YW, Lİ YQ (2009) Three dimensional morphometry of the knee to design the total knee arthroplasty for Chinese population. *The Knee,* 16(5): 341-347.

CHIN PL, TEY TT, IBRAHIM MYB, CHIA S-L, YEO SJ, LO NN (2011) Intraoperative morphometric study of gender differences in Asian femurs. *J Arthroplasty,* 26(7): 984-988.

DUSAD A, PEDRO S, MİKULS TR, HARTMAN CW, GARVİN KL, O'DELL JR, MİCHAUD K (2015) Impact of total knee arthroplasty as assessed using patient-reported pain and health-related quality of life indices: rheumatoid arthritis versus osteoarthritis. *Arthritis Rheumatol,* 67(9): 2503-2511.

EBOH DEO, IGBİNEDİON EN (2020) Morphometry of the distal femur in a South-south Nigerian population. *Mal J Med Health Sci,* 16: 197-201.

FAN L, XU T, LI X, ZAN P, LI G (2017) Morphologic features of the distal femur and tibia plateau in Southeastern Chinese population: A cross-sectional study. *Medicine,* 96: 46.

GRIFFIN FM, MATH K, SCUDERI GR, INSALL JN, POILVACHE PL (2000) Anatomy of the epicondyles of the distal femur: MRI analysis of normal knees. *J Arthroplasty,* 15(3): 354-359.

GUY S, FARNDON M, SIDHOM S, AL-LAMI M, BENNETT C, LONDON N (2012) Gender differences in distal femoral morphology and the role of gender specific implants in total knee replacement: a prospective clinical study. *The Knee,* 19(1): 28-31.

HAI-NAN C, KAN Y, QI-RONG D, YI W (2014) Assessment of tibial rotation and meniscal movement using kinematic magnetic resonance imaging. *J Orthop Surg Res,* 9: 65.

HERZOG RJ, SILLIMAN JF, HUTTON K, RODKEY WG, STEADMAN JR (1994) Measurements of the intercondylar notch by plain film radiography and magnetic resonance imaging. *Am J Sports Med,* 22(2): 204-210.

HO WP, CHENG CK, LİAU JJ (2006) Morphometrical measurements of resected surface of femurs in Chinese knees: correlation to the sizing of current femoral implants. *Knee,* 13: 12-14.

JEE W-H, MCCAULEY TR, KIM J-M, JUN D-J, LEE Y-J, CHOI B-G, CHOI K-H (2003) Meniscal tear configurations: categorization with MR imaging. *AJR,* 180(1): 93-97.

KAYA T (2008) Kas İskelet Yumuşak Doku Radyolojisi. 1, İstanbul, *Nobel&Güneş Tıp Kitabevi*, p 4-43: 358,359.

KIM D-I, KWAK D-S, HAN S-H (2013) Sex determination using discriminant analysis of the medial and lateral condyles of the femur in Koreans. *Forensic Sci Int,* 233(1-3): 121-125.

KIM DK, SEO MC, SONG SJ, KIM KI (2015) Are Korean patients different from other ethnic groups in total knee arthroplasty? *Knee Surg Relat Res,* 27(4): 199-206.

KOH IJ, CHO WS, CHOI NY, KIM TK Kleos Korea Research Group (2014) Causes, risk factors, and trends in failures after TKA in Korea over the past 5 years: a multicenter study. *Clin Orthop Relat Res,* 472(1): 316-326.

KWAK DS, SURENDRAN S, PENGATTEERI YH, PARK SE, CHOI KN, GOPINATHAN P, HAN SH, HAN CW (2007) Morphometry of the proximal tibia to design the tibial component of total knee arthroplasty for the Korean population. *The Knee,* 14(4): 295-300.

MENSCH JS, AMSTUTZ H (1975) Knee morphology as a guide to knee replacement. *Clin Orthop Relat Res,* 112: 231-241

MURSHED KA, ÇIÇEKCIBAŞI AE, KARABACAKOĞLU A, ŞEKER M, ZIYLAN T (2005) Distal femur morphometry: a gender and bilateral comparative study using magnetic resonance imaging. *Surg Radiol Anat,* 27(2): 108-112.

PINSKEROVA V, NEMEC K, LANDOR I (2014) Gender differences in the morphology of the trochlea and the distal femur. *Knee Surg Sports Traumatol Arthrosc,* 22(10): 2342-2349.

POİLVACHE PL, INSALL JN, SCUDERİ GR, FONT-RODRİGUEZ DE (1996) Rotational landmarks and sizing of the distal femur in total knee arthroplasty. *Clin Orthop,* 331: 3546.

SİNGH JA, SLOAN JA (2008) Health-related quality of life in veterans with prevalent total knee arthroplasty and total hip arthroplasty. *Rheumatology,* 47: 1826-1831.

SOURYAL TO, FREEMAN TR (1993) Intercondylar notch size and anterior cruciate ligament injuries in athletes: a prospective study. *Am J Sports Med,* 21(4): 535-539.

STANDRING S (2020) Gray's anatomy: The anatomical basis of clinical practice. Elsevier Health Sciences, London.

SUN T, LV H, HONG N (2007) Rotational landmarks and total knee arthroplasty in osteoarthritic knees. *Zhongguo Xiu Fu ChongJjian Wai Ke Za Zhi,* 21(3): 226-230.

TERZIDIS I, TOTLIS T, PAPATHANASIOU E, SIDERIDIS A, VLASIS K, NATSIS K (2012) Gender and side-to-side differences of femoral condyles morphology: osteometric data from 360 Caucasian dried femori. *Anat Res Int,* 2012.

TILLMAN MD, SMITH KR, BAUER JA, CAURAUGH JH, FALSETTI AB, PATTISHALL JL (2002) Differences in three intercondylar notch geometry indices between males and females: a cadaver study. *The Knee,* 9(1): 41-46.

URABE K, MAHONEY O, MABUCHI K, ITOMAN M (2008) Morphologic differences of the distal femur between Caucasian and Japanese women. *J Orthop Surg,* 16(3): 312-315.

USLU M, OZSAR B, KENDİ T, KARA S, TEKDEMİR I, ATİK OS (2005) The use of computed tomography to determine femoral component size: a study of cadaver femora. *Bull Hosp Jt Dis,* 63: 49-53.

WALKER PS, ERKMAN MJ (1975) The role of the menisci in force transmisión across the knee. *Clin Orthop Relat Res,* 109: 184-192.

WESTRICH GH, HAAS SB, INSALL JN, FRACHIE A (1995) Resection specimen analysis of proximal tibial anatomy based on 100 total knee arthroplasty specimens. *J Arthroplasty*, 10(1): 47-51.

YAZAR F, IMRE N, BATTAL B, BILGIC S, TAYFUN C (2012) Is there any relation between distal parameters of the femur and its height and width? *Surg Radiol Anat,* 34(2): 125-132.

YIP DK, ZHU Y, CHIU K, NG T (2004) Distal rotational alignment of the Chinese femur and its relevance in total knee arthroplasty. *J Arthroplasty,* 19(5): 613-619.

YUE B, VARADARAJAN KM, AI S, TANG T, RUBASH HE, LI G (2011) Gender differences in the knees of Chinese population. *Knee Surg Sports Traumatol Arthrosc,* 19(1): 80-88.

Insulin improves spermatogenesis in a mouse model of aging

Mohammad A.T. Zavareh[1,2†], Mohammadhosssein K. Godaneh[1†], Parnian Eslahi[1,2†], Ali Younesi[1], Mohammadmahdi Gheibi[1], Sanaz Ziaeipour[1], Shabboo Ansari[1], Ali Mohammadhosein[1], Mohammadamin S. Alvani[1], Fatemeh K. Godaneh[1], Abbas Aliaghaei[1], Shabnam Abdi[3], Vahid Ebrahimi[4], Mohammad-Amin Abdollahifar[1], Amir Raoofi[5]

[1] Department of Biology and Anatomical Sciences, School of Medicine, Shahid Beheshti University of Medical Sciences, Tehran, Iran

[2] Student research Committee, School of Medicine, Shahid Beheshti University of Medical Sciences, Tehran, Iran

[3] Department of Anatomical Sciences & Cognitive Neuroscience, Faculty of Medicine, Tehran Medical Sciences, Islamic Azad University, Tehran, Iran

[4] Department of Anatomical Sciences, School of Medicine, Zanjan University of Medical Sciences, Zanjan, Iran

[5] Department of Anatomy and Cell Biology, School of Medicine, Sabzevar University of Medical Sciences, Iran

SUMMARY

Aging can have adverse effects on the chance of fertility in men. In fact, men over 40 years old usually suffer from low sperm quality, sperm motility, and low level of serum testosterone that leads to infertility. In addition, the structure of DNA is more vulnerable in aged testes due to the high level of reactive oxygen species (ROS) and nitric oxide. However, it has been showed that insulin is able to decrease oxidative stress and apoptosis. Moreover, some studies showed that insulin can enhance both spermatogenesis and fertility. In this regard, we investigate the impacts of insulin on spermatogenesis, the number of sperm, and the level of gonadal hormones in aged testes of mice. Thirty-six adult male NMRI mice were used. They were kept under standard conditions. The animals were divided into two groups control and insulin. The insulin group received 100 µL insulin with a 72-hour interval by intraperitoneal (IP) injection for 33 weeks and the control group received water. At the 8, 12, and 33 weeks of treatment, the testes of mice were removed for histological, cellular (ROS and glutathione [GSH]) and molecular (Bcal2, caspase-3, and Bax) analysis. For measurement of the level of hormones (testosterone, LH, and FSH), the blood samples were collected from the heart. According to our findings, insulin could significantly increase the volume of the testes and the total number of spermatogonial stem cells, primary spermatocytes, round spermatids as well as leydig cells. In addition, activity of GPX was considerably high in the insulin group. Furthermore, in the insulin group, the level of ROS was reduced. In conclusion, insulin may be effective in enhancing the function of the testes in aged male mice.

Key words: Spermatogenesis – Insulin – Aging

Corresponding author:
Mohammad-Amin Abdollahifar, Department of Biology and Anatomical Sciences, School of Medicine, Shahid Beheshti University of Medical Sciences, Tehran, Iran. Phone: +98-2122439976; Fax: +98-2122439976. E-mail: m_amin58@yahoo.com & abdollahima@sbmu.ac.ir.
Amir Raoofi, Cellular and Molecular Research Center, Sabzevar University of Medical Sciences, Sabzevar, Razavi Khorasan, Iran. Iran. Phone: +985144018101. E-mail: amirrezaraoofi@yahoo.com & RaoufiA1@medsab.ac.ir
†These three authors contributed equally to this work.

Submitted: June 18, 2023. **Accepted:** July 22, 2023

https://doi.org/10.52083/WRTE3240

INTRODUCTION

Aging is a progressive process that is associated with impairment of physiological integrity, disability, and several diseases (López-Otín et al., 2013; Abdollahifar et al., 2019). During aging, free radicals attack cells and alter the cell membranes or inactive proteins which may lead to cell death (Salomon et al., 2013). Besides, aging affects fertility both in women and in men. Men who are over 40 years old have some infertility issues such as low sperm quality, reduction of testes volume, and low levels of serum testosterone (Bhanmeechao et al., 2018). However, in most developed societies, it is a trend amongst men to have children at older ages. Hence, they may face some problems with infertility (Almeida et al., 2017) and tend to try assisted reproductive techniques (ART) that are expensive and have many challenges in older persons (Abdollahifar et al., 2019; Almeida et al., 2017).

Aging has also adverse effects on spermatogenesis. Previous studies showed that ageing reduced semen quality, semen volume, the number of normal sperms, and sperm motility (Stone et al., 2013; Zhu et al., 2011). Salomon et al. revealed that the activity of antioxidant enzymes such as GPX and SOD in the testes of young rats (3-12 months) is significantly higher if compared to the old rats (24 months). Then, the testes of aged rats are more vulnerable to free radicals (Salomon et al., 2013). Moreover, a significant increase in sperm DNA fragmentation from the age of 30 to 35 years has been reported (Stone et al., 2013), because the production of nitric oxide increases in aged tissues that can damage the DNA structure (Salomon et al., 2013). On the other hand, it has shown that ageing in Leydig cells of testes can also reduce the production of serum testosterone (Barbutska et al., 2015). According to previous studies, mitochondrial dysfunction has a key role in Leydig-cell damages. The level of ROS in old cells are considerably higher than antioxidant enzymes, so exceeded ROS attacks mitochondria, which finally leads to cell apoptosis (Lacombe et al., 2006; Sastre et al., 2000).

Some studies showed that insulin can be considered a protective applicator, because it is able to decrease oxidative stress and apoptosis in neuron cells by activating SOD, CAT, and GSH-Px (Song et al., 2018). Moreover, it has been suggested that insulin can stimulate spermatogenesis (Nakayama et al., 2004) and enhance fertility through impact on hypothalamic-pituitary-gonadal axis, as well as normalize the levels of serum testosterone and LH (Schoeller et al., 2012). The aim of this study was to assess the effects of insulin on spermatogenesis, number of sperms, and level of gonadal hormones on testes aging according to stereological studies.

MATERIAL AND METHODS

Animals and treatments

Thirty-six male NMRI mice, weighing 25-30 g and aged 4 weeks, were purchased from the laboratory animal research center. The animal was kept in a standard situation. Healthy adult mice were divided into two groups, each group comprising sixteen mice. Control group: the animals were kept intact. Insulin group: the animals received insulin at the dose of 100 µL with a 72-hour interval by intraperitoneal (IP) injection for 8, 12, and 33 weeks. At the end of 8, 12, and 33 weeks the animals were euthanized, and their testes were collected and fixed in paraformaldehyde 4%. After that, all testes were embedded in paraffin blocks and cut into 5 µm and 25 µm thicknesses by using a systematic, uniformly random sampling (SURS) for the stereological studies. All tissue sections were stained with hematoxylin and eosin (H&E).

Stereological study

Volume of the testes and the length of seminiferous tubules

Using the Cavalieri principle, testis sections were examined under a projecting microscope. Using stereological software developed at Shahaid Beheshti University of Medical Sciences, a grid of points was superimposed on the images. Using a Nikon microscopy system (E-200: Japan) connected to a video camera, the volume of the testis was measured. The formula has been used for the estimation of the volume of testes (Raoofi et al., 2021):

$$V = \sum P \times \frac{a}{p} \times t$$

In this equation, Σp is the total points of the probe, (t) is the distance between the sections and a/p represents the area per point.

The length of the seminiferous tubules

To estimate the length density of seminiferous tubules using the optical dissector method, the following equation (described in the following section) was used (Hassani et al., 2020):

$$L_v = \frac{2\sum Q}{\sum P \times \frac{a}{f}}$$

In this equation, "ΣQ" is the number of seminiferous tubules, "a/f" is the area per frame, and "ΣP" is the number of filed views.

Total number of testicular cells

Optical dissector methods were used to in order to determine the number of testicular cells. We selected microscopic fields by systematic uniform random sampling, by moving the stage in equal distances in x- and y-directions. An unbiased bordered counting frame with inclusions and exclusions was superimposed on the images. To measure the z-axis travel, the microscope stage was fitted with a microcator. The upper and lower guard zones were used in order to avoid cutting artifacts that occurred at the upper and lower surfaces of the tissue sections. In each section, a guard zone defined the height of the dissector. Nuclei lying completely or partly within the counting frame and not touching the exclusion line were selected if they came into maximal focus within the next focal sampling plane. As a final step, the number of testicular cells was estimated using the following formula (Hasani et al., 2020):

$$\mathbf{N_v} = \frac{\sum \mathbf{Q}}{\sum \mathbf{P} \times \mathbf{h} \times \frac{\mathbf{a}}{\mathbf{f}}} \times \frac{\mathbf{t}}{\mathbf{BA}}$$

"ΣQ" represents the number of cells, "ΣP" represents the number of filed views, "h" represents the dissector height, "a/f" represents the frame area, "t" represents the real tissue section thickness, and "BA" represents the tissue section thickness. The total number of testicular cells was estimated by multiplying the numerical density by the total volume.

$$N_{total} = N_V \times V$$

Level of hormones

After deep anesthesia in mice, the blood samples were collected. Then, the blood samples were centrifuged at 6000 g for 5 minutes. Mice-specific ELISA kit has been utilized for measuring the levels of serum of testosterone, LH, and FSH in the blood (catalog No. CSB-E11162r).

Analysis of differential gene expression

All RNA samples were extracted. Then, for removing any contaminations caused by genomic DNA, DNase I (Roche; Basel: Switzerland) has been used. After that, for synthesizing cDNA a commercial kit (Fermentas: Lithuania) has been applied at 42 °C for sixty minutes in compliance with the directions defined in the Company's instructions. The next step, a real-time PCR (TaqMan) on the basis of the QuantiTect SYBR Green RT-PCR kit (Takara Bio Inc: Japan) has been utilized to quantify the genes' relative expression level. The PCR primers have been tested by the Primer-Blast tool that is available at the website, www.ncbi.nlm.nih.gov/tools/primer-blast.

Reactive oxygen species in testicular tissue

For isolating the testicular cells by adding trypsin EDTA and PBS, all tissue samples were centrifuged at 1200 RPM for 5 min at 4 ° C. After that, the DCFDA at a concentration of 20 µM in a 100 µl aliquot was added to the sample and stored in a 37° C incubator for 45 minutes in the dark. Finally, all samples were assessed by a flow cytometer with a wavelength of 495 nm (Hasani et al., 2020).

Glutathione disulfide content assessments

For determining the level of GSH in testis tissue samples, GPX assay kit (Zelbio GmbH) was used with 5U/ml sensitivity (5KU/L) according to the previous study (Hasani et al., 2020). All samples were assessed using a Shimadzu RF5000U fluorescence spectrophotometer set for 495 nm excitation and 530 nm emission wavelengths.

Statistical analysis

Our findings were analyzed by two-way repeated measures ANOVA test, using the SPSS software version 20 (IBM Corp., Armonk, NY, USA). P≤0.05 were considered significant.

RESULTS

Stereological Evaluations

Statistical analysis of stereological assay of histological study demonstrated precise results (Fig. 1).

Volume of testes and Length of seminiferous tubules

The total volume of testes at 33 weeks and the length of seminiferous tubules at 8, 12 and 33 weeks in the insulin-treated group were considerably higher compared to the control group (Fig. 2A and B). There was no significant different in the volume of testis at 8 and 12 weeks between study groups (Fig. 2B)

Total number of testicular cells

A significant increase was observed in the total number of spermatogonia, primary spermatocyte round spermatid, and Leydig cells in the testes of the insulin group at 33 weeks of treatment compared to the control group. However, the mean total number of Sertoli cells did not show a considerable change between groups (Fig. 3A-E).

DCF absorption and GPX activity

We also demonstrated that the absorption of DFC has been reduced in the insulin group after 33 weeks of treatment (P< 0.05) (Fig. 4). Besides, the activity of GPX in the insulin group was higher

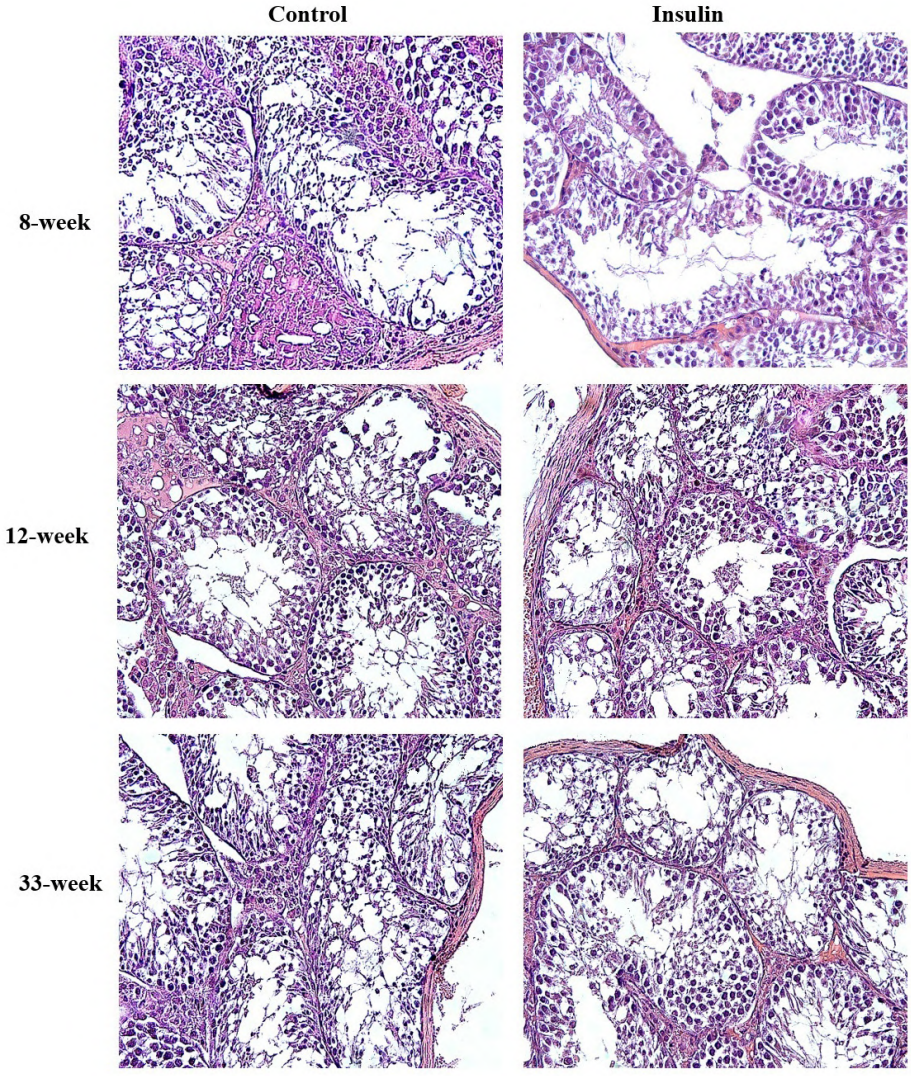

Fig. 1.- Photomicrograph of the testis stained with H&E (40x).

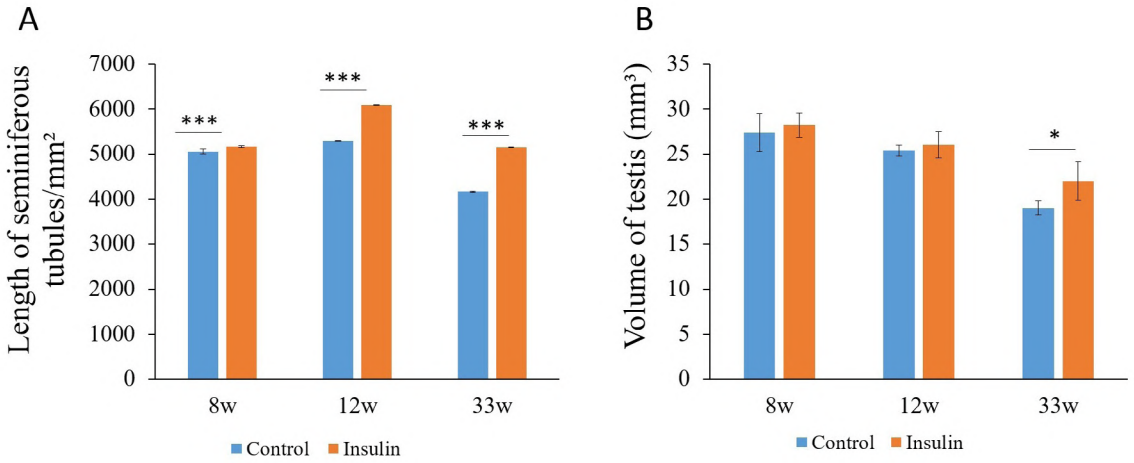

Fig. 2.- A: The effect of insulin on testis volume and seminiferous tubules length in mouse models of ageing. **B:** Mean±SD of the testis volume, seminiferous tubules length of testis in the study groups as compared by the ANOVA; (*P<0.05, **P<0.01, ***P<0.001).

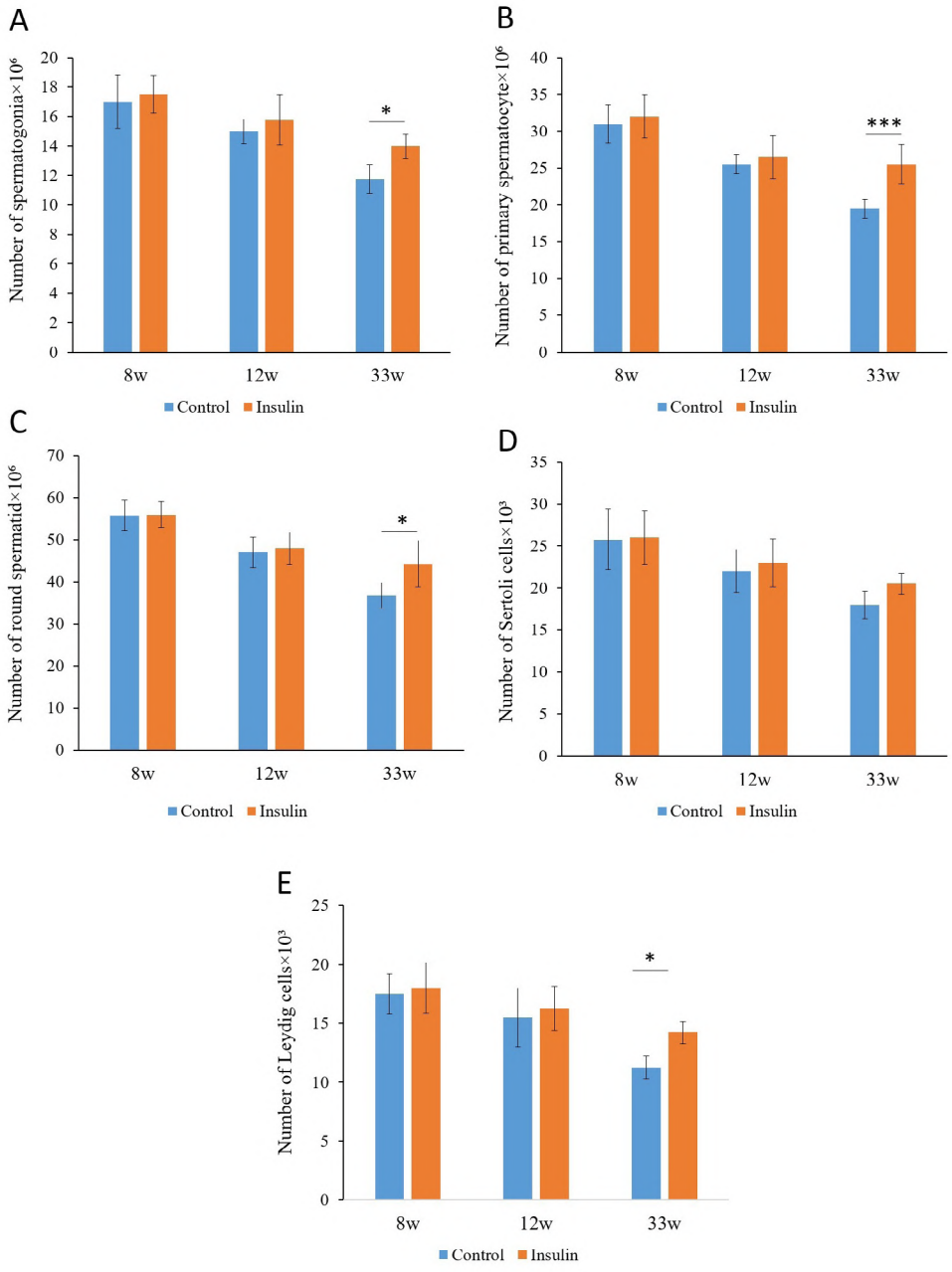

Fig. 3.- The effect of insulin on spermatogenic cells in mouse models of ageing. (*P<0.05, **P<0.01, ***P<0.001).

than the control group at 33 weeks of treatment (P<0.05) (Fig. 4A and B).

Gene expression

The levels of expression of caspase3 and Bax as apoptotic genes and Bcl2 as an inhibitor of apoptosis were assessed in the testes of mice in both insulin and control groups at 8, 12, and 33 weeks by using real-time qPCR. According to our findings, the level of gene expression of caspase3, Bax, and Bcl2 did not show any significant change between groups (Fig. 5A-C).

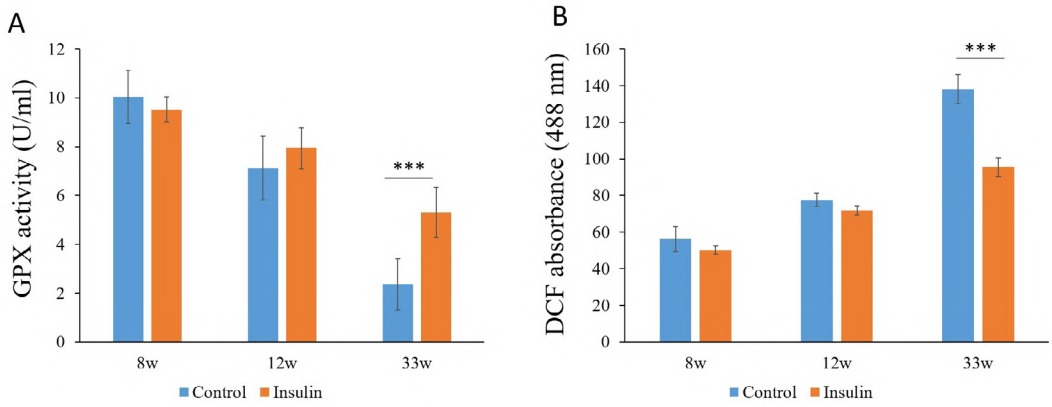

Fig. 4.- The effect of insulin on Reactive Oxygen Species (ROS) production and the level of glutathione (GSH) in mouse models of ageing. Mean±SD of the ROS production, GPX activity of testis in the study groups as compared by the ANOVA and LSD; (*P<0.05, **P<0.01, ***P<0.001).

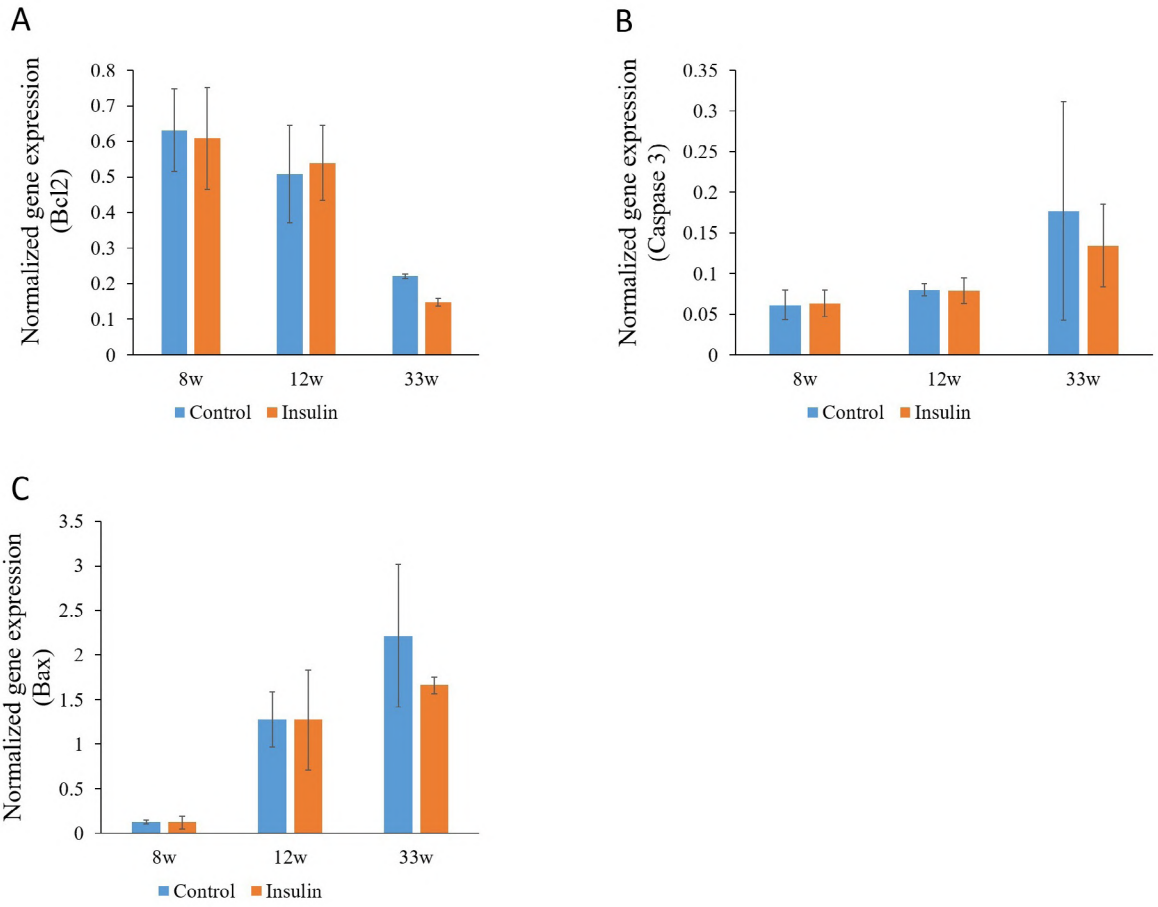

Fig. 5.- The effect of insulin on mRNA expression levels of Caspase3, Bax and Bcl2 in mouse models of ageing. **(A-C)** Mean±SD of the mRNA expression levels of Caspase3, Bax and Bcl2 of testis in the study groups as compared by the ANOVA; (**P<0.01 and ***P<0.001).

Hormone level of testosterone, LH, and FSH

According to the data, there were no any significant differences in the level of LH, FSH, and Testosterone hormones between groups (Fig. 6 A-C).

DISCUSSION

This study aimed to evaluate the beneficial effects of insulin on the testes of aging male rats according to a stereological study. We observed that insulin could significantly increase the spermatogenesis, the length of seminiferous tubules, and the activity of GPX.

In aging testes, various changes occur at the level of molecules and genes, which eventually lead to a reduction in steroidogenesis and spermatogenesis simultaneously (Matzkin et al., 2016). ROS play a key role during the aging of testes. In fact, ROS impair the normal function of cell organelles and stimulate lipid peroxidation (Matzkin et al., 2016; Amaral et al., 2013; Amaral et al., 2013). One of the important sources of the production of ROS is the energy transduction in the mitochondria (Valko et al., 2007). Mitochondria convert about 1 to 5 percent of oxygen consumption into the ROS. It has been proved that the integrity of mitochondrial function decreases during the process of ageing. Therefore, the production of ROS dramatically increases while mitochondria convert to the main source of free radicals (Abdollahifar et al., 2019; Valko et al., 2007). As a result, the balance between the generation of ROS and the antioxidant defense system is impaired (Amaral et al., 2013).

The testicles are prone to oxidative damage and lipid peroxidation. Because, besides other cells, Leydig cells and P450 enzymes involved in steroidogenesis produce ROS by the mitochondrial electron transport chain. However, the level of enzymatic and non-enzymatic antioxidants is enough in the normal and healthy male gonad to suppress the adverse effects of ROS (Brown-Borg et al., 2012; Chen et al., 2009). In aged testis, the level of oxidative stress and the production of free

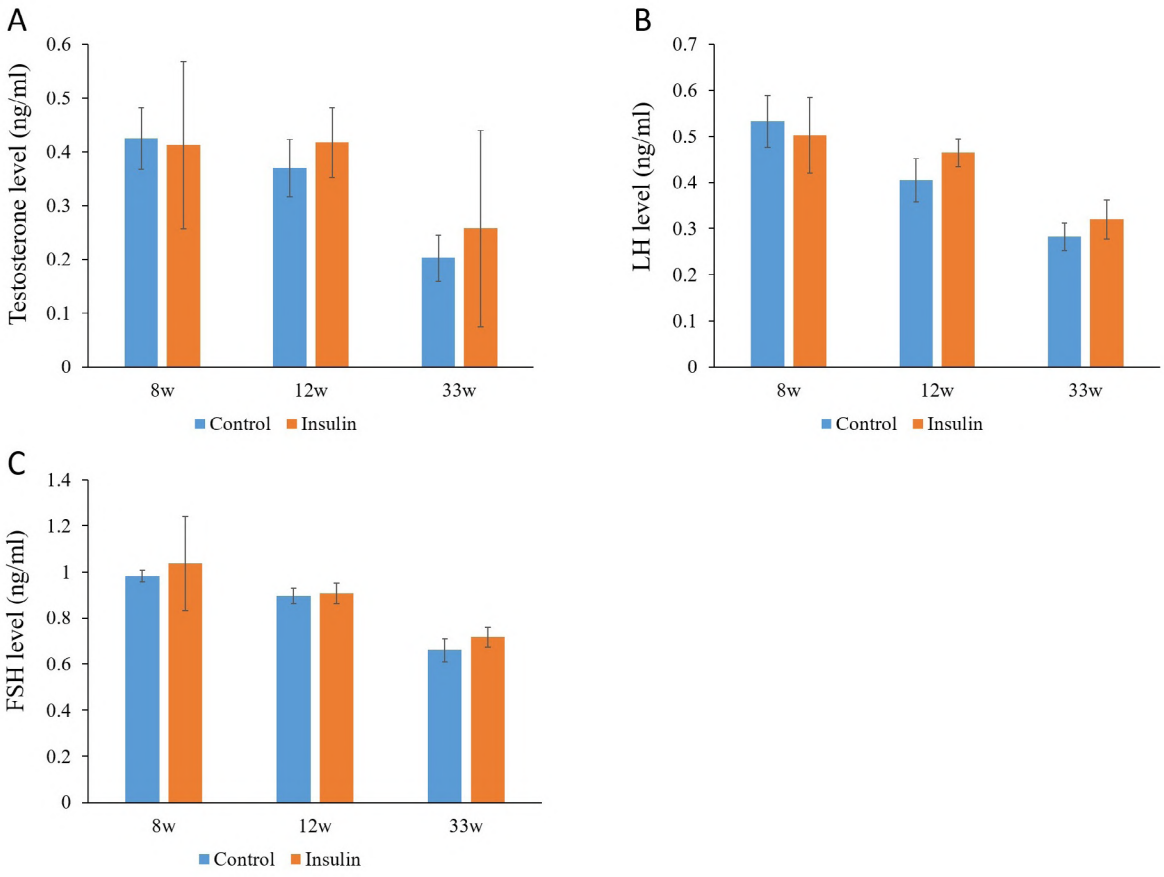

Fig. 6.- The effect of insulin on serum testosterone **(A)**, LH **(B)** and FSH **(C)** levels in mouse models of ageing. Mean±SD of the testosterone, LH and FSH level in the study groups as compared by the ANOVA (*P<0.05, **P<0.01, ***P<0.001).

radicals increase because of the alterations in the antioxidant enzymes such as glutathione-s-transferase (GST), an important enzyme that protects testes cells from oxidative stress, superoxide dismutase (SOD), and GPX (Salomon et al., 2013; Mueller et al., 1998; Cao et al., 2004). Overall, ROS and following oxidative stress significantly stimulate apoptosis in the testes of old men (Matzkin et al., 2016). In addition, with increasing age, the expression of pro-inflammatory cytokines including IL1β, IL6, and TNFα dramatically increase in the testicular mesenchymal stem cells (Matzkin et al., 2016).

We observed some histomorphological alterations in aged testes such as reduction of length of seminiferous tubules, reduction of Leydig cells, and a reduction in the volume and weight of them. These results were in line with previous studies (Johnson et al., 1984, 1986, 2015). Other studies also showed that aging has adverse effects on spermatogenesis, semen quality, and the thickness of the basal membrane of seminiferous tubules; besides, vacuolization, and multinucleation of spermatids are reported (Santiago et al., 2018; Miranda et al., 2018; Plas et al., 2000).

Insulin is a peptide hormone that has a fundamental role in maintaining blood glucose. This peptide is produced by the β cells of pancreatic islets of Langerhans (Wilcox et al., 2005). In addition to maintaining blood glucose, insulin has other vital cellular functions, such as transportation of amino acid, ion regulation, lipid metabolism, synthesis of glycogen, degradation and synthesis of protein, and DNA synthesis. Besides, insulin is effective in the cellular growth and differentiation (Cheatham et al., 1995).

Along with the effects of insulin, which are mentioned above, it is very important during spermatogenesis. It has been suggested that human sperms are able to release insulin. Besides, insulin receptors have also been found in sperms (Schoeller et al., 2012). According to our results, insulin can stimulate spermatogenesis and increase the number of testicular cells in the aged rats. Besides, insulin revitalize seminiferous tubules and the volume of the testis. It is suggested that insulin can regenerate the function of seminiferous tubules in culture medium by stimulating spermatogonial DNA synthesis in rats (Söder et al., 1992). In a study, Schoeller and et al. investigated the effect of insulin on the spermatogenesis of Akita mice with type-1 diabetes. They reported that these mice are infertile because of the absence of insulin due to *ins2* gene mutation in both testis and pancreas. The size and weight of the testes, and the level of serum testosterone were low in Akita mice. They showed that treatment with insulin in the Akita mice for 8 weeks led to regeneration of the seminiferous tubules and increase of volume and weight of testes. In addition, the total number of Sertoli cells, spermatogonia, and spermatid cells significantly increase (Schoeller et al., 2012).

Oxidative stress and apoptosis are common at aged testis. Mitochondria are well known as the main source of ROS damage. During aging of testis, the mitochondria of Leydig cells, as an endocrine cell, dramatically release free radicals (Barbutska et al., 2015). As a result, the proapoptotic genes such as Bax and caspase-3 significantly express (Dias et al., 2013). According to our results, insulin also has protective effects by increasing the activity of GPX as an antioxidant enzyme. It has been shown that a low level of insulin in diabetic patients causes inflammation and oxidative stress, while insulin therapy after 24 and 48 weeks enhanced the activity of enzymatic antioxidants such as GPX in them (Goyal et al., 2011).

We concluded that insulin improves spermatogenesis and restores morphological features of aged testes. In other words, insulin can alleviate the negative effects of aging on testicular function and increase the likelihood of fertility in older men.

ACKNOWLEDGEMENTS

This work was performed at the School of Medicine, Sabzevar University of Medical Science [Grant Number:400210].

REFERENCES

ABDOLLAHIFAR M-A, AZAD N, SAJADI E, MOFARAHE ZS, ZARE F, MORADI A, Rezaee F, Gholamin M, Abdi S (2019) Vitamin C restores ovarian follicular reservation in a mouse model of aging. *Anat Cell Biol*, 52(2): 196-203.

ALMEIDA S, RATO L, SOUSA M, ALVES MG, OLIVEIRA PF (2017) Fertility and sperm quality in the aging male. *Curr Pharm Des*, 23(30): 4429-4437.

AMARAL S, AMARAL A, RAMALHO-SANTOS J (2013) Aging and male reproductive function: a mitochondrial perspective. *Front Biosci (Schol Ed)*, 5: 181-197.

BARBUTSKA D, KOEVA Y (2015) Apoptotic changes in aging testis. Acta *Morphol Anthropol*, 21: 13-17.

BHANMEECHAO C, SRISUWATANASAGUL S, PRAPAIWAN N, PONGLOWHAPAN S (2018) Reproductive aging in male dogs: the epididymal sperm defects and expression of androgen receptor in reproductive tissues. *Theriogenology*, 108: 74-80.

BROWN-BORG HM, JOHNSON WT, RAKOCZY SG (2012) Expression of oxidative phosphorylation components in mitochondria of long-living Ames dwarf mice. *Age*, 34(1): 43-57.

CAO L, LEERS-SUCHETA S, AZHAR S (2004) Aging alters the functional expression of enzymatic and non-enzymatic anti-oxidant defense systems in testicular rat Leydig cells. *J Steroid Biochem Mol Biol*, 88(1): 61-67.

CHEATHAM B, KAHN CR (1995) Insulin action and the insulin signaling network. *Endocr Rev*, 16(2): 117-142.

CHEN H, GE R-S, ZIRKIN BR (2009) Leydig cells: from stem cells to aging. *Mol Cell Endocrinol*, 306(1-2): 9-16.

DIAS T, RATO L, MARTINS A, SIMÕES V, JESUS T, ALVES M, OLIVEIRA PF (2013) Insulin deprivation decreases caspase-dependent apoptotic signaling in cultured rat sertoli cells. *ISRN Urol*, 2013: 970370.

GOYAL R, SINGHAI M, FAIZY AF (2011) Glutathione peroxidase activity in obese and nonobese diabetic patients and role of hyperglycemia in oxidative stress. *J Mid-Life Health*, 2(2): 72.

HASANI A, KHOSRAVI A, RAHIMI K, AFSHAR A, FADAEI-FATHABADI F, RAOOFI A, RAEE P, AGHAJANPOUR F, ALIAGHAEI A, ABDI S, NOROUZIAN M, ABDOLLAHIFAR M-A (2020) Photobiomodulation restores spermatogenesis in the transient scrotal hyperthermia-induced mice. *Life Sci*, 254: 117767.

JOHNSON L, PETTY C, NEAVES W (1984) Influence of age on sperm production and testicular weights in men. *Reproduction*, 70(1): 211-218.

JOHNSON L, PETTY CS, NEAVES WB (1986) Age-related variation in seminiferous tubules in men: A stereologic evaluation. *J Androl*, 7(5): 316-322.

JOHNSON SL, DUNLEAVY J, GEMMELL NJ, NAKAGAWA S (2015) Consistent age-dependent declines in human semen quality: a systematic review and meta-analysis. *Ageing Res Rev*, 19: 22-33.

KAFAMI M, HOSSEINI M, NIAZMAND S, FARROKHI E, HAJZADEH MA-R, NAZEMI S (2019) The effects of estradiol and testosterone on renal tissues oxidative after central injection of angiotensin II in female doca–salt treated rats. *Horm Mol Biol Clin Investig*, 37(3).

LACOMBE A, LELIEVRE V, ROSELLI CE, SALAMEH W, LUE Y-H, LAWSON G, MULLER JM, WASCHEK JA, VILAIN E (2006) Delayed testicular aging in pituitary adenylate cyclase-activating peptide (PACAP) null mice. *Proc Natl Acad Sci*, 103(10): 3793-3798.

LÓPEZ-OTÍN C, BLASCO MA, PARTRIDGE L, SERRANO M, KROEMER G (2013) The hallmarks of aging. *Cell*, 153(6): 1194-1217.

MATZKIN ME, MIQUET JG, FANG Y, HILL CM, TURYN D, CALANDRA RS, BARTKE A, FRUNGIERI MB (2016) Alterations in oxidative, inflammatory and apoptotic events in short-lived and long-lived mice testes. *Aging (Albany NY)*, 8(1): 95-110.

MIRANDA EPD, LORENZINI F, NEVES BVD, MELCHIORETTO EF, HOTA T, FRAGA RD (2018) Stereological and morphological analysis of the effects of aging on spermatogenesis in rat testis. *Acta Cir Bras*, 33: 904-913.

MUELLER A, HERMO L, ROBAIRE B (1998) The effects of aging on the expression of glutathione S-transferases in the testis and epididymis of the Brown Norway rat. *J Androl*, 19(4): 450-465.

NAKAYAMA Y, YAMAMOTO T, ABE S-I (2004) IGF-I, IGF-II and insulin promote differentiation of spermatogonia to primary spermatocytes in organ culture of newt testes. *Intl J Dev Biol*, 43(4): 343-347.

PLAS E, BERGER P, HERMANN M, PFLÜGER H (2000) Effects of aging on male fertility? *Exp Gerontol*, 35(5): 543-551.

RAOOFI A, SADEGHI Y, PIRYAEI A, SAJADI E, ALIAGHAEI A, RASHIDIANI-RASHIDABADI A, FATABADI FF, MAHDAVI B, ABDOLLAHIFAR MA, KHANEGHAH AM (2021) Bone marrow mesenchymal stem cell condition medium loaded on PCL nanofibrous scaffold promoted nerve regeneration after sciatic nerve transection in male rats. *Neurotox Res*, 39(5): 1470-1486.

SALOMON TB, HACKENHAAR FS, ALMEIDA AC, SCHÜLLER AK, ALABARSE PVG, EHRENBRINK G, BENFATO MS (2013) Oxidative stress in testis of animals during aging with and without reproductive activity. *Exp Gerontol*, 48(9): 940-946.

SANTIAGO J, SILVA JV, ALVES MG, OLIVEIRA PF, FARDILHA M (2018) Testicular aging: an overview of ultrastructural, cellular, and molecular alterations. *J Gerontol*: Series A, 74(6): 860-871.

SASTRE J, PALLARDÓ FV, GARCÍA DE LA ASUNCIÓN J, VIÑA J (2000) Mitochondria, oxidative stress and aging. *Free Radic Res*, 32(3): 189-198.

SCHOELLER EL, ALBANNA G, FROLOVA AI, MOLEY KH (2012) Insulin rescues impaired spermatogenesis via the hypothalamic-pituitary-gonadal axis in Akita diabetic mice and restores male fertility. *Diabetes*, 61(7): 1869-1878.

SÖDER O, BANG P, WAHAB A, PARVINEN M (1992) Insulin-like growth factors selectively stimulate spermatogonial, but not meiotic, deoxyribonucleic acid synthesis during rat spermatogenesis. *Endocrinology*, 131(5): 2344-2350.

SONG Y, DING W, BEI Y, XIAO Y, TONG H-D, WANG L-B, AI L-Y (2018) Insulin is a potential antioxidant for diabetes-associated cognitive decline via regulating Nrf2 dependent antioxidant enzymes. *Biomed Pharmacother*, 104: 474-484.

STONE BA, ALEX A, WERLIN LB, MARRS RP (2013) Age thresholds for changes in semen parameters in men. *Fertil Steril*, 100(4): 952-958.

VALKO M, LEIBFRITZ D, MONCOL J, CRONIN MT, MAZUR M, TELSER J (2007) Free radicals and antioxidants in normal physiological functions and human disease. *Intl J Biochem Cell Biol*, 39(1): 44-84.

WILCOX G (2005) Insulin and insulin resistance. *Clin Biochem Rev*, 26(2): 19.

ZHU Q-X, MEADS C, LU M-L, WU J-Q, ZHOU W-J, GAO E-S (2011) Turning point of age for semen quality: a population-based study in Chinese men. *Fertil Steril*, 96(3): 572-576.

Histopathology and ultrastructural alterations in gastric mucus-secreting cells in diabetic model rats

Sani Baimai[1,2], Sirinush Sricharoenvej[2], Passara Lanlua[2], Narawadee Choompoo[1]

[1] Department of Anatomy, Faculty of Medical Science, Naresuan University, Phitsanulok, 65000, Thailand

[2] Department of Anatomy, Faculty of Medicine Siriraj Hospital, Mahidol University, Bangkok, 10700, Thailand

SUMMARY

Diabetes mellitus (DM) can cause gastric ulcers (GU), duodenal ulcers (DU), and gastroesophageal reflux disease (GERD). Mucus-secreting cells secrete mucus, which aids in the neutralization of HCl and inhibits bacteria. DM can alter mucus-secreting cells. Due to a lack of mucosal defense, external stimuli such as bacteria or ethanol can lead to the development of GU, DU, and GERD. This research study used a STZ-induced diabetic rat model to examine the short- and long-term histopathology and ultrastructural alterations in mucus-secreting cells in the cardia, body, and pyloric regions of the stomach. Quantitative analysis was also employed in this study to examine the distribution of mucin granules across all three locations. Twenty-four male adult Sprague-Dawley rats were utilized. Rats were divided into the control (n = 12) and DM (n = 12) groups. Each was separated into short-term (4 weeks) and long-term (24 weeks) rats. For DM induction, streptozotocin (STZ) can selectively destroy the beta cells of the pancreas. The DM was injected with STZ in citrate buffer at 60 mg/kg body weight. The control group was injected with citrate buffer. Histopathology was examined by Alcian blue-Periodic Acid Schiff staining under a light microscope. Image analysis was applied to quantify mucin accumulation. The ultrastructure was explored using transmission electron microscopy. In short-term and long-term DM, there was superficial erosion of the gastric epithelium and a significant decrease in the percentage of mucin granule accumulations in both surface mucous cells (SMCs) and mucous neck cells (MNCs). In short-term DM, SMCs were degenerated with vacuolation, disrupted cristae of mitochondria, and dilated rough endoplasmic reticulum (rER). MNCs were swollen with destroyed organelles. In long-term DM, degenerative nuclei and electron-lucent regions with unidentified structures of SMCs were observed. Nuclear chromatin condensation and the disappearance of mucin granules were present in MNCs. In conclusion, under both LM and TEM, STZ-induced diabetic rats demonstrated both short- and long-term damage to the gastric mucosa and gastric gland structures.

Key words: Surface mucous cells – Mucous neck cells – Stomach – Streptozotocin – Ultrastructure – Mucin granules

Corresponding author:
Narawadee Choompoo, Ph.D. Department of Anatomy, Faculty of Medical Science, Naresuan University, Phitsanulok, 65000, Thailand. Phone: (+66) 95-635-9305. E-mail: narawadeec@nu.ac.th

Submitted: June 5, 2023. **Accepted:** July 23, 2023

https://doi.org/10.52083/BIHZ6841

INTRODUCTION

Diabetes mellitus (DM) is a metabolic syndrome that is increasing worldwide. DM can be diagnosed based on a persistent high blood glucose level and HbA1c of more than 126 mg/dL and 6.5%, respectively. DM can be classified into two main categories: type 1 (T1DM, absolute insulin deficiency) and type 2 (T2DM, insulin resistance and relative insulin decrease) (Krishnan et al., 2013). DM has been reported to lead to several diabetes-related complications, such as diabetic neuropathy, diabetic endocrinology, and gastrointestinal symptoms (Baimai et al., 2020, 2021; Lerkdumnernkit et al., 2022). Diabetic patients with diabetic gastropathy (75%) appear to have many gastric symptoms, such as epigastric pain, nausea, vomiting, weight loss, abdominal bloating, postprandial fullness, hematemesis, and hematochezia (Sabatine, 2020). All of these symptoms are related to gastric ulcer (GU), duodenal ulcer (DU), and gastroesophageal reflux disease (GERD).

Gastric mucosal secretory cells play an essential role in the stomach secreting mucous to protect the gastric epithelium (Barrett et al., 2010). Mucus-secreting cells are composed of surface mucous (SMCs) and mucous neck (MNCs) cells of the gastric mucosa and gastric gland, which are an essential part of mucosal protection. SMCs and MNCs secrete mucus-containing alkaline bicarbonate (HCO3), which aids in the neutralization of HCl and inhibits bacteria (Barrett et al., 2010). DM can alter mucus-secreting cells, which leads to impaired protective defense. Gastric mucosal lesions in DM, for example, mucosal hyperemia, desquamation of surface epithelium, foci of mucosal necrosis and erosion, and decreased mucus-secreting cells, have been reported (Raafat et al., 2019). GU occurs when there is an imbalance between mucosal protection and gastric acid destruction. Reduced mucus containing alkaline bicarbonate (HCO3) from the gastric mucosa and gastric gland proper, which is located in the stomach's body, can reduce the factor inhibiting bacteria. As a result, external factors such as H. pylori, drugs such as NSAIDs, and ethanol can easily cause GU. All those external factors can pass from the stomach to the duodenum if the mucus-secreting cells in the pyloric mucosa and pyloric gland are reduced. These factors also consequently cause DU. In addition, decreased mucus-secreting cells at the cardiac part of the stomach allow acid to revert up into the esophagus, causing GERD.

The histopathology and ultrastructural changes in diabetic mucus-secreting cells in the mucosal and glandular regions have never been published, and it would be interesting to investigate the short- and long-term histopathology and ultrastructural changes in mucus-secreting cells in the cardia, body, and pyloric regions of the stomach in a STZ-induced diabetic disease rat model. This study also used quantitative analysis to compare the proportion of mucin granules in each area in all three regions. The results of this research can confirm the histopathological evidence and ultrastructural damage using various techniques to relate the cause of DM with cell damage and gastric symptoms. These discoveries could lead to the development of diagnostic strategies, preventive awareness, and treatments for DM.

MATERIALS AND METHODS

Animal model

Twenty-four male adult Sprague-Dawley rats (6-8 weeks old), weighing between 200-230 g, were employed. All animals were obtained from the National Laboratory Animal Center at Mahidol University in Thailand. The "Guide for the Care and Use of Laboratory Animals" was followed when caring for the animals used in this investigation, which was authorized by the Siriraj Animal Care and Use Protocol at Mahidol University in Thailand (COA No. 001/2564). Each animal was housed in a tidy individual cage and exposed to a set routine for temperature (25°C), illumination (12:12-hour light: dark cycle with the lights on at 7 a.m.), humidity (55±10%), and ventilation (15-20 times per hour). Throughout the trial, the animals had access to water and a standard laboratory food ad libitum (Baimai et al., 2020, 2021; Chookliang et al., 2021; Lerkdumnernkit et al., 2022).

Drug and animal induction

The rats were randomly divided into the control and DM groups that had been injected with streptozotocin (STZ) (Across Organics, Janssen

Pharmaceutical, Belgium) to induce DM. Twelve rats from the diabetic group received a single intraperitoneal injection of STZ at a dose of 60 mg/kg body weight in citrate buffer at pH 4.5 (Baimai et al., 2020, 2021; Chookliang et al., 2021; Lerkdumnernkit et al., 2022). The same amount of the buffer was intraperitoneally administered to 12 rats in the age-matched control group. As short- and long-term outcomes, all animals were slaughtered 4 and 24 weeks following intraperitoneal injection, respectively.

Measurement of glucose concentration before the experiment and after STZ induction

Each animal was subjected to a 7-day fast, during which time the amount of glucose in their urine was measured using urinalysis control strips (Diabur-Test 5000, Roche Ltd., Germany). Glucose strips (One Touch® Ultra®, USA) were used to measure the entire blood glucose in a blood sample that was also drawn from the tail vein. Animals were used in this experiment if the urine glucose concentration was 0 mg/dL and the whole blood glucose level was less than 300 mg/dL (Baimai et al., 2020, 2021; Chookliang et al., 2021; Lerkdumnernkit et al., 2022). After a 12-hour fast, the body weight, and urine glucose levels were checked each day. After STZ administration at 48 hours, 72 hours, and before sacrifice, whole-blood glucose levels were collected and assessed.

Histopathological study

A histopathological examination using light microscopy (LM) was conducted on six control and six STZ-induced diabetic rats in each period. Before the thoracic cage was dissected to reveal the heart, each animal was sedated by inhaling halothane. Immediately after that, 0.05 ml of heparin was administered into the left ventricle and allowed to circulate for 1-2 minutes to stop blood coagulation. The ascending aorta was accessed through the left ventricle with a blunt needle (18 gauge), which was then constricted tightly. To allow the outflow of the perfused blood, the right atrium was then severed. The animal received 500 ml of a 0.9% NaCl solution through the same catheter to flush the blood out of the circulation. The treatment was carried out following the needs of each group of animals until the outflow fluid was clear. To preserve the tissues after perfusion with 0.1 M phosphate buffer solution (PBS), 2.5% glutaraldehyde in 0.1 M PBS was manually administered into the ascending aorta (Baimai et al., 2020, 2021; Chookliang et al., 2021; Lerkdumnernkit et al., 2022;). The abdominal wall was surgically incised and opened after that. The stomach was then removed, cut open along the larger curvature, and left in the same fixative overnight.

The stomach was dissected from each region using a sharp blade. In the histopathological study, the stomach was serially sectioned at a thickness of 5 µm. SMCs and MNCs were stained using Alcian blue-Periodic Acid Schiff (PAS) to detect mucin. Under a light microscope attached to a digital camera, all specimens were examined and captured with a camera (Axiocam MRC, Jena, Germany). Small portions of the stomach (1 mm^3) in each location were postfixed in 1% osmium tetroxide in 0.1 M PBS before being cut into plastic blocks using an ultramicrotome; the plastic specimens were serially sectioned at 1-1.5 µm thickness (Leica EM UC6, Vienna, Austria) (Baimai et al., 2020, 2021; Chookliang et al., 2021; Lerkdumnernkit et al., 2022).

The mucin granule accumulations

Combined Alcian-blue and PAS staining was used to detect the mucin of SMCs and MNCs separately. The PAS-positive reaction can be used to locate the mucin of SMCs in addition to cell location. The MNCs, on the other hand, can be identified by a strong Alcian blue-positive reaction. Ninety sections per group were chosen to quantify mucin-stained mucus-secretory cell depositions, which were calculated as the percentage of mucin per area at 20x magnification. All quantitative data were counted, measured, calculated, and analyzed by using the ImageJ software tool (National Institute of Mental Health, Bethesda, Maryland, USA).

Ultrastructural study

Post-fixation of small sections of the stomach (1 mm^3) in 1% osmium tetroxide in 0.1 M PBS was followed by drying in a graded series of ethanol, cleaning in propylene oxide, and infiltration by

propylene oxide. The specimens were then implanted in plastic. An ultramicrotome (Leica EM UC6, Vienna, Austria) was used to section the tissue blocks. Semithin sections (1-1.5 µm) were stained with toluidine blue and examined under LM for representative areas (Axiostar plus, Jena, Germany). The ultramicrotome was then used to serially section the selected embedded specimens at 80-85 nm thickness. Then, 1% uranyl acetate and lead citrate were used to stain the serial sections (Baimai et al., 2020, 2021; Chookliang et al., 2021; Lerkdumnernkit et al., 2022). Under the TEM, the ultrastructure of the stomach was viewed and photographed (TECNI20, Phillips Electron Optics, Holland).

Statistical analysis

The data were calculated as the mean ± standard deviation (SD). Differences between independent groups were analyzed by using the independent t-test (SPSS version 20.0 software, Inc., Chicago, IL, USA). Differences were considered significant at a p-value < 0.05.

RESULTS

Diabetic rats exhibited symptoms such as polyuria, polydipsia, and polyphagia. Long-term diabetic rats had more severe symptoms than short-term diabetic rats. Most diabetic rats were lethargic, tended to sleep, were not active, and had grooming drops. Generalized myopathy with weight loss was significantly presented in diabetic rats [short-term control = 325.18 ± 2.34 g, short-term DM = 198.34 ± 4.35* g (p < 0.05); long-term control = 458 ± 3.45 g, long-term DM = 350.39 ± 3.43* g (p < 0.05)]. The glucose levels in both urine and blood were more than 500 mg/dL and 300 mg/dL, respectively. The external appearances of the stomach were similar between control and diabetic rats in both periods. When the gross anatomy of the diabetic rat stom-

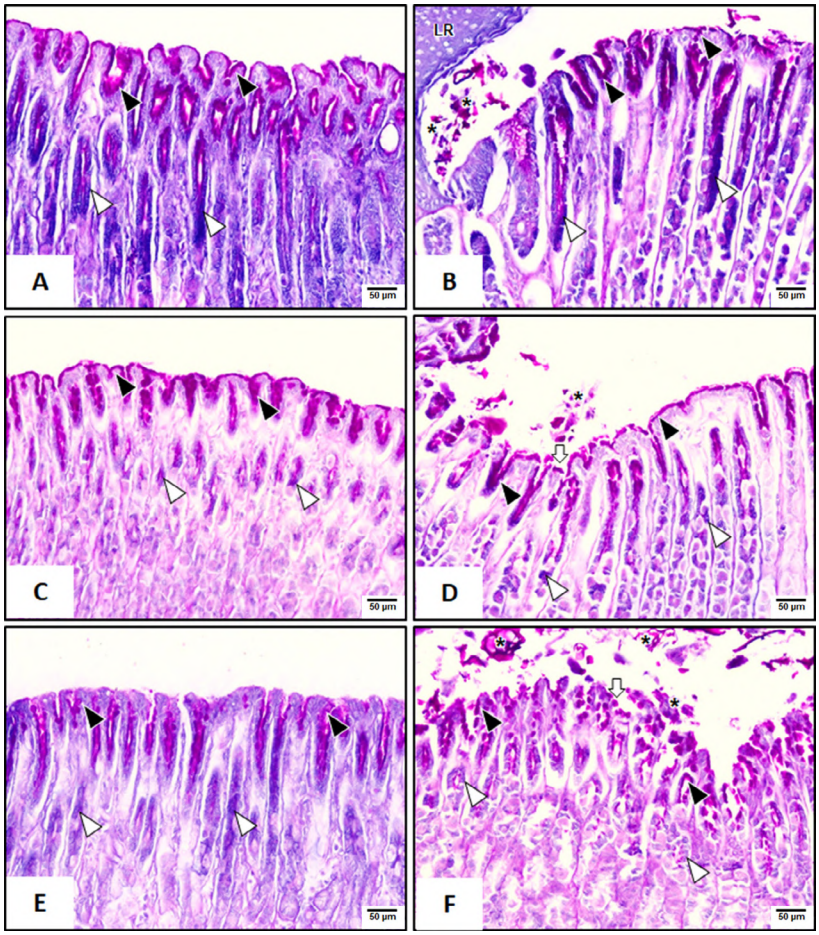

Fig. 1.- Light micrographs of gastric mucosa and gastric gland in the cardiac region (**A-B**), body region (**C-D**), and pyloric region (**E-F**) of short-term control (**A, C, E**) and short-term diabetic (**B, D, F**) rats. Positive reaction of PAS (black arrowheads); positive reaction PAS with strong Alcian blue (white arrowheads); limiting ridge (LR); slough tissue (asterisks); superficial erosion (white arrows). Combined Alcian blue-PAS staining. Scale bar = 50 µm.

ach was inspected visually, there was no apparent lesions or ulcers. The stomachs were divided into two sections of non-glandular and glandular parts, separated from each other by a limiting ridge. The non-glandular parts were shown as having whitish-brown mucosa, a translucent layer, and a thin wall. On the contrary, the glandular parts were represented by reddish mucosa and opaque, muscular, and thick wall.

Histopathological findings and mucin granule accumulations

The mucus-secreting cells were better visualized with Alcian-blue and PAS staining (Figs. 1-2), because the mucin granules were lost during HandE staining. In short-term DM rats, after Alcian-blue and PAS staining, greater sloughing of the gastric epithelium and gastric lumen and superficial erosions of the gastric glands were observed (Figs. 1B, 1D, 1F, 2B, 2D, 2F), compared to those of the control rats (Figs. 1A, 1C, 1E, 2A, 2C, 2E). Staining with Alcian-blue and PAS can separate the deep magenta color of insoluble mucinogen granules of SMCs from the lighter magenta color of soluble mucinogen granules of MNCs. There was a significantly decreased percentage of mucin granule accumulation in both SMCs and MNCs in short- and long-term diabetic rats when compared with the control rats in the cardiac region (Figs. 1A-B, 2A-B,), body region (Figs. 1C-D, 2C-D), and pyloric region (Figs. 1E-F, 2E-F), and Table 1. In addition, there were significantly decreased percentage of mucin granule accumulation in both SMCs and MNCs in long-term DM when compared to the short-term DM.

Ultrastructures of mucus-secreting cells

The mucus-secreting cells in this experiment represented secretory granules in both the supranuclear space and the apical surface of the cytoplasm.

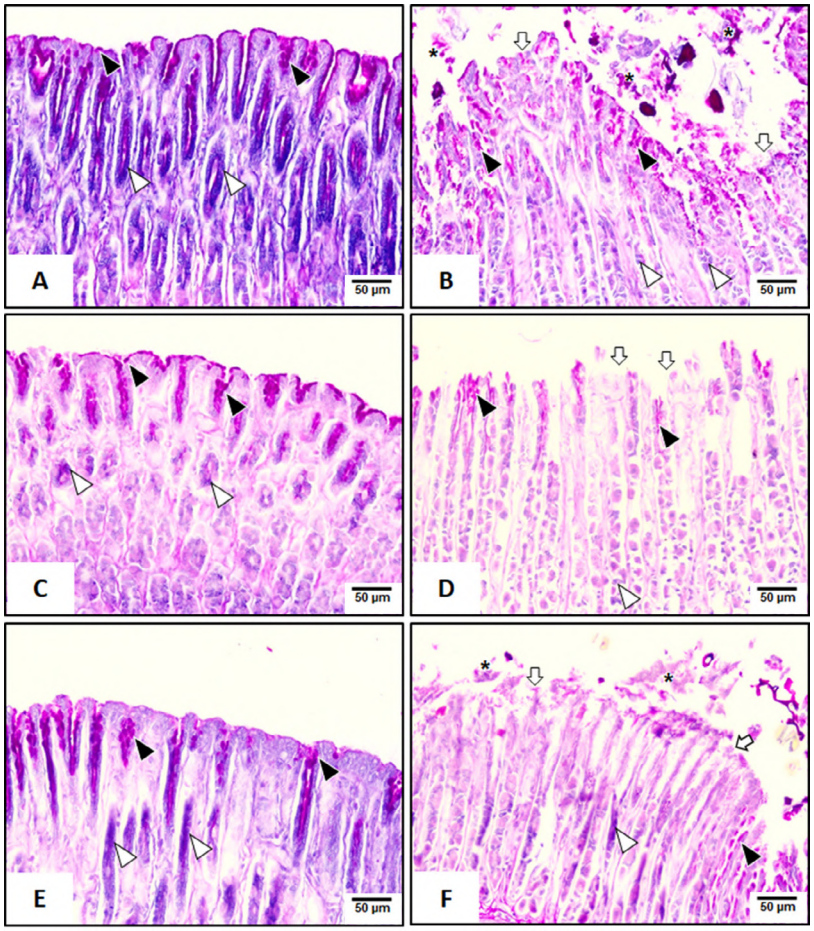

Fig. 2.- Light micrographs of gastric mucosa and gastric gland in the cardiac region (**A-B**), body region (**C-D**), and pyloric region (**E-F**) of long-term control (**A, C, E**) and long-term diabetic (**B, D, F**) rats. Positive reaction of PAS (black arrowheads); positive reaction PAS with strong Alcian blue (white arrowheads); slough tissue (asterisks); superficial erosion (white arrows). Combined Alcian blue-PAS staining. Scale bar = 50 µm.

Table 1. The percentage of mucin granule accumulations per area of SMCs and MNCs in all regions in both the short- and long-term periods.

Parameters			% Mucin granule accumulations per area (Mean ± SD)		
			Cardiac region	**Body region**	**Pyloric region**
SMCs	**Short term**	**Control** (n = 90)	29.20 ± 0.27	15.50 ± 0.84	20.03 ± 0.25
		DM (n = 90)	12.61 ± 0.16*	9.14 ± 0.97*	15.02 ± 0.15*
	Long term	**Control** (n = 90)	29.13 ± 0.18	18.47 ± 0.10	20.23 ± 0.24
		DM (n = 90)	8.93 ± 0.39*#	3.59 ± 0.76*#	1.58 ± 0.38*#
MNCs	**Short term**	**Control** (n = 90)	29.73 ± 0.69	6.85 ± 0.10	9.52 ± 0.85
		DM (n = 90)	14.98 ± 0.14*	4.93 ± 0.11*	6.54 ± 0.15*
	Long term	**Control** (n = 90)	29.54 ± 0.13	6.86 ± 0.16	9.68 ± 0.14
		DM (n = 90)	5.59 ± 0.14*#	2.34 ± 0.92*#	0.96 ± 0.85*#

*p<0.05; compared to the control rats in each gastric region in the same duration.
#p<0.05; compared to the short-term rats in each region.
Surface mucous cells (SMCs); Mucous neck cells (MNCs).

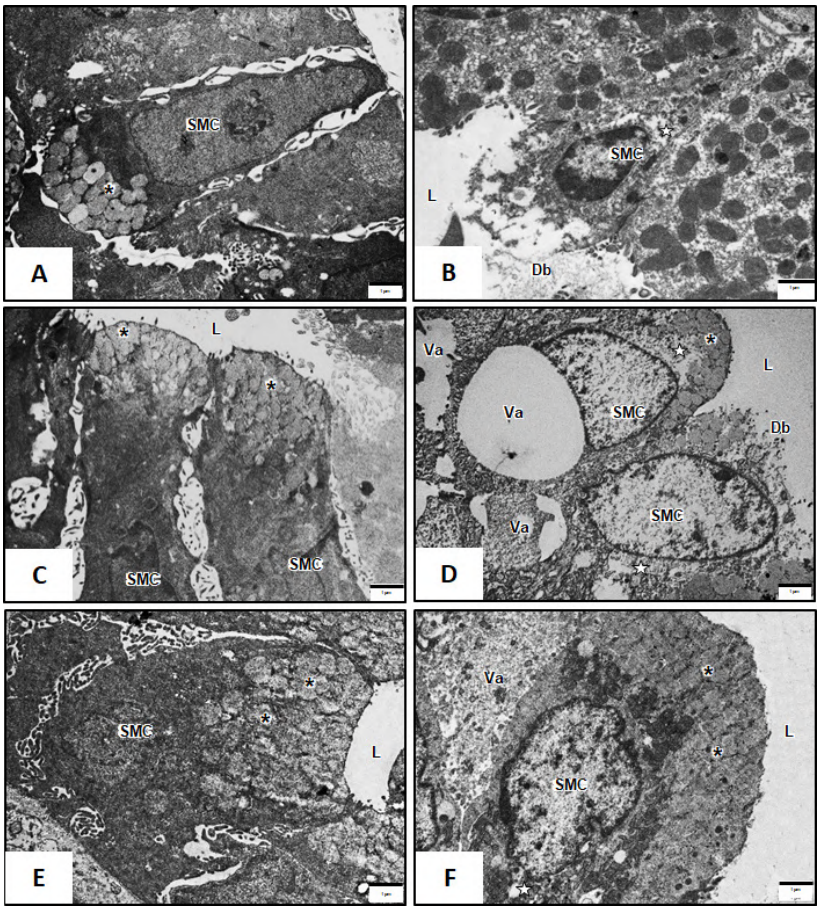

Fig. 3.- Transmission electron micrograph of surface mucous cells in the cardiac region **(A-B)**, body region **(C-D)**, and pyloric region **(E-F)** of short-term control **(A, C, E)** and short-term DM **(B, D, F)** rats. Surface mucous cell (SMC); lumen (L); vacuole (Va); debris (Db); black asterisks (mucin granules); electron lucent with unidentified structures (white stars). Scale bar = 1 µm.

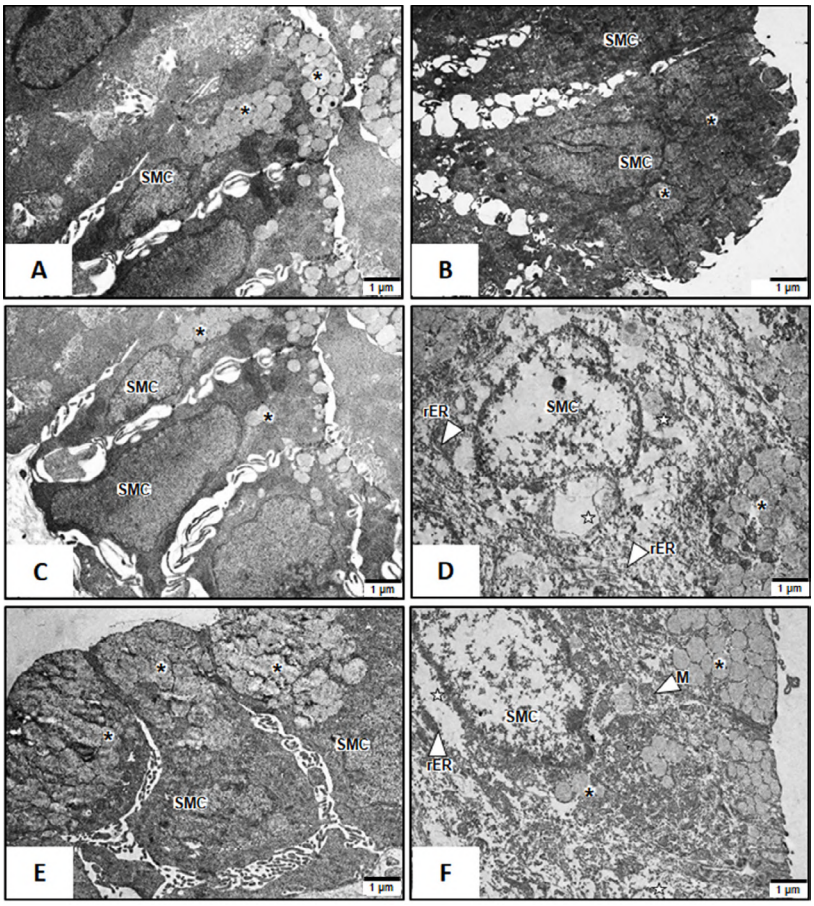

Fig. 4.- Transmission electron micrograph of surface mucous cells in the cardiac region (**A-B**), body region (**C-D**), and pyloric region (**E-F**) of long-term control (**A, C, E**) and long-term DM (**B, D, F**) rats. Surface mucous cell (SMC); rough endoplasmic reticulum (rER); black asterisks (mucin granules); rough endoplasmic reticulum (rER); mitochondria (M); electron lucent with unidentified structures (white stars). Scale bar = 1 µm.

Ultrastructures of surface mucous cells

In the control group, the mucous granule electron density varied in density at the apical area of SMCs (Figs 3A, 3C, 3E, 4A, 4C, 4E). SMCs in the apical areas of DM rats were swollen and damaged in short-term DM specimens. In addition, obvious cell debris and tiny fibrils (Figs. 3B, 3D), karyolitic nuclei (Fig. 3B), cytoplasmic vacuolation (Figs. 3D, 3F), and electron-dense granules at the apex were observed (Fig. 3F). Moreover, electron-lucent areas and unidentified structures were also demonstrated (Figs. 3B, 3D, 3F). In long-term DM specimens, destructive SMCs with degenerative nuclei (Figs. 4D, 4F) and mucous-filled cytoplasm were observed (Figs. 4B, 4D, 4F). Mucus from some SMCs was partially released (Fig. 4B). Cell organelles were destroyed (Fig. 4F). Dilated rER and electron-lucent regions and unidentified structures were also evident (Figs. 4D, 4F).

Ultrastructures of mucous neck cells

In the control group, bipartite secretory granules were present in MNCs (Figs. 5A, 5C, 5E, 6A, 6C, 6E). In the short-term DM group, cell swelling features of MNCs were observed (Figs. 5B, 5D). Numerous apical electron lucent mucous granules were present (Fig. 5D). In DM-MNCs, there was a large nucleolus in the euchromatin nucleus (Figs. 5B, 5D). This can be seen in the electron-lucent area, unidentified structures, and secondary lysosomes in their cytoplasm (Figs. 5B, 5D). Moreover, dilated rER was observed in the cytoplasm (Figs. 5B, 5D). In addition, a heterochromatin nucleus (Fig. 5F), and a dilated rER were found (Figs. 5B, 5D). The disappearance of mucous granules was seen (Fig. 5F). In long-term DM samples, MNCs with progressive swelling with nuclear chromatin condensation were also revealed (Fig. 6B). (Fig. 6B). Cytoplasmic organelles were degenerated, and electron-lucent areas were evident (Figs. 6B).

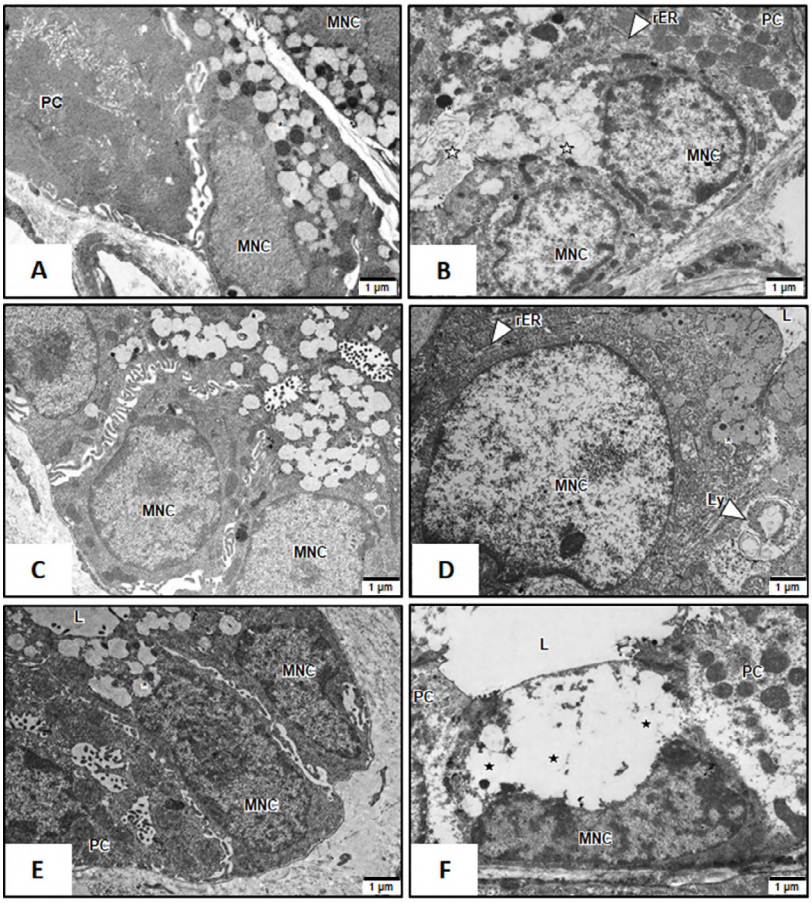

Fig. 5.- Transmission electron micrograph of mucous neck cells in the cardiac gland (**A-B**), gastric gland proper (**C-D**), and pyloric gland (**E-F**) of short-term control (**A, C, E**) and short-term DM (**B, D, F**) rats. Mucous neck cell (MNC); parietal cell (PC); lysosome (Ly); fibroblast (F); lumen (L); rough endoplasmic reticulum (rER); electron lucent with unidentified structures (white stars); mucin granules (black asterisks); disappeared mucin granules (black stars). Scale bar = 1 µm.

Secondary lysosomes, fragmented rER, and elongated mitochondria were also discovered (Figs 6D). Some MNC cells appeared to be characterized by the absence of mucin granules that previously existed in their cytoplasm (Fig. 6F).

DISCUSSION

The diabetic rats demonstrated diabetic symptoms such as polyuria, polydipsia, polyphagia, lethargy with sleep, inactivity with grooming, and unexplained weight loss, as well as abnormalities in both glucosuria and hyperglycemia, both of which were described in previous research (Baimai et al., 2020, 2021; Chookliang et al., 2021; Lerkdumnernkit et al., 2022). In this experiment, all rats were nourished with a standard diet and water. Therefore, there were no external factors, such as *H.pylori,* that affected the gastric epithelium. In addition, no other external stimuli, such as ethanol and NSAIDs were administered in this study. Although there was no visible lesions or ulcers when the gross structure of the diabetic rat stomach was examined with the naked eye, superficial erosion of the epithelium lining every region of the stomach was visible under LM. It may be inferred that DM can damage SMCs. In the experimental results obtained by the LM, the evident damage was confirmed from the TEM images.

The appearance of the SMC in short-term DM showed superficial erosion; superficial erosion was found to be more common in uncontrolled long-term diabetes, as reported in 2019 (Raafat and Hamam, 2019). Superficial erosion was observed on the gastric mucosa in every region, which can indicate the disruption of epithelial tight junctions on surface epithelial cells (Harhaj and Antonetti, 2004; Groschwitz and Hogan, 2009; Rao, 2018). There had been several reports about the relationship between reactive oxygen species (ROS) and the disruption of epithelial

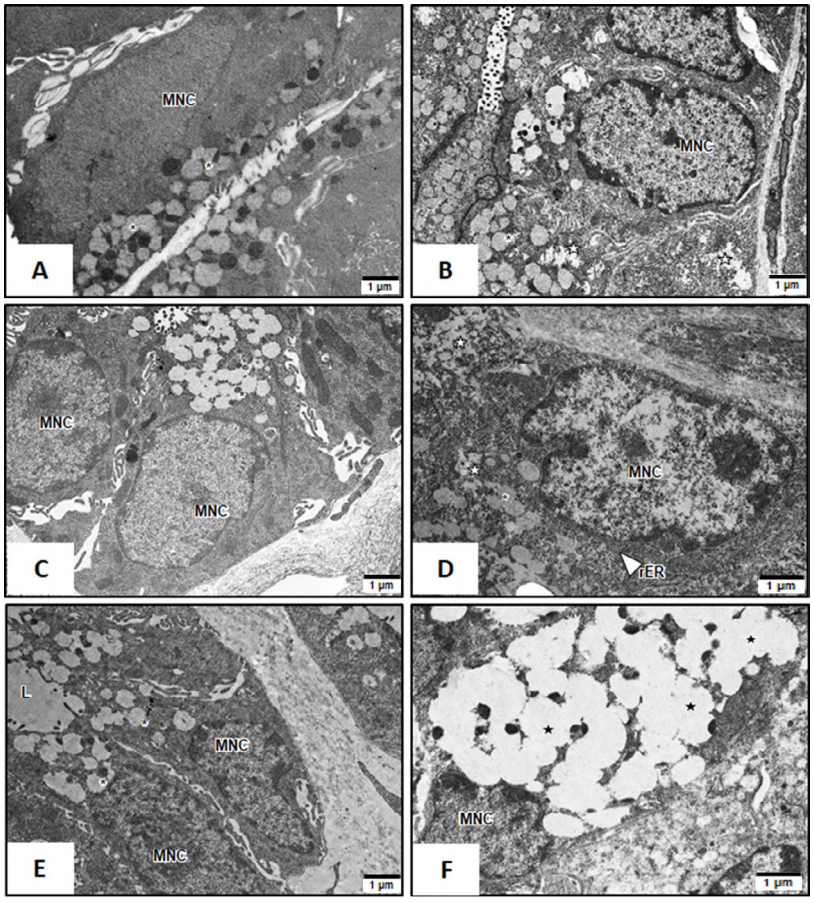

Fig. 6.- Transmission electron micrograph of mucous neck cells in the cardiac gland (**A-B**), gastric gland proper (**C-D**), and pyloric gland (**E-F**) of long-term control (**A, C, E**) and long-term DM (**B, D, F**) rats. Mucous neck cell (MNC); parietal cell (PC); lumen (L); electron lucent with unidentified structures (white stars); mucin granules (black asterisks); disappeared mucin granules (black stars). Scale bar = 1 µm.

tight junctions (TJs) in the gastrointestinal tract (Harhaj and Antonetti, 2004; Groschwitz and Hogan, 2009; Rao, 2018). The epithelial surface consequently showed signs of cell debris, sloughing, and superficial erosion. SMCs were harmed by ongoing hyperglycemia and uncontrolled DM. Thus, the epithelium was shed as a result of the vicious cycle of DM.

Image analysis also revealed that mucin granules of SMCs and MNCs were significantly reduced in rats with short-term diabetes. When short-term and long-term DM were compared, the percentage of mucin granules gradually decreased. Accordingly, it can be possible that chronic hyperglycemia can worsen the severity of the disease. In addition, the electron microscopy results showed that vacuoles, fragmented rER, and destroyed organelles were found in SMCs and MNCs. Therefore, the mechanism of cell damage from DM can be explained as hyperglycemic conditions destroying SMCs and MNCs via the ROS and apoptosis pathways.

Hyperglycemic blood can produce an excessive amount of sorbitol. A rise in the sorbitol content can cause water to enter the cells (Chung et al., 2003; Yan, 2018). Furthermore, sorbitol consumed a large amount of NADPH. The result was that DM generated excessive reactive oxygen species (ROS) production (Volpe et al., 2018; Ighodaro, 2018; Yaun et al., 2019). The cell membrane and organelles can be destroyed by ROS, which finally underwent fluid infusion. Vacuolated SMCs and MNCs were presented in both short- and long-term DM. Sustained hyperglycemia can change the mitochondria, causing them to malfunction. Then, ROS were produced, which triggered an apoptotic pathway via the recruitment of procaspase-9 (Krijnen et al., 2009). Caspase-9 promoted apoptosis by activating caspase-3. Chromatin condensation and pyknotic nuclei were

observed. SMCs and MNCs had pyknotic nuclei as a result of nuclear chromatin condensation. SMCs and MNCs that were destructive had dilated rER, damaged organelles, and unidentified features. Hyperglycemia condition can destroy SMCs by dilated rER in the cytoplasm and led to ER stress (Eizirik et al., 2008). Finally, apoptosis occurred in the cells. Sustained hyperglycemia can generate advanced glycation end products (AGE) (Singh et al., 2014; Saberzadeh-Ardestani et al., 2018). If AGEs were generated repeatedly, the ROS level would be increased and cause the DNA damages. Damaged DNA can stimulate the protein kinase C (PKC) pathway, which can also increase the ROS activities. Mucus-secreting cells found to dramatically decrease in short-term DM rats. Mucin granules in DM declined significantly over time, since ROS causes cell death with reduced mucin granules. Finally, during diabetic conditions, mucin granules were reduced in both cell types. From the DM group, it can be seen that the Golgi complex stores, packages, and concentrates proteins for export. If the organelle was destroyed, mucin within the Golgi disappears, which was consistent with the TEM images. DM can directly affect mucus-secreting cells. Consequently, stomach discomfort due to the mucosal protection damages can present in DM patients. Uncontrolled DM over a long period can increase the severity of destructive mucus-secreting cells and lead to GU, DU, and GERD.

CONCLUSION

STZ-induced diabetic rats showed both short-term and long-term destruction of the gastric mucosa and gastric gland structures under both LM and TEM. It was found that damage to SMCs and MNCs occurred in all regions of the stomach. Therefore, this is consistent with the occurrence of ulcers and GERD in diabetic patients presenting with gastrointestinal symptoms such as abdominal pain, nausea and vomiting, and stomach bleeding. Therefore, these DM model rats are a suitable model to explain how morphological changes develop over time. Thus, these findings provide insights and knowledge for future preventive medicine applications.

ACKNOWLEDGEMENTS

This research was supported by Chalermphrakiat Grant, Faculty of Medicine Siriraj Hospital, Mahidol University, Thailand.

REFERENCES

BAIMAI S, JANTA S, LANLUA P, CHOOKLIANG A, NIYOMCHAN A, SRICHAROENVEJ S (2020) Altered oligodendrocytes in spinal enlargements of streptozotocin diabetic rats. *Int J Morphol*, 38(6): 1606-1613.

BAIMAI S, PHANICHAKUL P, LANLUA P, NIYOMCHAN A, SRICHAROENVEJ S (2021) Modifications of adrenal gland ultrastructure in streptozotocin-induced diabetic model rats. *Int J Morphol*, 39(1): 109-115.

BARRETT K, BROOKS H, BOITANO S, BARMAN S (2010) *Ganong's review of medical physiology 23rd edition*. Mc Graw Hill, New York.

CHOOKLIANG A, LANLUA P, NIYOMCHAN A, SRICHAROENVEJ S (2021) Small bronchiolar histopathological changes related to prolonged diabetes. *Int J Morphol*, 39(2): 371-377.

CHUNG SSM, HO ECM, LAM KSL, CHUNG SK (2003) Contribution of polyol pathway of diabetes-induced oxidative stress. *J Am Soc Nephrol*, 14: S233-236.

EIZIRIK D, CARDOZO AK, CNOP M (2008) The role of endoplasmic reticulum stress in diabetes mellitus. *Endocrine Rev*, 29(1): 42-61.

GROSCHWITZ KR, HOGAN SP (2009) Intestinal barrier function: Molecular regulation and disease pathogenesis. *J Allery Clin Immunol*, 124(1): 3-22.

HARHAJ NS, ANTONETTI DA (2004) Regulation of tight junctions and loss of barrier functions in pathophysiology. *IJBCB*, 36: 1206-1237.

IGHODARO OM (2018) Molecular pathways associated with oxidative stress in diabetes mellitus. *Biomed Pharmocother*, 108: 656-662.

KRIJNEN PA, SIMSEK S, NIESSEN HWM (2009) Apoptosis in diabetes. *Apoptosis*, 14: 1387-1388.

KRISHNAN B, BABU S, WALKER J, WALKER AB, PAPPACHAN JM (2013) Gastrointestinal complications of diabetes mellitus. *WJD*, 4(3): 51-63.

LERKDUMNERNKIT N, SRICHAROENVEJ S, LANLUA P, NIYOMCHAN A, BAIMAI S, CHOOKLIANG A, PLAENGRIT K, PIANRUMLUK S, MANOONPOL C (2022) The effects of early diabetes on duodenal alterations in the rats. *Int J Morphol*, 40(2): 389-395.

RAAFAT MH, HAMAN GG (2019) The possible role of bee venom on gastric fundic mucosa in streptozotocin induced diabetes mellitus in rats. A histological study. *EJH*, 42(4): 1029-1042.

RAO R (2018) Oxidative stress-induced disruption of epithelial and endothelial junctions. *Front Biosci*, 13: 7210-7226.

SABATINE MS (2020) *Pocket medicine*, 7th edition. Wolters Kluwer, Philadelphia.

SABERZADEH-ARDESTANI B, KARAMZADEH R, BASIRI M, HAJIZADEH-SAFFAR E, FARHADI A, SHAPIRO J, TAHAMTANI Y, BAHARVAND H (2018) Type 1 diabetes mellitus: Cellular and molecular pathophysiology at a glance. *Cell J*, 20(3): 294-301.

SINGH YP, BALI A, SINGH N, JAGGI AS (2014) Advanced glycation end products and diabetic complications. *Korean J Physiol Pharmacol*, 18(1): 1-14.

VOLPE CMO, VILLAR-DELFINO PH, DOS ANJOS PMF, NOGUEIRA-MACHADO JA (2018) Cellular death, reactive oxygen species (ROS) and diabetic complications. *Cell Death Dis*, 9(2): 119.

YAN LJ (2018) Redox imbalance stress in diabetes mellitus: Role of the polyol pathway. *Animal Model Exp Med*, 1(1): 7-13.

YAUN T, YANG T, CHEN H, FU D, HU Y, WANG J, YUAN Q, YU H, XU W, XIE X (2019) New insights into oxidative stress and inflammation during diabetes mellitus-accelerated atherosclerosis. *Redox Biol*, 20: 247-260.

Three-dimensional characterization of zygomatic arch morphology and its relation to the articular eminence in a Brazilian population

Luciane N.O. Watanabe[1], Ana C. Rossi[1], Amanda L. Smith[2], Beatriz C. Ferreira-Pileggi[1], Eduardo Daruge Júnior[3], Felippe B. Prado[1], Alexandre R. Freire[1]

[1] Department of Biosciences, Anatomy Division, Piracicaba Dental School, University of Campinas, Piracicaba, São Paulo, Brazil

[2] Pacific Northwest University of Health Sciences, Yakima, Washington, USA

[3] Department of Health Science and Pediatric Dentistry, Forensic Dentistry Division, Piracicaba Dental School, University of Campinas, Piracicaba, São Paulo, Brazil

SUMMARY

Zygomatic arch and articular eminence are structures from the human skull involved in jaw muscle activity. The aim of the study was to evaluate three-dimensional morphological patterns of the zygomatic arch and its relationships with articular eminence in a Brazilian population. 122 computed tomography scans of human skulls were evaluated. The Mimics 18.0 software (Materialise, NV, Belgium) was used to perform segmentation of images from CT scans. 3D reconstructions of CT scans were imported into Rhinoceros 5.0 software (McNeel & Associates, Seattle, USA), in which linear measurements (mm) were obtained. Statistical analysis was performed in GraphPAD Prism v.8 (San Diego, CA, USA). The normality of the sample was checked by Shapiro-Wilks and significance level of 5% was considered. Based on cross-sectional area classification, out of 116 male zygomatic arches the incidence was 59% of type elliptical (E) and 41% of type blade-like (Bl). Out of 102 female zygomatic arches the incidence was 38% of type E and 62% of type Bl. There was no incidence of type cylindrical (C). Based on the classification proposed in the present study, the incidence for males was 58% of type parentheses (P), 38% of type bracket (B) and 4% of type M-shaped (M); and the incidence for females was 33% (type P), 66% (type B) and 1% (type M). The elliptical and convex body of the zygomatic arch prevailed in males and the blade-like and straight body of the zygomatic arch prevailed in females. There is no relationship between zygomatic arch type and zygomatic arch and articular eminence distances.

Key words: Anatomy – Skull – Temporomandibular joint – Tomography – Zygoma

INTRODUCTION

The zygomatic arch (ZA) is an anatomical structure originating from the union between the zy-

Corresponding author:
Prof. Alexandre Rodrigues Freire. Department of Biosciences, Anatomy Division, Piracicaba Dental School, University of Campinas. Avenida Limeira, nº 901 – Areião. CEP 13414-903, Piracicaba, São Paulo – Brazil. E-mail: a088452@dac.unicamp.br

Submitted: June 29, 2023 **Accepted:** August 5, 2023

https://doi.org/10.52083/HTWU4773

gomatic process of the temporal bone and the temporal process of the zygomatic bone (Smith and Grosse, 2016). The ZA is known to be the anatomical structure that joins the viscerocranium to the neurocranium (Franks et al., 2016). It is tenuous, elongated and is the site where the masseter muscle has its origin. Because it is a salient bilateral structure, the ZA is susceptible to several types of traumas (Song et al., 2009), such as isolated fractures or being a part of multiple facial fractures (Valdés and Zapata, 2021; Jones and Schmalbach, 2022; Estawrow and Elbarbary, 2022).

In the temporal bone, it arises from a triangular base, extends through the zygomatic process of the temporal bone to the region where the temporal and zygomatic bones communicate, the zygomaticotemporal suture, and then it crosses to articulate with the zygomatic bone through the temporal process of the zygomatic bone. Finally, the body of this last bone delimits the extension of the arch (Testut and Latarjet, 1954).

Adjacent to the ZA, in its part of the zygomatic process of the temporal bone, is the articular eminence (AE), part of the skeletal structures of the temporomandibular joint (TMJ). It consists of dense bone tissue that supports the load of forces that affect this region of the skull base from mandibular movements. The inferior surface of the temporal bone articulates with the mandible. In its lateral part, it is elevated and forms the articular tubercle, which can be also considered the medial root of the ZA (Sicher and Du Brul, 1980).

There are many works involving traumas that occurred in the ZA region (Song et al., 2009; Jones and Schmalbach, 2022), but few characterize its morphology. Examples that perform its local analysis are related to cephalometric measurements (Park et al., 2019) and regarding shape and biomechanics the studies are usually related to species of animals other than humans, such as chimpanzees (Smith and Grosse, 2016).

The shape of the ZA in mammals is quite variable. In a cross-section of this anatomical accident, cylindrical, elliptical and blade-like shapes can be observed. Smith and Grosse (2016) used three types of ZA in their study: cylindrical, elliptical and blade-like. They concluded that there are local effects on the magnitude of the tension force in the ZA caused by its morphological changes.

Certain parameters of masticatory muscles function have been shown to be associated with facial morphology, including electromyographic activity and occlusal force. The cross- sectional areas of these masticatory muscles can also correlate with the corresponding cross- sections of adjacent structures (Righetti et al., 2020), as has already been studied in the mandible through computed tomography (CT) scans, magnetic resonance imaging and ultrasound (Benington et al., 1999; Palinkas et al., 2019). This highlights the importance of studying biomechanical effects on anatomical structures by considering the full set of information, not just isolated structures, to understand craniofacial dynamics (Smith and Grosse, 2016).

The AE, as well as the mandibular fossa and the mandible condyle, undergoes bone remodeling during life (Kranjčić et al., 2016). Studies of the morphological relationship between the AE and the ZA are scarce in the literature. Therefore, considering the topographic relationships of proximity between the ZA and the AE and the mechanical relationships between the activity of the masseter muscle (a mandibular elevator) associated with the mandibular movements provided by the TMJ, the present study suggests the hypothesis that the variations in the shape of the ZA are associated with the variations of the AE. Thus, characterizing the morphology of the ZA and the AE helps to understand biomechanical aspects and guide clinical planning and treatment. So, the aim of this study was to evaluate the three-dimensional morphological patterns of the ZA, as well as the relationships between the morphology of the ZA and the AE in a Brazilian population.

MATERIALS AND METHODS

Ethics approval

The research was analyzed and approved by the Committee of Research Ethics of the University of Campinas (Protocol number CAAE 58958122.7.0000.5418).

Sample

The CT scans belong to an identified osteological collection (contemporary Southeast Brazilian population) of dry human skulls belonging to the Biobank "Prof. Dr. Eduardo Daruge" of Piracicaba Dental School - University of Campinas. The tomographic images were obtained in an Aisteion Multislice 4 CT System device (Toshiba Medical Systems Corporation – Japan), for the skull protocol: 100 mA, 120kV, with 1mm slices.

A total of 122 CT scans of human skulls of both sexes (66 male and 56 female) and both sides (right and left) were evaluated. The age group ranged from 18 to 80 years old, with a mean age of 59.42 years old (standard deviation: 16.71).

For the inclusion criteria of sample, CT scans of dry, intact skulls without fractures or any other macroscopic pathological or surgical alteration were included. The CT scans of skulls with fractures, bone destruction or any other macroscopic pathological or surgical alteration were excluded.

Processing of tomographic images

The Mimics 18.0 software (Materialise, NV, Belgium) was used to perform the segmentation of the images of each CT scan. Segmentation consisted of selecting pixels of the bone structure in each tomographic section. This selection was defined by evaluating a threshold of gray scale values to obtain voxels, whose values are in a range according to the bone components of interest. The 3D reconstruction was performed to enable the visualization of these components and each three-dimensional surface was exported in virtual stereolithography (STL) to perform the surface evaluation.

Morphometric analysis on CT scans of dry skulls

The 3D reconstructions of the CT scans were imported into the Rhinoceros 5.0 software (McNeel & Associates, Seattle, USA), in which linear measurements (mm) were obtained for evaluation and morphological characterization of the ZA and AE on both sides (right and left). The values obtained by the software were tabulated for statistical analysis.

The measurements were obtained, in millimeters, regarding the vertical and horizontal diameter of the ZA and the AE distance using the Mimics 18.0 software (Materialise, NV, Belgium) and regarding the ZA distance using the Rhinoceros 5.0 software (McNeel & Associates, Seattle, USA).

To obtain the measurements of the vertical and horizontal diameter of the ZA, it was necessary

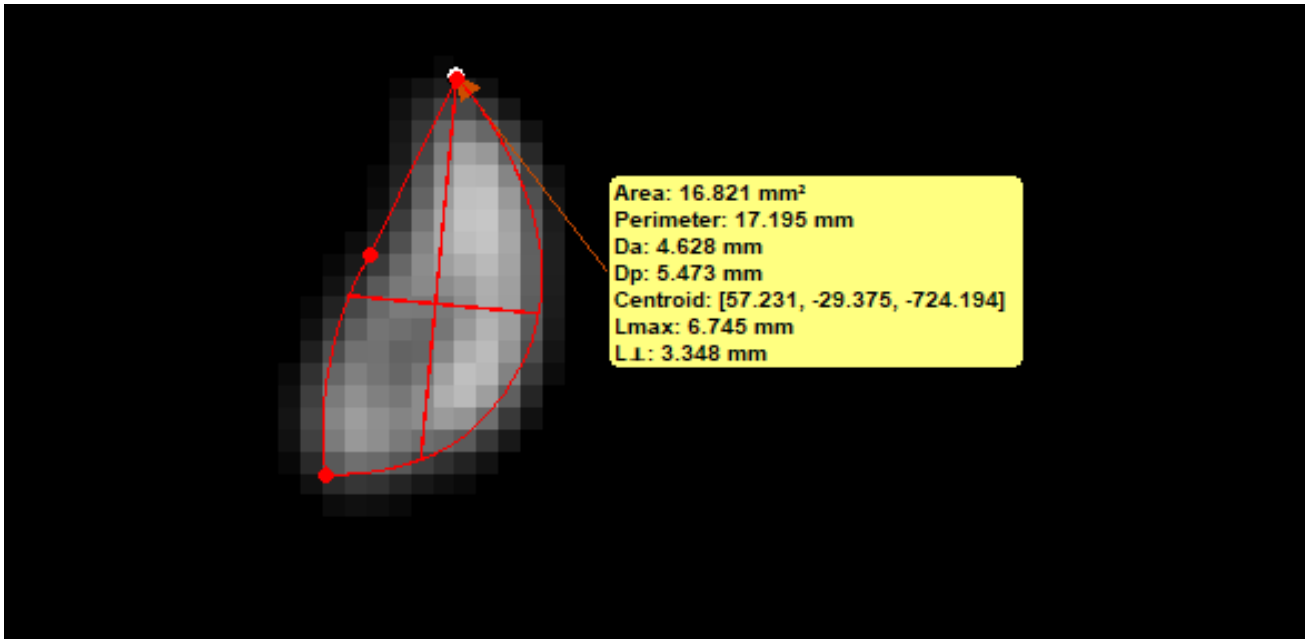

Fig. 1.- Measurement of the cross-sectional area of the ZA provided by the Mimics 18.0 software (Materialise, NV, Belgium) in a computed tomography scan. Lmax: vertical diameter (maximum diameter passing through the central point of the chosen cross-sectional area), L⊥: horizontal diameter (minimum diameter orthogonal to Lmax).

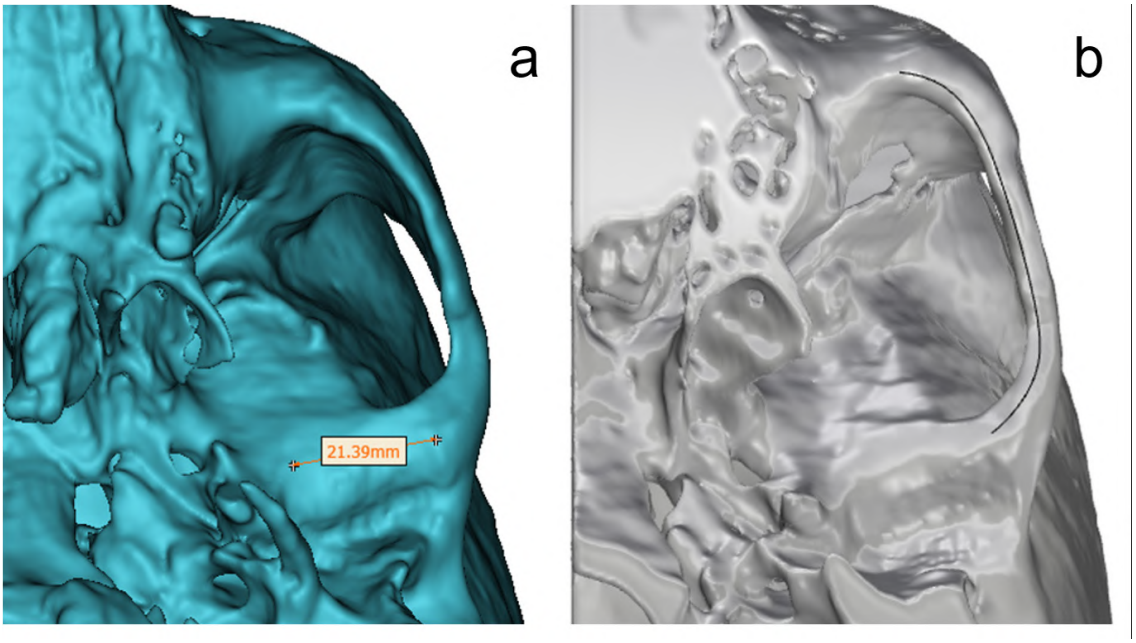

Fig. 2.- Images referring to the acquisition of measurements in 3D models. **a:** measurement of the AE distance, **b:** measurement of the ZA distance.

to define the cross-sectional area for its measurement. It was defined by choosing the lowest point in the region of the zygomaticotemporal suture.

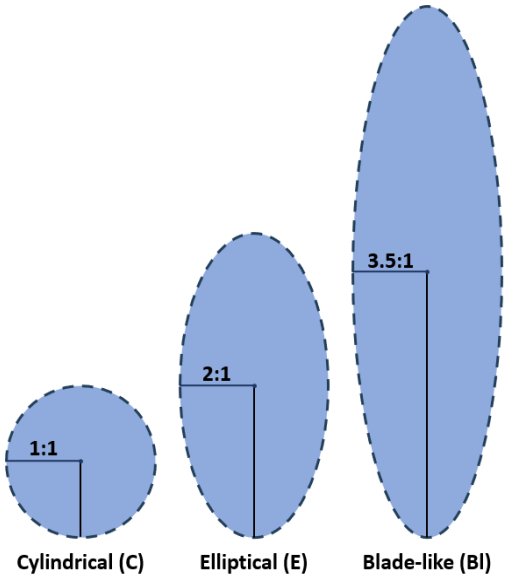

Fig. 3.- Cross-sectional classification of ZA by Smith and Grosse (2016). The shapes of the image represent the types with their respective proportions: Cylindrical (1:1), Elliptical (2:1) and Blade-like (3.5:1). To classify the sample of the present study, it was necessary to calculate the proportion between the maximum diameter, in milimeters, passing through the central point of the chosen cross-sectional area and the minimum diameter, in milimeters, orthogonal to it. With the resulting ratio, each cross-sectional area of zygomatic arch was classified according to the proximity with Cylindrical, Elliptical or Blade-like ratios. Image adapted from Smith and Grosse (2016).

The vertical diameter of the ZA was defined as the maximum diameter passing through the central point of the chosen cross-sectional area, and the horizontal diameter as the minimum diameter orthogonal to the maximum diameter obtained (Fig. 1).

The AE distance (Fig. 2) consists of the length from its lateral end to its medial end in an inferior view of the skull. The lateral end is the region of volume increase of the inferior and posterior part of the ZA, also known as the articular tubercle. The medial end is the region of articulation (sphenosquamous suture) of the temporal bone with the sphenoid bone closest to the axis of the LA.

The ZA distance (Fig. 2) consists of the length from its anterior end to its posterior end in an inferior view of the skull, the anterior end being the region close to the lowest point of the zygomaticomaxillary suture and the posterior end being the region closest and lateral to the articular tubercle.

Classification of the zygomatic arch regarding its cross-sectional area

Measurements of the vertical and horizontal diameter of the ZA were used to classify the ZAs according to the study by Smith and Grosse

(2016) (Fig. 3), in which the authors characterized three types of ZA: cylindrical (cylindrical, C), elliptical (elliptical, E) and blade- like (blade-like, Bl) with proportions of 1:1; 2:1 and 3.5:1 of the vertical and horizontal radius of the cross-sectional area of the ZA, respectively.

To classify the ZAs in the sample, the proportion between the vertical diameter and the horizontal diameter was calculated, and then the classification was made according to the closest proximity of the value obtained to the proportions of each type. In the present study, there was no incidence of morphological type C, so a classification of two morphological types (E and Bl) was considered.

Classification of the zygomatic arch regarding its morphology

In the Rhinoceros 5.0 software (McNeel & Associates, Seattle, USA), a linear representation of the ZA was drawn on each CT scan considering the anteroposterior morphology in an inferior view of the skull. Analyzing the linear shape obtained and the 3D reconstruction of each ZA, the classification according to the ZA morphology was obtained, consisting of parentheses (parentheses, P), bracket (bracket, B), and M-shaped (M-shaped, M) (Fig. 4). Silhouettes obtained from ZAs with a milder degree of curvature at the beginning and end (greater than 90°) and a body close to a convex aspect were classified as parentheses; silhouettes obtained from ZAs with a more accentuated degree of curvature at the beginning and end (near or less than 90°) and a body similar to a straight line were classified as bracket; finally, silhouettes obtained from ZAs with part of the body directed medially to the infratemporal fossa, regardless of the degree of curvature at its beginning and end, were classified as M-shaped.

Data analysis

After collecting all the data, they were tabulated in the Microsoft Office Excel® package. Statistical analysis was performed using GraphPAD Prism v.8 software (San Diego, CA, USA). The normality of the sample was checked by Shapiro-Wilks. Descriptive statistics were performed for each measurement in each sex and type. Measures of the morphological types of evaluated anatomical structures (ZA and AE) were compared using the Mann-Whitney test. For the classification with two morphological types, the Mann-Whitney test was also performed. For the classification with three morphological types, the Kruskal-Wallis test with multiple comparisons by Dunn's test was used. The Two-way ANOVA test was performed, with multiple comparisons by Sidak's test, in each measure evaluated to verify the relationship between sexes and the types found in each side. In all analyses, a significance level of 5% was considered.

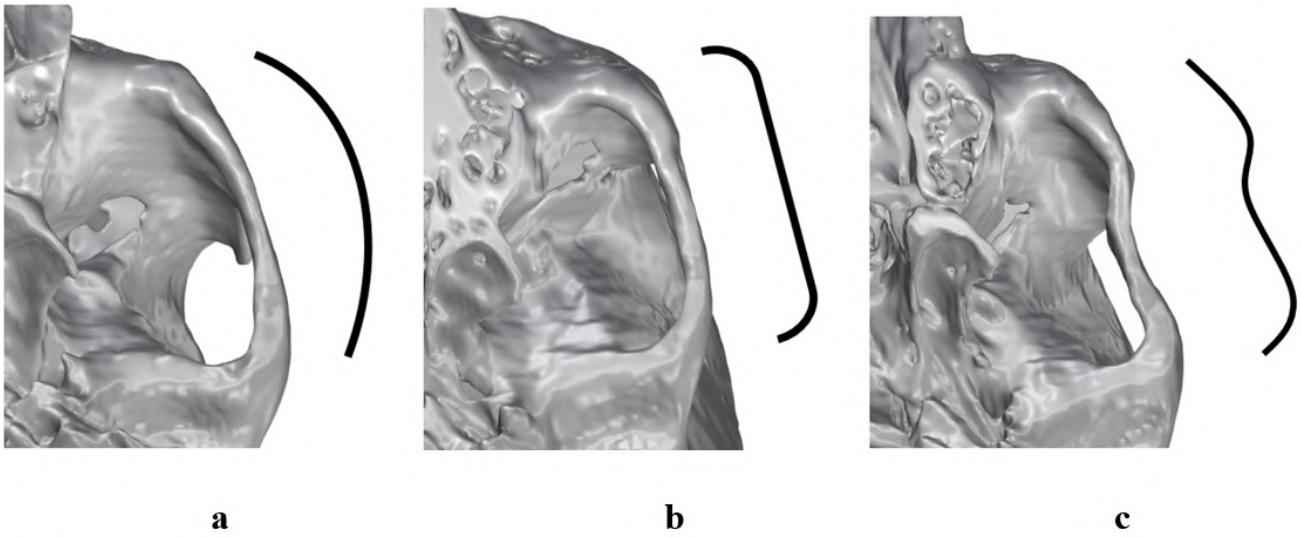

Fig. 4.- Representative images of the types of ZA regarding the anteroposterior morphology in inferior view. **a:** Parentheses type (P), **b:** Bracket type (B), **c:** M-shaped type (M).

RESULTS

Of the 122 CT scans evaluated, 110 CT scans were used to study the morphology of the ZA and AE, 52 (47%) of which were female and 58 (53%) were male. Sides of 2 CT scans (one on the left and one on the right) that showed variation in the morphology of the mandibular fossa with a bone opening in its concavity were excluded.

It was possible to classify the ZAs according to the method by Smith and Grosse (2016) with the results obtained from measuring the cross-sectional area. In the analysis in question, there was no incidence of the cylindrical type in the studied sample.

Of the 116 male ZAs, the incidence was 59% of type E and 41% of type Bl. Of the 102 female ZAs, the incidence was 38% of type E and 62% of type Bl. There was no incidence of type C in both sexes. The incidence of each type can be seen in Fig. 5.

After measuring the ZA distance, its silhouette and its 3D reconstruction were analyzed and then classified according to the method proposed in the present study. The incidence of each type can be seen in Fig. 6.

Based on the method proposed in the present study, the incidence for males was 58% (type P), 38% (type B) and 4% (type M); and the incidence for females was 66% (type B), 33% (type P) and 1% (type M).

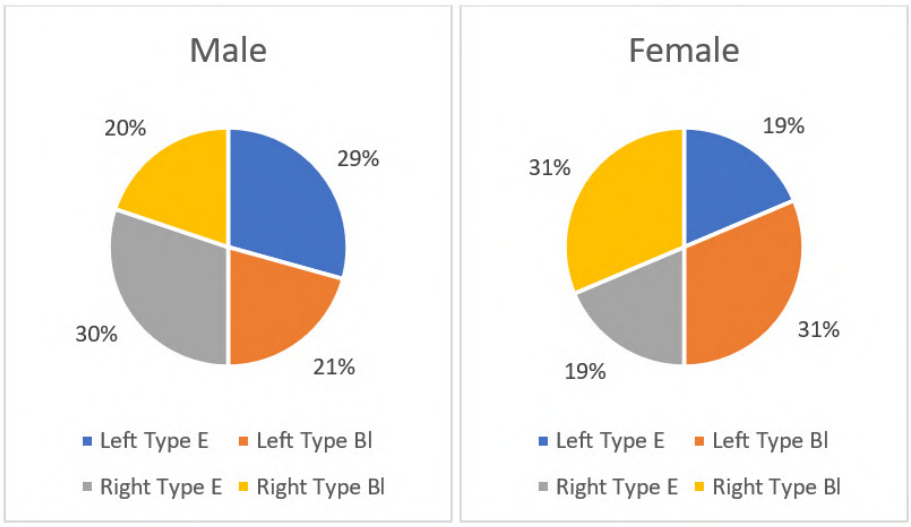

Fig. 5.- Incidence of types of ZA according to Smith and Grosse (2016) by sex. E: Elliptical type, Bl: Blade-like type.

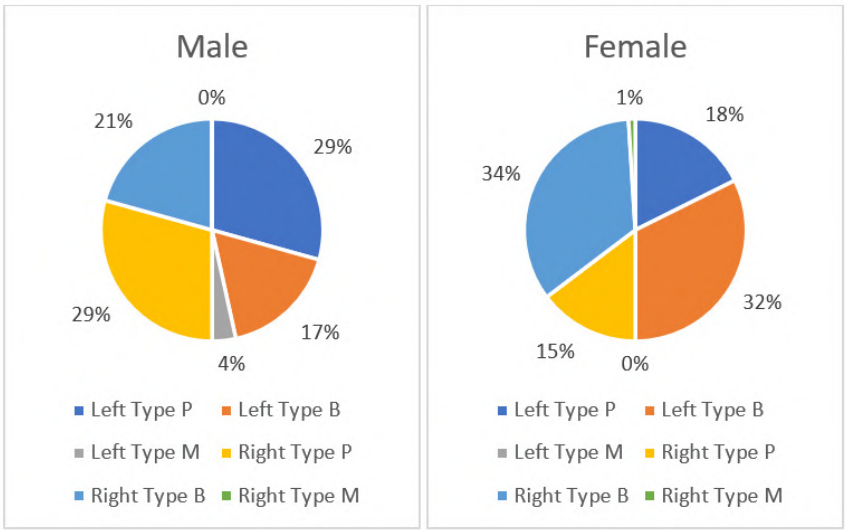

Fig. 6.- Incidence of types of ZA according to the method proposed by the present study by sex. P: Parentheses type, B: Bracket type, M: M-shaped type.

Zygomatic Arch Distance

For type E of ZA, the Median distance was 53.02 mm on the left side and 52.62 mm on the right side. For type Bl of ZA, the Median distance was 51.53 mm on the left side and 52.83 mm on the right side (Table 1). On both sides (left and right), when comparing measurements of morphological types E and Bl (Mann-Whitney test), no significant differences were found (left side P = 0.0628; right side P = 0.9171) (Table 1).

For type P of ZA, the Median distance was 51.81 mm on the left side and 51.51 mm on the right side. For type B of ZA, the Median distance was 52.14 mm on the left side and 52.99 mm on the right side. For type M of ZA, the Median distance was 58.73 mm on the left side and 58.25 mm on the right side (Table 2). When comparing the measures of the morphological types P, B and M (Kruskal-Wallis test), significant differences were found for the left side (P= 0.0310) while for the right side no differences were detected. Multiple comparisons by Dunn's test performed between the means of each morphological type on each side showed significant differences on the left side when comparing type P vs type M (P= 0.0456) and B vs M (P= 0.0252). For the other comparisons, there were no significant differences (Table 2).

For the classification of two morphological types, to assess the difference between the sexes within the same type, for the left side, the Two-way ANOVA test showed a significant difference when comparing the ZA distance between males and females (P = 0.0002), while, when comparing the morphological types E and Bl within the same sex, significant differences were not detected (P = 0.4469). Multiple comparisons by the Sidak test performed in both sexes between the means of each type showed significant differences when comparing type E between sexes (P = 0.0132) and type Bl between sexes (P = 0.0148). Thus, there was a tendency for the ZA distance to be greater in males than in females in both morphological types (Fig. 7). For the right side, the Two-way ANOVA test showed a significant difference when comparing the ZA distance between males and females (P = 0.0009), while, when comparing the morphological types E and Bl within the same sex, significant differences were not detected (P = 0.5108). Multiple comparisons by the Sidak test performed in both sexes between the means of each type showed significant differences when comparing type Bl between sexes (P = 0.0025). Thus, on the right side, the ZA distance is greater in males than in females in Bl morphological type (Fig. 7).

For the classification of three morphological types, to assess the difference between the sexes within the same type, for the left side, the Two-way ANOVA test showed a significant difference when comparing the ZA distance between males and females (P = 0.0004), while, when comparing the morphological types P and B within the same sex, significant differences were not detected (P = 0.6633). The morphological type M was not included in the comparisons, as it was not found in the evaluated sample. Multiple comparisons by the Sidak test performed in both sexes between the means of each type showed significant differences when comparing type P between sexes (P = 0.0186) and type B between sexes (P = 0.0240). Thus, there was a tendency for the ZA distance to be greater in males than in females in both morphological types (Fig. 8). For the right side, the Two-way ANOVA test showed a significant difference when comparing the ZA distance between males and females (P = 0.0001), while, when comparing the morphological types P and B within the same sex, significant differences were not detected (P = 0.1206). The morphological type M was not included in the comparisons, as it was not found in the evaluated sample. Multiple comparisons by the Sidak test performed in both sexes between the means of each type showed significant differences when comparing type P between sexes (P = 0.0067) and between types B (male) and P (female) (P = 0.0053) (Fig. 8).

Articular Eminence Distance

For type E of AE, the Median distance was 16.88 mm on the left side and 17.30 mm on the right side. For type Bl of AE, the Median distance was 16.88 mm on the left side, and 17.18 mm on the right side (Table 1). On both sides (right and left), when comparing measurements of morphological types E and Bl (Mann-Whitney test), no significant differences were found (left side P = 0.9362; right side P = 0.5449) (Table 1).

Table 1. Means, standard deviations (SD), quartiles and medians (in millimeters) of zygomatic arch distance and articular eminence distance per side in each category of two morphological types of zygomatic arch.

Measurement	Ea (mm)						Bla (mm)					
Zygomatic arch distance	Mean (SD)	Minimum	25% Percentile	Median	75% Percentile	Maximum	Mean (SD)	Minimum	25% Percentile	Median	75% Percentile	Maximum
Left	52.90 (4.472)	43.53	50.57	53.02	56.51	61.89	51.55 (4.550)	44.45	48.14	51.53	54.18	64.49
Right	52.28 (3.664)	43.37	49.78	52.62	54.43	59.79	52.26 (4.417)	44.78	49.29	52.83	55.23	63.37
Articular eminence distance												
Left	17.02 (1.971)	12.46	15.90	16.88	18.62	21.55	17.06 (2.198)	12.87	15.88	16.88	18.07	23.12
Right	17.63 (2.409)	13.82	15.60	17.30	18.95	24.56	17.24 (2.248)	12.02	15.52	17.18	18.81	22.18

[a]E: Elliptical type of zygomatic arch; Bl: Blade-like type of zygomatic arch.

Table 2. Means, standard deviations (SD), quartiles and medians (in millimeters) of zygomatic arch distance and articular eminence distance per side in each category of three morphological types of zygomatic arch.

Measurement	Ea (mm)						Bla (mm)						M[b] (mm)					
Zygomatic arch distance	Mean (SD)	Minimum	25% Percentile	Median	75% Percentile	Maximum	Mean (SD)	Minimum	25% Percentile	Median	75% Percentile	Maximum	Mean (SD)	Minimum	25% Percentile	Median	75% Percentile	Maximum
Left	52.21 (4.699)*	44.07	48.52	51.81	55.00	64.49	51.71 (4.077)*	43.53	48.78	52.14	54.61	61.18	58.80 (4.087)*	53.89	54.99	58.73	62.69	63.86
Right	52.10 (4.554)	44.35	48.26	51.51	55.34	63.37	52.31 (3.553)	43.37	50.14	52.99	54.32	60.80	58.25 (0.000)	58.25	58.25	58.25	58.25	58.25
Articular eminence distance																		
Left	17.30 (2.176)	12.46	16.01	17.23	18.53	23.12	16.65 (1.947)*	12.87	15.33	16.55	17.38	22.05	18.84 (1.197)*	17.49	17.71	18.78	20.02	20.30
Right	17.58 (2.569)	12.02	15.55	17.48	18.90	24.56	17.27 (2.113)	13.22	15.60	17.16	18.81	22.24	19.99 (0.000)	19.99	19.99	19.99	19.99	19.99

* Statistical difference between types.
b P: Parentheses type of zygomatic arch; B: Bracket type of zygomatic arch; M: M-shaped type of zygomatic arch.

For type P of AE, the Median distance was 17.23 mm on the left side and 17.48 mm on the right side. For type B of AE, the Median distance was 16.55 mm on the left side and 17.16 mm on the right side. For type M of AE, the Median distance was 18.78 mm on the left side and 19.99 mm on the right side (Table 2). When comparing the measures of the morphological types P, B and M (Kruskal-Wallis test), significant differences were found for the left side (P = 0.0153), while for the right side no differences were detected. Multiple comparisons by Dunn's test performed between the means of each morphological type on each side showed significant differences on the left side when comparing type B vs. M (P= 0.0408). For the other comparisons, there were no significant differences (Table 2).

For the classification of two morphological types, to assess the difference between the sexes within the same type, for the left side, the Two-way ANOVA test showed that there was no significant difference when comparing the AE distance between males and females (P= 0.4707), nor when comparing the morphological types E and Bl within the same sex (P = 0.8098). The multiple comparisons by the Sidak test performed

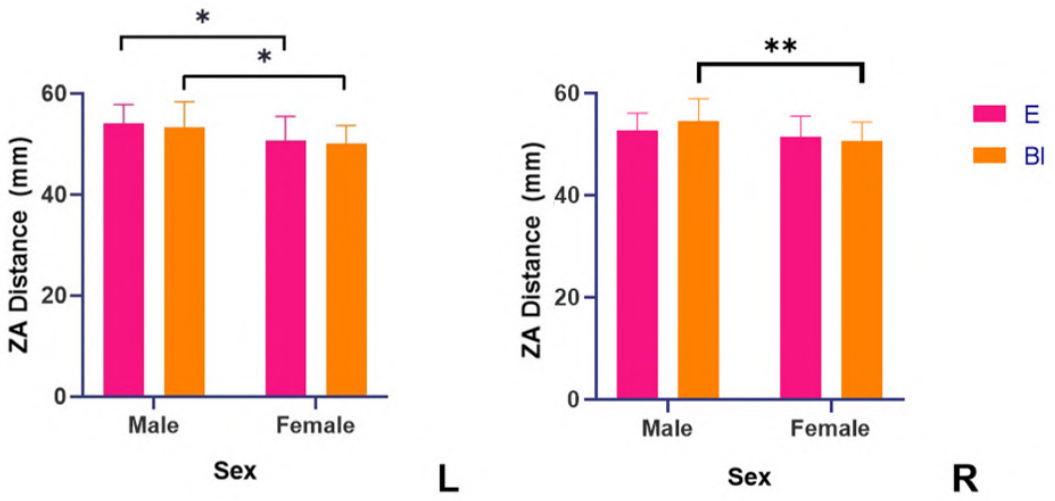

Fig. 7.- Mean ZA distance (mm) by sex in each morphological type (E and Bl). For the left side: type E – male versus female: P = 0.0132; type Bl – male versus female: P = 0.0148. For the right side: type Bl – male versus female: P = 0.0025. * and ** Statistical difference between sexes.

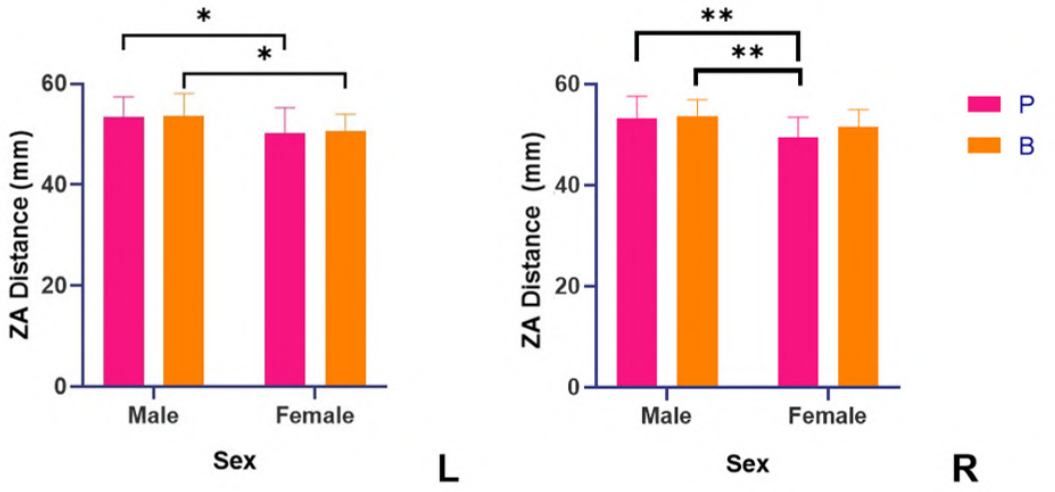

Fig. 8.- Mean ZA distance (mm) by sex in each morphological type (P and B). For the left side: type P – male versus female: P = 0.0186; type B – male versus female: P = 0.0240. For the right side: type P – male versus female: P = 0.0067; type B – male versus type P – female: P = 0.0053. * and ** Statistical difference between sexes.

in both sexes between the means of each type showed that there were no significant differences when comparing type E between sexes (P = 0.8281) and type Bl between sexes (P = 0 .8674) (Fig. 9). For the right side, the Two-way ANOVA test showed that there was no significant difference when comparing the AE distance between males and females (P= 0.5044), nor when comparing the morphological types E and Bl within the same sex (P = 0.3020). The multiple comparisons by the Sidak test performed in both sexes between the means of each type showed that there were no significant differences when comparing type E between sexes (P=0.9587) and type Bl between sexes (P> 0.9999) (Fig. 9).

For the classification of three morphological types, to assess the difference between the sexes within the same type, for the left side, the Two-way ANOVA test showed that there was no significant difference when comparing the AE distance between males and females (P = 0.9436), nor when comparing the morphological types P and B within the same sex (P = 0.1164). The morphological type M was not included in the comparisons, as it was not found in the evaluated sample. The multiple comparisons by the Sidak test performed in both sexes between the means of each type showed that there were no significant differences when comparing type P between sexes (P = 0.9059) and type B between

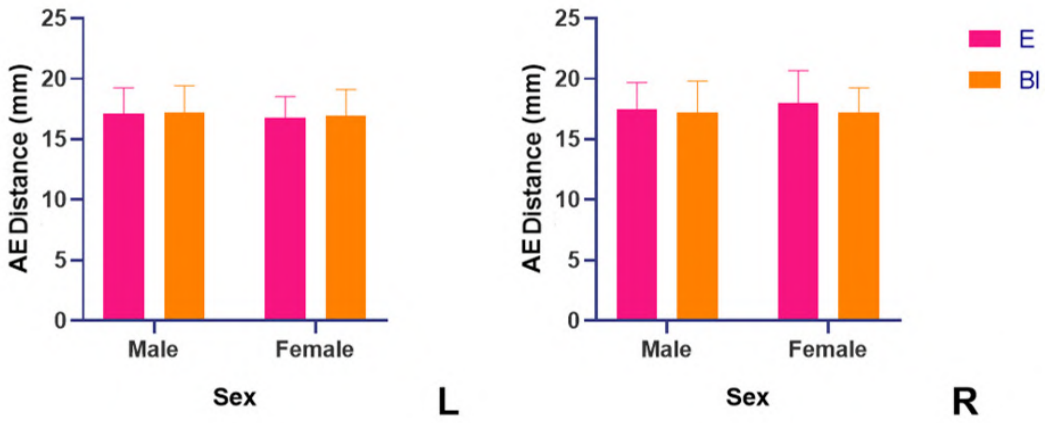

Fig. 9.- Mean AE distance (mm) by sex in each morphological type (E and Bl). There were no statistical differences.

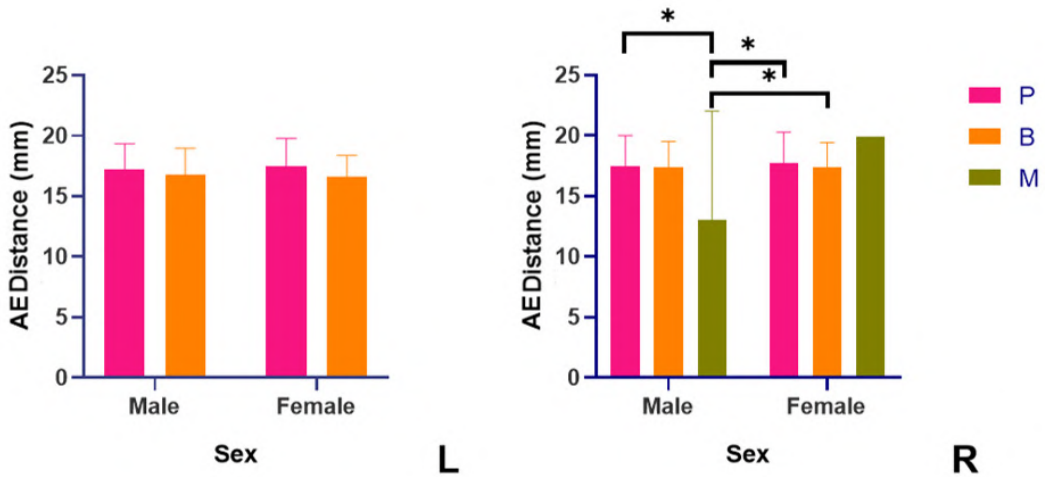

Fig. 10.- Mean AE distance (mm) by sex in each morphological type (P and B). For the right side: type P – male versus type M – male: P = 0.0374; type M – male versus type P – female: P = 0.0368; type M – male versus type B – female: P = 0.0484. * Statistical difference between sexes.

sexes (P = 0 .9428) (Fig. 10). For the right side, the Two-way ANOVA test showed that there was significant difference when comparing the AE distance between males and females (P = 0.0300). When comparing the morphological types P, B and M within the same sex (P = 0.7329) no difference was detected. The multiple comparisons by the Sidak test performed in both sexes between the means of each type showed significant differences when comparing types P and M within male sex (P=0.0374), between types M (male) and P (female) (P = 0.0368) and between types M (male) and B (female) (P = 0 .0484) (Fig. 10).

DISCUSSION

The study proposed to morphologically evaluate two anatomical structures, the ZA and the AE, for their individual characteristics and the possible relationships between them in a Brazilian population.

When applying the classification proposed by Smith and Grosse (2016), it is possible to observe that in the studied sample there was no incidence of the cylindrical type; therefore, the ZAs presented only the elliptical type or the blade-like type. This may be related to the direction of traction that the masseter muscle exerts on the ZA. Such a characteristic was previously described, in which the force performs torsion on the ZA through its long axis, and this tends to invert the lower edge of the arch and evert its upper edge (Hylander and Johnson, 1997).

For the percentage incidence of the classifications used, it is noted that in the classification by Smith and Grosse (2016) there was a greater tendency for type Bl in females and a greater tendency for type E in males. While in the classification proposed in the present study there was a greater tendency to type B in females and a greater tendency to type P in males. Therefore, in the sample analyzed, the female sex presented, for the most part, blade- like ZA morphology and straight body, and the male sex, mostly, elliptical ZA morphology and convex body. Thus, studies on the relationship between these two classifications and, thus, between the morphology of the cross-sectional area with the anteroposterior ZA distance, are necessary to verify the relationship between the morphology of the ZA and the sexes.

There was no statistical difference for the classification of the cross-sectional area of the ZA between the sides, both for ZA distance and AE distance. However, type M of the classification proposed in the present study was involved in all the statistical differences found. For the ZA distance, there was a difference on the left side when comparing the type P with the M and the B with the M. These two differences may be associated with the deviation of the body of the ZA towards the medial direction in the type M, since it has the shape of the ZA, which naturally increases its length because of the longer path it has when producing such a deviation. In types P and B, it does not occur, being a direct path in both.

This deviation in type M can be related to the activity of the masseter muscle because this mastication muscle has its origin in the inferior border of the ZA and insertion in the external surface of the mandibular ramus (Sicher and Du Brul, 1980). There are hypotheses suggesting that the differential distribution of muscle tension exerted by the areas of insertion in the mandibular ramus, angle and coronoid process has important consequences, since they involve large areas of bone and must affect biomechanical events in more distant areas, such as the TMJ and possibly the ZA. Presumably they affect growth patterns, but the characteristics are not well defined (McNeill, 1997).

Research involving the anteroposterior morphology of the ZA, as the classification proposed by this study suggests, and the facial morphology in the vertical dimension (Collett and West, 1993; Franco et al., 2013) are of great interest, because, in general, the cross- sectional areas of the masseter, lateral and medial pterygoids and temporal muscle are positively correlated with the bigonial and bizygomatic amplitudes, inferring that one might expect the elevator muscles to be thicker in brachycephalics (McNeill, 1997). It is possible to correlate the anteroposterior morphology of the ZA with the facial biotypes. According to McNeill (1997), the cross-sectional areas of the muscle are also affected by muscle utilization and by the growth of the individual.

For the AE distance, there was a difference on the left side when comparing type B with type M, which may be related to the biomechanical activity of mastication. It is possible that there is a relationship between the difference occurring on a specific side, since there are studies that relate the proportion of masseter muscle strength between the working side and the balancing side during chewing with the texture of the food. This proportion is lower with hard foods and higher with soft foods (Hylander et al., 1992). Furthermore, it is possible that the arch morphology may influence the AE due to its anatomical proximity since the posterior part of the ZA is adjacent to the AE. However, it is emphasized that further studies are needed to analyze these relationships.

Statistically, the results of the ZA distance showed a difference between sexes in the Smith and Grosse (2016) classification, both in type E and in type Bl. However, there was no difference between the two types found in the same sex. The ZA distance is greater in males than in females in both morphological types for the left side and this size difference appears in the cross-sectional area classification of the ZA for the right side. This may be related to the existing sexual differences in the skull, which refer to the lower power of the female musculature associated with the smaller volume that the female skull presents (Sicher and Du Brul, 1980).

For the classification proposed in the present study, the results of the ZA distance also showed difference between sexes, both in type P and in type B. There was no difference between the two types found in the same sex. The ZA distance is also greater in males than in females in both morphological types and sides.

Associating the results of the two classifications, it is possible to conclude that the ZA distance is greater in males than in females in the studied sample. This information may be useful for anthropometric studies, such as sexual dimorphism, since the ZA distance showed difference between sexes in both classifications.

As regards to sex, males had a higher incidence of type E and females had a higher incidence of type Bl, according to the cross-sectional area classification of the ZA. Males also had a higher incidence of type P and females had a higher incidence of type B, according to the new classification proposed by the present study. There is no relationship between ZA type and ZA and AE distances. However, as a limitation of the study, it is needed to seek anthropological variability once it is carried out in a sample that covers the population of a specific region of Southeast Brazil. Thus, it is important to expand the methodology to samples in other countries and/or to other regions within the same country.

ACKNOWLEDGEMENTS

The authors sincerely thank those who donated their bodies to science so that anatomical research could be performed. Results from such research can potentially increase mankind's overall knowledge that can then improve patient care. Therefore, these donors and their families deserve our highest gratitude (Iwanaga et al., 2020).

This study was funded by the Coordenação de Aperfeiçoamento de Pessoal de Nível Superior (CAPES), Brazil (Financial Code: 001).

REFERENCES

BENINGTON PC, GARDENER JE, HUNT NP (1999) Masseter muscle volume measured using ultrasonography and its relationship with facial morphology. *Eur J Orthod*, 21(6): 659-670.

COLLETT AR, WEST VC (1993) Terminology of facial morphology in the vertical dimension. *Aust Dent J*, 38(3): 204-209.

ESTAWROW MA, ELBARBARY AS (2022) Closed isolated zygomatic arch fracture management made easy. *J Craniofac Surg*, 33(4): e388-e390.

FRANCO FC, DE ARAUJO TM, VOGEL CJ, QUINTÃO CC (2013) Brachycephalic, dolichocephalic and mesocephalic: Is it appropriate to describe the face using skull patterns? *Dental Press J Orthod*, 18(3): 159-163.

FRANKS EM, HOLTON NE, SCOTT JE, MCABEE KR, RINK JT, PAX KC, PASQUINELLY AC, SCOLLAN JP, EASTMAN MM, RAVOSA MJ (2016) Betwixt and between: intracranial perspective on zygomatic arch plasticity and function in mammals. *Anat Rec (Hoboken)*, 299(12): 1646-1660.

HYLANDER WL, JOHNSON KR, CROMPTON AW (1992) Muscle force recruitment and biomechanical modeling: an analysis of masseter muscle function during mastication in Macaca fascicularis. *Am J Phys Anthropol*, 88(3): 365-387.

HYLANDER WL, JOHNSON KR (1997) In vivo bone strain patterns in the zygomatic arch of macaques and the significance of these patterns for functional interpretations of craniofacial form. *Am J Phys Anthropol*, 102(2): 203-232.

IWANAGA J, SINGH V, OHTSUKA A, HWANG Y, KIM HJ, MORYŚ J, RAVI KS, RIBATTI D, TRAINOR PA, SAÑUDO JR, APAYDIN N, ŞENGÜL G, ALBERTINE KH, WALOCHA JA, LOUKAS M, DUPARC F, PAULSEN F, DEL SOL M, ADDS P, HEGAZY A, TUBBS RS (2020) Acknowledging the use of human cadaveric tissues in research papers. Recommendations from Anatomical Journal Editors. *Clin Anat*, 34: 2-4.

JONES CM, SCHMALBACH CE (2022) Zygomaticomaxillary fractures. *Facial Plast Surg Clin North Am*, 30(1): 47-61.

KRANJČIĆ J, ŠLAUS M, VODANOVIĆ M, PERŠIĆ S, VOJVODIĆ D (2016) Articular eminence inclination in medieval and contemporary Croatian population. *Acta Clin Croat*, 55(4): 529-534.

MCNEILL C (1997) Science and Practice of Occlusion. Quintessence Pub Co, USA.

PALINKAS M, BORGES TF, JUNIOR MT, MONTEIRO SAC, BOTTACIN FS, MESTRINER-JUNIOR W, REGALO IH, SIÉSSERE S, SEMPRINI M, REGALO SCH (2019) Alterations in masticatory cycle efficiency and bite force in individuals with periodontitis. *Int J Health Sci (Qassim)*, 13(1): 25-29.

PARK JA, LEE JS, KOH KS, SONG WC (2019) Using the zygomatic arch as a reference line for clinical applications and anthropological studies. *Surg Radiol Anat*, 41(5): 501-505.

RIGHETTI MA, TAUBE OLS, PALINKAS M, GONÇALVES LMN, ESPOSTO DS, DE MELLO EC, REGALO IH, REGALO SCH, SIÉSSERE S (2020) Osteoarthrosis: analyze of the molar bite force, thickness and masticatory efficiency. *Prague Med Rep*, 121(2): 87-95.

SICHER H, DU BRUL EL (1980) Oral Anatomy. Mosby Inc, USA.

SMITH AL, GROSSE IR (2016) The biomechanics of zygomatic arch shape. *Anat Rec (Hoboken)*, 299(12): 1734-1752.

SONG WC, CHOI HG, KIM SH, KIM SH, HU KS, KIM HJ, KOH KS (2009) Topographic anatomy of the zygomatic arch and temporal fossa: a cadaveric study. *J Plast Reconstr Aesthet Surg*, 62(11): 1375-1378.

TESTUT L, LATARJET A (1954) Tratado de anatomía humana. Salvat, Spain.

VALDÉS REYES JM, ZAPATA OCAMPO S (2021) Functional classification of isolated zygomatic arch fracture: new proposal. *J Craniofac Surg*, 32(2): 757-758.

Characterization of the histological changes in ovaries of Goto-Kakizaki diabetic rats

Cristian Montero-Peña[1,4], José M. Morales-De Pando[2], Alfredo Díaz-Gómez[4], Gloria González-Medina[5], Antonio Ribelles-García[4], Gonzalo Pérez-Arana[3,4], José A. Prada-Oliveira[3,4]

[1] Don Benito Oeste Primary Care Center, Extremadura Health Service, Badajoz, Spain

[2] Puerta del Mar Hospital, Andalusian Health Service, Cadiz, Spain

[3] Biomedical Science Research and Innovation Institute (INIBICA), University of Cadiz, Cadiz, Spain

[4] Department of Human Anatomy and Embryology, Faculty of Medicine, University of Cadiz, Cadiz, Spain

[5] Faculty of Nursing and Physiotherapy. University of Cadiz, Cádiz, Spain

SUMMARY

Goto-Kakizaki (GK) rats are a useful animal model for studying type 2 diabetes mellitus (T2DM). However, this strain of rats exhibits poor fertility, so it is difficult to expand colonies. Based on previous studies, it was hypothesized that alterations in the oestrous cycle of diabetic rats are related to ovarian histology. The aim of this study was to determine the histology of the ovaries of diabetic rats compared to nondiabetic rats to understand the poor fertility of this strain of diabetic rats. An experimental study was thus conducted. Eight GK rats and eight Wistar rats were utilized. The rats were age-adjusted into two groups called "young rats" and "mature rats" at two and fourteen months of age, respectively. After sacrificing the rats, the ovaries were dissected and processed by fixation and paraffin embedding to perform the histological study. The results included the number of corpora lutea and the percentage of follicular fraction in each ovary, as well as qualitative data such as the presence of follicles in different stages of development. Our findings revealed differences between GK and Wistar rats. The ovarian histological findings were related to the presence of T2DM, polycystic ovary syndrome and poor fertility in female GK rats; the link between these pathologies is insulin resistance. Future lines of investigation into metabolic treatment, which may help improve insulin resistance, could also benefit the previously described pathologies in female GK rats.

Key words: Goto-Kakizaki rats – Type 2 diabetes mellitus – Ovary – Infertility – Ovulatory dysfunction – Polycystic ovary syndrome

INTRODUCTION

Type 2 diabetes mellitus (T2DM) is much more than a single pathology; it is a chronic disease based on a pathophysiological process consisting of tissue resistance to insulin action (WHO, 2022). T2DM continues to increase in prevalence and incidence and is a leading cause of death (Khan et al., 2020). T2DM is not a unique pathology, as there are many papers describing metabolic disorders related to insulin metabolism. These disorders involve diseases such as atherosclerosis (Ng

Corresponding author:
Dr. J.A. Prada-Oliveira. Department of Human Anatomy and Embryology, Faculty of Medicine, Plaza Fragela s/n, University of Cádiz, Cádiz 11003, Spain. E-mail: arturo.prada@uca.es

Submitted: January 17, 2023. **Accepted:** August 10, 2023

https://doi.org/10.52083/SJTL7284

et al., 2021), neuropathy (Selvarajah et al., 2019), hypothalamic-pituitary endocrine axis dysregulation (Lechuga-Sancho et al., 2006), nephropathy (Prattichizzo et al., 2021) and ocular lesions (Teo et al., 2021). Our current work focuses on the final consequences of this hypothalamic dysregulation.

For these reasons, the high interest in the research fields related to T2DM is clearly observed in the literature. Researchers need good animal models for these purposes. Thus, an excellent animal model of insulin resistance with spontaneous nonobese T2DM was developed, known as the Goto-Kakizaki rat (GK). The GK rat strain exhibits features of T2DM that are very similar to those observed in humans (Nandy et al., 2010; Akash and Chen, 2013). Among other diabetic symptoms, GK rats exhibit reproductive dysfunction. This dysfunction poses a serious problem for preclinical research in animal production facilities, which have a reduced capacity to ensure the maintenance of research activity. Colonies used to be scarce and to have low genetic turnover.

In our experience and in the literature, these rats have a shortened fertile period and reduced litter sizes (Diaz and Balibrea, 2007). One study described menstrual changes in the oestrous cycle, with a longer proestrous period and a shorter oestrous period, in six-month-old GK rats (Pinto-Souza et al., 2016). In addition, the scientific literature has recently reviewed many distinctive metabolic disorders, such as polycystic ovary syndrome (Bourgneuf et al., 2021).

Hormonal disorders that cause alterations in the reproductive cycles of GK rats are part of the hormonal physiology that affects the ovary. The main objective of this study was to perform a quantitative and qualitative analysis of ovarian histology in diabetic and nondiabetic rats. The qualitative analysis includes a description of the ovarian parenchymal architecture and the presence of germinal structures, fibrosis and adipose tissue. The quantitative analysis reveals the percentage of the follicular area between diabetic and nondiabetic rats. Our purpose is to understand the pathophysiological basis of infertility in Goto-Kakizaki (GK) rats.

METHODS

Animals and ethics

Eight female Wistar rats and eight female GK rats weighing approximately 100-120 g at an age of 5-7 weeks were provided and kept at the Experimentation and Animal Production Service of University of Cadiz (SEPA). The animal procedures were performed with the approval of the University of Cadiz Committee for the Ethical Use and Care of Experimental Animals, and every experiment was performed in accordance with relevant international guidelines and regulations for animal welfare.

Eight GK rats were randomly divided into two groups of 4 animals each. The first group was sacrificed after two months of survival. The second group was sacrificed after fourteen months of survival. The same procedure was performed with the group of 8 Wistar rats. All animals were maintained in an environmentally controlled room under standard conditions: temperature of 20-21°C, humidity of 45-65% and a 12-h:12-h light/dark cycle, and the animals were fed standard laboratory rat chow and water ad libitum.

Experimental procedures

The animals were sacrificed by isoflurane inhalation overdose. The ovaries were then dissected and fixed in Bouin's solution overnight at 4°C. Later, the samples were dehydrated, embedded in paraffin and cut into 10-µm sections with a microtome.

Histological study

Twelve serial rehydrated sections from ovary samples of each timepoint were used to study the number of corpora lutea, and the percentage of follicular fraction was assessed using haematoxylin & eosin staining. A minimum of ten fields at each point of study were analysed by a single investigator using a microscope (Olympus, GmbH. Hamburg, Germany) with a digital camera and ImageJ software. Data obtained were expressed as the number of corpora lutea/mm^2 of ovarian parenchyma or the percentage of follicular fraction.

Statistical analysis

Data are presented as the means ±SEMs. For histological analysis, the Mann–Whitney U test was conducted using SPSS v21.0 software. Statistical significance was accepted at $P<0.05$ (*).

RESULTS

Qualitative analysis

In the ovaries of young rats, no differences in ovarian sections were observed between the two groups of rats. The ovaries showed good architectural organization with many follicles in different stages of development, primordial/unilaminar follicles, multilaminar follicles and secondary follicles, as well as the corpus luteum (Fig. 1). A clearly visible increase in the corpus luteum was observed in the sixteen-month-old rats. These corpora lutea were immersed in a disorganized parenchyma. Similar follicular structures were observed in both groups of rats (Fig. 2).

Quantitative analysis

The percentage of follicular area decreased in Wistar rats as a function of age (6.3% in the young group and 3.6% in the old group). However, in aged GK rats, an increase in the follicular fraction was observed when comparing the follicular area with respect to the total ovarian area (4.7% in the young group and 5.6% in the old group). Thus, in Wistar rats, the follicular area progressively decreased, whereas in GK rats, the follicular area did not seem to decrease. In contrast, the follicular area of GK rats appeared to be increased relative to extrafollicular histology. Otherwise, the follicular area was slightly reduced in young GK rats versus Wistar rats. However, the number of corpora lutea continued the natural course of ovarian physiology progression in Wistar rats (3 in the young group and 7 in the old group) and GK rats (3 in the young group and 5 in the old group), but the increase in GK rats was less than that in Wistar rats.

DISCUSSION

The differences in oestrous disorders shown between GK rats and Wistar rats (Pinto-Souza et al., 2016) should be correlated with ovarian microanatomy. To demonstrate the histological changes in GK rats compared with a control group, ovarian morphology was studied in the Wistar rat group, with expected results and normal ovarian physiology: the follicular area was smaller and the number of corpora lutea was higher in aged rats. However, the results in GK rats are different; in this group, the follicular area was larger in aged rats, possibly related to a recent article proposing a new approach to fertility problems in correlation with the development of polycystic ovary syndrome (PCOS) in GK rats (Bourgneuf et al., 2021).

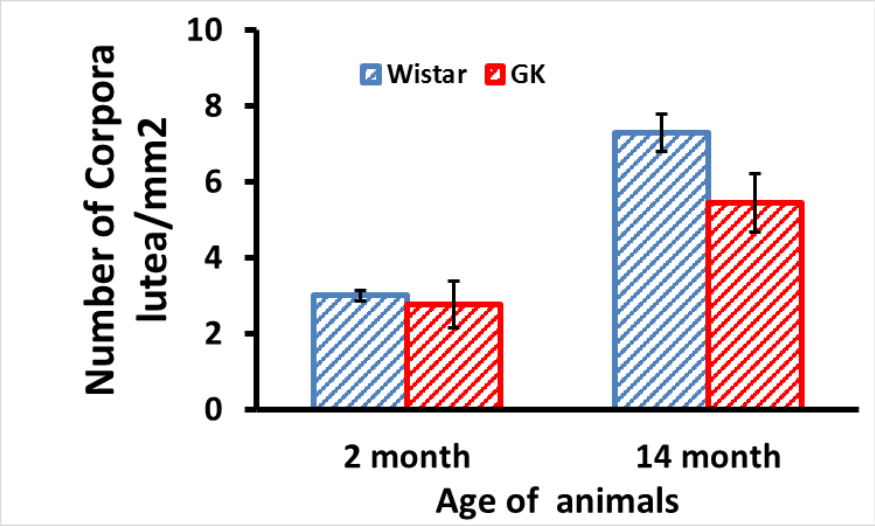

Fig. 1.- Analysis of the number of corpora lutea in Wistar (striped blue bar) and GK rats (striped red bar) at two and fourteen months after the start of the experiment. Age is represented on the X-axis, and the number of corpora lutea/mm^2 of ovarian parenchyma is represented on the Y-axis. Statistical significance at $p<0.05$ (*).

The aetiology of PCOS is still unclear. In the literature, two main physiological processes in this pathology are described: hormonal disorder and insulin resistance as a metabolic disorder (Hall, 2022).

GK rats are a good model animal to study T2DM because the insulin resistance present in these rats makes them diabetic rats. Furthermore, it should be emphasized that at this time we do not know whether hormonal disorders in female GK rats can cause molecular disorders in their future male offspring (Amaral et al., 2006).

Classically, in female subjects with PCOS, this disease has been established as the cause of metabolic complications. However, a new line of research could be formed to assess the hypothesis of the reversal of this argument based on the results of this study. Furthermore, due to the finding that 100% of GK rats developed PCOS, it may be interesting to know the specific genes that are modified in this species (Liu et al., 2015), as this could have a direct relationship with the development of PCOS and could ultimately be the origin of T2DM or vice versa. It would be interesting to contrast studies or develop new research in which the evolution of ovarian morphology and histology could be observed after prolonged periods of metabolic control.

Nevertheless, we need to incorporate a new perspective. In fertility reports about this strain, it is typical to find different methods to increase the colony when studying male rat conditions. No studies have been found about the fertility conditions or capabilities of male members of the GK rat strain. We proposed that this perspective has to be broadened. Male rats suffer from the same metabolic consequences of diabetic disorders. Thus, seminal, hormonal or sperm deficits should be considered when trying to improve fertility in these colonies. No studies have analysed fertility in male GK rats. As on many occasions, female rats initially represent the source of the infertility.

Two types of therapeutic alternatives could be assessed in female GK rats. To the best of our knowledge, there are no reports about the use of conventional insulin treatment to control glycaemic parameters. Otherwise, a hormonal-substitutive treatment related to PCOS could also be probed in colonies of this strain. The fertility rate is a parameter that provides information about the efficacy of these treatments.

Colonies of GK rats used to be complicated to maintain, which causes severe problems in diabetes research studies. The GK strain is a well-defined tool to study T2DM. As a genetically conditioned homeostasis, GK rats have been employed to study glucose- dependent peripheral resistance disorders in many research reports. Other gene-related strains, such as BB rats, are immu-

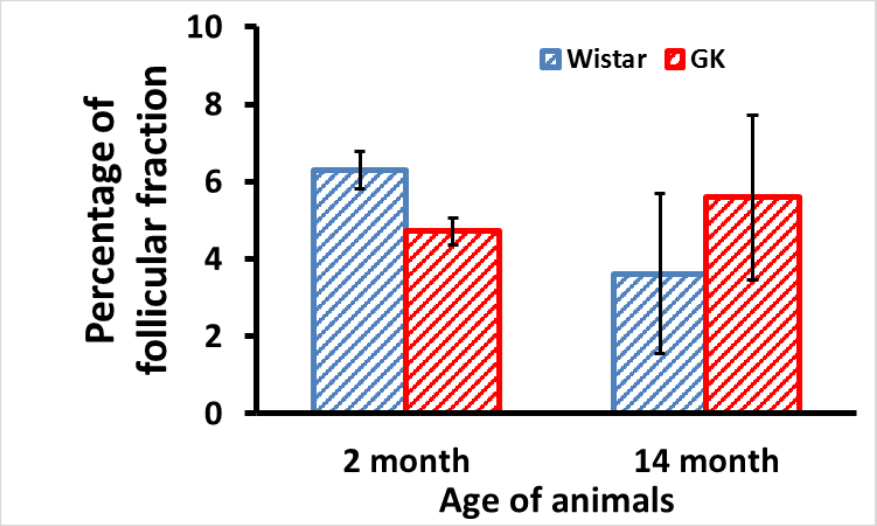

Fig. 2.- Percentage of the follicular fraction in Wistar (striped blue bar) and GK rats (striped red bar) at two and fourteen months after the start of the experiment. Age is represented on the X-axis, and the percentage of follicular fraction is represented on the Y-axis. Statistical significance at $p<0.05$ (*).

nologically conditioned to develop type 1 diabetes mellitus.

In our experience, according to several research groups in Spain using this strain of rat, the main problem in any research design is the modelling. Specifically, the sample size must be accounted for and the animals to be used must be prepared. Animal production services have difficulties maintaining requests for GK rats to meet the demands of research groups. Thus, any effort to improve the fertility of these colonies in animal production services would be welcome.

ACKNOWLEDGEMENTS

We appreciate the support of Tugiana-Peal of Becerra Association. The authors declare that the research project was supported by the University of Cádiz and Institute for Biomedical Science Research and Innovation (INIBICA).

REFERENCES

AKASH M, CHEN K (2013) Goto-Kakizaki rats: Its suitability as non-obese diabetic animal model for spontaneous type 2 diabetes mellitus. *Curr Diabetes Rev*, 9: 1-10.

AMARAL S, MORENO AJ, SANTOS MS, SEIÇA R, RAMALHO-SANTOS J (2006) Effects of hyperglycemia on sperm and testicular cells of Goto-Kakizaki and streptozotocin-treated rat models for diabetes. *Theriogenology*, 66(9): 2056-2067.

BOURGNEUF C, BAILBÉ D, LAMAZIÈRE A, DUPONT C, MOLDES M, FARABOS D, ROBLOT N, GAUTHIER C, D'ARGENT ME, COHEN-TANNOUDJI J, MONNIAUX D, FÈVE B, MOVASSAT J, DI CLEMENTE N, RACINE C (2021) The Goto-Kakizaki rat is a spontaneous prototypical rodent model of polycystic ovary syndrome. *Nature Commun*, 12: 1064.

DÍAZ J, BALIBREA J (2007) Modelos animales de intolerancia a la glucosa y diabetes tipo 2. *Nutr Hosp*, 22: 160-168.

HALL JE (2022) Trastornos del aparato reproductor femenino. In: Jameson J, Fauci AS, Kasper DL, Hauser SL, Longo DL, Loscalzo J (eds.) *Harrison. Principios de Medicina Interna*, 20th ed. McGraw Hill, Barcelona. ISBN 978-1-4562-6488-8, pp 2787-2794.

KHAN MAB, HASHIM MJ, KING JK, GOVENDER RD, MUSTAFA H, AL KAABI J (2020) Epidemiology of type 2 diabetes. Global burden of disease and forecasted trends. *J Epidemiol Glob Health*, 10(1): 107-111.

LECHUGA-SANCHO AM, ARROBA AI, FRAGO LM, GARCÍA-CÁCERES C, DELGADO-RUBÍN DE CÉLIX A, ARGENTE J, CHOWEN JA (2006) Reduction in the number of astrocytes and their projections is associated with increased synaptic protein density in the hypothalamus of poorly controlled diabetic rats. *Endocrinology*, 147: 5314-5324.

LIU T, LI H, DING G, WANG Z, CHEN Y, LIU L, LI Y, LI Y (2015) Comparative genome of GK and Wistar rats reveals genetic basis of Type 2 Diabetes. *PLoS One*, 10(11): e0141859.

NANDY A, WANG X, ACCILI D, WOLGEMUTH DJ (2010) The effect of insulin signaling on female reproductive function independent of adiposity and hyperglycemia. *Endocrinology*, 151: 1863-1871.

NG ACT, DELGADO V, BORLAUG BA, BAX JJ (2021) Diabesity: the combined burden of obesity and diabetes on heart disease and the role of imaging. *Nat Rev Cardiol*, 18(4): 291-304.

PINTO-SOUZA AR, FIRETTO C, PEREZ-ARANA G, LECHUGA-SANCHO AM, PRADA-OLIVEIRA JA (2016) Differences in the estrous cycles of Goto-Kakizaki and Wistar rats. *Lab Anim*, 45: 143-148.

PRATTICHIZZO F, DE CANDIA P, CERIELLO A (2021) Diabetes and kidney disease: emphasis on treatment with SGLT-2 inhibitors and GLP-1 receptor agonists. *Metabolism*, 120: 154799.

SELVARAJAH D, KAR D, KHUNTI K, DAVIES MJ, SCOTT AR, WALKER J, TESFAYE S (2019) Diabetic peripheral neuropathy: advances in diagnosis and strategies for screening and early intervention. *Lancet Diabetes Endocrinol*, 7(12): 938-948.

TEO ZL, THAM YC, YU M, CHEE ML, RIM TH, CHEUNG N, BIKBOV MM, WANG YX, TANG Y, LU Y, WONG IY, TING DSW, TAN GSW, JONAS JB, SABANAYAGAM C, WONG TY, CHENG CY (2021) Global prevalence of diabetic retinopathy and projection of burden through 2045: Systematic review and meta-analysis. *Ophthalmology*, 128(11): 1580-1591.

WORLD HEALTH ORGANIZATION (2022) Diabetes Fact sheet. (https://www.who.int/en/news-room/fact-sheets/detail/diabetes). Accessed May, 19.

The first report of using endoscopy to evaluate the structure of the internal nasal valve and the measurement of internal nasal valve angle value in Vietnamese people

Nguyen Trieu Viet, Nguyen Thi Ngoc Lien

Can Tho University of Medicine and Pharmacy, Can Tho City, Vietnam

SUMMARY

The objective of this work was to investigate the structural formations and angle of the internal nasal valve (INV) by using nasal endoscopy. A cross-sectional-description study was conducted on one hundred and thirty-nine students of the University of Medicine and Pharmacy without the complaint of chronic nasal obstruction. They were examined the internal nasal areas by using endoscopy two times: before spraying decongestant, and after 15-30 minutes spraying of the decongestant into the nasal cavity to identify the types of the internal nasal valve according to Miman's classification. The nasal valve angle value was determined by using Autocad software version 2007. The study was done at Can Tho University Hospital. Sharp angle type accounted for 32.01%, blunt angle type accounted for 12.23%, convex caudal border type accounted for 5.04%, concave caudal border type accounted for 5.04%, angle occupied by the septal body accounted for 34.17%, and twisted caudal border type accounted for 11.51% in our study, the average angle of 26°.8 ± 9°.28, with the smallest angle being 9° and the largest angle being 51°. When comparing the rate of internal nasal valve formation for each time in our study and that of Miman, we recognized that there is a difference among rates. Our nasal angle values were similar to those of Asians and different from those of Caucasians. By using endoscopy, we can easily determine the morphology of the internal nasal valve and measure the angle value of the internal nasal valve by using Autocad software version 2007.

Key words: Internal nasal valve – Angle – Nasal morphology – Nasal endoscopy

INTRODUCTION

The nasal valve plays a significant role in nasal airflow. During an examination of a patient with nasal obstruction, a common presenting symptom in otolaryngology (ORL) practices, it is essential for otolaryngologists not only to consider the nasal valve but also to understand a comprehensive evaluation to this area (Clark et al., 2018; Gelardi and Ciprandi, 2019).

The collapse of the internal nasal valve is one of the major causes of nasal airflow obstruction. The INV is a noticeable area for ORL surgeons to correctly evaluate before rhinoplasty and/or sep-

Corresponding author:
Nguyen Trieu Viet. Can Tho University of Medicine and Pharmacy, Can Tho City, Vietnam. Phone: +84 913708007. E-mail: ntviet@ctump.edu.vn

Submitted: July 30, 2023. **Accepted:** August 20, 2023

https://doi.org/10.52083/ETEL3025

toplasty surgery for patients with nasal obstruction and has a role in structural nasal obstruction separate from other anatomical pathologies, for example allergy (Melati et al., 2023; Shafik et al., 2020). Any further narrowing of INV will have a considerable impact on sinus and middle ear pathology (Murthy et al., 2013).

The internal nasal valve is the narrowest portion of the nasal cavity, located approximately 1.3 cm from the nares, and corresponds to the region under the upper lateral cartilages, bound medially by the dorsal septum, inferiorly by the head of the inferior turbinate, and laterally by the upper lateral cartilage (Murthy et al., 2013; Rhee et al., 2010). The average angle of the INV in a Caucasian population ranges from 9° to 15°, and inter-racial variance is well recognized, in part due to the morphology of the nose. Collapse of the valve is thought to obey Bernoulli's principle, and as such is a common cause of nasal obstruction (Gelardi and Ciprandi, 2019). In doing surgery for the nasal valve area, all the related structures (head of the inferior turbinate, nasal septum...) should be considered carefully and evaluated (Beriat et al., 2010).

Many tools have been used in assessing nasal resistance and INV, including rhinomanometry and acoustic rhinometry. However, they have limits that lack reliability and require expensive equipment (Shafik et al., 2020). Nasal endoscopy, either rigid or flexible, can allow for examination of the nasal airway and may indicate evidence of septal deviations in all parts, adenoid hypertrophy, or nasal tumors, mucosal inflammation, including edema, polyps, crusting, and rhinorrhea (Patel and Most, 2020; Schuman and Senior, 2018). The nasal endoscopic evaluation method is a cost-effective way to examine the internal nasal valve angle and is easy to access without side effects. In addition, this method provides the opportunity to see the whole nasal structures, accompanying their relations on three-dimensional images (Beriat et al., 2010).

Until now, there has been no published research in Vietnam on aspects such as nasal morphology assessment or nasal valve angle measurement. Therefore, this study aims to evaluate the usefulness of endoscopy in determining the structure of the internal nasal valve, to measure the INV angle value using AutoCAD software 2007 in the Vietnamese population, and to compare the results with those of Miman's study on Caucasians.

MATERIALS AND METHODS

This descriptive cross-sectional study was performed on 139 medical students with 278 nasal cavities from Can Tho University of Medicine and Pharmacy at Can Tho University Hospital, from November 2020 to December 2021. This study was accepted by ethical board of Can Tho University of Medicine and Pharmacy (code 359/20ĐHYD-HĐ). The patients provided their consent for the study.

Inclusion criteria were included the medical students of Can Tho University of Medicine and Pharmacy did not have any complaint of chronic nasal obstruction over 3 months. Excluding criteria were as follows: students under 18 years old; suffering an operation of nasal septum, inferior turbinate or nasal dorsum in advance, including traumatic nasal reconstruction; having acute sinusitis.

Research content

A hundred and thirty-nine students participating in the study were examined by endoscopy in each naris twice after determining that they had normal vital signs ranges. The vasoconstrictor used was Rhinex containing 0.5% naphazolin. A 4-mm 0 Karl Storz endoscope was used for endoscopic examinations. Digital images were taken with a Karl Storz camera and were analysis by using Windows Photo Viewer to identify the shape of INV and measurements of the angle. The internal nasal valve angle value was measured by using AutoCad 2007 software, processing the pictures taken on nasal endoscopy. The endoscopic method and location of image recording of the internal nasal valve area to analysis was performed as described by Miman. The types of the structural formation of the internal nasal valve were determined through endoscopic examination according to Miman's classification: convex, concave, sharp angle, blunt angle, twisted caudal border, and angle occupied by the septal body (Miman et al., 2006).

In the first time, the participants were examined by the endoscopy without nasal decongestant. Then the results were saved in two types of format. One was in static state, saved in .jpg; and the other was in kinetic state, saved in .mpg.

In the second time, the participants were examined again with nasal decongestant, 2-3 sprays over 15 minutes and the results were saved in 2 types of information like above. When examining by the endoscopy, the participants did not breathe to ensure that the lateral nasal wall was stable. The scope was put in parallel to the caudal border of the upper lateral cartilage to take the image of the internal nasal valve. The IVN angle value was measured by using Autocad software 2007 in many steps (see steps 1-3). The author of this study conducted these steps based on the captured images on nasal endoscopy.

The results were processed by SPSS 18.0.

RESULTS

There were 61 male (43.9%) and 78 female (56.1%) subjects in the data presented in Table 1, with an average age of 21.2 ± 1.4 years old. The youngest was 18 and the oldest was 26.

INV was classified into 6 different types according to the classification of Miman. The angular form formed by the septal body had the highest number, next followed by sharp angle, blunt angle, and twisted caudal border. Concave type and convex type were the same. The above results also showed that the number of septal body was large enough to form the angular structure formed by the septal body (n = 95, 34.17%) (Table 2).

The illustration of the nasal valve types in participants of this study (color image) and Miman's simulation (black and white) were showed in Figs. 1-6.

The INV angle was 26.75 ± 8.98 for the right nasal cavity and 26.85 ± 9.56 for the left one (Table 3).

A total of 117 internal nasal valve angles were determined out of a total of 278 sides of the nasal cavity surveyed, the ratio was 117/278 (42.1%). The results of the angular value of 117 internal nasal valves determined in this study are 26.80± 9.28°. The smallest is 9°; the largest is 51°.

Table 1. Characteristics before examination.

Gender	Male	Female
Number of participants	61	78
Rate	43.9%	56.1%
The average age	*21.2 ± 1.4*	

Table 2. The number of endoscopic internal nasal valve types according to the classification of Miman.

Types	**Sharp angle**	**Blunt angle**	**Concave caudal border**	**Convex caudal border**	**Angle occupied by the septal body**	**Twisted caudal border**
Right side	44	21	7	5	45	17
Left side	45	13	7	9	50	15
Total %	89 32.01%	34 12.23%	14 5.04%	14 5.04%	95 34.17%	32 11.51%

Table 3. The value of the internal nasal valve angle according to the form of the internal nasal valve.

		Sharp angle	**Concave caudal border**	**Convex caudal border**	**Total**
Right	Mean ± SD	26.59 ± 9.26	17.71 ± 8.08	40.80 ± 7.76	26.75 ± 8.98
	N	44	7	5	56
Left	Mean ± SD	26.73 ± 9.10	20.43 ± 7.39	32.44 ± 13.59	26.85 ± 9.56
	N	45	7	9	61
Internal nasal valve angle value of the study					26.80 ± 9.28°
					N=117

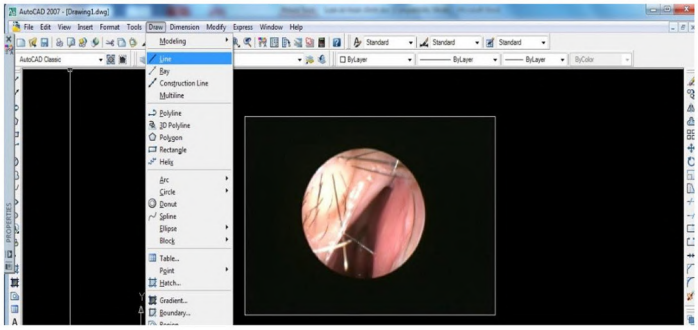

Step 1. Using the autocad software 2007 to determine the internal nasal valve angle

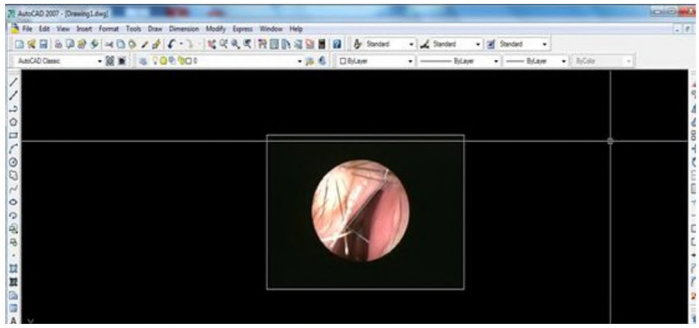

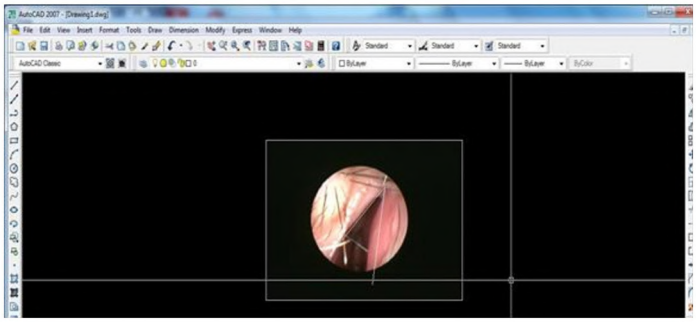

Step 2. Use the line command to define the second edge of the corner by dragging a line from the top of the corner along the vertical of the partition

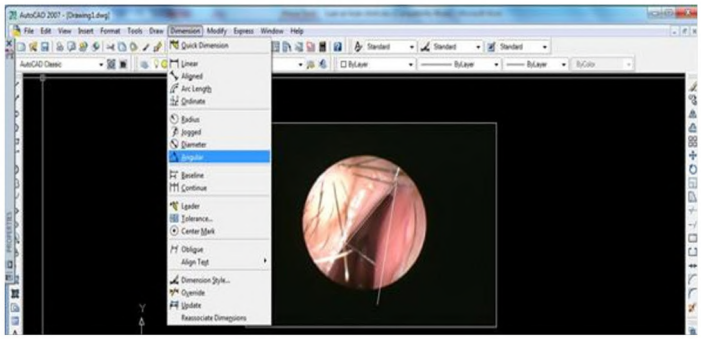

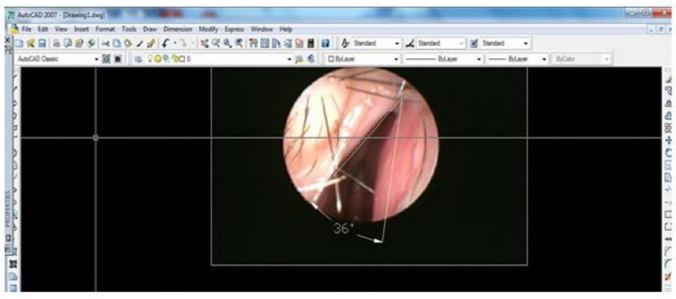

Step 3. Use the angular command to determine the internal nasal valve angle value

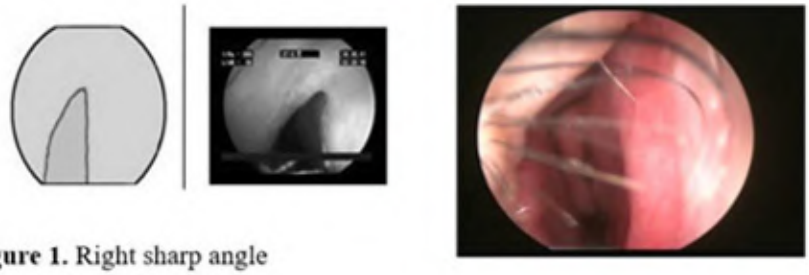

Figure 1. Right sharp angle

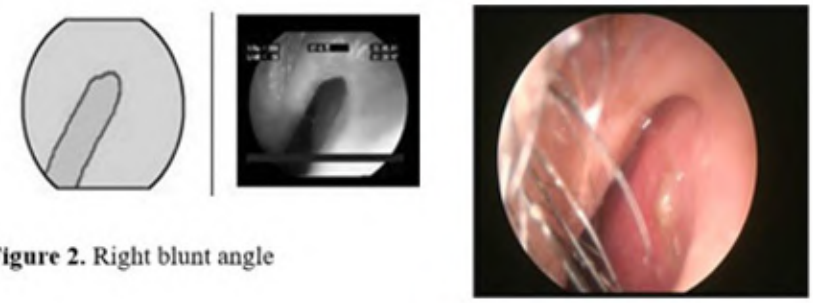

Figure 2. Right blunt angle

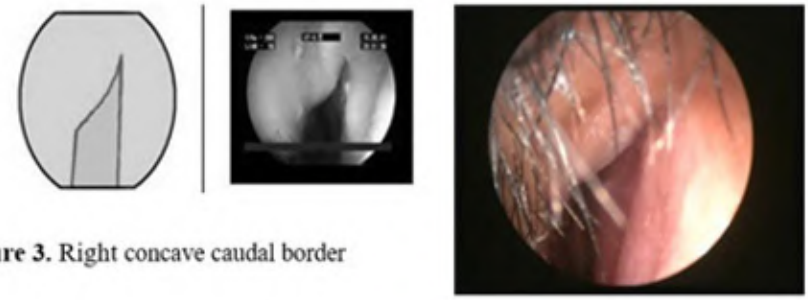

Figure 3. Right concave caudal border

DISCUSSION

Until now, the classification of the internal nasal valve morphology performed by Miman et al. in 2006 is a unique study that has been published and quoted in many international reports. Miman noted the relation between the caudal border of the upper lateral cartilage and the nasal septum to mention the septal body to classify the various shapes of the internal nasal valve (Miman et al., 2006). The septal body is an erectile structure, observed in CT-scan and MRI. It has not been mentioned carefully in rhinology in past decades.

In our study, in the relation between the septal body and the formation of the angle, the septal body was determined as a notable anatomical landmark in the internal nasal valve area. The percentage of the possibility that a big-enough septal body may appear to form the type of internal nasal valve corresponding with the angle of this type was 34.2%.

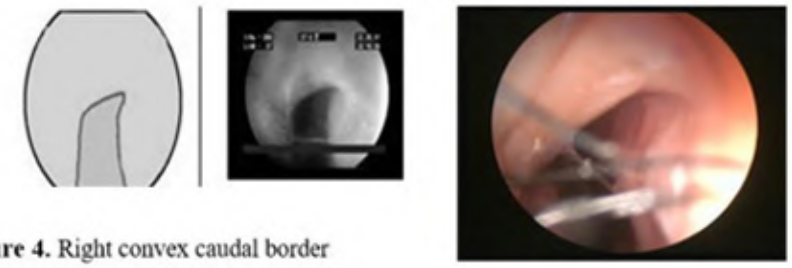

Figure 4. Right convex caudal border

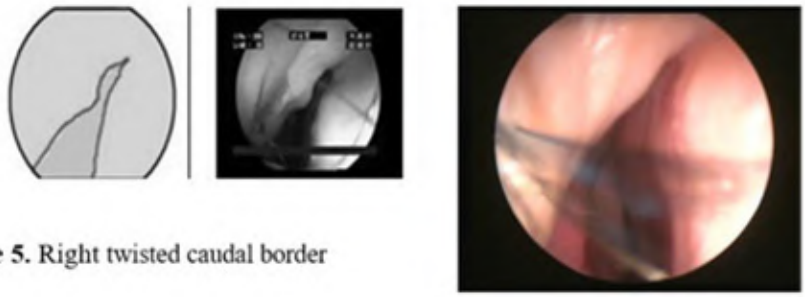

Figure 5. Right twisted caudal border

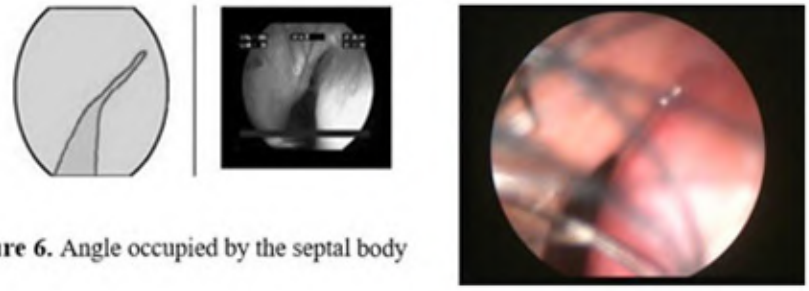

Figure 6. Angle occupied by the septal body

The results of our study on the ratio of internal nasal valve types compared with the corresponding ratio in Miman's study are different, which can be explained by the structure of the nasal pyramid in Vietnamese people being markedly different from that of European nasal pyramids in Miman's study. This difference, according to the study of Nguyen Thanh Van, shows that the Vietnamese nose has the characteristics of Asian people: low nose, high concave nose bridge, and bulging nose wings. Vietnamese noses are shorter, lower and less protruding than Caucasian noses (Van et al., 2016). In our study, we found that there was a big difference in the rate of caudal torsion of 11.6% compared with 1.6% in Miman's study. This is due to overlapping of the superior alar cartilage with the lower alar cartilage appearing in 20% of cases according to Nguyen Thanh Van's study (Van et al., 2016).

Miman's research did not provide a common angle value for all nasal valves measured. Miman divided them into 3 groups with corresponding results for 3 different types of nasal valves: sharp

angle, concave type, and convex type. The angle value of the nasal valve in twisted type, blunt type, and angles formed by the septum could not be determined (Miman et al., 2006). In our study, we also did not determine the angle value of the nasal valve in blunt angles, twisted type, and angles formed by the septum because the vertex and the precise angle could not be determined in these shapes to measure the angle value. We determined the angle value in each sharp angle, concave type, and convex type of internal nasal valve angle and the common value for all three groups as above.

Ichimura did not calculate each type separately, but only presented the average results for males and females and the overall result for both genders as 28.9± 6.3°, with a minimum of 16° and a maximum of 45° (Ichimura et al., 1997). Our result was 26.8 ± 9.28°, with a minimum of 9° and a maximum of 51°. Comparing the research results, we found that ours were similar to those of Ichimura. This could be explained by the similarity of race – yellow-skinned Asians with similar nasal structures.

Regarding the angle value of Caucasians, many references mention that the value is 10-15°, which Mink presented in 1903. However, until now, there has been no complete study or interpretation of the origin of this information on the internal nasal valve angle value. Therefore, with the results we obtained on the angle value of the nasal valve for the first time studied in a group of Vietnamese people without chronic nasal obstruction complaints, and the results from the study of Ichimura, the angle value of the nasal valve in Asians could be considered double that of Caucasians.

Methods used to determine the value of an angle: Miman's study used Scion Image for Windows software to determine the value of the internal nasal valve angle. Meanwhile, Ichimura used conventional geometrical measurements on printed endoscopic images of the clear nasal valve.

With the function of drawing and measuring all images like conventional geometric tools, Autocad software is widely used in measuring and determining structural forms, and calculating values of angles. Therefore, in this study, we used Autocad software version 2007 to measure and determine the value of the internal nasal valve angle.

This is the first study to apply this software to determine the value of the internal nasal valve angle made in Vietnam and around the world. Actual measurement and processing of images recorded directly from the endoscopic device without editing shows that this software provides a true image of the internal nasal valve area that needs to be determined. In addition, the software's concentric magnification or reduction function helps to enlarge or reduce the concentricity of the image without changing the angle value, so it is easy to measure and determine the exact angle value. In addition, the function of automatically determining the equivalent length of the two sides of the angle to be measured when using the "angular" command ensures the exact value of the angle being measured.

CONCLUSION

The results of the types of internal nasal valves in 139 patients based on Miman's classification included sharp angle (32.01%), blunt angle (12.23%), convex caudal border (5.04%), concave caudal border (5.04%), angle occupied by the septal body (34.17%), twisted caudal border (11.51%). The internal nasal valve angle value was assessed in 139 asymptomatic individuals using endoscopic examination and Autocad 2007 software, offering an average angle value of 26°.8± 9°.28, with the smallest angle being 9° and the largest angle being 51°. This value were similar to that of Japanese and two times larger than that of Caucasians. Using the endoscopy and Autocad software version 2007 can easily determine the morphology and measure the angle value of internal nasal valve.

DECLARATIONS ETHICS

This study was accepted by ethical board of Can Tho University of Medicine and Pharmacy (code 359/20ĐHYD-HĐ).

REFERENCES

BERIAT GK, KARADAĞ D, KOCATÜRK S (2010) The value of computed tomography in evaluation of internal nasal valve angle. *Trakya Universitesi Tip Fakultesi Dergisi*.

CLARK DW, SIGNORE AGD, RAITHATHA R, SENIOR BA (2018) Nasal airway obstruction: Prevalence and anatomic contributors. *Ear Nose Throat J*, 97(6): 173-176.

GELARDI M, CIPRANDI G (2019) The clinical importance of the nasal valve. *Acta Biomedica Atenei Parmensis*, 90(2-S).

ICHIMURA K, ISHIZUKA T (1997) Measurement of the so-called "Nasal Valve" in Japanese subjects. *J Rhinol*, 4(1): 26-28.

MELATI T, REKSODIPUTRO MH, KOENTO T, ILJANTO S (2023) Analysis of internal nasal valves shapes and angle due to nasal obstruction in Asian nose. *eJournal Kedokteran Indonesia*, 10(3): 212-218.

MIMAN MC, DELIKTAŞ H, OZTURAN O, TOPLU Y, AKARÇAY M (2006) Internal nasal valve: revisited with objective facts. *Otolaryngol Head Neck Surg*, 134(1): 41-47.

MURTHY VA, REDDY RR, PRAGADEESWARAN K (2013) Internal nasal valve and its significance. *Indian J Otolaryngol Head Neck Surg*, 65(Suppl 2): 400-401.

PATEL P, MOST SP (2020) Functionally crippled nose. *Facial Plast Surg*, 36(1): 66-71.

RHEE JS, WEAVER EM, PARK SS, BAKER SR, HILGER PA, KRIET JD, MURAKAMI C, SENIOR BA, ROSENFELD RM, DIVITTORIO D (2010) Clinical consensus statement: Diagnosis and management of nasal valve compromise. *Otolaryngol Head Neck Surg*, 143(1): 48-59.

SCHUMAN TA, SENIOR BA (2018) Treatment paradigm for nasal airway obstruction. *Otolaryngol Clin North Am*, 51(5): 873-882.

SHAFIK AG, ALKADY HA, TAWFIK GM, MOHAMED AM, RABIE TM, HUY NT (2020) Computed tomography evaluation of internal nasal valve angle and area and its correlation with NOSE scale for symptomatic improvement in rhinoplasty. *Braz J Otorhinolaryngol*, 86(3): 343-350.

VAN NT, VINH LG, ANH TN, KHOA TD (2016) Anatomical features of structural applications cartilage structure of the nose tip. *Vietnam Med J*, 441(1): 21-24.12.

Ossification pursue of the lower ends of radius and ulna and age determination in a sample of Egyptian population between 12 and 19 years

Ahmed F. AlDomairy[1], Ashraf Kotb[2], Manar A. Eldesouky[3], Mohamed A. Yehia[4], Yasmine H. Eisa[5], Ahmed T. Farag[6], Mahmoud M. Assem[7], Radwa M. Elsabban[8]

[1] Dept. of Anatomy and Embryology, [2] Dept. of Physiology, [3] Lecturer of Pediatrics, [4] Lecturer of Forensic Medicine and Clinical Toxicology, [5] Lecturer of Public Health and Preventive Medicine, [6] Lecturer of Orthopedic Surgery, [7] Lecturer of Radiology, [8] Lecturer of Anatomy and Embryology, Faculty of Medicine, October 6 University, 6th of October City, Giza, Egypt

SUMMARY

The epiphyseal plates of cartilage of ulna and radius is responsible for bone elongation, the fusion of their distal ends and bodies is used for age estimation. Variation exists due to many factors including ethnicity; accordingly, it is important to create a national profile for age determination using an affordable easy method. The aim of the work was to follow up the ossification of the lower end of the radius and the ulna in the Egyptian population between 12-19 years using X-ray, validating the use of Greulich and Pyle atlas. 197 subjects (103 males and 94 females) aged between 12-19 years were included. Skeletal age was determined using a plain X-ray on the lower end of the radius and the ulna comparing it to Greulich and Pyle's atlas, and also to chronological age.

In males, the mean of chronological age, skeletal age, and the difference between them were 15.35, 15.53 and +0.18 years respectively. In females, the ages were 14.77, 14.92 and +0.15. There was high correlation in all age groups. Examination of the lower end of the radius and the ulna is a suitable method for age detection in Egyptians between the ages of 12-19 years old.

Key words: Egyptian – Greulich and Pyle – Ossification – Radius and ulna – Skeletal age

INTRODUCTION

Like most of the upper limb bones, both the ulna and the radius develop from an intrauterine cartilaginous model, which is the precursor of the future bone. The cartilage is formed of chondrocytes and a collagen-rich matrix, and is surrounded by the perichondrium, formed of connective tissue (Hunziker et al., 2014). The innermost layer of the perichondrium differentiates into osteoblasts, which secrete bone matrix forming a perichondral bony collar around the cartilage model. At the same time, ossification starts within the body of the cartilage model by a primary ossifica-

Corresponding author:
Dr. Ahmed F. AlDomairy. Department of Anatomy and Embryology, Faculty of Medicine, October 6 University, 6th of October city, Giza, 12566 Egypt. Phone: 00201005208027. E-mail: aaldomairy@o6u.edu.eg / aaldomairy@hotmail.com

Submitted: July 14, 2023. **Accepted:** August 23, 2023

https://doi.org/10.52083/IMGK7845

tion center leading to its transformation into bone (Hellings et al., 2016).

The primary ossification centers of both radius and ulna appear in the eighth week of fetal life. Unlike the proximal end of the ulna, which develops from two secondary centers of ossification, and the occasional radial tuberosity ossification center, the distal ends of both bones develop from a single secondary ossification center for each of them. Ossification begins in the distal end of the radius by the end of the first year of life. As regards that of the ulna, it appears as late as the fifth and sixth years in females and males respectively (Standring, 2020).

An epiphyseal plate of cartilage persists between the ossified body and ends. This cartilage is responsible for the longitudinal growth of the bone by chondrocyte proliferation and matrix secretion (Dupuis et al., 2019). The cartilage is gradually transformed into bone, thins with age, and is finally completely replaced by bone tissue (Blumer, 2021). The compromisation between cellular hypertrophy, removal of excess of unwanted tissues by apoptosis and autophagy regulate this process (Shapiro et al., 2005).

Broadly speaking, the fusion between the distal ends of both bones and their shafts begins in females at the age of thirteen or fourteen years, and in males at the age of fifteen or sixteen years (Hassan et al., 2016; Ottow et al., 2022). The distal ends of both bones completely fuse with their shafts at the age of the seventeenth year in females and the eighteenth to the nineteenth year in males. (Standring, 2020).

As expected, ethnic variation appears in the process of ossification. For example, using a five ossification-stage classification, Al-Khater et al. (2020) noticed an earlier appearance of ossification of the distal end of the ulna in females in the third year of life. Baumann et al. (2009) concluded that a complete union of the lower end and the shaft with a visible epiphyseal scar in the radius or the ulna in the males and the indiscernible scar in the female radius points to a fourteen-year-old subject or older, while the disappearance of the scar in the male radius proves that he reached the age of eighteen years.

Age estimation has always been a matter of interest in both medical and criminal cases. In pediatric practice, age estimation is important for the assessment of normal growth and the detection of any abnormalities (Gilsanz and Ratib, 2005). On the other hand, in different countries, abandoned individuals of unknown age, illegal age falsification at marriage, crimes and even sports competitions are not uncommon practices. Accordingly, there is an increasing demand for a reliable –yet affordable– method of age determination.

In 1959, Greulich and Pyle developed their famous Radiographic atlas of skeletal development of the hand and wrist. Despite the long duration, and because of its simplicity and rapid application, the atlas has been found to be more suitable for practice in comparison to other methods (Horter et al., 2012), the most used SA reference worldwide (Gilsanz and Ratib, 2005) and even figured as the ideal bone age detection method (Daneff et al., 2015).

Many trials have been made to assess the reliability of different methods of ossification detection and age determination using wrist scans. MRI (Tomei et al., 2014; Schmidt et al., 2014; Serin et al., 2016; Laor et al., 2016), CT scan (Ekizoglu et al., 2016) and Ultrasonography (Schmidt et al., 2013; Daneff et al., 2015; Hajalioghli et al., 2015) have been all examined. However, the relatively high cost of these methods has eliminated their use in developing countries.

Bone ossification, and accordingly SA estimation, may be affected by many genetic as well as environmental factors: race (Zhang et al., 2009), ethnics (Patil et al., 2012; Zabet et al., 2015), socioeconomic status (Schmeling et al., 2006), hormone levels (Kwon et al., 2017; Zhao et al., 2020) and nutritional habits (Nicholas et al., 2019) are all known to be important factors for variability in ossification and age estimation results. That is why it is important to provide a profile of a correlation between chronological age (CA) and skeletal age (SA) based on known individual ages.

The aim of the present work is to follow up the ossification of the lower ends of the radius and the ulna in the Egyptian population between 12-19 years using plain X-ray as an available, afford-

able, and easy method, exploring the coincidence between CA and SA, and to detect the correspondence of GP atlas in ossification and age determination in Egyptian population.

MATERIALS AND METHODS

197 healthy subjects (103 males and 94 females) aged between 12-19 years were included in the present study. Approval of this study was obtained from Institutional Ethics Committee. The subjects were outpatient individuals checking themselves after simple injuries. All the cases of fractures were excluded. A careful history was taken to exclude individuals with chronic diseases or developmental disorders. Their exact CA was obtained by identity proof, as well as written consent from the parents. The age range of the subjects (12-19) was detected to follow the process of ossification of the lower ends of the radius and the ulna from the beginning until its complete fusion (Serin et al., 2016); it also coincided with the maximum ages used in GP atlas (19 years in males and 18 years in females). The subjects were divided according to their age into 7 groups in males and 6 in females, each consisting of a chronological year (12-12.99, 13-13.99, etc.) (Table 1).

As earlier reports insured the absence of significant difference in bone maturation of both wrists (Hackman and Black, 2012), and to harmonize with most of the previous studies, an anteroposterior plain X-ray was done on the left forearm and hand. The left side is often frequently used due to the larger number of right-handed persons, making it more vulnerable to injury. The X-ray were obtained in October 6 University hospital – Giza – Egypt.

The fusion of the epiphysis of the lower ends of the ulna and the radius was inspected. SA was concluded using GP atlas, which consists of a series of standard plates to compare the examined radiograph with the most similar item in the atlas. This was considered the SA of the radiograph. In some cases, the examined X-ray inset between two plates specified the age of the radiograph, which was considered a fairly practice (Greulich and Pyle, 1959).

The same investigator examined all the X-ray films twice two weeks apart. Corresponding results were directly included in the research. Those who did not match (11 cases) were re-examined after two weeks, and they matched one of the previous results. Each time, the CA of the subject and the previous results were hidden. This protocol was previously used by Safer et al. (2015).

The SA was then compared to the CA of the subject, and the results were analyzed using Statistical Package for the Social Science computer software (SPSS, version 20.0, SPSS Inc., Chicago, IL, USA).

RESULTS

This study was conducted on 197 subjects (103 males & 94 females) ranging between 12 and 19 years old. The results were arranged according to the CA groups and compared with the estimated SA according to GP atlas (Figs. 1-2). The differences between both values were calculated, where the positive values indicate that the mean of the SA exceeds the CA, while negative values indicate delayed SA compared to CA.

Table 1. Showing the age intervals groups, and the number of subjects of each interval.

Males		Females	
Age	**No**	**Age**	**No**
12 – 12.99	18	12 - 12.99	18
13 – 13.99	14	13 - 13.99	20
14 – 14.99	10	14 - 14.99	14
15 – 15.99	21	15 -15.99	13
16 – 16.99	14	16 - 16.99	16
17 – 17.99	11	17 - 17.99	13
18 -18.99	15		
Total	**103**	**Total**	**94**

The mean of the CA in males was 15.35 (12.08-18.87) years, whereas the mean of the SA was 15.53 (11-19), with a mean difference between them + 0.18. There was a low heterogeneity with no statistically significant differences in all age groups ($P < 0.05$). The mean difference between the CA and SA ranged between -0.07 years (between 13-13.99 years old) to +0.38 years (between 17-17.99 years old) (Table 2 and Fig. 3).

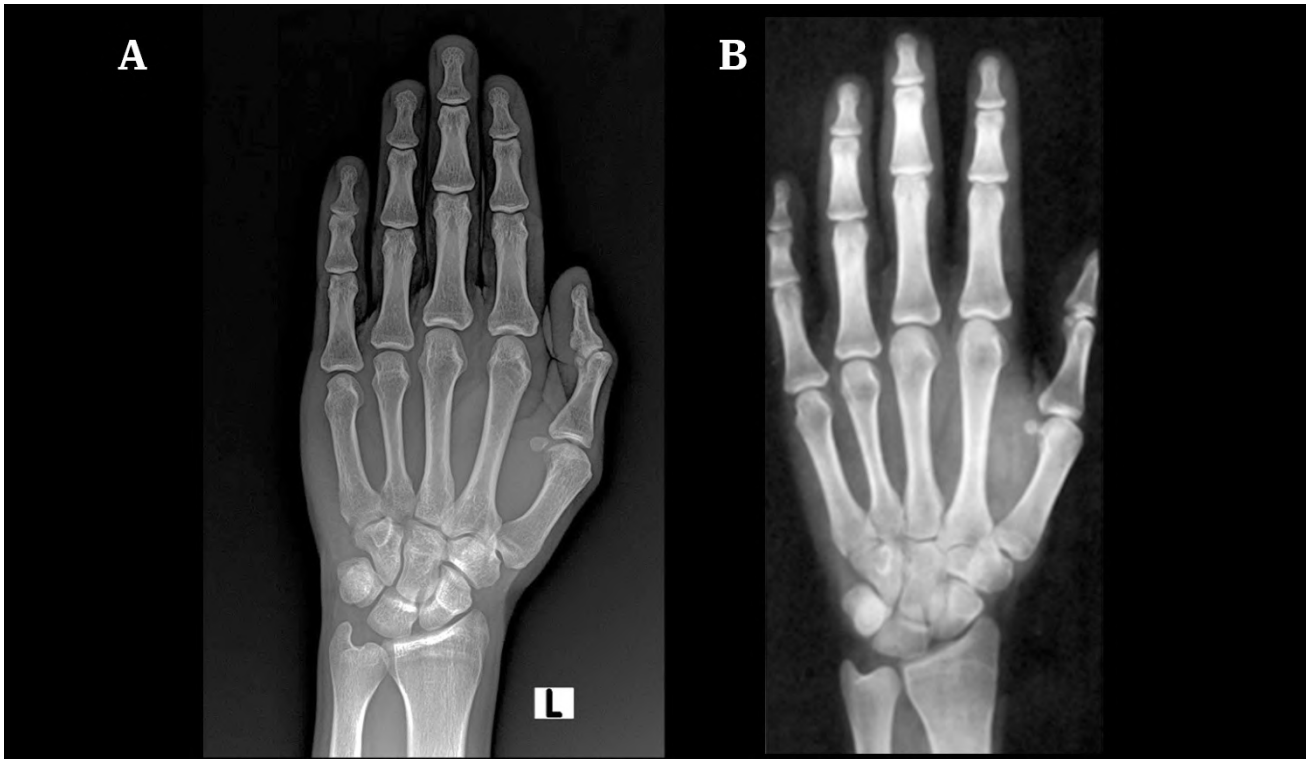

Fig. 1.- A) Hand radiograph of a male subject (CA= 12.13 years) matched with **B)** male standard 22 image in GP atlas (SA= 12.5 years).

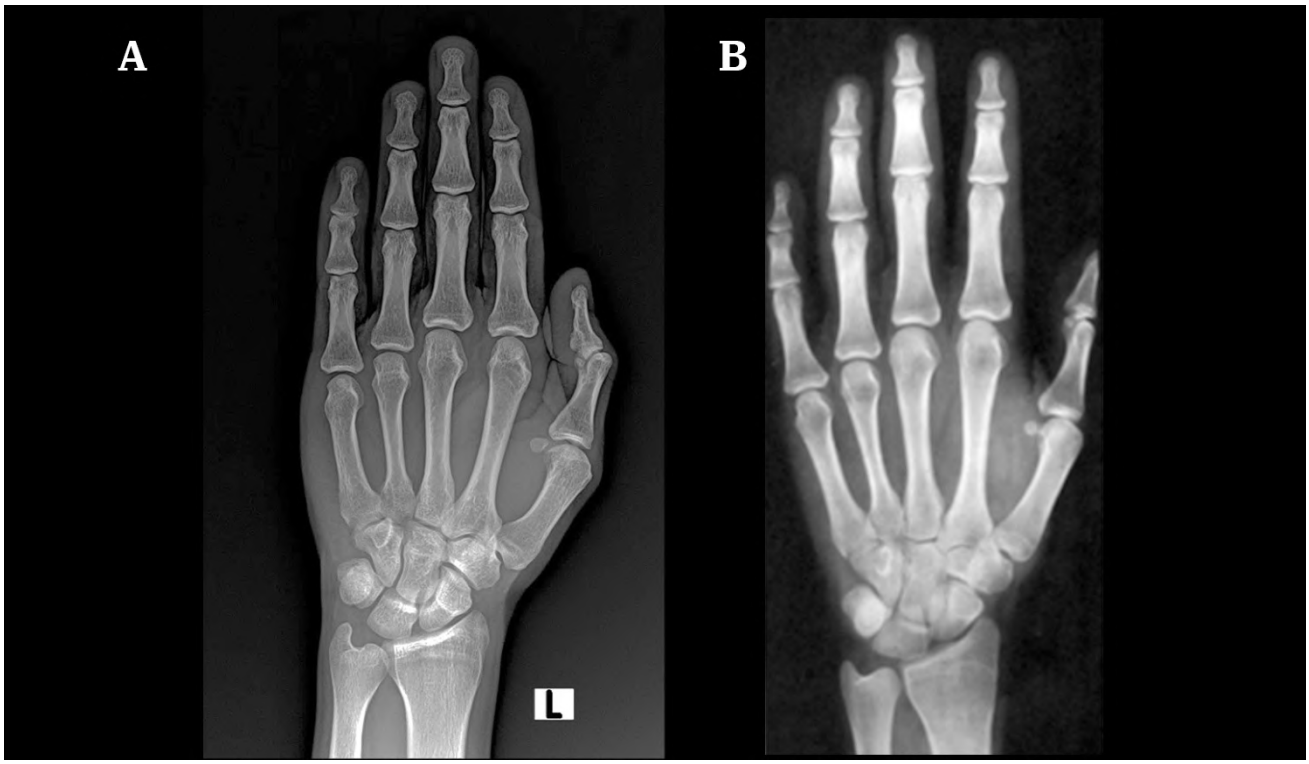

Fig. 2.- A) Hand radiograph of a female subject (CA= 16.23 years) matched with **B)** female standard 26 image in GP atlas (SA= 17 years).

The mean of CA in females was 14.77 (12.13-17.82) years and the mean of their SA was 14.92 (11-18) years, with a mean difference between them + 0.15. Again, no statistically significant differences were found in any age group ($P < 0.05$). The mean difference between the CA and SA ranged between -0.08 years (at 13-13.99 years old) to +0.28 years (at 16-16.99 years old) (Table 3 and Fig. 4).

Table 2. Mean, standard deviation, minimal and maximal CA and SA and difference between them in different age groups in males.

Age	No	CA				SA				SA-CA	
		Mean	SD	Min	Max	Mean	SD	Min	Max	Mean	SD
12 – 12.99	18	12.44	0.38	12.08	12.83	12.58	0.84	11.00	14.00	+ 0.14	0.24
13 – 13.99	14	13.50	0.68	13.15	13.88	13.43	0.76	12.00	15.00	- 0.07	0.40
14 – 14.99	10	14.50	0.72	14.24	14.90	14.60	0.84	13.00	16.00	+ 0.1	0.56
15 – 15.99	21	15.46	0.46	15.03	15.91	15.60	0.86	14.00	17.00	+ 0.14	0.74
16 – 16.99	14	16.47	0.52	16.12	16.94	16.71	0.91	15.00	18.00	+ 0.24	0.62
17 – 17.99	11	17.48	0.56	17..16	17.82	17.86	0.95	16.00	19.00	+ 0.38	0.58
18 -18.99	15	18.40	0.64	18.09	18.87	18.77	0.42	18.00	19.00	+ 0.37	0.47
Total	**103**	**15.35**	**2.03**	**12.08**	**18.87**	**15.53**	**2.27**	**11**	**19**	**+ 0.18**	**0.65**

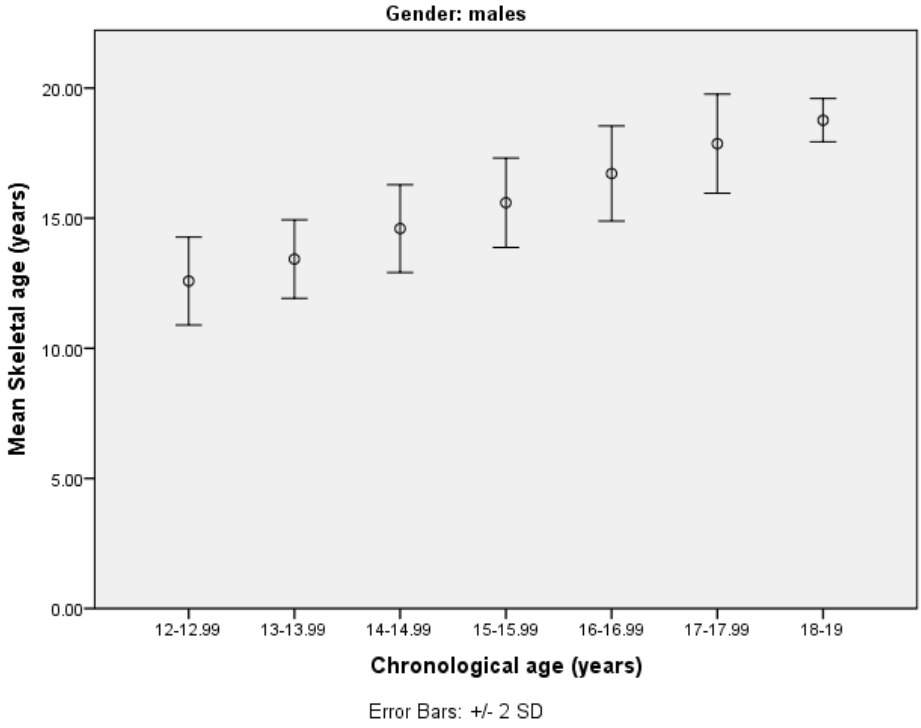

Fig. 3.- Error bar showing the mean and standard deviation of CA and SA in different age groups in males.

Pearson Correlation between CA and SA showed a highly significant positive correlation in both males and females (r = 0.96 in males and 0.95 in females, P <0.001 in both groups). The linear regression model of variables showed that SA significantly affect occurrence of CA by O.R. 0.96 in males and 0.96 in females (Figs. 5-6). The accuracy of the GP atlas in age determination was assured by the 95% confidence interval between the CA and SA in both groups (0.810-0.907 in males and 0.810-0.907 in females), both results were highly significant (P<0.001) (Figs. 7-8). Average measures of interclass correlation coefficient (ICC) indicated a high agreement between the CA and SA. Average measures ICC is calculated the same way Cronbach's alpha and is almost equal to it. It is, however, reliable to use a single measure instead of both as seen by single measures values.

DISCUSSION

In the present study, there was a high degree of agreement between the CA and SA detected based on the GP atlas, in Egyptian males between 12-19 years, and females between 12-18 years old. The SA is highly comparable to the CA in earlier ages, with more variance in later ages. All age groups

Table 3. Mean, standard deviation, minimal and maximal CA and SA and difference between them in different age groups in females.

Age	No	CA				SA				SA-CA	
		Mean	SD	Min	Max	Mean	SD	Min	Max	Mean	SD
12 - 12.99	18	12.45	0.12	12.13	12.86	12.58	0.73	11.00	14.00	+ 0.13	0.35
13 - 13.99	20	13.46	0.56	13.08	13.84	13.4	0.94	12.00	15.00	- 0.08	0.43
14 - 14.99	14	14.46	0.69	14.02	14.93	14.71	0.83	13.00	16.00	+ 0.25	0.52
15 -15.99	13	15.55	0.52	15.18	15.89	15.69	0.85	14.00	17.00	+ 0.14	0.65
16 - 16.99	16	16.50	0.51	16.06	16.91	16.78	0.80	15.50	18.00	+ 0.28	0.56
17 - 17.99	13	17.41	0.43	17.12	17.82	17.65	0.47	17.00	18.00	+ 0.24	0.42
Total	**94**	**14.77**	**1.75**	**12.13**	**17.82**	**14.92**	**1.97**	**11.00**	**18.00**	**+ 0.15**	**0.64**

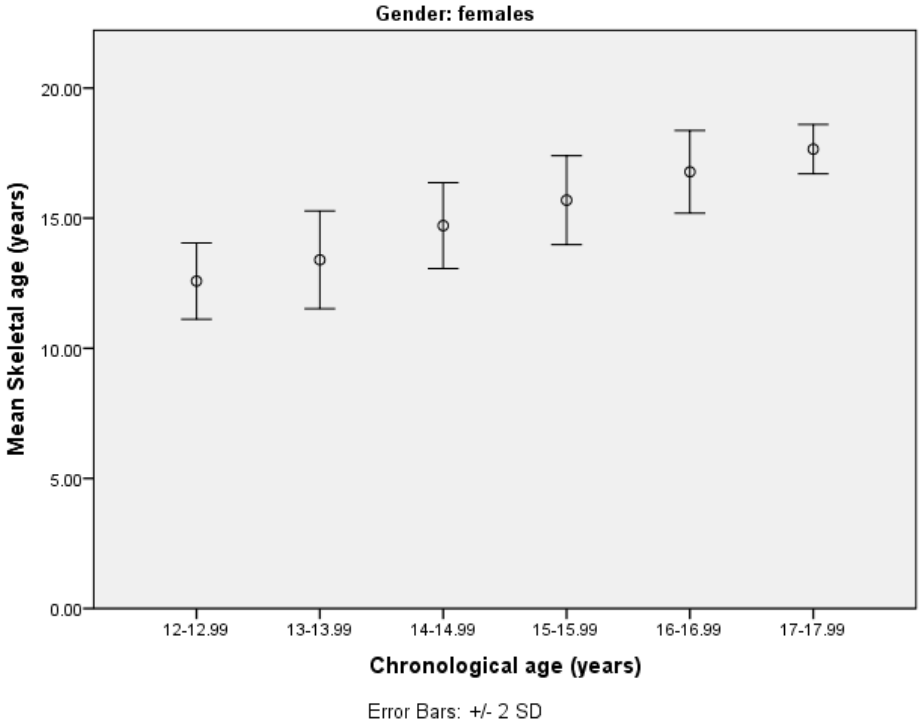

Fig. 4.- Error bar showing the mean and standard deviation of CA and SA in different age groups in females.

showed a preceding SA in comparison to the CA, except for the age 13-13.99 years in both males and females. Although the difference was slight and statistically non-significant, it points to a pattern in the Egyptian population.

To reach a convenient method for age estimation, many researchers have examined the lower ends of the radius and the ulna, which is easy to evaluate even by a non-radiological physician (Kaplowitz et al., 2011). Kaplan (1990) has proved the exceptional advantage of the examination of distal ends of the radius and the ulna over that of the hand bones. Serin et al. (2016) deduce that examination of the distal end of the radius only evenness the examination of the distal epiphyses of the radius, ulna, and the base of the first metacarpal.

Significant variation was ascertained in the evaluation of the applicability of GP atlas as an age determination method. In relation to CA, Koc et al. (2001) have reported a delayed SA in Turkish boys between 7-13 years old and an advanced relation between 14-17 years. However, the unisex appraisal and the less specific evaluation using a pubic hair correlation have been criticized. Supportively, Buken et al. (2007) found a more than

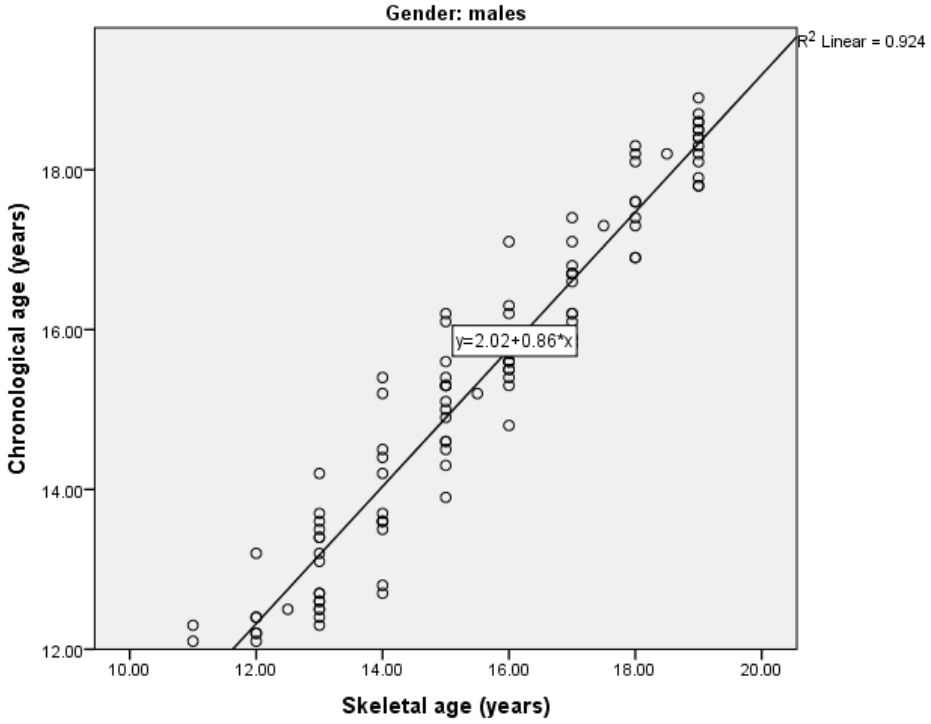

Fig. 5.- Scatter plots representing correlation line between CA and SA in males.

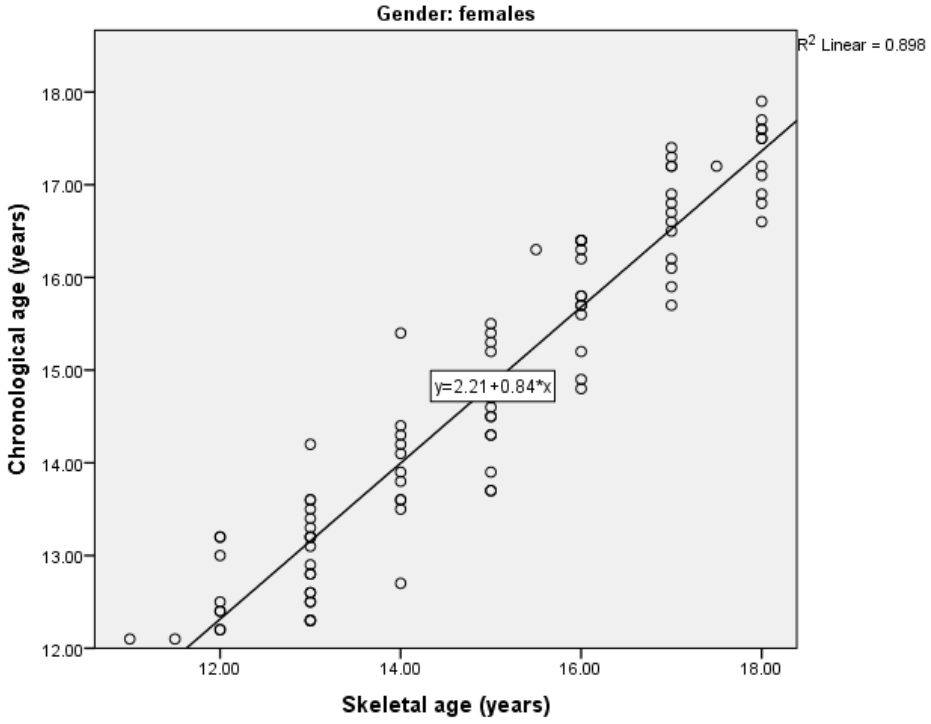

Fig. 6.- Scatter plots representing correlation line between CA and SA in females.

one-year standard deviation at 12 and 15 years of age for girls, and 12, 15 and 18 years of age for boys in the Turkish population, eliminating the criticism directed to the former study. On the other hand, Patil et al. (2012) denied the applicability of GP atlas in Indian children, and found a retarded SA of 0.7 and 0.33 years in males and females respectively.

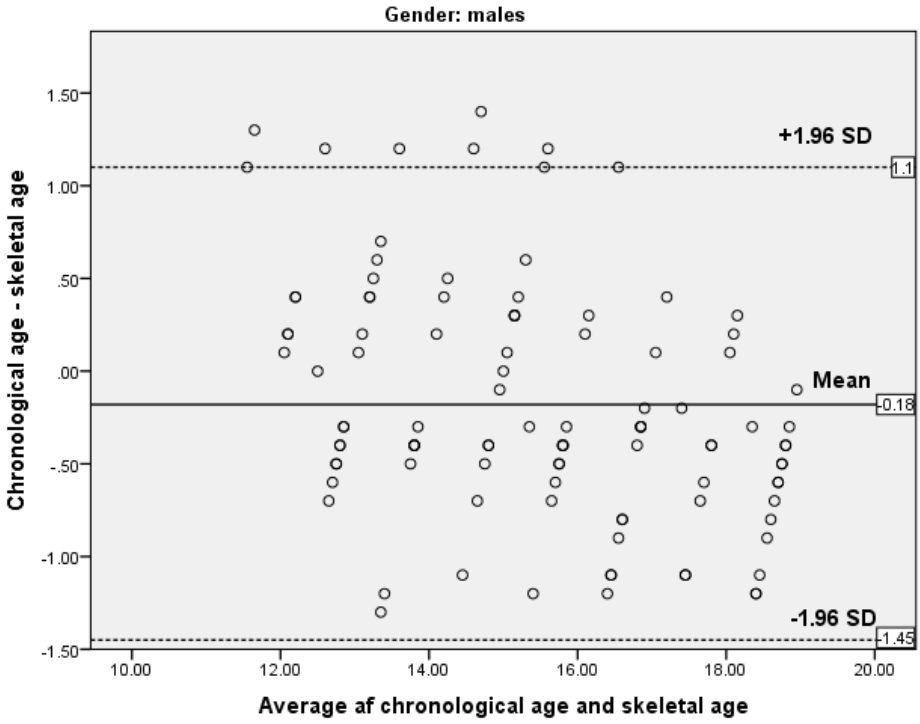

Fig. 7.- Bland Altman Plot showing variability in measurement between CA and SA among males. The line at the middle represents the mean difference and the upper and lower lines represent the upper and lower limits of 95% Confidence interval (CI).

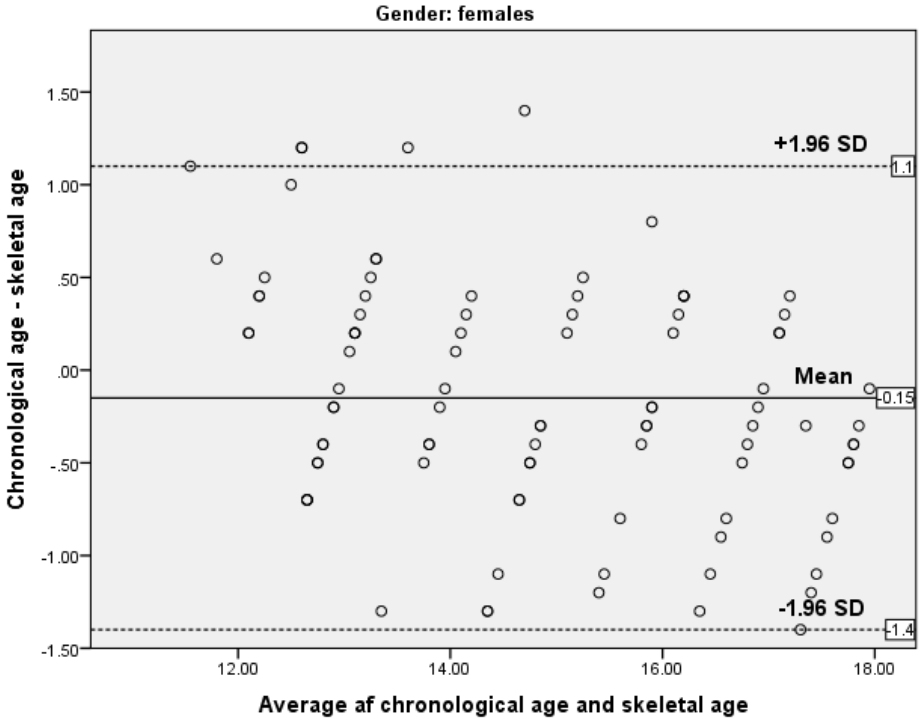

Fig. 8.- Bland Altman Plot showing variability in measurement of CA and SA among females. The line at the middle represents the mean difference and the upper and lower lines represent the upper and lower limits of 95% CI.

In a study concerning the Iranian population, the SA of males was 4.5 months less than CA, and it was 0.5 month more than it was in females. Considering the few months' difference, the authors considered the GP atlas as an applicable method with an acceptable accuracy (Moradi et al., 2012). On the other hand, Zhang et al. (2009) found a significantly overestimated bone age in both male

and female Asian and Hispanic subjects. They appeared to mature sooner than their African-American and white study-fellows. In contrast, Mansourvar et al. (2014) found a strong correlation between Caucasians and Hispanic and a non-applicability in African-American and Asian groups.

Hackman and Black (2013) and Zabet et al. (2015) found that the GP atlas can be applied to a modern Scottish and French population respectively. However, the later pointed to a tendency for this method to overestimate age. On the other hand, Nang et al. (2023) found that GP atlas underestimates age in east Malaysia.

This variation was not surprising. The fashioning of the GP atlas has no doubt included a larger number of radiographs, with the selection of the most centralized ones. With the known ethnic variation, it will be much easier to evaluate the age of different ethnicities. The reliability of GP atlas in the determination of age in Caucasians has been proven (Moradi et al., 2012; Hackman and Black, 2013; Mansourvar et al., 2014; Zabet et al., 2015), as well as in the present study. That is why, in our consideration, the Egyptian dominant Caucasian ethnicity and other variants and mixed ethnicities (African, Middle Eastern, Mediterranean, Arabic) showed less variation and more reliability with the GP atlas than other countries.

The dose range of a wrist radiograph is 0.003-0.005 mSv. This dose poses minimal risk and is considered negligible (Safer et al., 2015). The risk for a fatal cancer development caused by this dose is 1 in 5,460,000 (Cross et al., 2003). However, to overcome the ethical dilemma of the cumulative radiological hazards (Eikvil et al., 2012; Daneff et al., 2015), it is better to allocate the conventional X-ray in age determination for single uses in forensic and medico-legal cases. Other methods with less hazardous radiological effects seem to be more convenient in repetitive and follow up cases.

Considering the propitious results obtained from the present study, it can be assumed that the GP atlas is a reliable way for age determination in the Egyptian population at the examined ages. GP atlas, although old, has been regarded as the golden standard for bone-age estimation (Daneff et al., 2015), it is even applied as a reliable reference to other methods of age estimation (Lee et al., 2021). Despite that, the use of SA estimation to assume the CA in legal cases as an age of consent and criminal responsibility must take in consideration the variability and lack of complete accuracy, and must add other methods of assessment (Serinelli et al., 2015). The subjective evaluation as well as personal, ethnic, racial, and even socioeconomic variations limit the complete reliance on this method alone. This limitation is not confined to the present work, but rather to all radiological methods. Adding a physical, dental, and psychological examination may aid to the accuracy of age detection (Willems 2001; Mesotten et al., 2002; Benson and Williams, 2008; Kumari et al., 2022) and fulfill the guidelines for the estimation of the biological age of living individuals (Schmeling et al., 2008).

The present work is, to our knowledge, the first study concerning the comparison between the CA and SA using the GP atlas in the Egyptian population. In such a case, further studies with a larger number of individuals with different socioeconomic status and different methods of scanning are required to extract an affirmed profile.

CONCLUSION

Examination of the lower end of the ulna and the radius is a suitable method for age detection of Egyptian males between the ages of 12-19 years old and females between 12-18 years old. Using a plain X-ray of the left wrist region for that purpose appears as an easy and affordable method. The reliance on GP atlas as a cushy, trustworthy -although old- way should not be discouraged. However, the repeated examination should be performed using other methods with less hazardous radiological effects. Due to the presence of personal variations, such an examination should be used in forensic, medico-legal, and criminal cases with extensive prudence.

DECLARATIONS

Authors contribution

Conceptualization, Ahmed F. AlDomairy and Radwa M. Elsabban; Methodology, Ahmed F. Al-

Domairy, Tamer T. Farag, Manar A. Eldesouky and Radwa M. Elsabban; Validation, Mohamed A. Yehia; Formal Analysis, Yasmine H. Eisa; Investigation, Mahmoud M. Assem; Data Curation, Ashraf Kotb; Writing – Original Draft Preparation, Ahmed F. AlDomairy; Writing – Review & Editing, Ashraf Kotb, Radwa M. Elsabban; Supervision and Project Administration, Ahmed F. AlDomairy. All authors shared the literature search, revised and commented on previous versions of the manuscript and approved the final manuscript. They all agree to be personally accountable for their own contribution and for the accuracy and integrity of all parts of the work.

Institutional Review Board Statement and Compliance with Ethical Standards

The study was conducted according to the guidelines of the Declaration of Helsinki and approved by the Ethics Committee of October 6 University (protocol code PRC-Me-2105013 4- 5-2021).

Consents and privacy rights

A written informed consent was obtained from the parents of the subjects included in this study. The privacy rights of the subjects were preserved.

Funding and Competing interests

The authors declare that they have no known competing financial interests or personal relationships that could have appeared to influence the work reported in this paper. This research did not receive any specific grant from funding agencies in the public, commercial, or not-for-profit sectors.

REFERENCES

AL-KHATER KHM, HEGAZI TM, AL-THANI HF, AL-MUHANNA HT, AL-HAMAD BW, ALHURAYSI SM, ALSFYANI WA, ALESSA FW, AL-QWAIRI AO, AL-QWAIRI AO, BAYER SB, SIDDIQUI FB (2020) Time of appearance of ossification centers in carpal bones: A radiological retrospective study on Saudi children. *Saudi Med J,* 41(9): 938-946.

BAUMANN U, SCHULZ R, REISINGER W, HEINECKE A, SCHMELING A, SCHMIDT S (2009) Reference study on the time frame for ossification of the distal radius and ulnar epiphyses on the hand radiograph. *Forensic Sci Int,* 191(1-3): 15-18.

BENSON J, WILLIAMS J (2008) Age determination in refugee children. *Aust Fam Physician,* 37: 821-825.

BLUMER MJF (2021) Bone tissue and histological and molecular events during development of the long bones. *Ann Anat,* 235: 151704.

BUKEN B, SAFAK AA, YAZICI B, BUKEN E, MAYD AS (2007) Is the assessment of bone age by the Greulich-Pyle method reliable at forensic age estimation for Turkish children? *Forensic Sci Int,* 173(2-3): 146-153.

CROSS TM, SMART RC, THOMSON JEM (2003) Exposure to diagnostic ionizing radiation in sports medicine: assessing and monitoring the risk. *Clin J Sport Med,* 13(3): 164-170.

DANEFF M, CASALIS C, BRUNO CH, BRUNO DA (2015) Bone age assessment with conventional ultrasonography in healthy infants from 1 to 24 months of age. *Pediatr Radiol,* 45(7): 1007-1015.

DUPUIS H, PEST MA, HADZIC E, VO TX, HARDY DB, BEIER F (2019) Exposure to the RXR agonist SR 11237 in early life causes disturbed skeletal morphogenesis in a rat model. *Int J Mol Sci,* 20(20): 5198.

EIKVIL L, KVAAL SI, TEIGLAND A, HAUGEN M, GRØGAARD J (2012) Age estimation in youths and young adults. A summary of the needs for methodological research and development. *Publication number Samba/52/12. Published online.*

EKIZOGLU O, INCI E, ERDIL I, HOCAOGLU E, BILGILI MG, KAZIMOGLU C, REISOGLU A, CAN I (2016) Computed tomography evaluation of the iliac crest apophysis: age estimation in living individuals. *Int J Legal Med,* 130(4): 1101-1107.

GILSANZ V, RATIB O (2005) Hand bone age: a digital atlas of skeletal maturity. Springer Science & Business Media, Heidelberg.

GREULICH WW, PYLE SI (1959) Radiological atlas of skeletal development of the hand and the wrist. 2nd ed. Stanford University Press, Stanford.

HACKMAN L, BLACK S (2012) Does mirror imaging a radiograph affect reliability of age assessment using the Greulich and Pyle atlas? *J Forensic Sci,* 57: 1276-1280.

HACKMAN L, BLACK S (2013) The reliability of the Greulich and Pyle atlas when applied to a modern Scottish population. *J Forensic Sci*, 58: 114-119.

HAJALIOGHLI P, TARZAMNI MK, ARAMI S, FOULADI DF, GHOJAZADEH M (2015) The utility of ultrasonographic bone age determination in detecting growth disturbances; a comparative study with the conventional radiographic technique. *Skeletal Radiol,* 44(9): 1351-1356.

HASSAN N, NOOR F, AHMAD SH, FAZILI KH M (2016) Age of fusion of the distal radial and ulnar epiphyses from hand radiographs-A study in Kashmiri population. *Sci Justice,* 56(6): 431-436.

HELLINGS IR, EKMAN S, HULTENBY K, DOLVIK NI, OLSTAD K (2016) Discontinuities in the endothelium of epiphyseal cartilage canals and relevance to joint disease in foals. *J Anat,* 228(1): 162-175.

HORTER MJ, FRIESEN S, WACKER S, VOGT B, LEIDIGER B, ROEDL R, SCHIEDEL F (2012) Determination of skeletal age: comparison of the methods of Greulich and Pyle and Tanner and Whitehouse. *Orthopade,* 41(12): 966-976.

HUNZIKER EB, LIPPUNER K, SHINTANI N (2014) How best to preserve and reveal the structural intricacies of cartilaginous tissue. *Matrix Biol,* 39: 33-43.

KAPLAN SA (1990) Growth and growth hormone: disorders of the anterior pituitary. In: *Kaplan, S.A. Clinical Pediatric Endocrinology.* (2nd ed.) Philadelphia, W.B. Saunders Company, pp 1-62.

KAPLOWITZ P, SRINIVASAN S, HE J, MCCARTER R, HAYERI MR, SZE R (2011) Comparison of bone age readings by pediatric endocrinologists and pediatric radiologists using two bone age atlases. *Pediatr Radiol,* 41: 690-693.

KOC A, KARAOGLANOGLU M, ERDOGAN M, KOSECIK M, CESUR Y (2001) Assessment of bone ages: Is the Greulich-Pyle method sufficient for Turkish boys? *Pediatr Int,* 43: 662-665.

KWON JH, LEE HA, KIM YJ, LEE H, PARK EA, CHO SJ, GWAK HS, HA E, PARK H, KIM HS (2017) Effects of adrenal androgen levels on bone age advancement in prepubertal children: using the ewha birth and growth cohort study. *J Korean Med Sci,* 32(6): 968-973.

KUMARI S, SAHU AK, RAJGURU J, BISHNOI P, GARG AJ, THAKUR R (2022) Age estimation by dental calcification stages and hand-wrist radiograph. *Cureus,* 14(9): e29045.

LAOR T, CLARKE JP, YIN H (2016) Development of the long bones in the hands and feet of children: radiographic and MR imaging correlation. *Pediatr Radiol,* 46(4): 551-561.

LEE KC, LEE KH, KANG CH, AHN KS, CHUNG LY, LEE JJ, HONG SJ, KIM BH, SHIM E (2021) Clinical validation of a deep learning-based hybrid (Greulich-Pyle and modified Tanner-Whitehouse) method for bone age assessment. *Korean J Radiol,* 22(12): 2017-2025.

MANSOURVAR M, ISMAIL MA, RAJ RG, ABDUL KAREEM S, AIK S, GUNALAN R, ANTONY CD (2014) The applicability of Greulich and Pyle atlas to assess skeletal age for four ethnic groups. *J Forensic Legal Med,* 22: 26-29.

MESOTTEN K, GUNST K, CARBONEZ A, WILLEMS G (2002) Dental age estimation and third molars: a preliminary study. *Forensic Sci Int,* 129: 100-115.

MORADI M, SIROUS M, MOROVATTI P (2012) The reliability of skeletal age determination in an Iranian sample using Greulich and Pyle method. *Forensic Sci Int,* 223: 372.

NANG KM, ISMAIL A, TANGAPERUMAL A, WYNN AA, THEIN TT, HAYATI F, TEH YG (2023) Forensic age estimation in living children: how accurate is the Greulich-Pyle method in Sabah, East Malaysia? *Front Pediatr,* 11: 1137960.

NICHOLAS JL, DOUGLAS KE, WATERS W, GALLEGOS CA, CHAPNICK M, HABIF DVJR, TRUE S, MUSONZA C, IANNOTTI L (2019) Ultrasound evaluation of bone age in rural Ecuadorian children and its association with nutrition. *Curr Dev Nutr,* 3(Suppl 1): Published online.

OTTOW C, SCHMIDT S, HEINDEL W, PFEIFFER H, BUERKE B, SCHMELING A, VIETH V (2022) Forensic age assessment by 3.0 T MRI of the wrist: adaption of the Vieth classification. *Eur Radiol,* 32(11): 7956-7964.

PATIL ST, PARCHAND MP, MESHRAM MM, KAMDI NY (2012) Applicability of Greulich and Pyle skeletal age standards to Indian children. *Forensic Sci Int,* 216: 200.

SAFER AN, HOMEL P, CHUNG DD (2015) Lateral comparisons using Fishman's skeletal maturation assessment. *The Angle Orthodontist,* 85(3): 408-412.

SCHMELING A, SCHULZ R, DANNER B, ROSING FW (2006) The impact of economic progress and modernization in medicine on the ossification of hand and wrist. *Int J Legal Med,* 120: 121-126.

SCHMELING A, GRUNDMANN C, FUHRMANN A, KAATSCH HJ, KNELL B, RAMSTHALER F, REISINGER W, RIEPERT T, RITZ-TIMME S, ROSING FW, ROTZSCHER K, GESERICK G (2008) Criteria for age estimation in living individuals. *Int J Legal Med,* 122: 457-460.

SCHMIDT S, SCHIBORR M, PFEIFFER H, SCHMELING A, SCHULZ R (2013) Age dependence of epiphyseal ossification of the distal radius in ultrasound diagnostics. *Int J Legal Med,* 127(4): 831-838.

SCHMIDT S, VIETH V, TIMME M, JUNGE A, DVORAK J, SCHMELING A (2014) Examination of ossification of the distal radial epiphysis using magnetic resonance imaging. New insights for age estimation in young footballers in FIFA tournaments. *Sci Justice,* 55: 139-144.

SERIN J, REROLLE C, PUCHEUX J, DEDOUIT F, TELMON N, SAVALL F, SAINT-MARTIN P (2016) Contribution of magnetic resonance imaging of the wrist and hand to forensic age assessment. *Int J Legal Med,* 130: 1121-1128.

SERINELLI S, PANEBIANCO V, MARTINO M, BATTISTI S, RODACKI K, MARINELLI E, ZACCAGNA F, SEMELKA RC, TOMEI E (2015) Accuracy of MRI skeletal age estimation for subjects 12-19. Potential use for subjects of unknown age. *Int J Legal Med,* 129: 609-617.

SHAPIRO IM, ADAMS CS, FREEMAN T, SRINIVAS V (2005) Fate of the hypertrophic chondrocyte: microenvironmental perspectives on apoptosis and survival in the epiphyseal growth plate. *Birth Defects Re. C Embryo Today.* 75(4): 330-339.

STANDRING S (2020) Forearm. In: *Gray's Anatomy, The Anatomical Basis of Clinical Practice.* 42nd ed. Elsevier, Amsterdam, pp 867-873.

TOMEI E, SARTORI A, NISSMAN D, AL ANSARI N, BATTISTI S, RUBINI A, STAGNITTI A, MARTINO M, MARINI M, BARBATO E, SEMELKA RC (2014) Value of MRI of the hand and the wrist in evaluation of bone age: preliminary results. *J Magn Reson Imaging,* 39(5): 1198-1205.

WILLEMS G (2001) A review of the most commonly used dental age estimation techniques. *J Forensic Odontostomatol,* 19: 9-17.

ZABET D, REROLLE C, PUCHEUX J, TELMON N, SAINT-MARTIN P (2015) Can the Greulich and Pyle method be used on French contemporary individuals? *Int J Legal Med,* 129(1): 171-177.

ZHANG A, SAYRE JW, VACHON L, LIU BJ, HUANG HK (2009) Racial differences in growth patterns of children assessed on the basis of bone age. *Radiology,* 250(1): 228-235.

ZHAO Q, ZHANG M, CHU Y, JI B, PAN H, SUN H, BAN B (2020) Association between insulin-like growth factor-1 and relative skeletal maturation: a retrospective cohort study of short children and adolescents. *Biomed Res Int,* 2020: 8052143.

Exit point of the external nasal nerve-cadaveric study

Bijo Elsy[1], Mansour A. Alghamdi[1,2], Lina E.S. Osman[1]

[1] Department of Anatomy, College of Medicine, King Khalid University, Abha, 62529, Saudi Arabia

[2] Genomics and Personalized Medicine Unit, College of Medicine, King Khalid University, Abha, 62529, Saudi Arabia

SUMMARY

This study aims to confirm how the external nasal nerve exits from the internal surface of the nasal bone to the dorsum of the nose and to determine the exact point of nerve emergence by macroscopic examination. Twenty external nasal nerves of both sexes from the elderly and adult age groups were dissected. The exit point of the external nasal nerve, the width of the nasocartilaginous joint, and the inferior border of the nasal bone from the midline to the nasomaxillary suture were measured. The nerve was classified according to its branching pattern. In this study, in the elderly group, the external nasal nerve enters the dorsum of the nose through the pyriform ligament and exits laterally to the nasocartilaginous joint. But in the adult age group the external nasal nerve exits between the nasal bone and the upper nasal cartilage. We observed mainly three types of nerve but did not find any subtypes or variations in the branching pattern. Among this main classification of nerves, more cases (70%) of type I were observed. However, based on our study, we concluded that the external nasal nerve enters the dorsum of the nose either between the nasal bone and the upper nasal cartilage, or it passes through the pyriform ligament and exits lateral to the nasocartilaginous joint. In rhinoplasty, knowledge about the course, exit point, branching pattern, and variations of the external nasal nerve is unavoidable.

Key words: External nasal nerve – Nasocartilaginous joint – Nasomaxillary suture – Pyriform ligament

INTRODUCTION

The external nasal nerve is the terminal branch of the anterior ethmoidal nerve; it exits at the inferior margin of the nasal bone (Standring, 2016). The course, exit point, and branching pattern of the external nasal nerve are important in rhinoplasty. The nasal tip's numbness after rhinoplasty is mainly due to damage to the external nasal nerve. There is an obvious difference in the anatomical structure of the external nasal nerve between Caucasians and Asians (Chen and Carr, 2022).

The pyriform ligament is a fascial support between the bones of the pyriform aperture and the adjacent cartilages (Rohrich et al., 2008). It has various other names, such as the lateral sesamoid complex ligament, the lateral crural complex, and the nasal hinge. Hamilton (Hamilton, 2021) reported that the lateral crus of the alar cartilage and accessory cartilages are connected to the frontal process of the maxilla through the pyriform ligament.

Corresponding author:
Bijo Elsy. College of Medicine, Department of Anatomy, King Khalid University, Abha, Saudi Arabia. Phone: 00966533600396. E-mail: bijobaby22@yahoo.com

Submitted: June 18, 2023. **Accepted:** September 4, 2023

https://doi.org/10.52083/JAXA5021

Kim and Jeong (2023) reported that the pyriform ligament is condensed along the pyriform aperture. The pyriform aperture ligament, or vertical pyriform ligament, attaches between the soft tissue envelope and the border of the pyriform aperture (Saban et al., 2008; Hamilton, 2021).

The fracture of the nasal bone is the most common injury in the facial skeleton, as are any injuries on the dorsum of the nose that affect the external nasal nerve. Many authors (Han et al., 2004; Chen and Carr, 2022) have reported that there are variations in the course, exit point and branching pattern of the external nasal nerve.

Based on the reported findings, our aim is to determine the width of the nasocartilaginous joint, the width of the inferior border of the nasal bone, the exit point of the external nasal nerve, how it exits, and its branching pattern.

MATERIALS AND METHODS

Twenty external nasal nerves of both sexes, 14 male and 6 female, were dissected. Among the 20 specimens, 12 were elderly, and 8 were adult age groups. In neither the elderly nor the adult age groups the exact age is unknown. We examined the pyriform aperture ligament, the pyriform ligament with adjoining parts of the bones and cartilages, and the point of emergence of the external nasal nerve. The images were recorded through photography. We measured the distance from midline to the exit point of the external nasal nerve, along the inferior border of the nasal bone. We also measured the width of the nasocartilaginous joint and the inferior border of the nasal bone from the midline to the nasomaxillary suture. We finally classified the nerve according to its branching pattern. Statistical data analysis was carried out in MS Excel 2019.

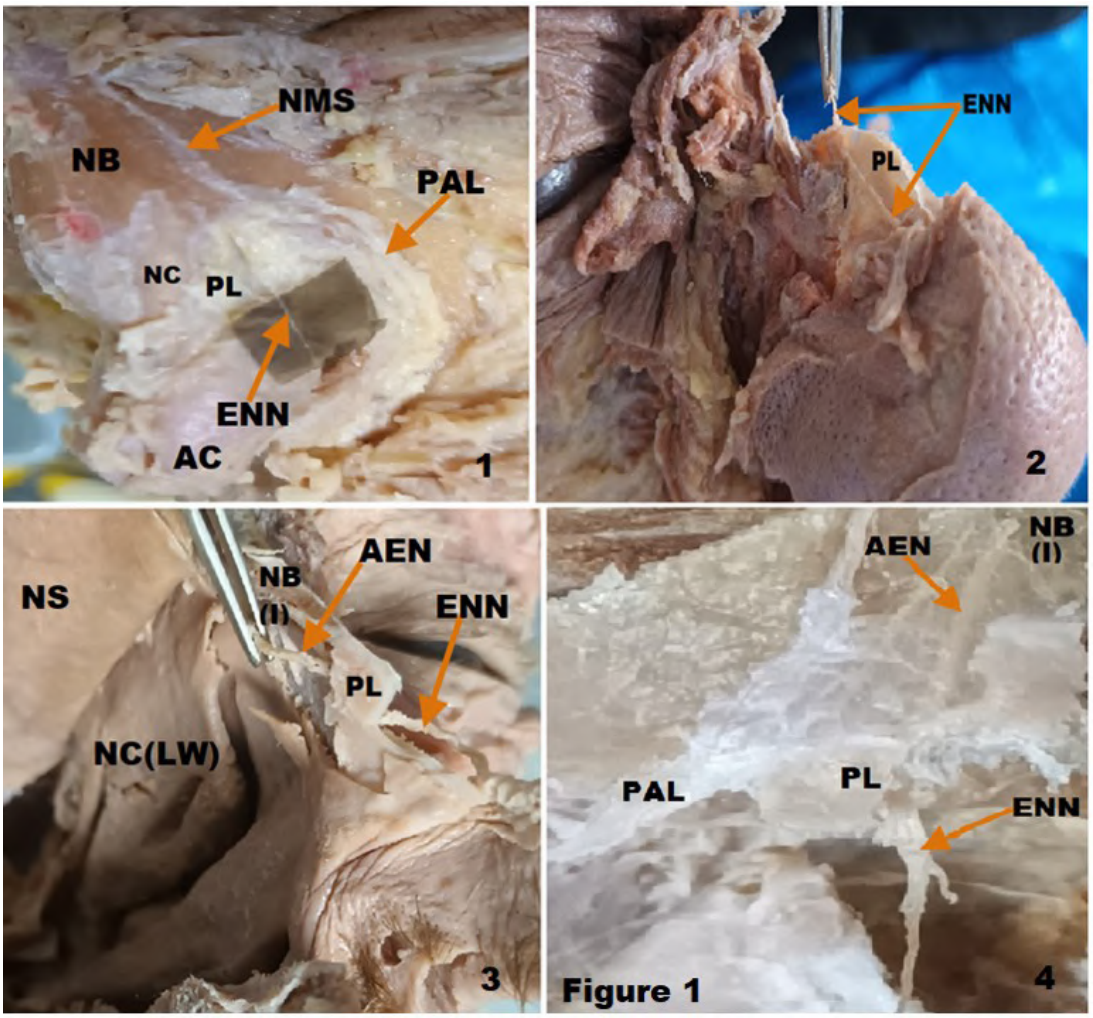

Fig. 1.- Representative images (1, 2, 3 and 4) of the elderly group showing the external nasal nerve (ENN) passing through the pyriform ligament (PL). NB: Nasal bone, NB (I): Nasal bone internal surface, NC: Upper nasal cartilage, PAL: Pyriform aperture ligament, AC: Alar cartilage, AEN: Anterior ethmoidal nerve, NS: Nasal septum, NC (LW): Nasal cavity lateral wall.

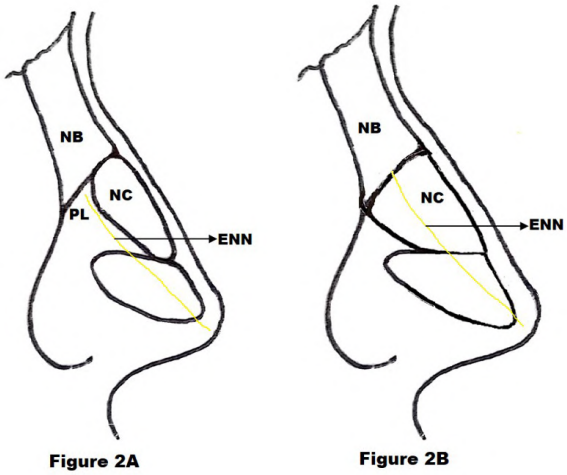

Figs. 2.- Drawing illustrating the exit of the external nasal nerve (ENN). **A:** Nerve exit through pyriform ligament (PL) in the elderly group. **B:** Nerve exit between nasal bone (NB) and the upper nasal cartilage (NC) in the adult age group.

This study was conducted in the Anatomy Department of King Khalid University, Abha, Saudi Arabia, and approved by the Research Ethics Committee (ECM #2023-2118) of King Khalid University.

RESULTS

In this cadaveric study, in both sexes of the elderly group, the external nasal nerve exits through the pyriform ligament before entering the dorsum of the nose (Figs. 1 and 2A). But in both sexes of the adult age group, the external nasal nerve exits between the nasal bone and the upper nasal cartilage (Figs. 2B, 3A and 3B). In all specimens, the nerve exits at the same level on its right and left sides.

In the elderly group, the nerve exit point lies lateral to the nasocartilaginous joint (Fig. 4A). The distance from midline to the exit point of the external nasal nerve, the medial main branch of the type-III nerve, along the inferior border of the na-

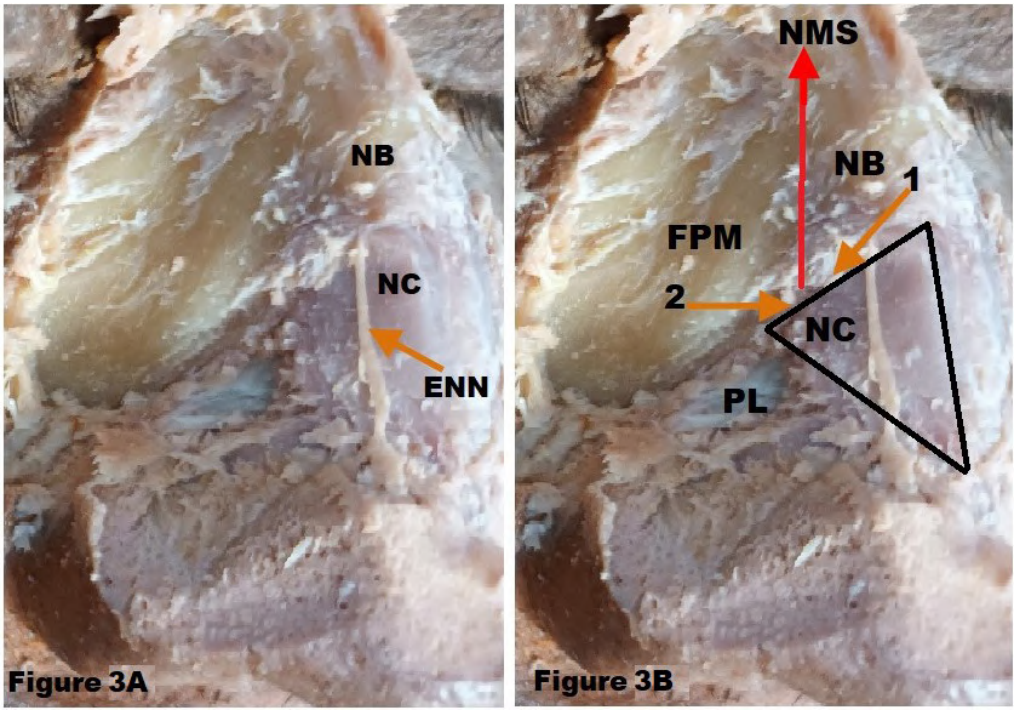

Figs. 3A and 3B.- Representative images of the adult age group showing the external nasal nerve (ENN) passing between the nasal bone (NB) and the upper nasal cartilage (NC). Pyriform ligament (PL), NMS: Nasomaxillary suture, FPM: Frontal process of maxilla, 1: Nasal part of nasocartilaginous joint, 2: Maxillary part of nasocartilaginous joint.

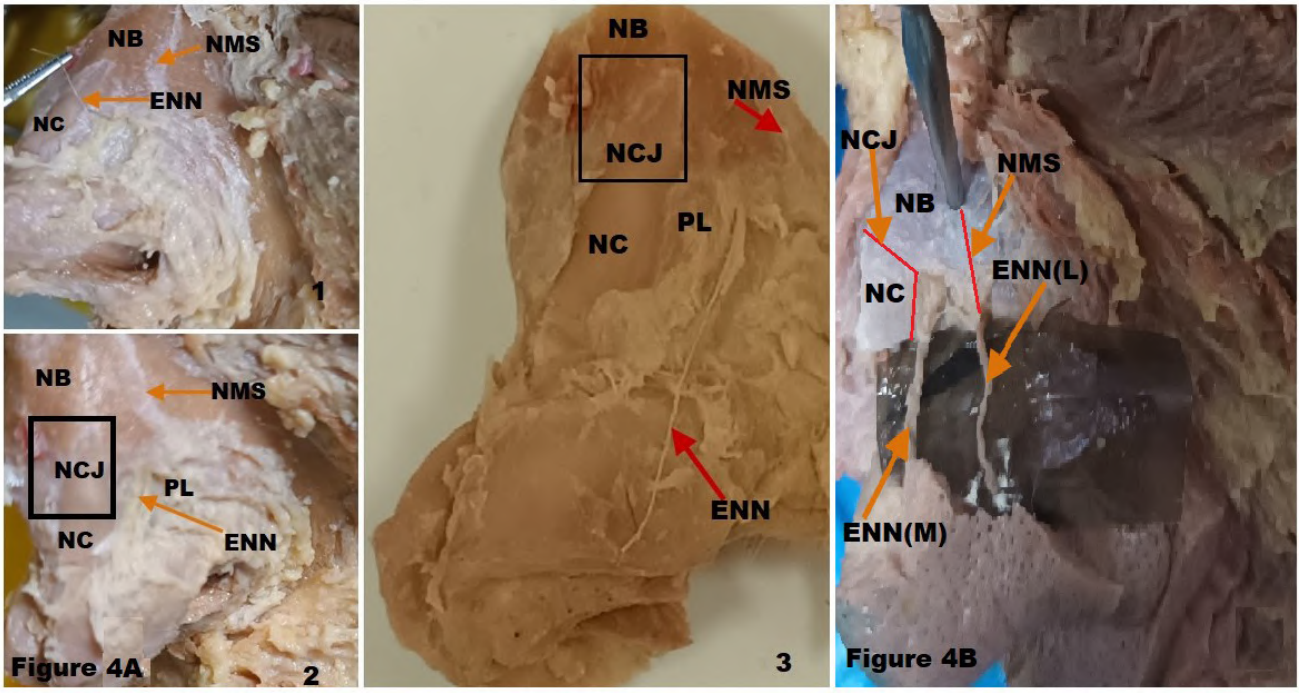

Figs. 4A and 4B.- Representative images of the elderly group showing the exit of the external nasal nerve (ENN) lateral to the nasocartilaginous joint (NCJ) through pyriform ligament (PL), Nasal bone (NB), Upper nasal cartilage (NC), NMS: Nasomaxillary suture. ENN (M): Medial main branch of external nasal nerve, ENN (L): Lateral main branch of external nasal nerve.

sal bone ranged from 7.5 to 9.5 mm (mean, 8.36 ± 0.80 mm). The type-III branching pattern was observed in two specimens. Its lateral main branch exits at the level of the nasomaxillary suture, which is 11 mm away from the midline (Fig. 4B).

In the adult age group, the nerve exits between the nasal bone and the upper nasal cartilage. Its exit point lies 5.5 to 6.5 mm (mean, 6 ± 0.5 mm) away from the midline.

The width of the nasocartilaginous joint varies from 6 to 8 mm (mean, 7 ± 0.79 mm) in the elderly group (Fig. 4A). In the adult age group, the nasocartilaginous joint's width varies from 11 to 12 mm (mean, 11.5 ± 0.5 mm) (Fig. 3B). The width of the inferior border of the nasal bone from the midline to the nasomaxillary suture varies in the adult age group from 10.5 to 11.5 mm (mean, 11 ± 0.5 mm), but in the elderly group, it varies from 9.5 to 11 mm (mean, 10.25 ± 0.64 mm).

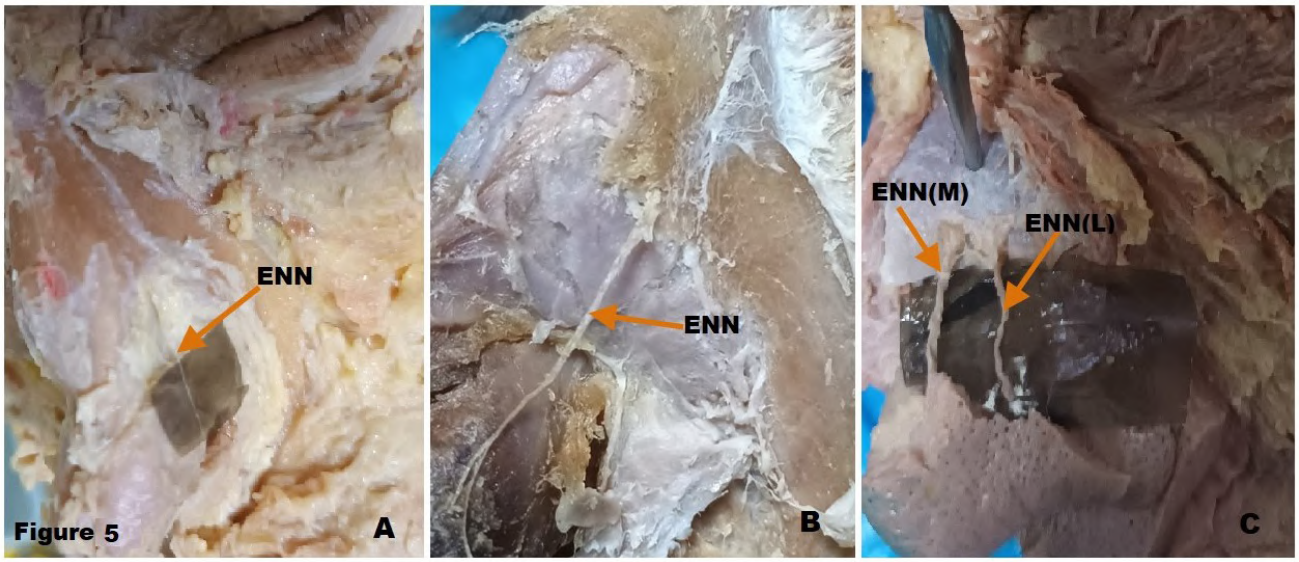

Fig. 5.- Representative images of the classification of the external nasal nerve (ENN). **A:** Type I. **B:** Type II. **C:** Type III. ENN (M): Medial main branch of external nasal nerve, ENN (L): Lateral main branch of external nasal nerve.

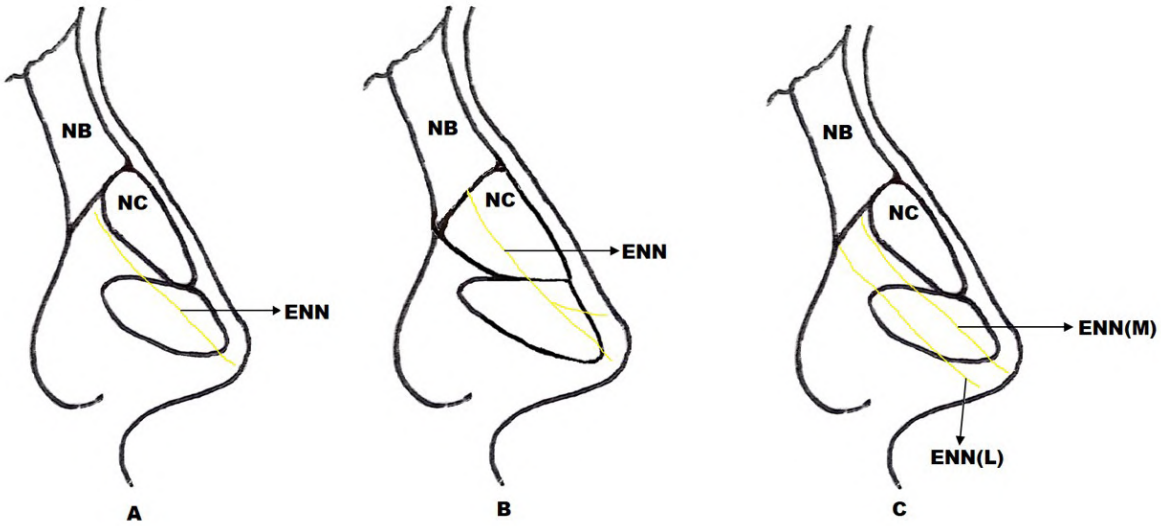

Figure 6

Fig. 6.- Drawing illustrating the classification of the external nasal nerve. **A:** Type I. **B:** Type II. **C:** Type III. Nasal bone (NB), Upper nasal cartilage (NC), ENN (M): Medial main branch of external nasal nerve, ENN (L): Lateral main branch of external nasal nerve.

In the adult age group, the superior margin of the upper nasal cartilage is attached to the frontal process of the maxilla at 0.5 to 1 mm (Fig. 3B).

Based on the branching pattern, we found mainly three types of nerve classification. Among these, type I was observed in 14 of 20 nerves (70%), type II was seen in 4 of 20 (20%), and type III was observed in 2 of 20 (10%) (Figs. 5 and 6). We have not seen any other variations or subtypes.

DISCUSSION

The anterior ethmoidal nerve runs in a groove on the internal surface of the nasal bone, and its terminal sensory branch is the external nasal nerve that innervates the nasal tip (Standring, 2016; Kim and Jeong, 2023). The absence of an external nasal nerve may result in a lack of sensation at the tip of the nose (Bergman et al. 2006). The external nasal nerve anastomoses with the terminal branch of the facial nerve. Knowledge of such neural anastomoses is important in facial reconstructive surgery (Diamond et al., 2011; Shoja et al., 2014).

Most available and recent studies (Chen and Carr, 2022; Standring, 2016) report that the external nasal nerve exits between the nasal bone and the upper nasal cartilage. The same findings were observed in the adult age group of our study. The exit point of the nerve lies between 5.5 and 6.5 mm (mean, 6 ± 0.5 mm) away from the midline. Whereas in the elderly group, the nerve exits through the pyriform ligament. Its exit point lies lateral to the nasocartilaginous joint and between 7.5 and 9.5 mm (mean, 8.36 ± 0.80 mm) away from midline. In the elderly group, type-III branching patterns were observed. Its lateral main branch exits at the level of the nasomaxillary suture, which is 11 mm from the midline. Chen and Carr (2022) reported that the nerve exit point ranged from 5.08 to 11.94 mm (mean, 8.31 ± 1.85 mm). Another study (Han et al., 2004) observed that the exit point of the external nasal nerve lies lateral to the nasal midline from 6.5 to 8.5 mm (mean, 7.3 ± 0.6 mm).

In the elderly group of this study, the pyriform ligament is connected to the nasal bone, the frontal process of the maxilla, and the upper nasal cartilage (lateral nasal cartilage). The pyriform ligament is a vestigial ligamentous sheet that connects the periosteum of the bony pyriform aperture and the perichondrium of the adjacent cartilage (Daniel and Palhazi, 2018). Our finding in the elderly group is that the external nasal nerve passes through the pyriform ligament. With age, changes occur in the nasal bone and upper nasal cartilage. Thus, the exit point of the external nasal nerve can change (Chen and Carr, 2022). On the

nose, the age-related changes are not uniform. With age, only cartilage moves, and both bone and cartilage become weak (Shastri et al., 2021).

The superior margin of the triangular upper nasal cartilage is attached to the nasal bone and the frontal process of the maxilla. The width, thickness, and length of the nasal bones vary (Standring, 2016). The inferior border of the nasal bone is attached to the superior margin of the upper nasal cartilage to form a tight synchondrosis (Kenyon, 2013). We observed tight synchondrosis only in the elderly group, but it is not seen in the adult age group. In the elderly group, the width of the nasocartilaginous joint ranges from 6 to 8 mm (mean, 7 ± 0.79 mm), and the pyriform ligament is attached to the remaining part of the inferior border of the nasal bone and the frontal process of the maxilla. In the adult age group, the nasocartilaginous joint's width ranges from 11 to 12 mm (mean, 11.5 ± 0.5 mm). The width of the inferior border of the nasal bone from the midline to the nasomaxillary suture ranges from 9.5 to 11 mm (mean, 10.25 ± 0.64 mm) in the elderly group. Whereas in the adult age group, it ranges from 10.5 to 11.5 mm (mean, 11 ± 0.5 mm), but from 0.5 to 1 mm, the superior margin of the cartilage is attached to the frontal process of the maxilla. Kenyon (Kenyon, 2013) reported that the upper nasal cartilage is attached to the nasal bone at a level of 6 to 8 mm.

The present study agrees with previously reported classification and branching patterns (Chen and Carr, 2022; Han et al., 2004). Among 20 nerves, 70% of type I (14 nerves), 20% of type II (4 nerves), and 10% of type III (2 nerves) were observed, but we have not seen any other variations or subtypes.

CONCLUSION

Based on our study, we concluded that in the elderly group the external nasal nerve passes through the pyriform ligament and exits lateral to the nasocartilaginous joint. But in the adult age group the external nasal nerve exits between the nasal bone and the upper nasal cartilage. All available data indicate that the external nasal nerve exits between the nasal bone and the nasal cartilage. Anatomical knowledge of the external nasal nerve is necessary to avoid nerve injury in rhinoplasty. A clear understanding of the anatomical structure of the nasal bones and cartilages and their changes with age is helpful in surgical procedures.

ACKNOWLEDGEMENTS

The authors extend their appreciation to the Deanship of Scientific Research at King Khalid University for funding this work through large group Research Project under grant number RGP2/302/44. Also, all kinds of support availed from the Department of Anatomy, College of Medicine, King Khalid University, Abha, Saudi Arabia are gratefully acknowledged.

REFERENCES

BERGMAN RA, AFIFI AK, MIYAUCHI R (2006) Illustrated Encyclopaedia of Human Anatomic Variation. Available at: *http://www.anatomyatlases. org/ AnatomicVariants/ AnatomyHP.shtml* (accessed 17 November 2015).

CHEN Y, CARR CB (2022) Anatomical comparative study of the external nasal nerve in caucasian and asian: application for minimizing nerve damage in rhinoplasty. *Aesth Plast Surg*, 46: 852-861.

DANIEL RK, PALHAZI P (2018) The nasal ligaments and tip support in rhinoplasty: an anatomical study. *Aesth Surg J*, 38(4): 357-368.

DIAMOND M, WARTMANN CT, TUBBS RS, SHOJA MM, COHEN-GADOL AA, LOUKAS M (2011) Peripheral facial nerve communications and their clinical implications. *Clin Anat* 24: 10-18.

HAMILTON GS (2021) Rhinoplasty as an adjunct to facial rejuvenation. *Facial Plast Surg*, 37: 211-217.

HAN SK, SHIN YW, KIM WK (2004) Anatomy of the external nasal nerve. *Plast Reconstr Surg*, 114: 1055-1059.

KENYON G (2013) Nasal anatomy and analysis. *Int J Otorhinolaryngol Clin*, 5(1): 34-42.

KIM TK, JEONG JY (2023) Surgical anatomy for Asian rhinoplasty. *Arch Craniofac Surg*, 20(3): 147-157.

ROHRICH RJ, HOXWORTH RE, THORNTON JF, PESSA JE (2008) The pyriform ligament. *Plast Reconstr Surg*, 121(1): 277-281.

SABAN Y, ANDRETTO AMODEO C, HAMMOU JC, POLSELLI R (2008) An anatomical study of the nasal superficial musculoaponeurotic system: surgical applications in rhinoplasty. *Arch Facial PlastSurg*, 10: 109-115.

SHASTRI D, TANDON P, SINGH A (2021) Nasal changes in different age groups. *Natl J Maxillofac Surg*, 12(3): 367-371.

SHOJA MM, OYESIKU NM, GRIESSENAUER CJ, RADCLIFF V, LOUKAS M, CHERN JJ, BENNINGER B, ROZZELLE CJ, SHOKOUHI G, TUBBS RS (2014) Anastomoses between lower cranial and upper cervical nerves: A comprehensive review with potential significance during skull base and neck operations, Part I: Trigeminal, facial, and vestibulocochlear nerves. *Clin Anat*, 27: 118-130.

STANDRING S (2016) The Anatomical Basis of Clinical Practice. *Gray's Anatomy*, 41st ed. Elsevier Ltd, pp 557-676.

Dimorphic comparative histological and histometric study of the lateral and medial knee menisci in male and female human cadavers

Waheeb Aggad[1], Gamal Abd El-Aziz[2], Mervat Halawani[2], Emad Hindi[2], Rasha AlShali[2], Raid Hamdy[2], Hamid Saleh[2]

[1] *Department of Anatomy, Faculty of Medicine, University of Jeddah, Jeddah, Saudi Arabia*

[2] *Department of Clinical Anatomy, Faculty of Medicine, King Abdulaziz University, Jeddah, Saudi Arabia*

SUMMARY

The knee menisci are fibrocartilaginous discs present in between the femur and the tibia. They play a pivotal role in withstanding the weight-bearing forces and help to maintain the stability of the knee joint. Descriptive knowledge of the menisci is essential to understand the mechanism and design of the appropriate management of their pathological lesions. Several investigations have identified the anatomical and morphological differences between the medial (MMi) and lateral menisci (LMi) in humans. What remains unclear, however, is the comparative analysis of histological and histometric parameters of these menisci, especially between males and females. To evaluate and compare the different histological, histometric and biochemical parameters of different structural components (collagen, proteoglycans, cellularity, and vascularity) of MMi and LMi in male and female human cadavers, twenty-four knee joints, 12 males and 12 females, were dissected, and the menisci were excised and labeled. The middle region of each meniscus was cross-sectioned and subjected to different histological, histometric and biochemical studies.

Histological examination of MMi and LMi in both males and females yielded several observations regarding different meniscal components; the orientation of collagen fibers was circumferential with intermingled radial fibers. Both fibroblasts and fibrochondrocytes were arranged singly or in rows alongside the direction of the collagen fibers. Also, the blood vessels were present toward the periphery, whereas the proteoglycans-rich areas were more evident in the inner region of each meniscus. Nevertheless, collagen fibers organization, safranin-O staining intensity, and cellular arrangement were all different between males and females. The analysis of these changes was further compared histometrically between MMI and LMi in males and females. The gained comparative histological, histometric and biochemical findings of this work are critical for providing detailed information on the microstructure and composition of both MMi and LMi in males and females. The present results also highlight the detrimental

Corresponding author:
Mervat Mohammed Halawani. Department of Clinical Anatomy, Faculty of Medicine, King Abdulaziz University, Jeddah, Saudi Arabia. Phone: +966569000060. E-mail: mhalwani@kau.edu.sa / skgtmmh@gmail.com

Submitted: June 25, 2023. **Accepted:** September 7, 2023

https://doi.org/10.52083/ZCPM8648

effects of histological structure on different meniscal injuries.

Key words: Meniscus – Collagen – Proteoglycan – Cellularity – Male – Female

INTRODUCTION

The management of meniscal injuries, which impair the proper function of the knee, remains difficult and challenging. Although several clinical options are available for the treatment of such injuries, complete cure of the damaged meniscus has proved difficult due to the limited healing capacity of the tissue (Ozeki et al., 2021).

The complex and multiple functions of menisci depend on their unique cellular and biochemical composition, perhaps more importantly on the organization and interactions of their constituents. In general, the basic structure of menisci is not homogeneous, and their composition differs with age, in injury or under pathological conditions (López-Franco and Gómez-Barrena, 2018; Battistelli et al., 2019).

Histologically, two types of cell populations have been identified in the meniscal cartilage; the fusiform cells, similar to the fibroblasts, located along the superficial zone of the meniscus, and the other polygonal cells, the fibrochondrocytes, located interior to the superficial margin. The collagen fibers, predominantly type I, form a network that entraps different types of cells in proteoglycans-rich extracellular matrix (McDevitt and Webber, 1990; Fox et al., 2015; Puetzer and Bonassar, 2016). It was also reported that the orientation of collagen fibers changes throughout the cross-sectional surface of the meniscus depending on the function of each region. Based on that, the meniscal structure consists of three distinct layers: a superficial layer, a lamellar layer, and a deep layer. The superficial layer is composed of randomly oriented fibers that provide a smooth and lubricated surface for articulation. The lamellar layer, immediately deep to the superficial layer, is also composed of randomly oriented fibers and interspersed with radially oriented fibers. While in the deep layer of the cartilage, fibers are arranged circumferentially and bound together by interspersed, radially oriented tie fibers to provide the structural support. This organization allows the conversion of vertically oriented compressive forces into circumferential hoop stresses distributed throughout the meniscus (Rattner et al., 2011; Andrews et al., 2014). On the other hand, two distinct regions of different collagen fibers exist; the inner one-third bundles having a radial pattern, and the outer two-thirds fibers are oriented in a circumferential manner (Cengiz et al., 2017; Danso et al., 2017).

Biochemically, the normal meniscal tissue is highly hydrated and predominantly composed of water (65-75%), while the remaining 20-25% consists of organic component, namely extracellular matrix proteins (ECM) and cells. The ECM that surrounds meniscus cells is largely composed of several types of collagens (75%), proteoglycans (GAGs) (17%) and small percentages of adhesion glycoproteins. Meniscus composition differs with age, in injury or under pathological conditions (Makris, 2011; Cengiz et al., 2017; Bahcecioglu et al., 2019).

Reviewing the literature, we found that there was some available data, which support that the women are more affected and burdened by knee osteoarthritis (OA) than men. Nevertheless, the etiology and implications for this sex difference remained unclear (Zhou et al., 2018; Pringle et al., 2019). In our previous study (Aggad et al., 2022), we found several differences of morphological and morphometric parameters of the MMi and LMi between males and females, which supported this gender-specific differences. Also, it was assumed that the alteration in cartilage composition, acting together with different walking mechanics between men and women, can potentially predispose women to a greater risk of OA (Blagojevic et al., 2010; Wise et al., 2012; Litwic et al., 2013; Kumar et al., 2015; Battistelli et al., 2019; Peshkova et al., 2022).

Also, it was documeted that the function of meniscal fibrocartilage is dependent mainly on the structural and biochemical components of ECM; during degenerative conditions, the changes of collagen and proteoglycan contents could impair cartilage integrity (Alaqeel et al., 2020). Therefore, we aimed in this work to evaluate and compare the

different histological, histometric, and biochemical parameters of the structural components (collagen, proteoglycans, cellularity, and vascularity) of MMi and LMi in both male and female human cadavers. Further insight into the basic science of meniscal structure is necessary for the diagnosis of different knee injuries and for guiding the treatment strategies for such diseases.

MATERIAL AND METHODS

Cadaveric material collection

Twenty-four human embalmed cadavers (12 males and 12 females), aged between 50 and 70 years, were chosen from the dissection lab of the department of Anatomy, faculty of medicine at King Abdulaziz University (KAU). The study was done under the approval of the Biomedical Ethics Research Committee unit at the Faculty of Medicine, KAU (HA-02-J-008). The normality of the cadavers' knee-joint regions was confirmed macroscopically at the time of sample collection. After removing the skin and muscles, the knee joints were dissected anteriorly by a longitudinal incision on each side of the knee-joint capsule, and by cutting the patellar ligament and the collateral ligaments transversely. To expose the menisci clearly, the joint capsule and the intra-articular ligaments (anterior and posterior cruciate ligaments) were cut to reveal the tibial plateau. The menisci in pairs of right (Rt) and left (Lt) sides, and from male and female cadavers, were excised gently by cutting their anterior and posterior attachments from the tibial plateau with scalpel blades. The menisci were then numbered, labeled, and kept in 10% buffered formalin solution for 1 week for the downstream experiments.

Histological Studies

Chemicals and reagents used in tissue processing and staining techniques were purchased from sigma-Aldrichunless otherwise stated. Tissue processing for histological techniques was performed using the protocol described recently by Charnwichai et al. (2023). Each meniscus was cut transversely at the middle point of the body to prepare 2 mm thick triangular pieces. Consequently, both femoral and tibial surfaces, as well as the inner and outer regions were exposed as shown in Figs. 1-4. The meniscal pieces were then immersed in 14% of Ethylene-diamine-tetra-acetic acid (EDTA) solution for 3 days to enhance the softening of the tissues. Following this step, the meniscal tissues were manually dehydrated in a graded series of ethanol concentration (50, 70, 80, 90, and 100%, for 20 min each), cleared with xylene for 20 min, and embedded in paraffin wax. A minimum of 6 sections, 5 μm thick each, were produced per block using LEICA RM 2255 (Leica Microsystem, Germany).

The sections were then stained by Hematoxylin and eosin (H&E), Masson Trichrome (MT) and Safranin-O (Saf-O) stains following the previously described methods by Bancroft et al. (2013);

Fig. 1.- Representative photomicrograph showing the gross appearance and the sectioning site of the MMi and LMi: sections were made across the radial width in the body middle-segment of each LM (A) and MM (B) respectively.

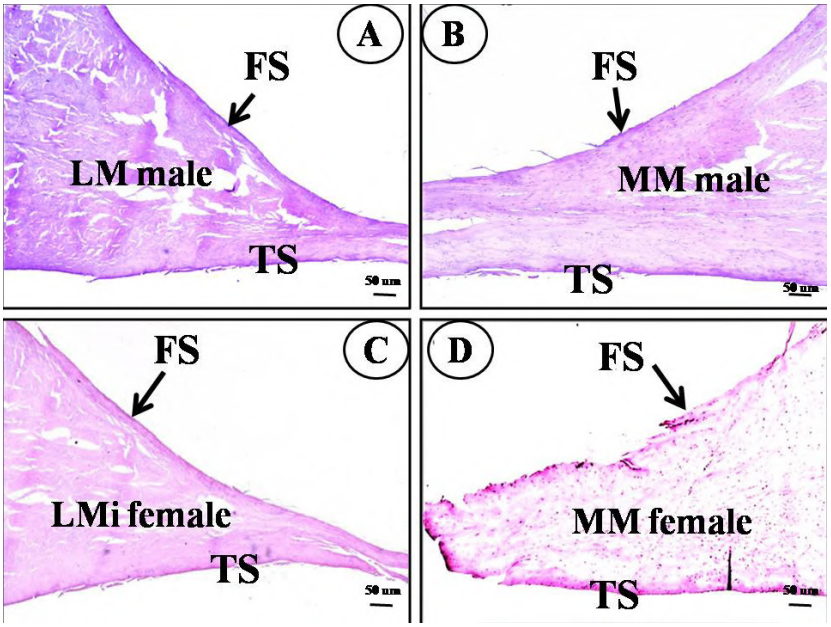

Fig. 2.- Cross sections from middle portion of LMi and MMi in male (**A,B**) and female (**C,D**) cadavers: FS = femoral surface, TS = tibial surface. H&E staining (x40). Scale bars = 50 µm.

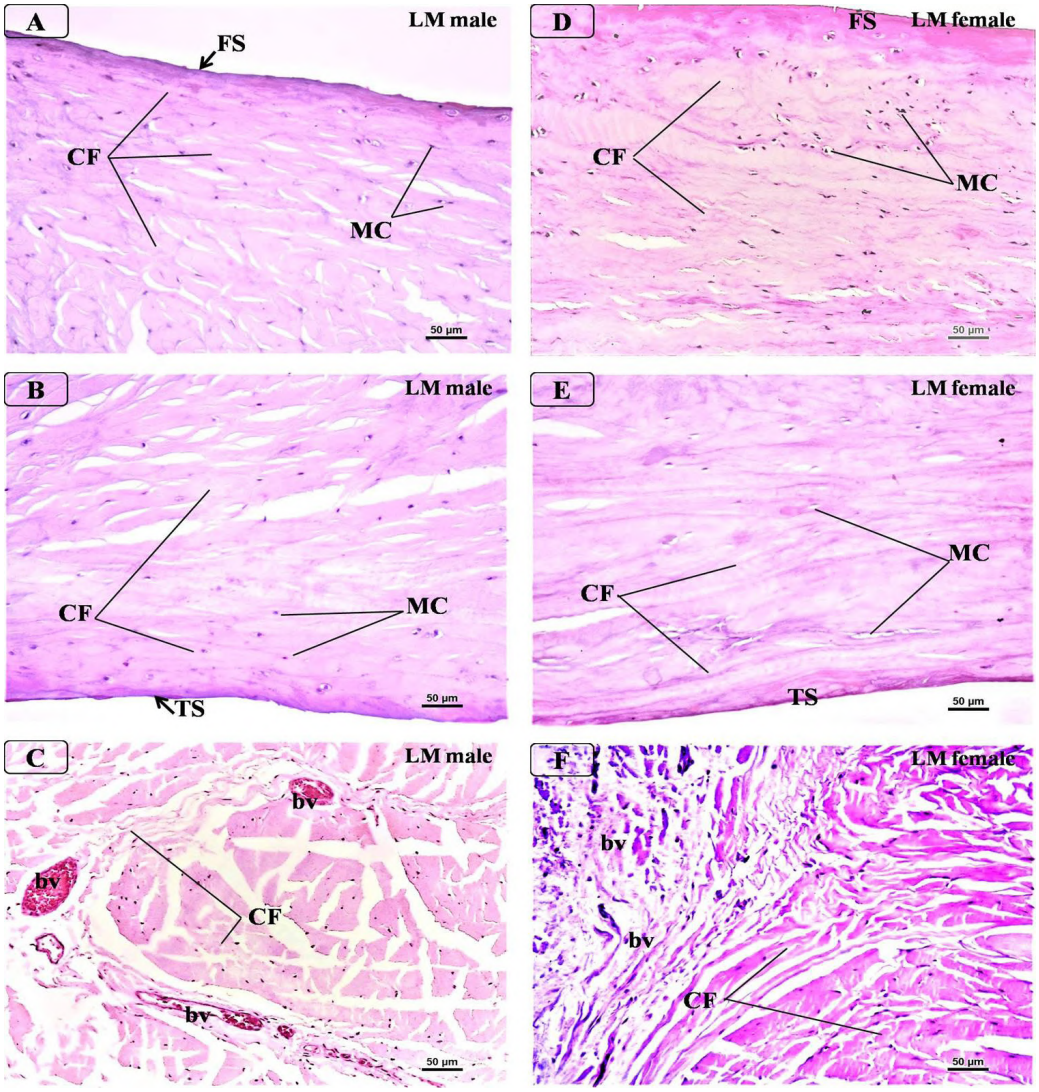

Fig. 3.- Cross sections LMi in male and female cadavers: **A**) femoral surface (FS) of male LM, **B**) tibial surface (TS) of male LM, **C**) peripheral part of male LM, **D**) femoral surface (FS) female LM, **E**) tibial surface (TS) of female LM, **F**) peripheral part of female LM. CF = collagen fibers, MC = meniscal cells, bv = blood vessels. H&E staining (x200). Scale bars = 50 µm.

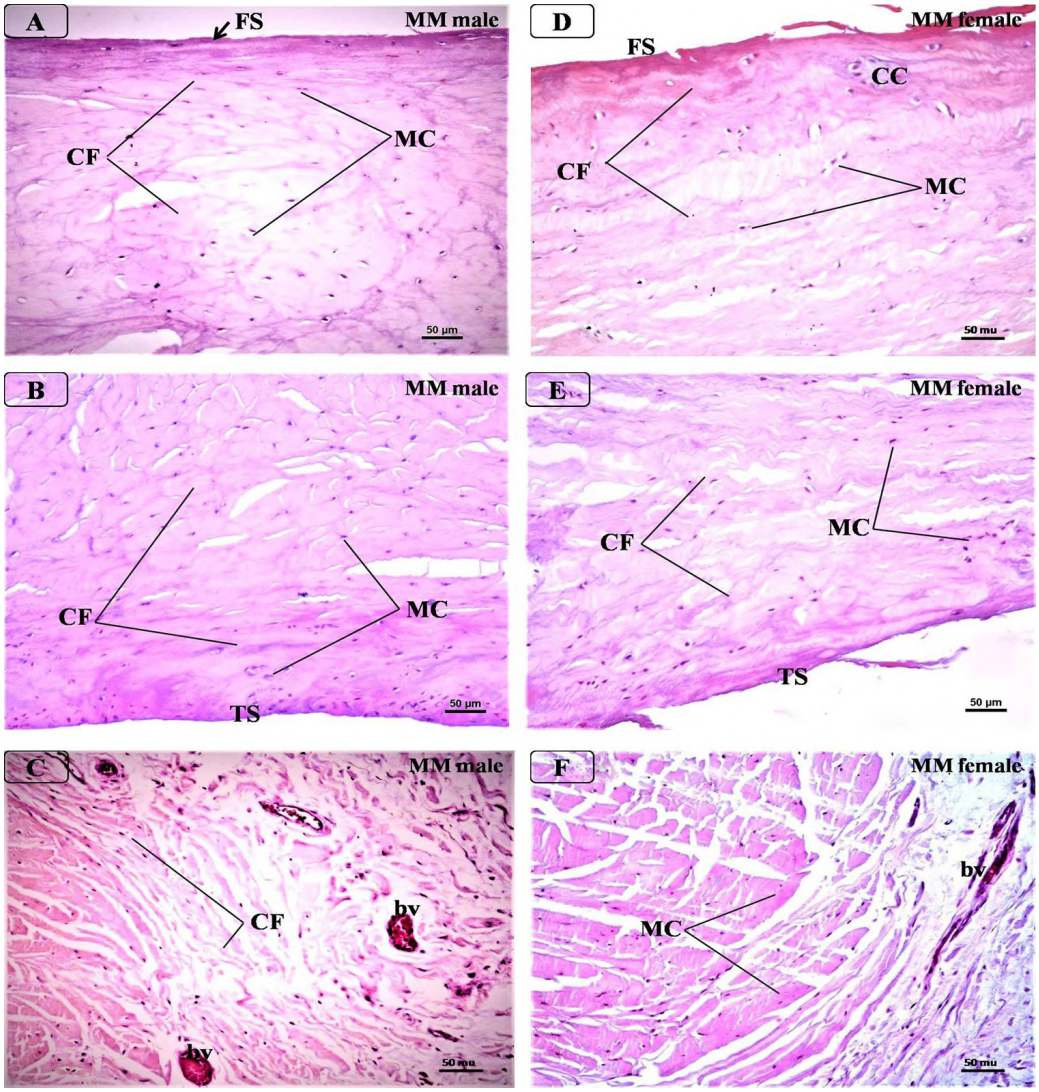

Fig. 4.- Cross sections MMi in male and female cadavers: **A**) femoral surface (FS) of male MM, **B**) tibial surface (TS) of male MM, **C**) peripheral part of male MM, **D**) femoral surface (FS) female MM, **E**) tibial surface (TS) of female LM, **F**) peripheral part of female MM. CF = collagen fibers, MC = meniscal cells, bv = blood vessels. H&E staining (x200). Scale bars = 50 µm.

H&E staining was used for depicting the general structure, cellularity and vascularity of tissues, MT stain was used to estimate the collagen fibers content and organization whereas Saf-O stain was used for assessing the content and distribution of the glycosaminoglycan (GAG) (Bancroft et al., 2013). Finally, all histological preparations were examined and representative photomicrographs, snapped under Olympus BX41 photomicroscope equipped with an Olympus DP25 digital camera (Olympus, Tokyo, Japan), were obtained.

Histometric Studies

With the use of image analysis software (Image J, version 1.45s, National Institutes of Health, Bethesda, USA), we obtained a quantitative assessment of the cellularity and vascularity of the tissues, the distribution and orientation of collagen fibers and Saf-O staining of proteoglycans. In brief, six photomicrographs were taken on each section at the magnification of X200. On each photo, the scoring system of degenerative changes adopted from Pauli et al. (2011) was used herein with some modifications to grade the morphological criteria in the tissues from (0) to (3) as illustrated in Table 1.

Biochemical Analyses

a) Determination of hydroxyproline (Hyp) content

The amount of free hydroxyproline in the meniscal extracts was quantified utilizing the method described previously by Reddy and Enwemeka (1996). The LMi and MMi pieces were homogenized

Table 1. Histometric analysis of the menisci. A modified scoring system of the degeneration changes in meniscal tissues based on histometric analysis of 4 parameters. Each parameter was given a score from 0 to 3 depending on the observational findings.

Criteria	Histological features	Score
Cellularity (H & E)	A. Normal arrangement of cells	0
	B. Disorderly arrangement of cells	1
	C. Hypercellularity	2
	D. Hypocellularity (empty lacuna)	3
Vascularity (H & E)	A. No vascularity	0
	B. Little vascularity	1
	C. Moderate vascularity	2
	D. Extensive vascularity	3
Collagen fibers (MT)	A. Well-arranged collagen fibers	0
	B. Moderately arranged collagen fibers	1
	C. Slightly arranged collagen fibers	2
	D. Distorted collagen fibers	3
GAG staining (Saf-O)	A. Minimal pink-red staining	0
	B. Slightpink-red staining	1
	C. Moderate pink-red staining	2
	D. Strong pink-red staining	3

and hydrolyzed in 2N of sodium hydroxide (Fisher Scientific, R74700501A). The samples were then incubated for 6 hours at 105°C, after which they were mixed with a buffered chloramine-T reagent (sigma, 402869, 98%). The oxidation was allowed to proceed for 25 minutes at room temperature, and the reaction started by adding 0.5M of a freshly prepared Ehrlich's reagent (Sigma, D2004), followed by incubating samples at 65°C for 20 minutes with shaking. Each sample was measured in duplicate, and the absorbance of reddish-purple complex in each sample was measured at A_{530} nm using a microplate reader (Thermo, Kyoto, Japan). The collagen value was calculated, assuming that 13.5% of collagen is Hyp, which was used as the conversion factor for calculating collagen content.

b) Determination of Proteoglycan content

The sulphated glycosaminoglycan content of meniscal tissues was quantified using the Dimethyl methylene Blue (DMB) assay previously described in Farndale et al. (1986). First, the DMB color reagent was prepared by dissolving 16 mg of DMB (Serva Fein biochemica, 931418-92-7) in 1:1 water containing 3.04 g glycine, 2.37 g NaC1 and 95 ml 0.1 M HC1, to give a solution at pH 3.0. To digest the interfering proteins or glycoproteins, LMi and MMi tissue samples were incubated with 1ml of papain solution made of (20 mM sodium phosphate buffer (pH 6.8), 1 mM EDTA, 2 mM dithiothreitol, and 300 µg papain) at 65°C for 6 hours to ensure a full digestion of all tissues. For the selective digestion of glycosaminoglycan, the papain-digested samples were incubated in chondroitin AC lyase (merk, 904757) for 30 min at 37°C, after which they were mixed with the previously prepared DMB to form the sulphated GAG-DMB complex. The colour reactivity of this complex was measured at A_{525}nm using a microplate reader (Thermo, Kyoto, Japan).

Data Analysis

Data were analyzed using IBM SPSS Statistics software for Windows, version 23 (IBM SPSS, IBM Corp., Armonk, N.Y., USA). Shapiro-Wilk test was used to evaluate normal data distribution. Statistical comparisons between male and female made by unpaired student *"t"* test and in the same group by paired student *"t"* test. Data were expressed as mean ±standard deviation (SD) and a *P*-value ≤ 0.05 was considered significant.

RESULTS

Histological findings of LMi versus MMi in male and female cadavers

The cross sections of MMi and LMi allowed studying of their fibrocartilagee from both the femoral and the tibial surfaces. Our microstructure analysis

addressed the compositional aspects of the menisci, and our approach was oriented to the meniscal cells, the extracellular matrix components, particularly collagen fibers and proteoglycans. Additionally, we explored the vascularity in various regions of the menisci. We found variations in the spatial distribution of these elements and in architectural characteristics among MMi and LMi in both sexes.

a) H & E-staining

Tables 2 and 3 presented the histological analyses of H&E-stained sections derived from male and female groups. The lateral and medial menisci were separately compared between genders; refer to Tables 2 and 3 and the related figures for a concise presentation of the key histology findings.

b) MT staining

Sections stained with MT allowed the identification of the new (blue) and old (red) collagen fibers in the meniscus. The majority of male LMi and MMi tissues depicted in Fig. 5A and B exhibited a robust MT reactivity, implying a greater presence of collagen. Nonetheless, certain MMi sections

Table 2. Comparison of histological findings in lateral menisci between male and female groups.

	Male LMi (Figure 3 A, B, C):	Female LMi (Figure 3 D, E, F):
Collagen fibers Oriantation and Vascularity	▪ The collagen fibers demonstrated an organized orientation, aligning parallel to the surfaces of both the femur and tibia. ▪ In the inner portion, the collagen fibers exhibited a circular orientation, while in the outer portion, they displayed a circumferential arrangement characterized by fewer tightly packed radial fibers and a higher density of blood vessels.	▪ Compared to the LMi in males, the collagen fibers oriented towards the femoral and tibial surfaces exhibited a heightened radial alignment. ▪ Within the inner portion, the fibers displayed a densely concentrated radial orientation, whereas in the outer segment, they showcased a circumferential arrangement featuring closely packed radial fibers and a reduced number of blood vessels.
Cellularity	▪ The predominant cellular type in the meniscus was fibroblast-like, particularly in proximity to the surfaces. In the central region, cells exhibited a polygonal shape reminiscent of fibrochondrocytes.	▪ Meniscal cells, displaying a fibroblast-like morphology, were predominantly situated near the surfaces, while a higher concentration of fibrochondrocytes was evident in the central region.

Table 3. Comparison of histological findings in medial menisci between male and female groups.

	Male MMi (Figure 4 A, B, E):	Female MMi (Figure 4 D, E, F):
Collagen fibers Oriantation and Vascularity	▪ The alignment of collagen fibers bore similarity to LMi, albeit with a less regular arrangement of superficial fibers near the surfaces. ▪ In the inner region, the fibers exhibited a network that was less tightly packed compared to LMi. Conversely, in the outer region, they demonstrated a circumferential orientation intertwined with radial fibers and a lower density of blood vessels.	▪ The collagen fibers in female MMi were not as densely packed as those in male MMi. In certain regions, the fibers appeared less compact and disorganized. ▪ Both the inner and outer portions exhibited an uneven distribution of collagen fibers, alongside fewer blood vessels intermixed within the matrix.
Cellularity	▪ The arrangement of meniscal cells resembled that of LMi; nonetheless, a greater presence of fibroblast-like cells was detected near the surface and central regions.	▪ The arrangement of meniscal cells was characterized by irregular patterns, and instances of increased cell density were noted in the form of clusters near the surfaces of the meniscus.

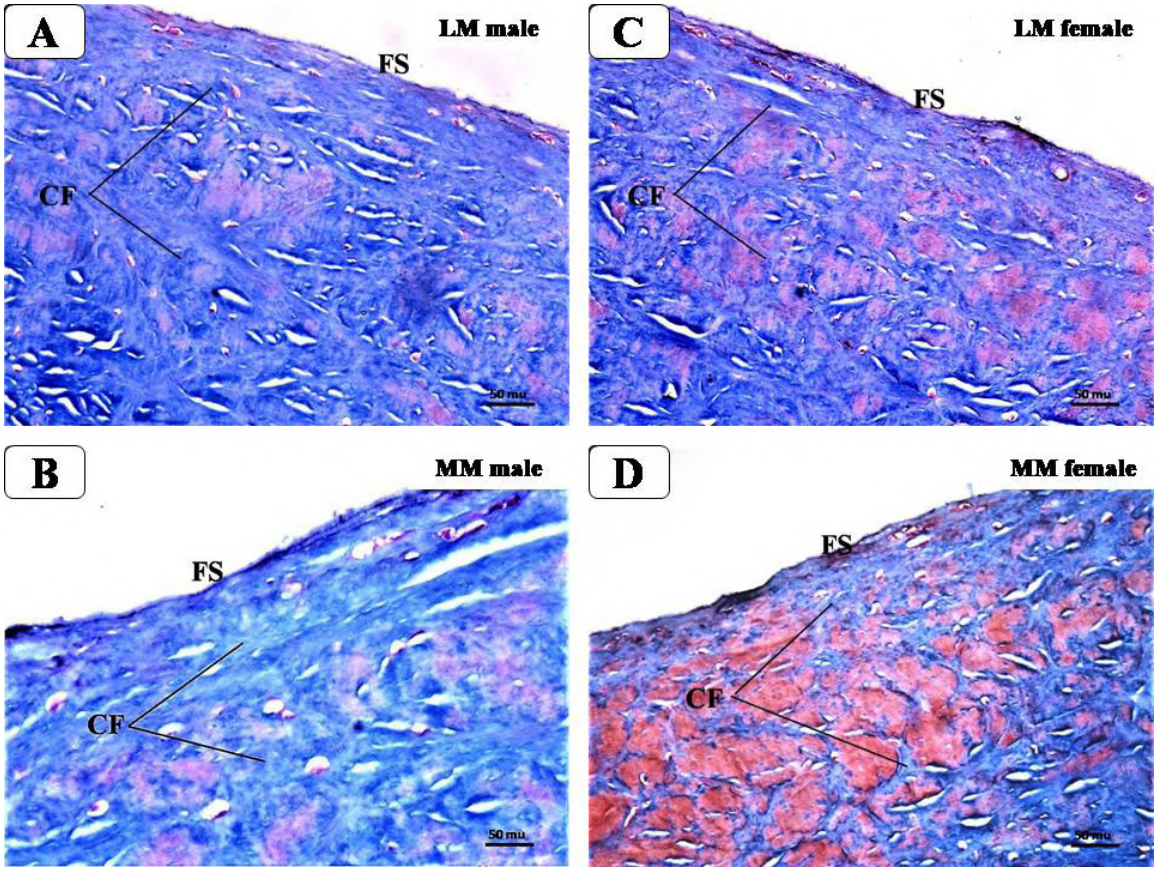

Fig. 5.- Cross sections LMi and MMi in male (**A,B**) female (**C, D**) cadavers: Masson Trichrome staining (x200). Scale bars = 50 µm.

displayed reduced levels of newly formed collagen fibers compared to LMi, evident through weak blue staining. Furthermore, the collagen fiber density on the femoral side of MMi was less than that on the tibial side. Within female menisci, sections with MT (Fig. 5C, D) exhibited comparatively weaker staining for both LMi and MMi, signifying a diminished collagen content, particularly noticeable in MMi when compared to their male counterparts. Additionally, it was evident that the density of fibers facing the femoral side was lower than those oriented toward the tibial side.

c) Saf-O staining

Saf-O statining was utilized to visualize the presence of proteoglycans (GAGs) within the meniscal tissue, indicated by a pink to red coloration. Both in males and females, a notable difference in the intensity of Saf-O staining (represented by a red hue) were between the peripheral (Fig. 6) and the central region (Fig. 7) of both LMi and MMi. Notably, both LMi and MMi showcased heightened GAG content in their central regions compared to the peripheral regions, where GAG stating was less prominent and sporadic. Upon comparing male and female menisci, a diminished stating intensity was observed in the peripheral parts of female LMi and MMi when contrasted with their male counterparts. Nevertheless, the central areas of female LMi demonstrated a more robust staining intensity when compared to male menisci.

Histometric findings of LMi versus MMi in male and female cadavers

Table 4 and Fig. 8 present the histometric findings encompassing cellularity, vascularity, collagen fiber arrangement, and Safranin-O staining for both male and female menisci. Our analysis unveiled significant alterations in microstructural integrity, evident by the cellular disorganization and increased cell populations within male MMi compared to LMi ($P = 0.01$). Conversely, the distribution of cells within the female menisci exhibited no significant change, ($P= 0.39$). Furthermore, while statistical significance wasn not reached, a more pronounced degree of cellular disorganization was observed in female LMi when compared to its male equivalent. This similar trend of cel-

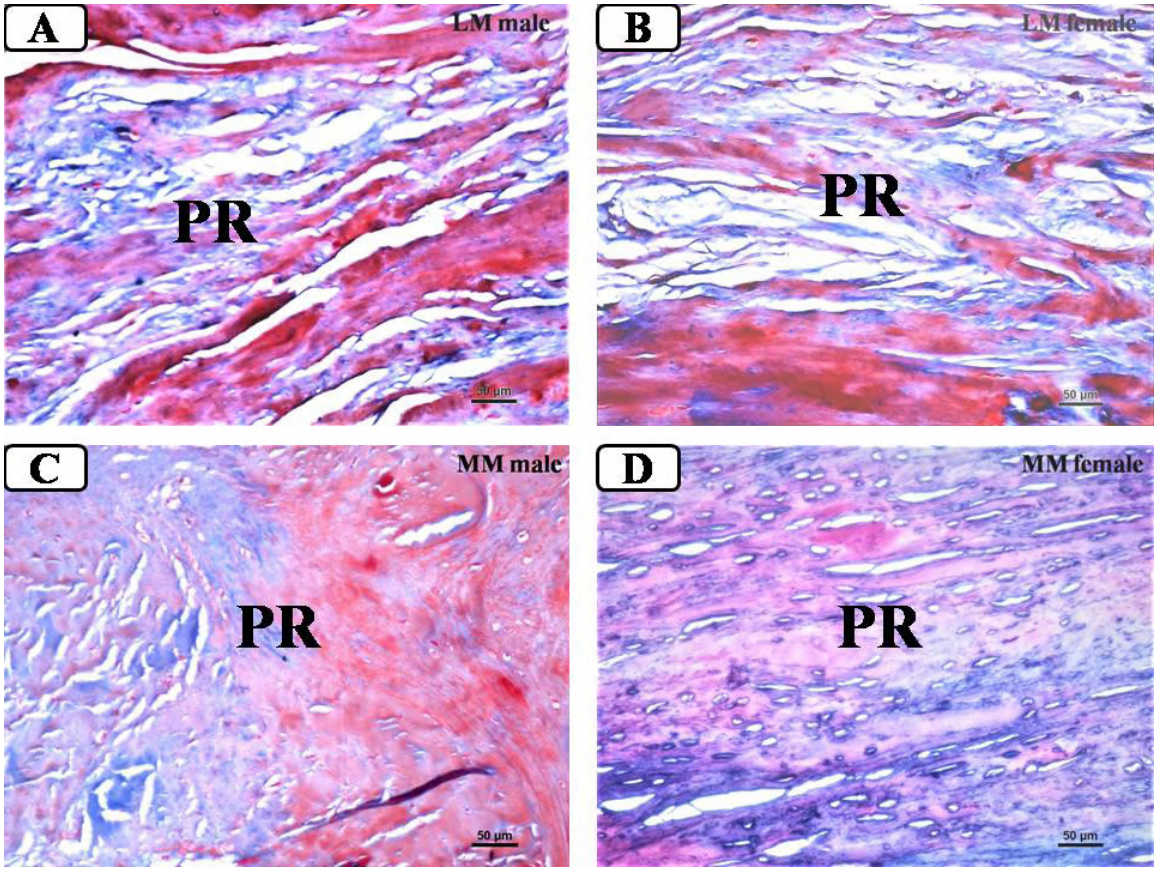

Fig. 6.- Saf-O-stained sections in the peripheral regions (PR) of male LMi (**A**) and female LMi (**B**), male MMi (**C**) and female MMi (**D**): Saf-O staining (x200). Scale bars = 50 µm.

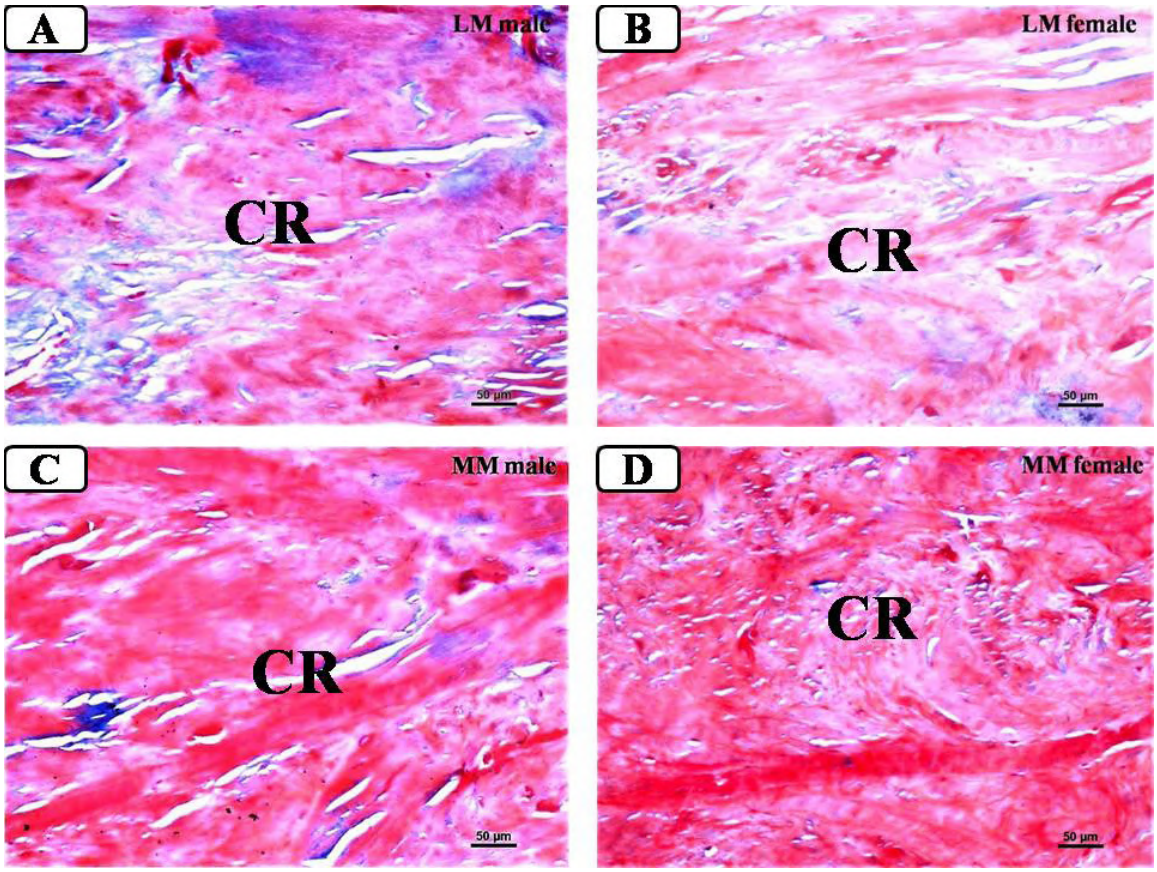

Fig. 7.- Saf-O-stained sections in the central regions (CR) of male LMi (**A**) and female LMi (**B**), male MMi (**C**) and female MMi (**D**): Saf-O staining (x200). Scale bars = 50 µm.

Table 4. Histometric findings of MM versus LM in male and female cadavers: Data were expressed as mean+/- Standard deviation. P: significance LMi versus MMi; P: significance male versus female.

Parameters	LMi (males)	MMi (males)	LMi (females)	MMi (females)
Cellularity	1.48 ± 0. 24	1.72 ± 0. 18	1.66 ± 0. 33	1.77 ± 0. 28
Significance	-	^{1}P =0.0111	^{2}P=0.1407	^{1}P=0.3881 ^{2}P=0.608
Vascularity	2.16 ± 0. 54	2.42 ± 0. 38	2.55 ± 0. 75	2.77 ± 0. 66
Significance	-	^{1}P =0.1864	^{2}P=0.1579	^{1}P=0.4537 ^{2}P=0.1257
Collagen fibers	1.23 ± 0. 15	1.54 ± 0. 17	1.62 ± 0. 22	1.66 ± 0. 33
Significance	-	^{1}P =0.0001	^{2}P=0.0001	^{1}P=0.7301 ^{2}P=0.2749
GAG staining	2.86 ± 0. 38	2.74 ± 0. 43	2.60 ± 0. 36	2.56 ± 0. 52
Significance	-	^{1}P =0.4765	^{2}P=0.0994	^{1}P=0.8286 ^{2}P=0.3655

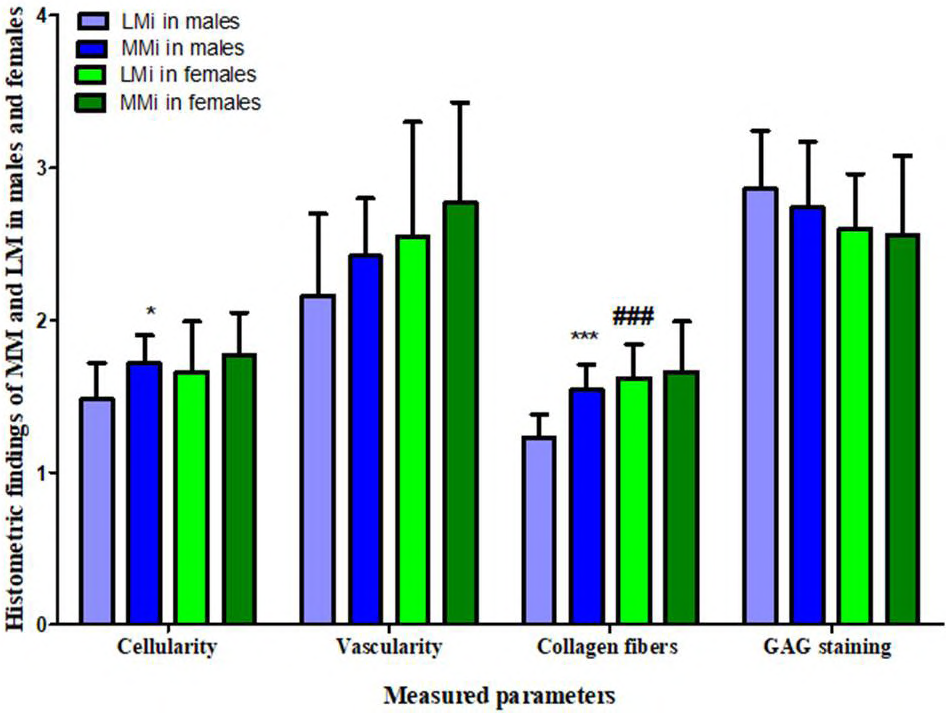

Fig. 8.- Histometric findings of MM versus LM in male and female cadavers: Data were expressed as mean ± SD, (*) represents the significance in LMi versus MMi while (#) is the significance male versus female.

lular modification manifested when comparing MMi between male and female groups.

In addition, MMi demonstrated an elevated degree of vascularity relative to LMi in both male and female groups, although without reaching statistical significance (*P*= 0.19 and 0.45 for male and female menisci, respectively). Likewise, a marginal yet statistically insignificant augmentation in vasculatrity was discerned in both female menisci when compared to their male counterparts. interestingly, and in line with the histological observations, a significant disruption in collagen fiber

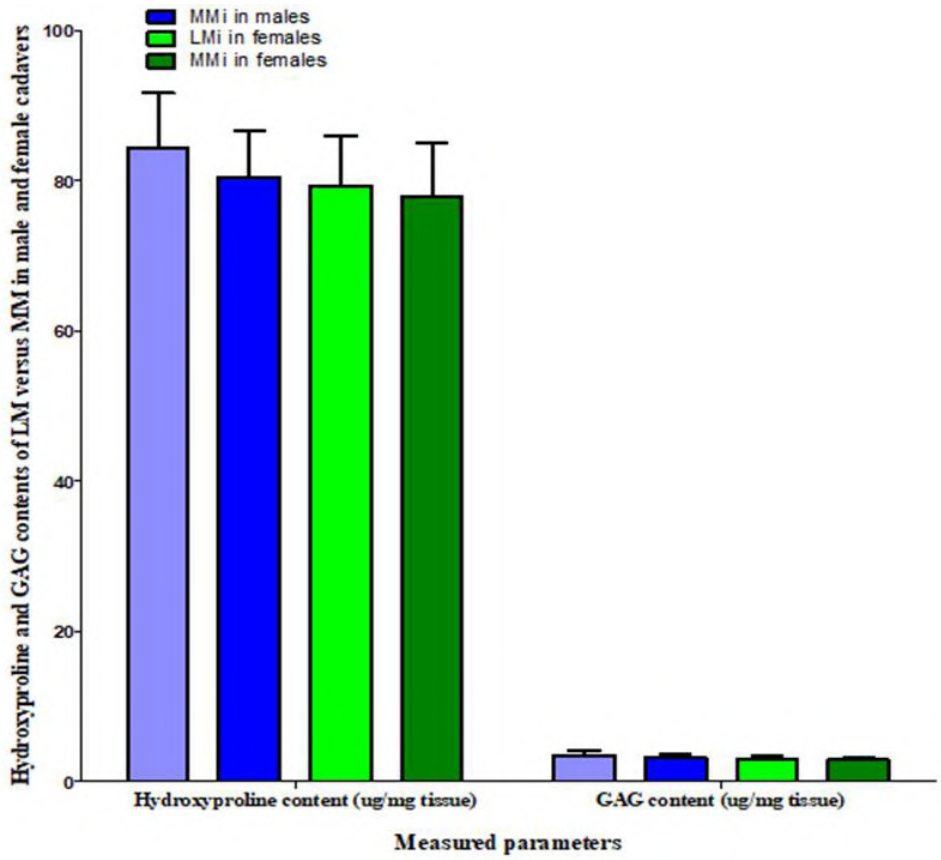

Fig. 9.- Hydroxyproline and GAG contents of LM versus MM in male and female cadavers: Data were expressed as mean ± SD. *: significance LMi versus MMi; #: significance male versus female.

Table 5. Hydroxyproline and GAG contents of LM versus MM in male and female cadavers.

Parameters	LMi (males)	MMi (males)	LMi (females)	MMi (females)
Hydroxyproline content (ug/mg tissue)	84.42 ± 7.24	80.55 ± 6.15	79.34 ± 6.68	77.82 ± 7.33
Significance	-	^{1}P =0.0783	^{2}P=0.0878	^{1}P=0.6008 ^{2}P=0.3337
GAG content(ug/mg tissue)	3.5 ± 0.66	3.2 ± 0.48	3.1 ± 0.34	2.9 ± 0.23
Significance	-	^{1}P =0.2162	^{2}P=0.0754	^{1}P=0.1056 ^{2}P=0.0637

arrangement was evident in MMi relative to LMi within male group (*P*= 0.001). This disarrangement was significantly more noticeable in the LMI of female participants when juxtaposed with the LMi of the male group (*P*= 0.001). A comparable albeit statistically insignificant pattern of disorganization was also observable in the MMI of the female cohort in comparison to their male counterparts.

Biochemical results

As shown in Table 5 and Fig. 9, the average hydroxyproline content was observed to be greater in LMi compared to MMi in both male and female menisci. Additionally, a higher hydroxyproline content was noted in the lateral and medial menisci of males when contrasted with their respective female counterparts. Although these observations

did not attain statistical significance, they aligned with the aforementioned microstructure examinations and histometric analyses of the meniscal tissues. The decreased hydroxyproline content in the female medial and lateral menisci suggested a lower collagen content within these tissues. Regarding GAG content, the mean values were also found to be higher in LMi compared to MMi in both male and female groups. The increased GAG content was also reflected on both male menisci when compared to those of the female group.

DISCUSSION

The microstructure of the extracellular matrix (ECM) components as well as cellularity and vasculatrity of the meniscus were specifically investigated in order to find and compare the structural disparities between the lateral and medial menisci within both male and female subjects. The motivation for conducting this study stemmed from the fact that the basic knowledge of meniscal cartilage architecture and gender-specific differences would be of great value, as it provides a deep understanding and a customized interpretation for the indications and outcome of regenerative, tissue repair and engineering strategies for the meniscal injuries (Cengiz et al., 2017; Pereira et al., 2019).

In the current study, the findings revealed distinctions in the organization and distribution of collagen fibers, cells, and blood vessels between male and female menisci. In both genders, the orientation of collagen fibers differed between the surface and deeper layers in all meniscal regions, with subtle variations observed in both lateral (LMi) and medial (MMi) menisci. This observation aligns with the studies by Makris et al. (2011) and Baker et al. (2011), which similarly highlighted the site- and depth-specific arrangement of collagen fibers that enhance the meniscus's ability to withstand tensile forces.

Despite the already established variability in collagen fiber orientation in MMi and LMi, we found that some female MMi displayed loose and unorganized collagen fibers distribution near the surfaces and in the inner region of the meniscus. This was further associated with irregular cellular arrangement and the presence of cell clusters. The above findings were supported by those of MT sections, which showed weaker reaction, particularly that of MMi in female group suggesting less collagen content. The density of the collagen fibers of the femoral side was even lower than the opposing tibial side in female menisci. Interestingly and consistent with the microstructural findings, quantitative image analysis of these sections showed significant disturbance in collagen fiber arrangement in female menisci when compared to those of male, which exhibited more dominance in the LMi among both groups.

We further extended our analysis to measure the amount of collagen in each meniscus by the assessment of hydroxyproline content. Collagen was found higher in male menisci when compared to female, and was once again higher in LMi than MMi in both male and female groups. Based on the above observations, we proposed that the menisci of female knees possess lower collagen content and less organization of ECM than those of male joints, and hence they are more prone to degeneration. It was proposed that knee degeneration is linked to the disruptions in particular structural elements rather than being a generalized effect across all histological components (Våben et al., 2020; Warnecke et al., 2020). Further investigation is therefore necessary to determine the precise relationship between these deficits or disarrangements and the overall degenerative process.

In addition, the previous work by Katsuragawa et al. (2010) showed that, in spite of the modest histological changes in the degenerating menisci, there was an enhanced mRNA expression of procollagen gene and ECM components. The increased expression of procollagen was not, however, proportional to protein content in the tissues, as the [^{3}H] proline incorporation was only modest in the degenerating menisci, suggesting an impaired collagen synthesis. We also assumed in this work that the overt matrix gene expression could be the result of a reparative response that occurred within OA menisci. The above findings and this speculation in fact explain why we noticed more collagen fiber content in LMi than MMi, irrespective of being more disarranged in female menisci. This difference between LMi and MMi is also reflected in knee biomechanics. It was

reported that MM covers 64% of the medial tibial plateau, while LM covers 84% of the lateral tibial plateau (Park et al., 2017). Thus, LM is responsible for most of the load transmission within the lateral compartment (up to 70%) while MM is responsible for 50% within its respective compartment. LM is more mobile, while the more static MM is known to play an additional secondary role as a joint stabilizer to resist the anterior tibial displacement (Masouros et al., 2008; Bloecker et al., 2012). Due to this spatial structural and conformation variability, the LM shows greater degree of activity and more stability compared with MMi (Swamy et al., 2018).

We found an alteration in the GAGs staining pattern of Safranin-O sections in which the high intensity areas of GAGs were more pronounced in the inner region of menisci in both genders. We also observed a regional and zonal variation of GAGs in the menisci. In accordance, it was documented that the inner two-thirds contained a relatively higher proportion of proteoglycans than the outer one-third (Melrose et al., 2005; Sanchez-Adams and Athanasiou, 2009).

The increased GAGs staining in the LMi vs MMi in female group was confirmed by the biochemical evaluation of GAGs content in the corresponding menisci. In contrast, GAGs histological findings seemed contradictory to those of biochemical results in the male group. Despite these discrepancies, the total amount of GAGs measured in female menisci was less than that of male samples. In fact, any changes in the GAGs synthesis and organization can lead to extracellular framework perturbation and, consequently, render the female menisci more vulnerable to degeneration. In line with our observation, López-Franco et al. (2016) reported a tendency towards proteoglycan reduction in human OA menisci. Also, it was stated that GAGs play an important role in the hydration of meniscal tissue and its viscoelastic ability to resist compression and loading. Accordingly, regional variations can be observed in terms of viscoelastic properties (Mahmood et al., 2019; Murphy et al., 2019).

In the current study, the examination of the meniscal cellularity revealed the presence of spindle-shaped fibroblasts-like cells without lacunae at peripheral two-thirds, which decreased as we extend toward the inner concave margin of the menisci. We also noticed round or oval cells lying in the lacunae resembling cartilage cells, which were interspersed toward the inner margin. Our findings were in accordance with previous studies done by Niu et al. (2016) and Cengiz et al. (2017). They reported the distribution of the meniscal cells as three different morphologies; the superficial zone contains fusiform cells directly located beneath the tissue surface; the outer one-third contains fibroblast-like cells with elongated morphology; and the inner two-thirds contain fibrochondrocytes with polygonal or oval morphology.

Our histometric analysis showed alteration in term of cellular disorganization and increased cell populations in male MMi versus LMi. It is also worth noting the increase in cellular disarray in female MMi and LMi, as opposed to their male counterparts, although this increase was not statistically significant. Also, a progressive decline in cell density was observed from the outer vascular zones to the inner avascular zones in both LMi and MMi.

In accordance with our findings, it was reported that different types of cells are distributed in a regional-specific manner and account for the double nature of the meniscus. In the outer zone, fibrocyte-like cells reflect the fibrous pattern of the meniscus and contribute to the healing capability, while in the inner zone chondrocyte-like cells are responsible for the cartilaginous-like behavior of the tissue (Sanchez-Adams and Athanasiou, 2009; Makris et al., 2011; Osawa et al., 2013; Pereira et al., 2014; Chahla et al., 2021).

In this study, we noticed that both LMi and MMi displayed some differences with respect to vascularity, in which the periphery of MM is slightly more vascularized (10–30%) than LM (10-25%). Correspondingly, Gupta et al. (2018) noted that the highest vasculature rates were recorded in the anterior horn of the MMi, ranging from 22% to 83% (with an average of 40%), while the meniscal body exhibited vascular indices spanning from 20% to 62% (averaging at 30%). In the case of the LMi, heightened vasculature was particularly evident in two key areas: the anterior horn, displaying rates of 18% to 95% (with an average of 48%),

and the posterior horn, registering rates ranging from 22% to 52% (averaging at 31%).

Also, previous studies have mentioned that each meniscus is classified into three zones: vascularized, intermediate, and avascular. Therefore, tears within the vascular zone have a higher healing rate comparing with that in avascular zone whereas the white–white zone is more susceptible to degenerative and posttraumatic lesions and the damaged menisci have limited repair capacity in the avascular region of meniscus (Majeed et al., 2015; Cinque et al., 2019).

At the end, this study provides valuable information about the microstructure of medial and lateral menisci, including collagen fiber orientation, cell arrangement, and blood vessel distribution, shedding light on their histological and biochemical differences in males and females. However, our study utilizes cadaveric samples, which might not fully represent the dynamic nature of living tissue. Also, while comparing between males and females is valuable, the study does not explicitly discuss why gender differences might exist or how hormonal or physiological factors could contribute to the observed variations. Moreover, although this study offers valuable insights into the histological and biochemical characteristics of the menisci, it does not directly correlate these findings with clinical conditions or pathological lesions, potentially limiting the practical implications. Nevertheless, this study could be further followed by conducting additional research that discuss the potential functional implications and integrates the clinical correlations of its findings.

CONCLUSION

Our work provides the first line of entry into the comparative analysis of knee menisci. The histological and histometric data gained here are crucial to give additional information on microstructure of MMi and LMi in males and females. This is necessary for the correlation with different meniscal injuries and degeneration that can help in reconstructive and surgeries of knee. Taken together, we hypothesised that the main structural features cellularity, collagen structure and vascularity exhibited differences in MMi and LMi in males and females, which are expected to influence the repair processes.

ACKNOWLEDGEMENTS

The authors sincerely thank those who donated their bodies to science so that anatomical research and teaching could be performed. Results from such research can potentially increase scientific knowledge and can improve patient care. Therefore, these donors and their families deserve our highest respect.

REFERENCES

AGGAD WS, ABD EL-AZIZ GS, HAMDY RM, SALEH HA, ALYAZIDI AS (2022) Comparative morphological and morphometric study between medial and lateral menisci in aged male and female human cadavers. *J Microsc Ultrastr,* 10(4): 159.

ALAQEEL M, GRANT M, EPURE L, SALEM O, ALSHAER A, HUK O, BERGERON S, ZUKOR D, KC R, IM H (2020) Link N suppresses interleukin-1β-induced biological effects on human osteoarthritic cartilage. *Eur Cells Materials,* 39: 65-76.

ANDREWS SH, RATTNER JB, ABUSARA Z, ADESIDA A, SHRIVE G, RONSKY JL (2014) Tie fibre structure and organization in the knee menisci. *J Anat,* 224(5): 531-537.

BAHCECIOGLU G, BILGEN B, HASIRCI N, HASIRCI V (2019) Anatomical meniscus construct with zone specific biochemical composition and structural organization. *Biomaterials,* 218: 119361.

BAKER BM, SHAH RP, HUANG AH, MAUCK RL (2011) Dynamic tensile loading improves the functional properties of mesenchymal stem cell-laden nanofiber-based fibrocartilage. *Tissue Eng Part A,* 17(9-10): 1445-1455.

BANCROFT JD, LAYTON C, SUVARNA SK (2013) Bancroft's theory and practice of histological techniques. Churchill Livingstone Elsevier.

BATTISTELLI M, FAVERO M, BURINI D, TRISOLINO G, DALLARI D, DE FRANCESCHI L, GOLDRING SR, GOLDRING MB, BELLUZZI E, FILARDO G, GRIGOLO B, FALCIERI E, OLIVOTTO E (2019) Morphological and ultrastructural analysis of normal, injured and osteoarthritic human knee menisci. *Eur J Histochem,* 63(1): 2998.

BLAGOJEVIC M, JINKS C, JEFFERY A, JORDAN K (2010) Risk factors for onset of osteoarthritis of the knee in older adults: a systematic review and meta-analysis. *Osteoarthritis Cartilage,* 18(1): 24-33.

BLOECKER K, WIRTH W, HUDELMAIER M, BURGKART R, FROBELL R, ECKSTEIN F (2012) Morphometric differences between the medial and lateral meniscus in healthy men–a three-dimensional analysis using magnetic resonance imaging. *Cells Tissues Organs*, 195(4): 353-364.

CENGIZ IF, PEREIRA H, PÊGO JM, SOUSA N, ESPREGUEIRA MENDES J, OLIVEIRA JM, REIS RL (2017) Segmental and regional quantification of 3D cellular density of human meniscus from osteoarthritic knee. *J Tissue Eng Regen Med,* 11(6): 1844-1852.

CHAHLA J, PAPALAMPROU A, CHAN V, ARABI Y, SALEHI K, NELSON TJ, LIMPISVASTI O, MANDELBAUM BR, TAWACKOLI W, METZGER MF (2021) Assessing the resident progenitor cell population and the vascularity of the adult human meniscus. *J Arthrosc Rel Surg*, 37(1): 252-265.

CHARNWICHAI P, TAMMACHOTE R, TAMMACHOTE N, CHAICHANA T, KITKUMTHORN N (2023) Histological features of knee osteoarthritis treated with triamcinolone acetonide and hyaluronic acid. *Biomed Rep,* 18(6): 1-8.

CINQUE ME, DEPHILLIPO NN, MOATSHE G, CHAHLA J, KENNEDY MI, DORNAN GJ, LAPRADE RF (2019) Clinical outcomes of inside-out meniscal repair according to anatomic zone of the meniscal tear. *Orthop J Sports Med*, **7**(7): 2325967119860806.

DANSO EK, OINAS JM, SAARAKKALA S, MIKKONEN S, TÖYRÄS J, KORHONEN RK (2017) Structure-function relationships of human meniscus. *J Mech Behav Biomed Mat,* 67: 51-60.

FARNDALE RW, BUTTLE DJ, BARRETT AJ (1986) Improved quantitation and discrimination of sulphated glycosaminoglycans by use of dimethylmethylene blue. *Biochim Biophys Acta,* 883(2): 173-177.

FOX AJ, WANIVENHAUS F, BURGE AJ, WARREN AF, RODEO SA (2015) The human meniscus: a review of anatomy, function, injury, and advances in treatment. *Clin Anat,* 28(2): 269-287.

GUPTA M, GOYAL PK, SINGH P, SHARMA A (2018) Morphology of intra-articular structures and histology of menisci of knee joint. *Int J Appl Basic Med Res,* 8(2): 96-99.

KATSURAGAWA Y, SAITOH K, TANAKA N, WAKE M, IKEDA Y, FURUKAWA H, TOHMA S, SAWABE M, ISHIYAMA M, YAGISHITA S (2010) Changes of human menisci in osteoarthritic knee joints. *Osteoarthr Cartilage,* 18(9): 1133-1143.

KUMAR D, SOUZA RB, SUBBURAJ K, MACLEOD TD, SINGH J, CALIXTO NE, NARDO L, LINK TM, LI X, LANE NE (2015) Are there sex differences in knee cartilage composition and walking mechanics in healthy and osteoarthritis populations? *Clin Orthop Relat Res,* 473: 2548-2558.

LITWIC A, EDWARDS MH, DENNISON EM, COOPER C (2013) Epidemiology and burden of osteoarthritis. *Brit Med Bull,* 105(1): 185-199.

LÓPEZ-FRANCO M, GÓMEZ-BARRENA E (2018) Cellular and molecular meniscal changes in the degenerative knee: a review. *J Exp Orthop*, 5(1): 1-8.

LÓPEZ-FRANCO M, LÓPEZ-FRANCO O, MURCIANO-ANTÓN M, CAÑAMERO-VAQUERO M, FERNÁNDEZ-ACEÑERO M, HERRERO-BEAUMONT G, GÓMEZ-BARRENA E (2016) Meniscal degeneration in human knee osteoarthritis: in situ hybridization and immunohistochemistry study. *Arch Orthop Trauma Surg,* 136: 175-183.

MAHMOOD F, CLARKE J, RICHES P (2019) The ionic contribution of proteoglycans to mechanical stiffness of the meniscus. *Med Eng Phys,* 64: 23-27.

MAJEED H, KARUPPIAH S, SIGAMONEY KV, GEUTJENS G, STRAW RG (2015) All-inside meniscal repair surgery: factors affecting the outcome. *J Orthop Traumatol,* 16(3): 245-249.

MAKRIS EA, HADIDI P, ATHANASIOU KA (2011) The knee meniscus: structure–function, pathophysiology, current repair techniques, and prospects for regeneration. *Biomaterials,* 32(30): 7411-7431.

MASOUROS S, MCDERMOTT I, AMIS A, BULL A (2008) Biomechanics of the meniscus-meniscal ligament construct of the knee. *Knee Surg Sports Traumatol Arthrosc,* 16: 1121-1132.

MCDEVITT CA, WEBBER RJ (1990) The ultrastructure and biochemistry of meniscal cartilage. *Clin Orthop Rel Res*, 252: 8-18.

MELROSE J, SMITH S, CAKE M, READ R, WHITELOCK J (2005) Comparative spatial and temporal localisation of perlecan, aggrecan and type I, II and IV collagen in the ovine meniscus: an ageing study. *Histochem Cell Biol,* 124: 225-235.

MURPHY CA, CUNNIFFE GM, GARG AK, COLLINS MN (2019) Regional dependency of bovine meniscus biomechanics on the internal structure and glycosaminoglycan content. *J Mech Behav Biomed Mat,* 94: 186-192.

NIU W, GUO W, HAN S, ZHU Y, LIU S, GUO Q (2016) Cell-based strategies for meniscus tissue engineering. *Stem Cells Int*, 2016: 4717184.

OSAWA A, HARNER CD, GHARAIBEH B, MATSUMOTO T, MIFUNE Y, KOPF S, INGHAM SJ, SCHREIBER V, USAS A, HUARD J (2013) The use of blood vessel–derived stem cells for meniscal regeneration and repair. *Med Sci Sports Exercise*, 45(5): 813.

OZEKI N, SEIL R, KRYCH AJ, KOGA H (2021) Surgical treatment of complex meniscus tear and disease: state of the art. *J ISAKOS,* 6(1): 35-45.

PARK H-J, LEE H-D, CHO JH (2017) The efficacy of meniscal treatment associated with lateral tibial plateau fractures. *Knee Surg Relat Res,* 29(2): 137-143.

PAULI C, GROGAN S, PATIL S, OTSUKI S, HASEGAWA A, KOZIOL J, LOTZ M, D'LIMA D (2011) Macroscopic and histopathologic analysis of human knee menisci in aging and osteoarthritis. *Osteoarthritis Cartilage,* 19(9): 1132-1141.

PEREIRA H, CARIDADE S, FRIAS S, SILVA-CORREIA J, PEREIRA D, CENGIZ I, MANO J, OLIVEIRA JM, ESPREGUEIRA-MENDES J, REIS R (2014) Biomechanical and cellular segmental characterization of human meniscus: building the basis for Tissue Engineering therapies. *Osteoarthritis Cartilage,* 22(9): 1271-1281.

PEREIRA H, CENGIZ IF, GOMES S, ESPREGUEIRA-MENDES J, RIPOLL PL, MONLLAU JC, REIS RL, OLIVEIRA JM (2019) Meniscal allograft transplants and new scaffolding techniques. *EFORT Open Rev,* 4(6): 279-295.

PESHKOVA M, LYCHAGIN A, LIPINA M, DI MATTEO B, ANZILLOTTI G, RONZONI F, KOSHELEVA N, SHPICHKA A, ROYUK V, FOMIN V (2022) Gender-related aspects in osteoarthritis development and progression: a review. *Int J Mol Sci,* 23(5): 2767.

PRINGLE L, TANAKA M, FAYAD L (2019) Lady or gentleman? Sex differences in osseous and cartilaginous structures of the knee. *Int J Sports Exerc Med*, 5: 153.

PUETZER JL, BONASSAR LJ (2016) Physiologically distributed loading patterns drive the formation of zonally organized collagen structures in tissue-engineered meniscus. *Tissue Eng Part A,* 22(13-14): 907-916.

RATTNER J, MATYAS J, BARCLAY L, HOLOWAYCHUK S, SCIORE P, LO I, SHRIVE N, FRANK C, ACHARI Y, HART D (2011) New understanding of the complex structure of knee menisci: implications for injury risk and repair potential for athletes. *Scand J Med Sci Sports,* 21(4): 543-553.

REDDY GK, ENWEMEKA CS (1996) A simplified method for the analysis of hydroxyproline in biological tissues. *Clin Biochem*, 29(3): 225-229.

SANCHEZ-ADAMS J, ATHANASIOU KA (2009) The knee meniscus: a complex tissue of diverse cells. *Cell Mol Bioeng,* 2: 332-340.

SWAMY N, WADHWA V, BAJAJ G, CHHABRA A, PANDEY T (2018) Medial meniscal extrusion: detection, evaluation and clinical implications. *Eur J Radiol,* 102: 115-124.

VÅBEN C, HEINEMEIER KM, SCHJERLING P, OLSEN J, PETERSEN MM, KJAER M, KROGSGAARD MR (2020) No detectable remodelling in adult human menisci: an analysis based on the C14 bomb pulse. *Brit J Sports Med,* 54(23): 1433-1437.

WARNECKE D, BALKO J, HAAS J, BIEGER R, LEUCHT F, WOLF N, SCHILD N, STEIN S, SEITZ A, IGNATIUS A, REICHEL H, MIZAIKOFF B, DÜRSELEN L (2020) Degeneration alters the biomechanical properties and structural composition of lateral human menisci. *Osteoarthritis Cartilage,* 28(11): 1482-1491.

WISE BL, NIU J, YANG M, LANE NE, HARVEY W, FELSON DT, HIETPAS J, NEVITT M, SHARMA L, TORNER J (2012) Patterns of compartment involvement in tibiofemoral osteoarthritis in men and women and in whites and African Americans. *Arthritis Care Res*, 64(6): 847-852.

ZHOU M, CHEN J, WANG D, ZHU C, WANG Y, CHEN W (2018) Combined effects of reproductive and hormone factors and obesity on the prevalence of knee osteoarthritis and knee pain among middle-aged or older Chinese women: a cross-sectional study. *BMC Public Health,* 18: 1-9.

An exceedingly rare case of separated drainage of the cystic duct, the common bile duct and the main pancreatic duct documented on magnetic resonance cholangiopancreatography

Nicolò Brandi[1], Marta Fiscaletti[2], Matteo Renzulli[1]

[1] Department of Radiology, IRCCS Azienda Ospedaliero-Universitaria di Bologna, Via Albertoni 15, Bologna, Italy

[2] Radiology Units, Bellaria and Maggiore Hospitals, AUSL Bologna, Bologna, Italy

SUMMARY

Anatomical variations of the intra- and extra-hepatic biliary system are common, including those affecting the course and insertion point of the cystic duct. Adequate knowledge of such variations and an appropriate roadmap before any surgical, endoscopic or percutaneous procedure help in preventing associated iatrogenic complications. Magnetic resonance cholangiopancreatography (MRCP) can precisely delineate the anatomy of the biliary system preoperatively. We report the case of a 72-year-old female patient who presented with chronic right upper quadrant abdominal pain of 6 months duration, which had acutely worsened over the previous 2 weeks, and no other comorbidities. Blood tests were normal. Abdominal ultrasound revealed a slight dilatation of the common hepatic duct (10 mm), but no gallstones or sludge were demonstrated. MRCP excluded choledocholithiasis but revealed a cystic duct coursing medial to the common bile duct before anastomosing at the level of the ampulla of Vater. Trifurcation (Type 2 variant) of the intra-hepatic bile system was also observed. To the best of the authors' knowledge, this is the very first report to clearly document this exceptionally rare anatomic cystic duct anomaly on MRCP.

Key words: Biliary tract – Cystic duct – Cholangiopancreatography – Magnetic resonance

ABBREVIATIONS:

CBD: common bile duct
CD: cystic duct
CHD: common hepatic duct
CT: computed tomography
EHBD: extra-hepatic biliary ducts
ERCP: endoscopic retrograde cholangiography
FIESTA: fast imaging employing steady-state acquisition
FSEGR: fast spoiled gradient echo
HR: high resolution
IHBD: intra-hepatic biliary ducts
MRCP: magnetic resonance cholangiopancreatography
SSFSE: single shot fast spin echo
US: ultrasound

Corresponding author:
Nicolò Brandi. Department of Radiology, IRCCS Azienda Ospedaliero-Universitaria di Bologna, Via Albertoni 15, 40138 Bologna, Italia. Phone: +390512142958, Fax: +390512142805. E-mail: nicolo.brandi2@unibo.it

Submitted: June 2, 2023. **Accepted:** July 18, 2023

https://doi.org/10.52083/JHOF9715

INTRODUCTION

Anomalies of the biliary ductal system have been appreciated by physicians and anatomists for centuries and are common findings, possibly involving both the intra-hepatic biliary ducts (IHBD) and the extra-hepatic biliary ducts (EHBD).

Normally, the cystic duct (CD) joins the common hepatic duct (CHD) from a right lateral position approximately halfway between the porta hepatis and the ampulla of Vater. The significance of a low CD union was first described by Eisendrath in 1918, who noted that such anatomy might predispose to inadvertent bile duct injury during cholecystectomy (Eisendrath, 1918). Reports concerning the further clinical significance of this anatomic anomaly are relatively rare, but they observed an association with gallstone pancreatitis, Mirrizi syndrome, gallbladder cancer, and cystic dilatation of the biliary duct (Kubota et al., 1993; Uetsuji et al., 1993).

Despite a medial insertion of CD is reported in about 16-18% of patients, its low insertion has been observed as more infrequent and has been described in only 6-16%; in addition, the combination of these two anatomical variations is even more uncommon, presenting merely in 4-5.5% of cases (Gündüz et al., 2021; Sarawagi et al., 2016; Shaw et al., 1993; Taourel et al., 1996; Tsitouridis et al., 2007; Turner & Fulcher, 2001).

A medial and extremely low (intraduodenal) insertion of CD is an exceedingly rare finding, with percentages ranging from 1.66% in cadaveric studies (Sangameswaran, 2021) to 2% in cholangiopancreatographic studies (Garg et al., 2022), and only very few cases reported in the literature. Moreover, evidence of this singular configuration is supported only by endoscopic retrograde cholangiopancreatography (ERCP) images (Dodda et al., 1998; Turner & Fulcher, 2001). The present case is a unique case of medial and extremely low (intraduodenal) insertion of CD and, to the best of the authors' knowledge, the very first report to clearly document this exceptionally rare anatomic anomaly on magnetic resonance cholangiopancreatography (MRCP).

CASE REPORT

A 72-year-old female reported to our Institution with chronic right upper quadrant abdominal pain of 6 months duration, which had acutely worsened over the previous 2 weeks. She had no other comorbidities. The patient had been empirically treated with ursodeoxycholic acid prescribed by her primary care physician without improvement. Blood tests were normal, with lipase levels within normal limits and no leukocytosis. In the suspicion of biliary stones, an abdominal ultrasound (US) was requested. US revealed a slight dilatation of the CHD (10 mm), but no gallstones or sludge were demonstrated; furthermore, the gallbladder and the intrahepatic biliary ducts did not reveal any obvious abnormality. To definitively exclude choledocholithiasis and gallstones, an MRCP was then performed.

The MRCP was performed using a 1.5T MRI superconductive scanner (HDX-t Signa; General Electric®, Milwaukee, WI, USA) after the administration of one glass of pineapple juice to reduce the signal hyperintensity of gastro-enteric fluids; in particular, the MRCP protocol included the following sequences: axial fast spoiled gradient echo (FSEGR) T1-weighted images (including both in- and out-of-phase), axial single-shot fast spin echo (SSFSE) T2-weighted images, high resolution (HR) thick slab images and 3D fast imaging employing steady-state acquisition (FIESTA) images. The MRCP excluded the presence of any stones in the biliary system and in the gallbladder, but revealed a very rare cystic duct anomaly, demonstrating a CD coursing parallel and medial to the common bile duct (CBD) before anastomosing at the level of the ampulla of Vater; therefore, three distinct bile draining ducts were noted separately arising from the ampulla: the CD, the CBD and the main pancreatic duct (Fig. 1A-C). In addition, an anatomical variation of the IHBD was also observed, with a common confluence of the right posterior duct, the right anterior duct and the left hepatic duct (i.e., trifurcation or Type 2) (Fig. 1D). Furthermore, the gallbladder showed the folding of its fundus back upon the body, configuring a "Phrygian cap" anomaly, and demonstrated the presence of fundal adenomyomatosis (Fig. 1D-E).

COMMENTS

The CD normally joins the CHD approximately halfway between the porta hepatis and the ampulla of Vater from a right lateral position.

However, anatomical anomalies of the CD might occur in 18-23% of patients (Shaw et al., 1993) due to variations in the length, course and/or pattern of entry of the CD into the EHBT. According to the available literature, despite the level of insertion of the CD generally occurring in the middle one-third of the EHBT (51-88% of cases), the union may also occur in both the proximal and distal one-third (6-35% and 6-16%, respectively). Moreover, when it inserts distally, the CD may run parallel with the CHD for a long distance before fusion (12-33%) or, occasionally, even spiral around it (10%). In some rare cases of abnormal proximal insertion, the CD may drain directly into the right or left hepatic duct. As concerns the pattern of entry, the CD enters the CBD from the lateral aspect in most cases (37-68%), whereas a medial insertion after crossing the front or from behind is less common (16-18%); in some cases, the CD may present an anterior or posterior insertion (13-17% and 19-26%, respectively). Other unusual and rarer anomalies include double CDs and an absent CD with the gallbladder often emptying via a different pathway (Garg et al., 2022; Gündüz et al., 2021; Mortelé and Ros, 2001; Pina et al., 2015; Turner and Fulcher, 2001).

The possible anatomical variants of the CD are therefore extremely various and most probably depend on both the timing of the process of separation of pars hepatica (which will become the liver, the IHBD system and the CHD) from pars cystica (which will form the CD, the CBD and the

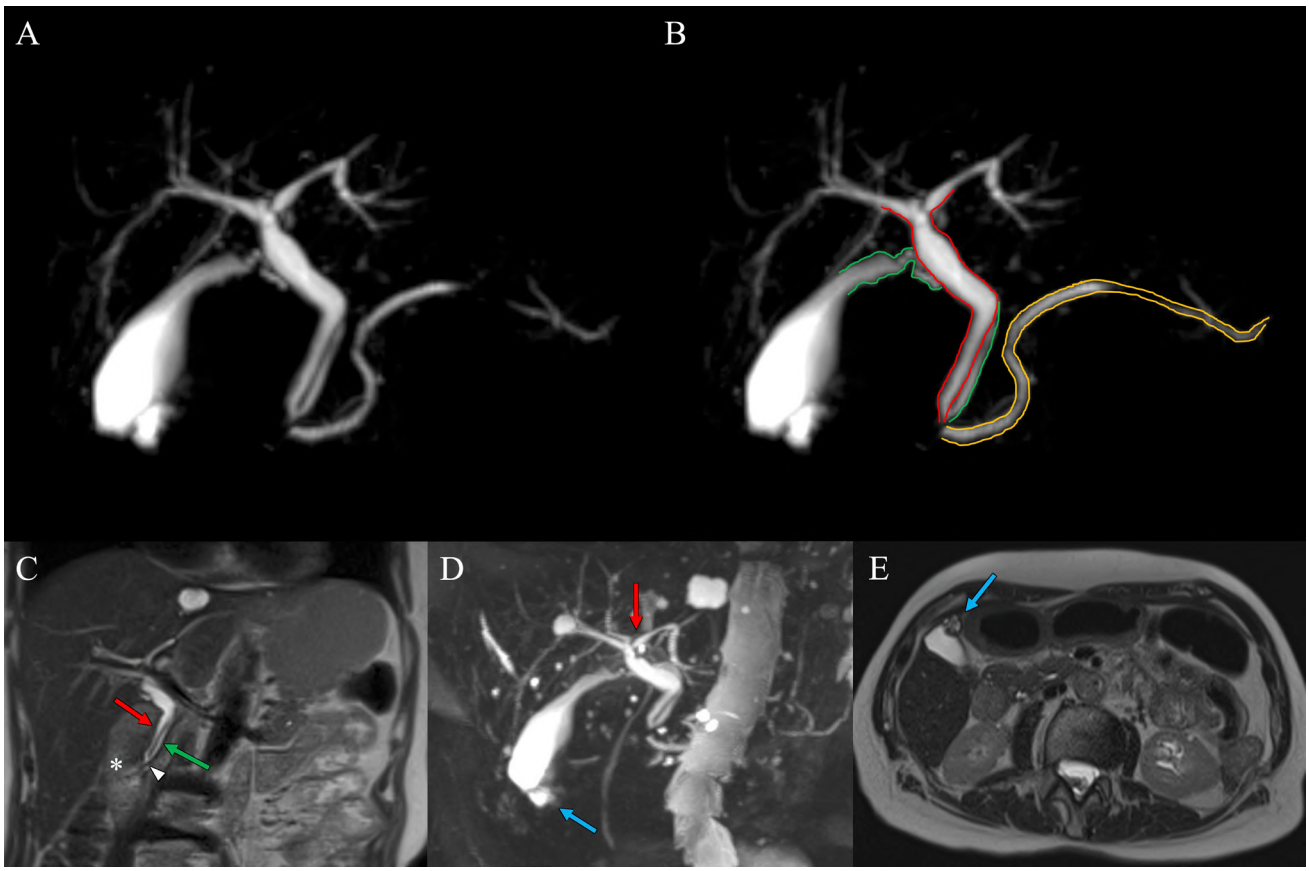

Fig. 1.- Coronal MRCP HR images (**A** and **B**) demonstrating a cystic duct (CD, green outline in B) coursing parallel and medial to the common bile duct (CBD, red outline in B) before anastomosing at the level of the ampulla of Vater with the main pancreatic duct (yellow outline in B); no stones were detected in both the gallbladder and the extra-hepatic biliary system. Coronal T2-w image (**C**) demonstrating the confluence of the CBD (red arrow) and the CD (red arrow) in the ampulla of Vater (white arrowhead) and showing the second portion of the duodenum (white asterisk). Oriented MRCP HR image obtained after maximum intensity projection (MIP) reconstruction (**D**) of the same patient demonstrating the concomitant presence of Type 2 variant (trifurcation) of the intra-hepatic bile duct (red arrow) and "Phrygian cap" anomaly of the gallbladder fundus (blue arrow). Axial T2-w image (**E**) demonstrating the presence of fundal adenomyomatosis in the gallbladder (blue arrow).

gallbladder), and the grade of rotation of the CD itself induced by the rotation of the duodenum during the fetal stages (Lamah et al., 2001; Tan and Moscoso, 1994). Whether these anatomical variations are due to simple stochastic events or rather represent the outcome of delays and/or alterations in the "normal" rates of differential growth in the different embryonic duct structures is still unknown. Moreover, since the EHBD and the IHBD maintain luminal continuity from the very start of organogenesis (Roskams and Desmet, 2008), it cannot be excluded that variations in the configuration of one system may induce or, at least, contribute to a concomitant alteration in the other system, causing some sort of "ripple effect" on the following morphogenetic phases. Nonetheless, recent evidence seems to support well-distinct mechanisms regulating the development of both the EHBD and the IHBD systems, suggesting that the molecular pathways involved in the development of the EHBD are more closely related to the formation of the duodenum and the pancreas (Zong and Stanger, 2011). Therefore, further studies are warranted to elucidate the mechanisms responsible for variations in the remodeling process of the biliary system during embryogenesis.

Variations in the course and insertion point of the CD are common in clinical practice and they typically remain asymptomatic throughout life. However, these anomalies still demand considerable attention during diagnostic investigations and interventional and surgical procedures since they might be the source of complications. For example, a CD with an extremely low and medial insertion has the tendency to overlie the CBD and thus be misidentified prior to interventional procedures, thus increasing the risk of inadvertent ERCP stent malposition during stone retrieval (George et al., 2009). In addition, in the case of an extremely low union, the CD and the CBD may be joined by fibrous tissue, thus making clamping the CD difficult or resulting in the inadvertent iatrogenic injury of the CD. Finally, the presence of an unusually long CD remnant after cholecystectomy or living donor liver transplantations has been associated with inflammatory changes and the formation of calculi (Turner and Fulcher, 2001).

Therefore, noninvasive techniques that can precisely delineate the anatomy of the biliary tract preoperatively could be of clinical value. In most cases, the normal-caliber CD is not seen on US or computed tomography (CT). Conversely, MRCP proved to be an accurate non-invasive imaging modality for mapping the CD anatomy and detecting aberrant ductal anatomy, relying on the high signal intensity of fluid-containing structures in T2-weighted images (Taourel et al., 1996). This technique allows to obtain high-resolution cross-sectional imaging, with both two- and three-dimensional projection, and its results are comparable to the more invasive ERCP and intraoperative cholangiograms (Hekimoglu et al., 2008; Xu et al., 2013). Moreover, MRCP is quick, is not associated with radiation exposure and does not require the administration of contrast media, needing only a simple glass of juice to evaluate the anatomy of both the intra- and extrahepatic biliary ducts (Renzulli et al., 2022). Finally, it allows the synchronous evaluation of the IHBD, whose anatomical variations are often associated with variations of the downstream biliary system, as was demonstrated also in the present case (Renzulli et al., 2023).

Despite the potential surgical complications associated with these rare congenital malformations, CD aberrations have been demonstrated to predispose to several pathologic pancreaticobiliary conditions. For example, a low union of the CD has previously been associated with a higher risk of pancreatitis and even periampullary cancer, and this association was ascribed to an anatomy-induced pressure process leading to chemical/bilious irritation (Muraki et al., 2020); this association is probably supported also by the shorter and lesser exposure of the biliary epithelium to the protective or dilutional effect of peri-biliary mucus glands in the upper biliary tree which happens in the presence of a low union (Dodda et al., 1998). In addition, previous studies have found an association between low insertion of the CD and choledocholithiasis (Renzulli et al., 2021) which can be due to increased retrograde pressure in the CD leading to both bile stagnation and impaired gallbladder emptying. In the present case, however, no calculi were detected on both US and MRCP. Despite

being contradictory to previous reports, the absence of biliary stones in the present case may be explained by differences in terms of biochemical and clinical contributors to stone formation. At the same time, the chronic abdominal pain reported by the patient could be attributed to unusual bile reflux into the CD or the pancreatic duct, likely favored by the relative proximity of these canals and the increased intra-luminal pressure at the level of the anastomosis. This hypothesis could also justify the evidence of the slightly wider CHD diameter reported on US and MRCP.

CONCLUSION

A CD coursing parallel and medial to the CBD before anastomosing at the level of the ampulla of Vater is an extremely rare anatomical variant of the biliary system that, if unrecognized, may complicate both surgical and interventional procedures. In an era of ever-increasing laparoscopic, endoscopic and percutaneous procedures of the hepatobiliary system, it is extremely important to have adequate knowledge of such variations before the actual procedure is performed. MRCP is pivotal to correctly identifying anatomic variants of both the IHBD and the EHBD, whose association is not unusual.

REFERENCES

DODDA G, BROWN, RD, O'NEIL HK, VENU RP (1998) Cystic duct insertion at ampulla as a cause for acute recurrent pancreatitis. *Gastrointest Endosc*, 47(2): 181-183.

EISENDRATH DN (1918) Anomalies of the bile ducts and blood vessels as the cause of accidents in biliary surgery. *JAMA*, 71(11): 864-867.

GARG S, DUTTA U, CHALUVASHETTY SB, KUMAR KH, KARLA N, SAHINI D, AGGARWAL A (2022) The anatomy of the cystic duct and its association with cholelithiasis: MR cholangiopancreatographic study. *Clin Anat*, 35(7): 847-854.

GEORGE RA, DEBNATH J, SINGH K, SATIJA L, BHARGAVA S, VAIDYA A (2009) Low insertion of a cystic duct into the common bile duct as a cause for a malpositioned biliary stent: demonstration with multidetector computed tomography. *Singapore Med J*, 50(7): e243-e246.

GÜNDÜZ N, DOĞAN MB, ALACAGÖZ M, YAĞBASAN M, PERÇEM ORHAN SÖYLEMEZ U, ATALAY B (2021) Anatomical variations of cystic duct insertion and their relationship with choledocholithiasis: an MRCP study. *Egypt J Radiol Nucl Med*, 52: 202.

HEKIMOGLU K, USTUNDAG Y, DUSAK A, ERDEM Z, KARADEMIR B, AYDEMIR S, GUNDOGDU S (2008) MRCP vs. ERCP in the evaluation of biliary pathologies review of current literature. *J Diag Dis*, 9(3): 162-169.

KUBOTA Y, YAMAGUCHI T, TANI K, TAKAOKA M, FUJIMURA K, OGURA M, YAMAMOTO S, MIZUNO T, INOUE K (1993) Anatomical variation of pancreatobiliary ducts in biliary stone diseases. *Abdom Imaging*, 18(2): 145-149.

LAMAH M, KARANJIA ND, DICKSON GH (2001) Anatomical variations of the extrahepatic biliary tree review of the world literature. *Clin Anat*, 14(3): 167-172.

MORTELÉ KJ, ROS PR (2001) Anatomic variants of the biliary tree: MR cholangiographic findings and clinical applications. *Am J Roentgenol*, 177(2): 389-394.

MURAKI T, REID MD, PEHLIVANOGLU B, GONZALEZ RS, SEKHAR A, MEMIS B, XUE Y, CHENG J, JANG KT, MITTAL P, CARDONA K, KOOBY DA, MAITHEL S, SARMIENTO JM, EL-RAYES B, LOMBERK G, URRUTIA RA, CHRISTIANS K, TSAI S, EVANS DB, ADSAY V (2020) Variant anatomy of the biliary system as a cause of pancreatic and peri-ampullary cancers. *HPB (Oxford)*, 22(12): 1675-1685.

PINA LN, SAMOILOVICH F, URRUTIA S, RODRÍGUEZ A, ALLE L, FERRERES AR (2015) Surgical considerations of the cystic duct and Heister valves. *Surg J (N Y)*, 1(1): e23-e27.

RENZULLI M, BRANDI N, BROCCHI S, BALACCHI C, LANZA C, PETTINARI I, STEFANINI B, CARRAFIELLO G, PISCAGLIA F, GOLFIERI R, MARASCO G (2023) Association between anatomic variations of extrahepatic and intrahepatic bile ducts: Do look up!. *J Anat*, 242(4): 683-694.

RENZULLI M, BROCCHI S, MARASCO G, SPINELLI D, BALACCHI C, BARAKAT M, PETTINARI I, GOLFIERI R (2021) A new quantitative classification of the extrahepatic biliary tract related to cystic duct implantation. *J Gastrointest Surg*, 25(9): 2268-2279.

RENZULLI M, CARETTI D, PETTINARI I, BISELLI M, BROCCHI S, SERGENTI A, BRANDI N, GOLFIERI R (2022) Optimization of pineapple juice amount used as a negative oral contrast agent in magnetic resonance cholangiopancreatography. *Sci Rep*, 12(1): 531.

ROSKAMS T, DESMET V (2008) Embryology of extra- and intrahepatic bile ducts, the ductal plate. *Anat Rec (Hoboken)*, 291(6): 628-635.

SANGAMESWARAN K (2021) Variations of cystic duct and its clinical significance. *Int J Anat Res*, 9(4): 8120-8126.

SARAWAGI R, SUNDAR S, GUPTA SK, RAGHUWANSHI S (2016) Anatomical variations of cystic ducts in magnetic resonance cholangiopancreatography and clinical implications. *Radiol Res Pract*, 2016: 3021484.

SHAW MJ, DORSHER PJ, VENNES JA (1993) Cystic duct anatomy: an endoscopic perspective. *Am J Gastroenterol*, 88(12): 2102-2106.

TAN CE, MOSCOSO GJ (1994) The developing human biliary system at the porta hepatis level between 29 days and 8 weeks of gestation a way to understanding biliary atresia. Part 1. *Pathol Int*, 44(8): 587-599.

TAOUREL P, BRET PM, REINHOLD C, BARKUN AN, ATRI M (1996) Anatomic variants of the biliary tree: diagnosis with MR cholangiopancreatography. *Radiology*, 199(2): 521-527.

TSITOURIDIS I, LAZARAKI G, PAPASTERGIOU C, PAGALOS E, GERMANIDIS G (2007) Low conjunction of the cystic duct with the common bile duct: does it correlate with the formation of common bile duct stones? *Surg Endosc*, 21(1): 48-52.

TURNER MA, FULCHER AS (2001) The cystic duct: normal anatomy and disease processes. *Radiographics*, 21(1): 3-294.

UETSUJI S, OKUDA Y, KOMADA H, YAMAMURA M, KAMIYAMA Y (1993) Clinical evaluation of a low junction of the cystic duct. *Scand J Gastroenterol*, 28(1): 85-88.

XU YB, BAI YL, MIN ZG, QIN SY (2013) Magnetic resonance cholangiography in assessing biliary anatomy in living donors a meta-analysis. *World J Gastroenterol*, 19(45): 8427-8434.

ZONG Y, STANGER BZ (2011) Molecular mechanisms of bile duct development. *Int J Biochem Cell Biol*, 43(2): 257-264.

A systematic literature study of anatomical variations in human lung fissures and hilar structures

Burkay Akar[1], Zafer K. Coşkun[1], Yunus E. Kaban[1], Dilan Ece[2]

[1] Department of Anatomy, Faculty of Medicine, Gazi University, Ankara, Turkey
[2] Department of Internal Medicine, Karadeniz Eregli State Hospital, Zonguldak, Turkey

SUMMARY

This study aimed to examine the anatomical features and variation prevalence of human lung fissures and hilar structures. Anatomical variations can be seen in these structures and morphometrical data are not consistent. Studies in the literature were reviewed using the PubMed, Scopus, and Google Scholar databases. The method of the study was prepared in accordance with the Preferred Reporting Items for Systematic Reviews and Meta-analysis [PRISMA] protocol. Data on the complete, incomplete, absent and accessory fissures, accessory fissure types, number of arteries, veins and bronchi were extracted and included in the analysis. The Anatomical Quality Assessment (AQUA) tool was used in order to examine potential risks of bias within the included studies. Out of 302 studies initially evaluated, 68 were included in the analysis. It was determined that the prevalence of completion of horizontal fissure of the right lung (56,5%) was lower than oblique fissures, while the prevalence of incomplete and absent fissure (43,4%) were higher than oblique fissures. The prevalence of the left horizontal accessory fissure (9,9%) in the left lung and the inferior accessory fissure type (8,9%) in the right lung were found to be the highest. It has been found that the number of arteries and bronchi in the hilum of the right lung are different from the general anatomy. Although studies on lung fissure variations are more common, studies examining accessory fissures and hilar structures are rare. We think that this study will be useful for clinicians in interpreting radiological images, diagnosing lung pathologies, and applying surgical procedures.

Key words: Lung – Fissure – Accessory fissure – Hilum – Variation

INTRODUCTION

On the surfaces of the lungs, there are clefts called fissures separating lobes from each other (Arıncı, 2005). In the right lung, a horizontal fissure (minor fissure) separates the upper and middle lobes, and the right oblique fissure (major fissure) separates the lower lobe from the upper and middle lobes. In the left lung, there is only the oblique fissure (major fissure) that separates the lung into the upper and lower lobe and these fissures are presented in Fig. 1 (Ugalde et

Corresponding author:
Burkay Akar. Department of Anatomy, Faculty of Medicine, Gazi University, Emniyet Mahallesi, Mevlâna Bulvarı, No: 29, 06500, Yenimahalle, Ankara, Turkey. Phone: +90 534 051 95 24; Fax: +90 312 202 4647. E-mail: burkay96akar@gmail.com - Orcid: 0000-0002-5058-2454

Submitted: June 11, 2023. **Accepted:** August 11, 2023, 2023

https://doi.org/10.52083/YPWC5380

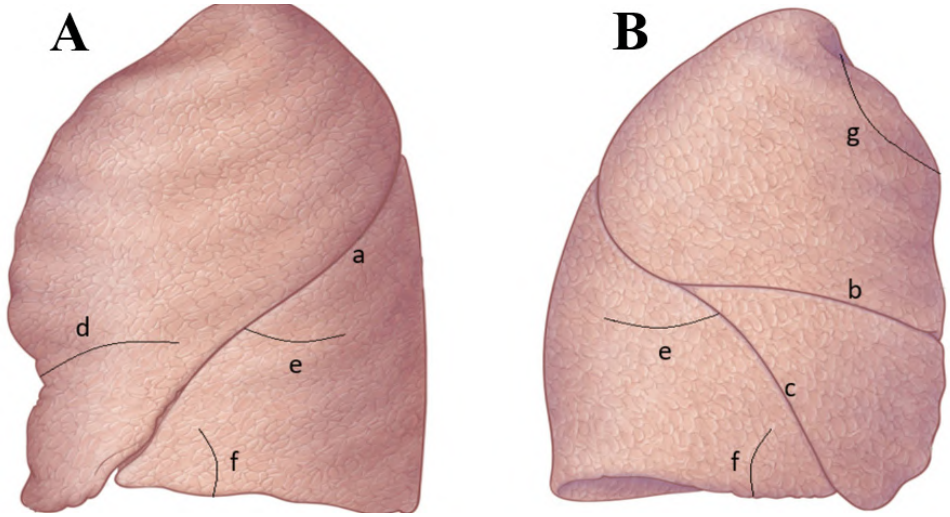

Fig. 1.- Horizontal, oblique and accesory fissures in the right (**B**) and left (**A**) lung. a: Left oblique (major) fissure; b: Right horizontal (minor) fissure; c: Right oblique (major) fissure; d: Left minor fissure; e: Superior accesory fissure; f: Inferior accesory fissure; g: Azygos fissure. Modified from Ugalde et al. (2007).

al., 2007). Fissures in the fully developed lungs embryologically separate the bronchopulmonary segments, which will develop in the next process (Kc et al., 2018). Completed fissures are defined as fissures that are held together only at the hilar level (by bronchi and pulmonary blood vessels), while incomplete fissures are defined as areas of parenchymal fusion between the lobes (Ugalde et al., 2007). Incomplete pulmonary fissures lead to interlobar collateral airway pathologies and common venolymphatic drainage between adjacent lobes or segments, which may influence surgical and endobronchial treatments of the lungs and the treatment outcomes. Although rare, the spread of small cell lung cancer to the adjacent lobe takes place due to incomplete fissures and affects the prognosis negatively (Bayter et al., 2021).

In addition to normal fissures, accessory fissures can also be observed in the lungs. Anatomically, the accessory fissure is a cleft with a varying depth, covered with visceral pleura. They usually appear at the borders between bronchopulmonary segments (Godwin and Tarver, 1985). The inferior accessory fissure that separates the medial basal segment from the rest of the lower lobe, the superior accessory fissure that separates the upper segment of the lower lobe from the basal segment, and the left horizontal fissure (minor fissure) that borders the lingula of the left lung are the most observed accessory fissures in the lungs (Bayter et al., 2021; Godwin and Tarver, 1985). Apart from these, the azygos fissure is frequently observed in the upper lobe of the right lung (Ozan, 2014). Accessory fissures may change the usual pattern of lung collapse in patients with endobronchial lesions and make it difficult to identify the size of the lesion (George et al., 2014). Moreover, the accurate identification of accessory fissures is important since they may be misinterpreted as linear atelectasis, pleural scars, or bullae walls (Manicka et al., 2019).

The hilum of the lung, where the anatomical structures entering and leaving the organ are located, is found on the mediastinal surface of the lungs. The root of the lungs, which is known as the stalk of the lung, is surrounded by the mediastinal pleura of the lung and connects to the hilum of the lung (Arıncı, 2005; Ozan, 2014). The root of the lungs contains a pulmonary artery, 2 pulmonary veins, main bronchus, bronchial vessels, nerves, and lymph nodes (Drake et al., 2020). Having knowledge about arteries and veins can be useful for surgeons to prevent excessive bleeding during pulmonary lobectomy (Manicka et al., 2019). Knowing the variations of hilar structures is important, as they are often associated with misinterpretation of radiography and computed tomography images. (Saha and Srimani, 2019).

Our study aimed to examine the prevalence of variations according to previous studies by reviewing those studies that discussed the variations of fissures in human lungs and structures in the hilum of the lungs. In our literature review, there were many studies on fissure variations in the lungs, but we could not find any systematic reviews examining the variations of lung fissures and hilar structures together.

MATERIALS AND METHODS

Search strategy

Studies in the literature examining the variations of lung fissures and hilar structures were reviewed by two researchers using the PubMed, Scopus, and Google Scholar databases. During the search done in the databases, the keywords "variations", "fissures", "hilum", "human", "lung", "accessory fissures" and search terms such as "variations of fissures in human lung", or "variations of hilum in lung" were used. To prevent any location and interviewer bias during the search, an inclusive search strategy was determined. Furthermore, no date and language restrictions were set during the search, and the search was expanded using the references of the articles suitable for the study. The method of the study was prepared in accordance with the Preferred Reporting Items for Systematic Reviews and Meta-analysis [PRISMA] protocol (Henry et al., 2016).

Eligibility assessment

Inclusion and exclusion criteria of potential articles were determined by 2 different researchers. Regardless of sex, age, and ethnicity, articles involving different populations and different methods, in which no pathologies were found in the lungs, were selected and included in the study. Case reports, letters to the editor, conference proceedings, unpublished articles, and published articles with incomplete or uncertain results were excluded from the study. Studies in languages other than English were translated into English by medical professionals. The review team made a compromise in case of disagreements during the conformity assessment of the studies.

Data extraction

Data extraction of articles that met the inclusion criteria was obtained by two different researchers. Data on lung counts, publication date and location of study, prevalence of variation of lung fissures, prevalence of variation of accessory fissure types, and prevalence of variation of hilar structures were extracted. The authors of the articles were contacted due to inconsistencies in the data of some articles.

Study endpoints

The primary endpoint was to find the prevalence of variation of lung fissures and hilar structures relative to the right and left lungs in the general population. The secondary endpoints included various anatomical variation features associated with the lung fissures and hilar structures: developmental status of fissures (complete, incomplete and absent), types of accessory fissures (superior accesory fissures, inferior accesory fissures, left minor fissures, azygos fissures and other accessory fissures), number of hilar structures (one artery, two arteries or more, one vein, two veins, three veins and more, one bronchus, two bronchi and more).

Quality assessment

Anatomical Quality Assessment (AQUA) Tool was used to evaluate the quality and reliability of anatomical studies. The AQUA tool assesses the risks of study bias in 5 areas (1. Aim and subject characteristics 2. Study design, 3. Characterization of methods, 4. Descriptive anatomy, 5. Results reporting). Each of the fields was set to end with a bias question and rated as "Low", "High" or "Uncertain". Answering "yes" to the questions indicates that the study carries a low risk of bias, and answering "no" indicates that the study carries a high risk of bias. The ''unclear answer was given for studies that contain inconsistent data and cannot be clearly examined (Henry et al., 2017).

Statistical analysis

Statistical analysis was performed by two reviewers (B.A and D.E). The data were analyzed using MetaXL version 5.3 by EpiGear Interna-

tional Pty Ltd (Wilston, Queensland, Australia). The pooled prevalence of the parameters in the studies were represented by grouping them according to the right and left lung. The Chi2 test and Higgins I2 statistics were used in order to investigate the heterogeneity among the included studies. Cochran's Q p value of less than <0.10 (for the Chi2 test), indicates statistically significant heterogeneity between studies. Higgins I2 values between 0-40% were considered as "might not be important"; 30-60% as "might indicate moderate heterogeneity";50-90% as "may indicate substantial heterogeneity";, and 75-100% as "may represent considerable heterogeneity" (Henry et al., 2016).

RESULTS

Study identification

The study identification process is summarized in Fig. 2. The first search of the databases found 275 articles that could potentially meet the inclusion criteria of the study. Further 27 studies were identified during the reference search. A total of 53 studies were duplicates and were excluded. As a result of the detailed examination of the titles and abstracts of the articles, it was decided that 136 articles were not suitable for the study. Of the 113 articles obtained, 45 were excluded due to their being case reports, letters to the editor, conference proceedings, unpublished articles, and published articles with incomplete or uncertain results. Finally, 68 articles were included in this study.

Characteristics of the included studies

Characteristics of the included studies are summarized in Table 1 in detail. Of the 68 articles used in our study, 60 focused on fissures of the lungs (7366 lungs), 20 focused on accessory fissures observed in the lungs (2623 lungs), and 12 focused on the pulmonary hilum (944 lungs). The articles included in our study were published between 2001 and 2022. Lungs were examined on cadavers in 60 articles, CT (computed tomography) images in 6 articles, and medical autopsy in 2 articles. The vast majority of studies belonged to the Indian population (50 studies).

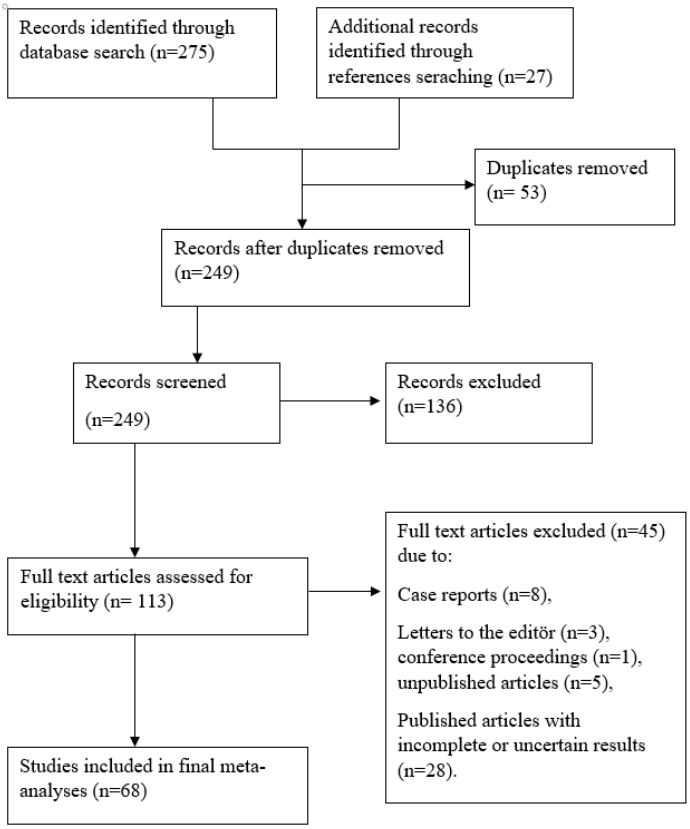

Fig. 2.- PRISMA flow diagram.

Table 1. Characteristics of the included studies & AQUA TOLL- risk of bias. Modified from Henry et al. (2016).

Studies	Method of study	Study population	Number of Lungs	Domain 1	Domain 2	Domain 3	Domain 4	Domain 5
Kc (2018)	Cadaver	Nepalese	Right (23) / Left (27)	High	Low	High	Low	Low
George (2014)	Cadaver	Indıa	Right (65) / Left (73)	Low	Low	High	Low	Low
Mahmut (2007)	CT	Japan	Right (1000) / Left (1000)	Low	Low	Low	Low	Low
Joshi (2022)	Cadaver	Indıa	Right (32) / Left (38)	High	Low	High	Low	Low
Manjunath (2021)	CT	Indıa	Right (70) / Left (58)	Low	Low	High	Low	Low
Thapa (2016)	Cadaver	Indıa	Right (20) / Left (20)	High	Low	High	Low	Low
Bostancı (2019)	Medicolegal autopsy	Turkey	Right (256) / Left (256)	High	Low	High	Low	High
Z. Hermanová (2014)	CT	Czech Republic	Right (250) / Left (250)	Low	Low	Low	Low	Low
N. U. Dogan (2015)	Medicolegal autopsy	Turkey	Right (210) / Left (210)	Low	Low	High	Low	Low
Murlimanju (2012)	Cadaver	Indıa	Right (32) / Left (28)	High	Low	High	Low	Low
James (2019)	Cadaver	Indıa	Right (25) / Left (25)	High	Low	High	Low	High
Jethva (2019)	Cadaver	Indıa	Right (25) / Left (25)	High	Low	High	Low	Low
V. Mutua (2021)	Cadaver	Kenya	Sağ (38) / Left (32)	High	Low	High	Low	Low
Khedekar (2017)	Cadaver	Indıa	Right (25) / Left (25)	High	Low	High	Low	High
Jacob (2019)	Cadaver	Indıa	Right (47) / Left (47)	High	Low	High	Low	High
Devi (2011)	Cadaver	Indıa	Right (22) / Left (22)	High	Low	High	Low	Unclear
Wahengbam (2019)	Cadaver	Indıa	Right (42) / Left (37)	High	Low	High	Low	Low
Jaiswal (2017)	Cadaver	Indıa	Right (55) / Left (0)	High	Low	High	Low	Low
Ranaweera (2022)	Cadaver	Sri Lanka	Right (26) / Left (24)	High	Low	High	Low	Low
Anbusudar (2016)	Cadaver	Indıa	Right (25) / Left (25)	High	Low	High	Low	Low
Sailaja (2019)	Cadaver	Indıa	Right (30) / Sol (30)	High	Low	High	Low	Low
Kumar (2014)	Cadaver	Indıa	Right (50) / Left (50)	High	Low	High	Low	Low

Studies	Method of study	Study population	Number of Lungs	Domain 1	Domain 2	Domain 3	Domain 4	Domain 5
Mamatha (2016)	Cadaver	India	Right (20) Left (20)	High	Low	High	Low	Low
Singh (2014)	Cadaver	India	Right (30) Left (30)	High	Low	High	Low	Low
Quadros (2014)	Cadaver	India	Right (36) Left (40)	Low	Low	High	Low	Low
Vasuki (2019)	Cadaver study	India	Right (40) Left (40)	High	Low	High	Low	High
Shivaleela (2018)	Cadaver study	India	Right (38) Left (46)	High	Low	High	Low	Low
Ughade (2018)	Cadaver study	India	Right (50) Left (50)	High	Low	High	Low	Low
Shinde &Patel (2022)	Cadaver study	India	Right (24) Left (24)	High	Low	High	Low	Low
Agrawal (2018)	Cadaver study	India	Right (40) Left (40)	High	Low	High	Low	Low
Subadha (2019)	Cadaver	India	Right (32) Left (38)	High	Low	High	Low	Low
Dhanalakshmi (2016)	Cadaver	India	Right (50) Left (50)	High	Low	High	Low	Low
Hema (2014)	Cadaver	India	Right (25) Left (25)	High	Low	High	Low	Low
Lakshmi (2018)	Cadaver	India	Right (32) Left (28)	High	Low	High	Low	High
Jacob & Pıllay (2013)	Cadaver	India	Right (30) Left (18)	High	Low	High	Low	Low
Nene (2011)	Cadaver	India	Right (50) Left (50)	High	Low	High	Low	High
Dutta (2013)	Cadaver	India	Right (52) Left (50)	High	Low	High	Low	Low
Magadum (2015)	Cadaver	India	Right (40) Left (40)	High	Low	High	Low	Low
Ambali Manoj (2014)	Cadaver	India	Right (50) Left (50)	High	High	High	Low	Low
Nakhate (2017)	Cadaver	India	Right (40) Left (40)	High	Low	High	Low	Low
Varalakshmi (2014)	Cadaver	India	Right (30) Left (34)	High	Low	High	Low	Low
Divya (2015)	Cadaver	India	Right (28) Left (27)	High	Low	High	Low	Low
Nisha Kaul (2014)	Cadaver	India	Right (50) Left (50)	High	Low	High	Low	Low
Wahane (2015)	Cadaver	India	Right (29) Left (21)	High	Low	High	Low	Low
Radha (2015)	Cadaver	India	Right (30) Left (30)	High	Low	High	Low	Low

Studies	Method of study	Study population	Number of Lungs	Domain 1	Domain 2	Domain 3	Domain 4	Domain 5
Mansur (2019)	Cadaver	Nepal	Right (38)	High	Low	High	Low	Low
			Left (31)					
Ghosh (2013)	Cadaver	Indıa	Right (46)	High	Low	High	Low	Low
			Left (36)					
Gebregziabher (2015)	Cadaver	Ethiopia	Right (23)	High	Low	High	Low	Low
			Left (20)					
Sumalatha (2019)	Cadaver	Saudi Arabia	Right (32)	High	Low	High	Low	Low
			Left (30)					
Gayathri (2016)	Cadaver	Indıa	Right (25)	High	Low	High	Low	Low
			Left (25)					
Sangeetha (2019)	Cadaver	Indıa	Right (25)	High	Low	High	Low	Low
			Left (25)					
Tallapaneni (2016)	Cadaver	Indıa	Right (30)	High	Low	High	Low	Low
			Left (30)					
West (2020)	Cadaver	UK	Right (81)	High	Low	High	Low	Low
			Left (81)					
Kommuru (2013)	Cadaver	Indıa	Right (40)	High	High	High	Low	Unclear
			Left (40)					
Gautam (2021)	Cadaver	Nepal	Right (42)	High	Low	High	Low	High
			Left (28)					
Amin (2020)	Cadaver	Egyptian	Right (21)	High	Low	High	Low	Low
			Left (19)					
Mathangasinghe (2021)	Cadaver	Sri Lanka	Right (12)	Low	Low	High	Low	Low
			Left (12)					
Anjankar (2017)	Cadaver	Indıa	Right (39)	High	Low	High	Low	Low
			Left (38)					
Meenakshi (2004)	Cadaver	Indıa	Right (30)	High	Low	High	Low	Low
			Left (30)					
Zareena SK. (2014)	Cadaver	Indıa	Right (40)	High	Low	High	Low	Low
			Left (40)					
Arıyürek (2001)	CT	Turkey	Right(186)	Low	Low	High	Low	Low
			Left (186)					
Rani (2020)	Cadaver	Indıa	Right (30)	High	Low	High	Low	Low
			Left (30)					
Kılıç (2006)	Cadaver	Turkey	Right (30)	High	Low	High	Low	Low
			Left (30)					
Cronin (2010)	CT	USA	Right(150)	Low	Low	Low	Low	Low
			Left (150)					
Yıldız (2004)	CT	Turkey	Right(115)	Low	Low	Low	Low	Low
			Left (115)					
Kumari (2022)	Cadaver	Indıa	Right (21)	High	Low	High	Low	Low
			Left (26)					
Saha (2019)	Cadaver	Indıa	Right (49)	High	Low	High	Low	Low
			Left (54)					
Ganapathy (2018)	Cadaver	Indıa	Right (36)	High	Low	High	Low	Low
			Left (39)					

Abbreviations: Domain 1: Objective(s) and study characteristics; Domain 2: Study design; Domain 3: Methodology characterization; Domain 4: Descriptive anatomy; Domain 5: Reporting of results.

Quality assessment

Quality assessment are summarized in Table 1. The majority of studies evaluated by the AQUA tool revealed that domain one (Objective(s) and subject characteristics) and domain three (Methodology characterization) were at "High" risk for bias (due to the lack of demographic data of the research group and no information on the experience of the researchers). Most other studies had a 'Low' risk of bias found in field two (study design), field four (descriptive anatomy) and field five (reporting results).

Variations of horizontal, oblique and accessory fissures in the lungs

A total of 7366 lungs, 3738 right and 3628 left lungs, were examined in 60 articles reviewed regarding the variations of fissures observed in them. The completion rate of horizontal fissures in 3738 right lungs examined was 56.5%, whereas the incompleteness rate of fissures was 34.5%, and the absence rate of horizontal fissures was 8.9%. The completion rate of the oblique fissures was 72.9%, the incompleteness rate of oblique fissures was 25.6%, and the absence rate of the oblique fissures was 1.4% in right lungs. The incidence rate of accessory fissures in the right lungs was found to be 10.2%. In 3628 left lungs, the incidence rate of the oblique fissures was 72.6%, the incompleteness rate of fissures was 25.7%, and the absence rate of the oblique fissures was 1.65%. The incidence rate of accessory fissures in the left lungs was 11.2%.

Variations types of accesory fissures in the lungs

In 20 articles on variation types of accessory fissures in the lungs, a total of 2623 lungs, 1341 right lungs and 1282 left lungs, were examined. In the right lungs, the incidence rate of superior accessory fissures was 4.7%, the incidence rate of inferior accessory fissures was 8.9%, the incidence rate of azygos fissures was 0.7%, and the incidence rate of other accessory fissures was 2.1%. In the left lungs, the incidence rate of superior accessory fissures was 3.3%, the incidence rate of inferior accessory fissures was 5.1%, the incidence rate of left horizontal fissures was 9.9%, and the incidence rate of other accessory fissures was 1.5%.

Variations of hilar structures in the lungs

In the 12 reviewed articles on variations of hilar structures in the lungs, a total of 944 lungs, 503 right lungs and 441 left lungs, were examined. The incidence rate of a single pulmonary artery in the right lungs was found to be 26.6%, and the incidence rate of two or more pulmonary arteries was found to be 38.2%. The incidence rate of a single pulmonary vein was 1.6%, whereas the incidence rate of two pulmonary veins was 38.6%, and the incidence rate of three or more pulmonary veins was 30.2%. While the incidence rate of a single bronchus was 3.4%, the incidence rate of two or more bronchi was 63.6%. In the left lungs, the incidence rate of a single pulmonary artery was 49.9%, while the incidence rate of two or more arteries was 12.5%. The incidence rate of a single pulmonary vein was 3.0%, the incidence rate of two pulmonary veins was 47.4%, and the incidence rate of three or more pulmonary veins was 19.5%. Whereas the incidence rate of a single bronchus was 45.1%, the incidence rate of two or more bronchi was 29.9%.

The heterogeneity between the studies

Heterogeneity statistics between studies are presented in table 2. Except for some parameters (superior accesory fissure in the right lung, other accessory fissures in the right and left lungs, azygos fissure in the right lung, single vein and single bronchus in the left lung), the heterogeneity between studies examining other parameters was statistically significant ($p<0.001$). For the I-square test, the heterogeneity of superior accessory fissures observed in the right (58.0%) lung, azygos fissure (56.3%), other accessory fissures observed in the right (40.2%) and left (0%) lungs, single vein (6.0%) and single bronchus (58,5%) in the left lung was found to be lower than in other parameters according to the studies.

DISCUSSION

Our study examined 68 articles on variations of lung fissures and hilar structures. The prevalence of variations of lung fissures and hilar structures differ according to studies. This may be due to the fact that the studies were conducted in different populations and with different methods, or the developmental state of the lungs.

Table 2. Heterogeneity statistics of studies on variations of fissures and hilar structures.

Parameter	Number of studies	Pooled Prevalance % (95% CI)	Chi- Square Test Cochran's Q, p-value	I^2 (Higgins) Test
Complete Horizontal Fissure (R)	60	56,5 (44,0-69,0)	P<0,001	90,3%
Incomplete &Absent Horizontal Fissure (R)	60	43,4 (30,9-55,9)	P<0,001	92,7%
Complete Oblique Fissure (R)	60	72,9 (61,6-84,2)	P<0,001	82,7%
Incomplete &Absent Oblique Fissure (R)	60	27,0 (15,7-38,3)	P<0,001	92,4%
Complete Oblique Fissure (L)	60	72,6 (61,3-83,9)	P<0,001	80,15%
Incomplete &Absent Oblique Fissure (L)	60	27,3 (16,1-38,5)	P<0,001	91,6%
Accesory Fissure (R)	60	10,2 (2,6-17,8)	P<0,001	94,4%
Accesory Fissure (L)	60	11,2 (3,3-19,1)	P<0,001	97,3%
Superior Accesory Fissure (R)	20	4,7 (0,0-13,9)	P>0,001	58,0%
Superior Accesory Fissure (L)	20	3,3 (0,0-11,1)	P<0,001	69,4%
Inferior Accesory Fissure (R)	20	8,9 (0,0-21,4)	P<0,001	76,2%
Inferior Accesory Fissure (L)	20	5,1 (0,0-14,7)	P<0,001	94,6%
Left Minor Fissure	20	9,9 (0,0-23,0)	P<0,001	93,0%
Azygos Fissure (R)	20	0,7 (0,0-4,3)	P>0,001	56,3%
Other Accesory Fissure (R)	20	2,1 (0,0-8,4)	P>0,001	40,2%
Other Accesory Fissure (L)	20	1,5 (0,0-6,8)	P>0,001	0%
One Artery (R)	12	26,6 (1,6-51,6)	P<0,001	95,0%
One Artery (L)	12	49,9 (21,6-78,2)	P<0,001	91,5%
Two Arteries and More (R)	12	38,2 (10,8-65,6)	P<0,001	91,4%
Two Arteries and More (L)	12	12,5 (0,0-31,2)	P<0,001	86,7%
One Vein (R)	12	1,6 (0,0-8,7)	P<0,001	99,7%
One Vein (L)	12	3,0 (0,0-6,1)	P>0,001	6,0%
Two Veins (R)	12	38,6 (11,1-66,1)	P<0,001	90,6%
Two Veins (L)	12	47,4 (19,2-75,6)	P<0,001	92,6%
Three Veins and More (R)	12	30,2 (0,2-60,2)	P<0,001	93,7%
Three Veins and More (L)	12	19,5 (0,0-41,9)	P<0,001	84,9%
One Bronchus (R)	12	3,4 (0,0-13,6)	P<0,001	99,3%
One Bronchus (L)	12	45,1 (17-73,2)	P>0,001	58,5%
Two Bronchi and More (R)	12	63,6 (36,4-90,8)	P<0,001	95,6%
Two Bronchi and More (L)	12	29,9 (4,0-55,8)	P<0,001	83,0%

The epithelium of the lungs starts to develop from the endoderm of the foregut after the 4th week. First, a laryngotracheal groove is formed, and a lung bud develops out of the groove. The laryngotracheal tube is formed when this groove grows longer, and its lower parts form the bronchial cartilage. In the following process, bronchial cartilages branch and form the bronchial tree of the lung (Waschke et al., 2016). After several generations of branching, bronchopulmonary segments start to emerge. Bronchopulmonary segments fuse to form fissures and lobes in fully developed lungs. Incomplete or absent fissures may result from a defect in the obliteration of these fissures (Kc et al., 2018). Accessory fissures may arise from the non-fusion of the spaces between the bronchopulmonary segments. Differences in the formation of lung fissures and lobes during development may result from the presence of any factor that triggers the fusion of bronchopulmonary buds (George et al., 2014).

According to the results of the data in our study, it is seen that the prevalence of the completion of the horizontal fissures of the right lung (56.5%)

was lower compared to the oblique fissures of the right and left lungs. The prevalence of incompleteness of the horizontal fissures of the right lung was found to be 34.5%, which is higher than that of the oblique fissures of right and left lung. In their study, Joshi et al. (2022) stated that the incidence rate of incomplete horizontal fissures was higher. The study by Lakshmi et al. (2018) reported that the development of fissures might be incomplete due to genetic and environmental factors during the development of the lungs. The incidence rate of the absence of the horizontal fissures of the right lung was found to be 8.9%, and the prevalence of the variation was higher than that of oblique fissures. In their study, Kc et al. (2018) stated that the absence of horizontal fissures was a common variation. Ranaweera et al. (2022) reported in their study that the incompleteness or absence of lung fissures might result from a defect due to complete or incomplete obliteration of the fissures before birth. The completion, incompleteness, and absence rates of the right and left oblique fissures were almost close to each other. In addition, the prevalence of accessory fissures in the right and left lungs is similar. The prevalence of oblique and accessory fissures in our study was close to each other, indicating that the number of lungs in the 60 studies examined and the number of variations observed in the fissures were parallel to each other.

As a result of 20 studies investigating the prevalence of variation types of accessory fissures, the inferior accessory fissure had the highest prevalence in the right lung (8.9%), and the left horizontal fissure had the highest prevalence in the left lung (9.9%). In their study, Arıyürek et al. (2001) reported that the incidence of inferior accessory fissure is the most common in the right lungs. Yıldız et al. (2004) and Kılıç et al. (2006) stated in their study that the incidence of left horizontal accessory fissure is common in the left lungs. Accessory fissures are formed as a result of the absence of permanence or obliteration of prenatal fissures. Any change in the structure of prenatal fissures shows that the way the lung develops is different (Sailaja et al., 2019). Knowing the accessory fissures enables the fissure to be distinguished from the other normal and pathological ones. Furthermore, it is helpful for segmental localization in numerous diseases (Hema, 2014). Accessory fissures lead to sharply limited pneumonia by assuming a preventive responsibility against the spread of the infection (Godwin and Tarver, 1985). Accessory fissures may form accessory lobes depending on their localization. This finding is frequently seen in infants (Nene et al., 2011). Moreover, knowing accessory fissures is important, since they are often misevaluated or not identified while the lung is examined on radiographs and CT scans (Magadum et al., 2015).

As a result of 12 studies examining the prevalence of variations in the structures in the lung hilum, the incidence rate of a single pulmonary artery was found to be 49.9%, two pulmonary veins to be 47.4%, and a single bronchus to be 45.1% in the left lungs. The incidence rate of two or more arteries in the right lung was 38.2%, the incidence rate of a two pulmonary vein was 38.6%, and the incidence rate of two or more bronchi was 63.6%. Our findings overlap with the study done by Wahengbam et al. (2019). Murlimanju et al. (2012) stated in their studies that left lung hilum variations were higher than the right lung and the frequency of variation was not clearly explained in the textbooks. In their study, Kc et al. (2018) reported that the variations in the number and model of hilar structures in human lungs were not examined in detail. Also reported a higher incidence of 2 arteries in the right lungs compared with previous studies. The study by Jacob et al. (2019) revealed that almost no studies were conducted on the hilar pattern in the literature. In their study, Wahengbam et al. (2019) explained that, in addition to the shape in lung morphology, fissures and lobes, different variations of hilar structures may appear, and the range of these variations observed within large and different populations and affecting lung development might result from genetic or environmental factors or both. Considering all these facts, knowing the lobar and hilar anatomy of the lungs is of great significance for clinicians, surgeons, and radiologists (Jethva et al., 2019).

This study is limited, as the lungs were mostly studied on cadavers and the majority of the studies were from the Indian population. In addition, while the number of studies examining fissure

variations of the lungs is high in the literature, studies examining accessory fissures and hilar structures are rare. In new studies to be conducted with different methods and techniques, lung samples should be examined by considering gender and age differences, and new studies should be performed more comprehensively in different and larger populations, including types of accessory fissures and hilar structures.

CONCLUSION

Our study examined variation types of lung fissures and hilar structures and their incidences. The completion rate of the horizontal fissures of the right lung (56.5%) was lower than that of oblique fissures, and the rates of incompleteness (34.5%) and absence (8.9%) were higher than those of oblique fissures. The completion, incompleteness, and absence rates of the oblique fissures of the right and left lung were close to each other. The incidence rate of accessory fissures was higher in the left lungs (11.2%) than in the right lungs (%10.2), whereas the incidence rates of the horizontal accessory fissure (9.9%) in the left lung and the inferior accessory fissure (8.9%) in the right lung were the highest. While the incidence rates of a single pulmonary artery (49.9%), two pulmonary veins (47.4%) and single bronchus (45.1%) were the highest in the left lungs, the incidence rates of two or more pulmonary arteries (38.2%), two pulmonary veins (38.6), and two or more bronchi (63.6%) were the highest in the right lungs. In this study, will be useful for clinicians in interpreting radiological images, diagnosing lung pathologies, and applying surgical procedures. We think that knowing the variations of lung fissures and hilar structures will be theoretically and clinically beneficial.

ACKNOWLEDGEMENTS

The authors received no specific funding for this work. The authors disclose no conflict of interest.

REFERENCES

AGRAWAL R, SİNGHAL MK (2018) A cadaveric study of anatomical variation of fissures of lung. *J Med Sci Clin Res,* 6(7): 711-716.

AMBALİ MP, JADHAV SD, DOSHİ M, RAOSAHEB P, ROY P, DESAİ RR (2014) Variations of lung fissures: A cadaveric study. *J Krishna Inst Med Sci Univ,* 3(1): 85-89.

AMİN MAS (2020) Morphological variations of the Egyptian human lungs and its clinical applications. *Int J Anat Res,* 8(3.2): 7674-7679.

ANBUSUDAR K, DHİVYA S (2016) Anatomical study on variations of fissures of lung. *Indian J Clin Anat Physiol,* 3(4): 449-451.

ANJANKAR V, WANKHEDE KP, MANGALGİRİ A (2017) Morphological study of lung lobes and fissure: Anatomical basis of surgical and imaging technique. *Int J Anat Res,* 5(1): 3447-3450.

ARINCI K (2005) Arıncı Anatomy. The Respiratory System. 4th ed. Güneş Bookstore, Ankara, pp 299-303.

ARIYÜREK MO, GÜLSÜN M, DEMİRKAZIK F (2001) Accessory fissures of the lung: Evaluation by high-resolution computed tomography. *Eur Radiol,* 11(12): 2449-2453.

BAYTER PA, LEE GM, GRAGE RA WALKER, CM, SUSTER DI, GREENE RE, STOWELL JT (2021) Accessory and incomplete lung fissures: Clinical and histopathologic implications. *J Thorac Imaging,* 36(4): 197-207.

BOSTANCİ K, OZYURTKAN MO, POLAT MO, BATİREL H, LACİN T, YUKSEL M, STAMENOVİC D (2019) Variations in pulmonary fissural anatomy: A medicolegal autopsy study of 256 cases. *ANZ J Surg,* 90(4): 608-611.

CRONİN P, GROSS BH, KELLY AM PATEL S, KAZEROONİ EA, CARLOS RC (2010) Normal and accessory fissures of the lung: Evaluation with contiguous volumetric thin-section multidetector CT. *Eur J Radiol,* 75(2): 1-8.

DEVİ NB, RAO BN, SUNİTHA V (2011) Morphological variations of lung-A cadaveric study in north coastal Andhra Pradesh. *Int J Biol Med Res,* 2(4): 1149-1152.

DHANALAKSHMİ V, MANOHARAN C, RAJESH R, ANANTHİ KS (2016) Morphological study of fissures and lobes of lungs. *Int J Anat Res,* 4(1): 1892-1895.

DİVYA C, VENKATESHU KV, SWAROOP RAJ BV (2015) Anatomical study of pulmonary fissures and lobes. *Int J Recent Sci Res,* 6(6): 4554-4557.

DOGAN NU, UYSAL II, DEMİRCİ S, DOGAN KH, KOLCU G (2015) Major anatomic variations of pulmonary fissures and lobes on postmortem examination. *Acta Clin Croat,* 54(2): 201-207.

DRAKE RL, VOGL AW, MİTCHELL AWM (2020) Gray's Anatomy for Students. Thorax Pleural Cavities. 4th ed. Elsevier, Philadelphia, pp 170-179.

DUTTA S, MANDAL L, MANDAL SK, BİSWAS J, RAY A, BANDOPADHYAY M (2013) Natural fissures of lung-anatomical basis of surgical techniques and imaging. *Natl J Med Res,* 3(2): 117-121.

GANAPATHY A, TANDON R, BAXLA M, KALER S (2018) Cadaveric study of lung anatomy: A surgical overview. *J Med Res Innov,* 3(1): 1-4.

GAUTAM A, CHAULAGAİN R, DHUNGEL D (2021) Morphological variations of the lungs: A cadaveric study. *Nepal Med Coll J,* 23(4): 315-318.

GAYATHRİ P, SARİTHA S, RAMANİ T, NAGAJYOTHİ D, HİMABİNDU N, ANJUM A (2016) A study of morphological variations of fissures and lobes in human cadaveric lungs correlating with surgical implications in the Telangana Zone. *Int J Anat Res,* 4(4): 3221-3326.

GEBREGZİABHER A, BERHE T, EKANEM P (2015) Variations of fissures and lobes of the lungs in human cadavers in selected universities of Ethiopia. *Int J Pharma Sci Res,* 6(6): 981-990.

GEORGE BM, NAYAK SB, MARPALLİ S (2014) Morphological variations of the lungs: A study conducted on Indian cadavers. *Anat Cell Biol,* 47(4): 253-258.

GHOSH E, BASU R, DHUR A, ROY A, ROY H, BİSWAS A (2013) Variations of fissures and lobes in human lungs-a multicentric cadaveric study from West Bengal, India. *Int J Anat Radiol Surg,* 2(1): 5-8.

GL JYOTHİ LAKSHMİ, BHARATHİ D, SARALA HS (2018) Variations in pulmonary fissures: An anatomical study. *Int J Anat Res,* 6(3.3): 5597-5601.

GODWİN D, TARVER RD (1985) Accessory fissures of the lung. *AJR Am J Roentgenol,* 144(1): 39-47.

HEMA L (2014) Lungs lobes and fissures: A morphological study. *Int J Recent Trends Sci Technol,* 11(1): 122-126.

HENRY BM, TOMASZEWSKI KA, WALOCHA JA (2016) Methods of evidence-based anatomy: a guide to conducting systematic reviews and meta-analysis of anatomical studies. *Ann Anat,* 205: 16-21.

HENRY BM, TOMASZEWSKI KA, RAMAKRISHNAN PK, ROY J, VİKSE J, LOUKAS M, WALOCHA JA (2017) Development of the anatomical quality assessment (AQUA) tool for the quality assessment of anatomical studies included in meta-analyses and systematic reviews. *Clin Anat,* 30(1): 6-13.

HEŘMANOVÁ Z, ČTVRTLÍK F, HEŘMAN M (2014) Incomplete and accessory fissures of the lung evaluated by high-resolution computed tomography. *Eur J Radiol,* 83(3): 595-599.

JACOB SM, PİLLAY M (2013) Variations in the inter-lobar fissures of lungs obtained from cadavers of South Indian origin. *Int J Morphol,* 31(2): 497-499.

JACOB SM, VENNİYOOR V, PİLLAY M (2019) Variations in the morphology of human lungs and its clinical implications. *J Morphol Sci,* 36(4): 231-236.

JAİSWAL P, KOSER T, MASİH W, BİHARİ K (2017) Morphological variations in right human lungs in Rajasthan: A cadaveric study. *J Dent Med Sci,* 16(4): 6-10.

JAMES N, KUMARİ KG, MUGUNTHAN N (2019) Morphological study of lobes, fissures and pulmonary hilar structures. *Int J Anat Res,* 7(1.3): 6298-6301.

JETHVA NK, CHAVDA HS (2019) A cadaveric study on morphological variations of lobar and hilar anatomy of human lungs. *Int J Anat Res,* 7(1.2): 6250-6253.

JOSHİ A, MİTTAL P, RAİ AM, VERMA R, BHANDARİ B, RAZDAN S (2022) Variations in pulmonary fissure: A source of collateral ventilation and its clinical significance. *Cureus,* 14(3): 1-7.

KAUL N, SİNGH V, SETHİ R, KAUL V (2014) Anomalous fissures and lobes of human lungs of North Indian population of western UP. *J Anat Soc India,* 63(2): 26-30.

KC S, SHRESTHA P, SHAH AK, JHA AK (2018) Variations in human pulmonary fissures and lobes: A study conducted in Nepalese cadavers. *Anat Cell Biol,* 51(2): 85-92.

KHEDEKAR D, HATTANGDİ S (2017) Morphological variations of the lung: A cadaveric study in Mumbai population. *Int J Anat Res,* 5(3.2): 4313-4316.

KILIÇ C, KOCABIYIK N, YALÇIN B, KIRICI Y, YAZAR F, OZAN H (2006) Akciğerlerin aksesuar fissürleri. *SDÜ Tıp Fak Derg,* 13(3): 12-16.

KOMMURU H, SREE LD, HEMA PJ, SWAYAM JS (2013) Pulmonary fissures and lobar variations in relation to surgical & radiological implications. *IOSR J Dent Med Sci,* 5(1): 51-54.

KUMAR D, PENSİ D (2014) Morphological variations of the fissures & lobes in cadaveric human lungs in Gujarat State. *Int J Sci Res,* 3(2): 27-29.

KUMARİ MT, RAJASREE G, CHAGANTİ G, NAGARAJ S (2022) Variations in lung fissures and lobes morphology in population of Andhra Pradesh of South India (a cadaveric study). *Sib Sci Med J,* 42(4): 74-78.

MAGADUM A, DİXİT D, BHİMALLİ S (2015) Fissures and lobes of lung-an anatomical study and its clinical significance. *Int J Current Res Acad Rev,* 7(3): 8-12.

MAHMUT M, NİSHİTANİ H (2007) Evaluation of pulmonary lobe variations using multidetector row computed tomography. *J Comput Assist Tomogr,* 31(6): 956-960.

MAMATHA Y, MURTHY CK, PRAKASH BS (2016) Study of morphological variations of fissures and lobes of lung. *Int J Anat Res,* 4(1): 1874-1877.

MANİCKA VASUKİ AK, KRİSHNAN KK, JAMUNA M, JOY HEPZİBAH D, SUNDARAM KK (2019) Anatomical study of lobes and fissures of lungs and its clinical significance-a cadaveric study. *Int J Anat Radiol Surg,* 8(1): 15-19.

MANJUNATH M, SHARMA MV, JANSO K, JOHN PK, ANUPAMA N, HARSHA DS (2021) Study on anatomical variations in fissures of lung by CT scan. *Indian J Radiol Imaging,* 31(04): 797-804.

MANSUR DI, BİSTA N, SHRESTHA P, MASKEY S (2019) A study on morphological variations of fissures and lobes of human lungs with its clinical significance. *J Nobel Med Coll,* 8(2): 21-25.

MATHANGASİNGHE Y (2021) Morphological variations of lung lobes and fissures: A preliminary study. *Sri Lanka J Surg,* 39(3): 24-27.

MEENAKSHİ S, MANJUNATH KY, BALASUBRAMANYAM V (2004) Morphological variations of the lung fissures and lobes. *Indian J Chest Dis Allied Sci* 46(3): 179-182.

MURLİMANJU BV, PRABHU LV, SHİLPA K, PAİ MM, GANESH KUMAR C, RAİ A, PRASHANTH KU (2012) Pulmonary fissures and lobes: A cadaveric study with emphasis on surgical and radiological implications. *Clin Ter,* 163(1): 9-13.

MUTUA V, CHERUİYOT I, BUNDİ B, MONG'ARE N, KİPKORİR V, OTHİENO E (2021) Variations in the human pulmonary fissures and lobes: A cadaveric study. *Open Access Libr J,* 8(8): 1-13.

NAKHATE M, BAPAT R, SAWANT VG, GHOSHAL J (2017) Morphological variations of fissures of lungs in Indian Population. *Int J Innov Res Med Sci,* 2(6): 811-814.

NENE AR, GAJENDRA KS, SARMA MVR (2011) Lung lobes and fissures: A morphological study. *Anat*, 5(1): 30-38.

OZAN H (2014) Ozan Anatomy. The Respiratory System. 3rd ed. Medical Bookstore, Ankara, pp 242-246.

QUADROS LS, PALANİCHAMY R, D'SOUZA AS (2014) Variations in the lobes and fissures of lungs-a study in South Indian lung specimens. *Eur J Anat,* 18(1): 16-20.

RADHA K, DURAİ PK (2015) Fissures and lobes of lungs: A morphological and anatomical study. *Int J Anat Res*, 3(2): 995-998.

RANAWEERA L, SULANİ WN, NANAYAKKARA WLRL (2022) Morphological variations of human pulmonary fissures: An anatomical cadaveric study in Sri Lanka. *Ital J Anat Embryol,* 126(1): 161-169.

RANİ S, SHARMA J, SHARMA DK, SHARMA R, PAREEK B, SİNSİNWAR P (2020) Morphological anatomy of accessory fissures in lungs and its surgical importance. *Int J Sci Res*, 9(1): 25-26.

SAHA A, SRİMANİ P (2019) Comprehensive study of pulmonary hilam with its clinical correlation. *Ann Anat,* 222: 61-69.

SAİLAJA G, SUDHAKARA RAO M, SATİSH KUMAR P (2019) Anatomical study of pulmonary fissures and lobes in human cadavers. *IOSR J Dent Med Sci,* 18(4): 45-49.

SANGEETHA A, NAYEEMUDDİN SM, CHAKRADHAR V, NANDHA KUMAR S (2019) Variations of human lung fissures and its clinical significance- A cadaveric study. *Int J Sci Res,* 8(5): 663-665.

SHİNDE AA, PATEL DK (2022) Morphometric variations in lobes and fissures of the lung: A cadaveric study in Pune region of Maharashtra. *Natl J Clin Anat,* 11(3): 154-158.

SHİVALEELA C, LAKSHMİPRABHA S, AFROZE MKH (2018) A study of anatomical variations in patterns of fissures and lobes in human lungs: A cadaveric study with clinical significance. *Int J Anat Res,* 6(1.1): 4819-4823.

SİNGH AK, NİRANJAN R (2014) A cadaveric study of anatomical variations of fissures and lobes of lung. *Natl J Clin Anat,* 3(2): 76-80.

SK ZAREENA (2014) A study of morphology and variations of lungs in adults and foetus. *Int J Adv Res Technol,* 3(4): 150-157.

SUBADHA C, GAYATHRİ M (2019) An anatomical study of variation in fissures and lobar pattern of human lungs. *Int J Anat Res,* 7(1.1): 6059-6063.

SUMALATHA J, SUNİL KUMAR U (2019) A study on fissural anatomy of lungs in adult human cadavers – Its clinical importance. *IOSR J Dent Med Sci,* 18(3): 49-52.

TALLAPANENİ S (2016) Variations of fissures and lobes in adult human lungs: A cadaveric study from Telangana. *Int J Anat Res,* 4(4): 3267-3272.

THAPA P, DESAİ SP (2016) Morphological variation of human lung fissures and lobes: An anatomical cadaveric study in North Karnataka, India. *Indian J Health Sci Biomed Res (KLEU),* 9(3): 284-287.

UGALDE P, DE JESUS CAMARGO J, DESLAURİERS J (2007) Lobes, fissures and bronchopulmonary segments. *Thorac Surg Clin,* 17(4): 587-599.

UGHADE JM, KARDİLE PB, TEKADE PR (2018) Variation in lobes and fissures of lung. *Int J Anat Res,* 6(1.3): 5020-5023.

VARALAKSHMİ KL, NAYAK NJ, SANGEETHA M (2014) Morphological variations of fissures of lung: An anatomical study. *Indian J Appl Res,* 4(8): 467-469.

WAHANE A, SATPUTE C (2015) A cadaveric study of morphological variations of lung in Vidarbha region. *Int J Sci Res,* 4(1): 2163-2166.

WAHENGBAM S, DEVİ HR, TARUNKUMAR G (2019) Morphological study of human lungs. *Int J Anat Res*, 7(2.1): 6345-6352.

WASCHKE J, BÖCKERS TM, PAULSEN F (2016) Sobotta Anatomi Konu Kitabı. In: Mustafa Fevzi Sargon (ed.). *Thorax İçerisinde Yer Alan Organlar*. 1st ed. Güneş Medical Bookstore, Ankara, pp 279-285.

WEST CT, SLİM N, STEELE D, CHOWDHURY A, BRASSETT C (2020) Are textbook lungs really normal? A cadaveric study on the anatomical and clinical importance of variations in the major lung fissures, and the incomplete right horizontal fissure. *Clin Anat,* 34(3): 387-396.

YILDIZ A, GÖLPINAR F, ÇALIKOĞLU M, DUCE MN, ÖZER C, APAYDIN FD (2004) HRCT evaluation of the accessory fissures of the lung. *Eur J Radiol,* 49(3): 245-249.

European Journal of Anatomy